

Electromagnetic and Quasi-Optical Analysis of Cavity Coupled Bolometers for Far-Infrared and Terahertz Receivers

Presented by

Eimantė Kalinauskaitė, B.Sc.

A thesis submitted for the degree of

Doctor of Philosophy



Terahertz Space Optics Group,

Department of Experimental Physics,

Maynooth University,

National University of Ireland, Maynooth,

Maynooth,

County Kildare,

Ireland

August 2018

Research Supervisor

Prof. J. Anthony Murphy

Head of Department

Prof. J. Anthony Murphy

<u>1</u>	<u>INTRODUCTION</u>	<u>1</u>
1.1	OVERVIEW	1
1.2	TECHNOLOGY RESEARCH PROGRAMME	2
1.3	FAR-IR ASTRONOMY MISSIONS	4
1.4	SPICA SPACE OBSERVATORY	8
1.5	THE PLANCK SATELLITE AND THE COSMIC MICROWAVE BACKGROUND	11
1.6	FOREGROUND SOURCES	16
1.7	DETECTOR TECHNOLOGY	18
1.8	THESIS OVERVIEW	21
<u>2</u>	<u>SINGLE MODE AND MULTIMODE HORN ANTENNAS</u>	<u>24</u>
2.1	INTRODUCTION	24
2.2	CYLINDRICAL WAVEGUIDE MODES	26
2.3	MODE MATCHING IN CYLINDRICAL WAVEGUIDES	35
2.4	MODE MATCHING IN CYLINDRICAL WAVEGUIDES WHEN ABSORBER IS INCLUDED	44
2.5	MODE COUPLING AT A CIRCULAR ABSORBER IN A CIRCULARLY SYMMETRIC SYSTEM	47
2.6	RECTANGULAR WAVEGUIDE MODES	50
2.7	MODE MATCHING IN RECTANGULAR WAVEGUIDES	55
2.8	OTHER ELECTROMAGNETIC ANALYSIS TECHNIQUES	59
2.9	EXPERIMENTAL VERIFICATION OF MULTIMODE PROPAGATION	63
2.9.1	VECTOR NETWORK ANALYSER	64
2.9.2	EXPERIMENTAL SETUP	65
2.9.3	COMPARISON OF MEASUREMENTS WITH THEORETICAL PREDICTIONS	66
2.10	CONCLUSION	76
<u>3</u>	<u>QUASI-OPTICAL PROPAGATION AND THE DESIGN OF A 4MM RECEIVER FOR THE ONSALA SPACE OBSERVATORY</u>	<u>77</u>
3.1	INTRODUCTION	77
3.2	GAUSSIAN BEAM MODE ANALYSIS	79
3.3	GRASP9 SOFTWARE DESCRIPTION	82
3.4	DESIGN PARAMETERS OF CORRUGATED HORNS	87
3.5	4 MM OSO CHANNEL DESIGN	89
3.5.1	CORRUGATED HORN WITH 30 MM APERTURE (WIDER APERTURE)	90
3.5.2	CORRUGATED HORN WITH 18.8 MM APERTURE (NARROWER APERTURE)	97
3.5.3	PROFILED HORN DESIGN	101
3.6	TOLERANCE ANALYSIS	103
3.7	MODELLING OF THE OSO 4 MM RECEIVER CHANNEL IN GRASP9	110
3.8	CONCLUSION	117

<u>4</u>	<u>MODELLING OF CAVITY COUPLED BOLOMETERS USING MODE MATCHING TECHNIQUES</u>	118
4.1	INTRODUCTION	118
4.2	MODELLING OF ABSORBING CAVITIES	121
4.3	SOFTWARE VERIFICATION	124
4.4	ABSORBER OF ARBITRARY SHAPE	131
4.5	OFFSET ABSORBING CYLINDRICAL CAVITIES	143
4.5.1	IMPLEMENTING OFFSETS IN GAMMA	144
4.5.2	CODE VERIFICATION	149
4.6	OPTIMIZATION OF CAVITY DESIGN	155
4.7	CONCLUSION	159
<u>5</u>	<u>THE PLANCK MULTIMODE CHANNELS</u>	162
5.1	INTRODUCTION	162
5.2	HYBRID MODES	165
5.3	BEAM PATTERN SIMULATIONS OF THE 857 GHz CHANNEL	166
5.4	INCLUDING THE FILTER GAP	169
5.5	MODELLING THE DETECTOR IN THE CAVITY	174
5.6	MODELLING OF THE PLANCK TELESCOPE IN GRASP9	182
5.7	PRE-LAUNCH LABORATORY MEASUREMENTS	192
5.8	PLANCK 545 GHz CHANNEL	196
5.9	CONCLUSION	203
<u>6</u>	<u>INCLUDING FREE SPACE PROPAGATION AND OPEN CAVITIES IN GAMMA</u>	205
6.1	INTRODUCTION	205
6.2	WAVEGUIDE TO FREE SPACE COUPLING	206
6.3	IMPLEMENTING AN ABSORBER IN FREE SPACE	211
6.4	EXAMPLE CASE OF ABSORBER IN AN OPEN CAVITY WITH INFINITE WALLS	216
6.5	EXAMPLE CASE OF ABSORBER IN AN OPEN CAVITY WITH POWER LOSS THROUGH THE GAP	220
6.6	MODELLING A SAFARI-LIKE PIXEL	224
6.7	CONCLUSION	230
<u>7</u>	<u>CONCLUSIONS</u>	232
<u>8</u>	<u>REFERENCES</u>	239

Abstract

The primary concern of this thesis is the development of theoretical and computational techniques for the modelling of cavity coupled bolometric detectors for future millimetre wave and terahertz astronomical receivers. Hypersensitive bolometer based receivers will be required to answer current open questions in astronomy concerning star and planetary formation, solar system physics as well as galaxy evolution and interaction. As part of the work for this thesis, fast and efficient Python code, GAMMA (Generalised Absorber Mode Matching Analysis), was developed and applied to existing and proposed future systems.

One of the main goals of GAMMA was to analyse the performance of the proposed multimode pixel for the SAFARI instrument on the next generation SPICA terahertz space telescope. The pixels contain a free space gap between the horn and the cavity. The array of detectors will lie on a chip with an array of horns feeding them from the frontside and an array of backshort cavities behind them. The beam patterns for a SAFARI-like pixel were computed, using a direct calculation of the power absorbed by the bolometer in free space. This shows how the formalism can be used to directly calculate the power absorbed by a detector in a realistic terahertz receiver system.

The impact of the various potential manufacturing tolerance levels for the feed horn on the predictions of the beam on the sky were also analysed for a millimetre-wave system. The specific example considered was the new 4 mm receiver on the Onsala Space Observatory 20 m millimetre-wave telescope. Mode matching, Gaussian Beam Mode Analysis and Physical Optics were used to determine the behaviour of the optical relay system.

GAMMA was also applied to the multimode 857 and 545 GHz ESA Planck HFI channels. Agreement between previous predictions and both laboratory and in-flight measurements reported in literature was improved on.

Acknowledgements

I would like to express my sincere thanks to my supervisor Prof. J. Anthony Murphy for his support and guidance over the years of this work. His door was always open and he had unlimited time and patience to discuss my research. It has been enjoyable to work with and learn from him.

I would also like to thank the other members of the Terahertz Space Optics group, Dr. Cr  idhe O’Sullivan, Dr. Marcin Gr  dzziel and Dr. Neil Trappe for their advice and assistance throughout. Thanks also go to the other academic staff of the Department of Experimental Physics, Dr. Frank Mulligan, Dr. Emma Whelan, Dr. Peter van der Burgt and Dr. Michael Cawley, who made my time here enjoyable, both during my undergraduate and postgraduate years.

I would like to express my appreciation to the administrative and technical staff of the department, including Ms. Gr  ainne Roche for her friendship and advice, Mr. John Kelly for support with computer related issues, Mr. Derek Gleeson for his help with technical issues, Mr. Dave Watson for making some components for my experimental work, Mr. Pat Seery for helping me out in the third year laboratory and Ms. Marie Galligan for her help in both the first and third year laboratories.

I would like to thank Dr. Darragh McCarthy and Mr. George Walker for their help with the 4 mm receiver channel design. Thanks also go to Dr. Ian McAuley and Dr. Dan Wilson whose work on the Planck HFI proved to be very helpful for my own. I would also like to thank Dr. Stephen Doherty for providing me with his version of the Mathematica SCATTER code and sharing his expertise with me.

Thanks to the staff at the Onsala Space Observatory: Dr. Miroslav Pantaleev, Dr. Leif Helldner and Mr. Jonas Flygare for their collaboration on the 4 mm receiver channel design and for providing me with the opportunity to visit the Onsala Space Observatory.

I would like to thank my fellow postgraduates: Joe, Mark, Sharon, Julianne, David, Donnacha, Eoin, Aisling and James, and former postgraduates: Niamh, Anthony, Adam, Rory, George, Andrew, Niall, Stephen, Steven, Fiachra, Melissa and Michael. Thank you for your friendship and making the past 4 years so enjoyable. Special thanks to Sharon, Joe and Julianne for proof reading my thesis with a great level of detail and also for your words of encouragement. Thank you to Adam for helping me get started with GRASP9.

Thank you also to Niamh and Anthony for helping me with my transition from undergraduate to postgraduate.

I am very grateful for the financial support I received through the European Space Agency (ESA) science programme for the Strategic Initiative for Irish Industry, Academia and Research Institutions.

Finally, a special thank you to my family – Mum, Dad, Martynas and Minnie – for always believing in me and offering your encouragement and support during all my years of studying.

1 Introduction

1.1 Overview

The main subject of this thesis is the quasi-optical and electromagnetic design and analysis of millimetre wave and far infrared receiver systems. In this chapter an overview of the motivation for the detailed work undertaken in this thesis, including the science drivers which set challenging technical requirements for the receiver systems, will be presented.

The terahertz (THz) band occupies the part of electromagnetic spectrum between the infrared and microwaves. It is loosely defined to lie between a frequency of 0.1 THz to 10 THz (wavelength of 30 μm to 3 mm). However, sometimes it is more conservatively defined to lie between 0.3 THz and 3 THz, since below 0.3 THz (300 GHz or wavelength of 1 mm) it is also referred to as the millimetre-wave band and above 3 THz (100 μm) the mid-infrared begins.

For a number of years, much research effort has been expended in order to accurately predict the electromagnetic performance of terahertz receiver systems. Prior to the work in this thesis, the program SCATTER (Colgan, 2001; Gleeson, 2004), based on the mode matching technique (Wexler, 1967) and written in Mathematica, was developed to accurately predict the beam patterns of horn antennas, both of cylindrical and rectangular geometries. The technique has been applied to both single mode coherent detector systems and incoherent multimode bolometric detectors. Generally, a thorough analysis of the horn, absorber and cavity system is required for a complete understanding of a typical multimode bolometric system in the far-infrared. Horn antennas coupled to absorber cavities operating at high frequencies are, however, computationally intensive to model as they tend to be electrically large (in terms of wavelength). With the development of large arrays of direct detectors, many real systems now employ a free space gap between the feed horn and the detector cavity, which could not be adequately modelled with the SCATTER code. Commercial software packages, such as CST, which use Finite Element Analysis, are also computationally intensive and cannot easily model electrically large systems.

It is for these reasons that a Generalised Absorber Mode Matching Analysis (GAMMA) software has been developed, which was one of the main achievements of this thesis. GAMMA is structured in a similar way to the SCATTER software, however, it is now written in Python. It is able to model electrically large structures in a computationally time efficient manner in comparison to the Mathematica SCATTER code. Absorber cavities can also be efficiently modelled in GAMMA and the absorber can be of an arbitrary shape. This has proved to be a significant advancement on previous code capabilities. The software can also model misalignments between sections, such as between an absorbing cavity and its feed waveguide, where the misalignments are deliberate in an attempt to capture more power at the absorber. This feature of the software could also be applied for tolerance analysis of section misalignment for corrugated horns manufactured using the stacked rings approach, for example. GAMMA is able to couple cylindrical waveguide modes to Bessel beams (modes, which can be used to describe free space propagation), and it was thus used to model a SAFARI-like pixel where there exists a free space gap between the horn and the cavity and the absorber is placed in the free space gap. Standard, on-axis, rectangular horn antennas can also be modelled using the GAMMA software. Thus, with the innovations made to the mode matching technique, systems with very high coupling to the incoming signal can be designed, as will be discussed in this thesis.

The output from the GAMMA software has been used as input to the GRASP physical optics programme to allow the horn beams to be propagated through the telescope and optical systems so as to predict the beams on the sky for a number of millimetre-wave and terahertz systems (the Planck high frequency channels and the Onsala Space Observatory 4 mm channel on the 20 m millimetre-wave telescope)

The final section of this chapter consists of an outline of the chapters which make up the rest of this thesis.

1.2 Technology Research Programme

The main driver for the work in this thesis was a successful proposal by Maynooth University under the European Space Agency (ESA) science programme for the Strategic Initiative for Irish Industry, Academia and Research Institutions, which was concerned with the development of receiver technology (in particular optics) for future mm-wave

and far-infrared applications. The SPICA mission, summarised in Section 1.4, is one of the future missions under consideration requiring such technology and the proposed SAFARI instrument in particular is relevant for the work presented in this thesis.

As part of the ESA Special Initiative programme, the main work packages of the proposed research are outlined in Table 1.1.

WP 1	Optical characterisation of low noise TES detectors
WP 1.1	Profiled horn design
WP 1.2	Design and analysis of the far-IR TES detector cavity structures
WP 1.3	Experimental verification of the optical analysis of far-IR TES detector array
WP 1.4	Telescope optics coupling to waveguide / cavity mounted TES devices
WP 2	Technology development and component test facilities for future B-polarisation missions
WP 2.1	Development of high precision experimental verification capability
WP 2.2	Analysis and experimental verification of refractive components for potential focal plane pixel designs
WP 3	Other ESA programmes
WP 3.1	Other instruments proposed and under study related to far-infrared astronomy

Table 1.1: Summary of work packages

The author of this thesis was involved in the analysis of far-IR TES detector cavity structures as part of WP 1.2 and the analysis of the Planck multimode horns (857 GHz and 545 GHz) as part of WP 3.1.

Work as part of WP 1.2 included the development of the required software tools, as modelling such multimode horn-absorber-cavity combinations at high frequencies presents difficulties for standard simulation packages due to their electrically large nature. In this case, mode matching may be used as a more computationally efficient alternative technique (*i.e.* the GAMMA software referred to earlier). As part of this programme, techniques were developed to analyse the efficiency of SAFARI-like pixel geometries and also model absorbers of arbitrary shapes both on-axis and offset. The GAMMA code developed can also extract the power absorbed directly at the absorber, which is useful when distinguishing between power absorbed and power lost through a free space gap.

Some work was also continued in the case of other relevant missions and projects. In WP 3.1, the analysis of the Planck multimode horns and optics was improved upon, for example, and is reported on in this thesis. The Planck multimode horns on the high

frequency instrument (HFI) at 545 and 857 GHz were analysed more precisely as part of the work of this thesis, by taking a more detailed model of the back-to-back horn configuration into account. The eigenmodes of the horn were propagated through the Planck telescope and onto the sky using Physical Optics techniques (GRASP9 software). Comparisons were made (Chapter 5) with existing simulations (McAuley, 2015; Wilson, 2014) and laboratory measurements bringing better understanding to the original measurements.

1.3 Far-IR Astronomy Missions

A significant portion of the photons in the universe fall within the far-IR band as illustrated in Figure 1.1 below.

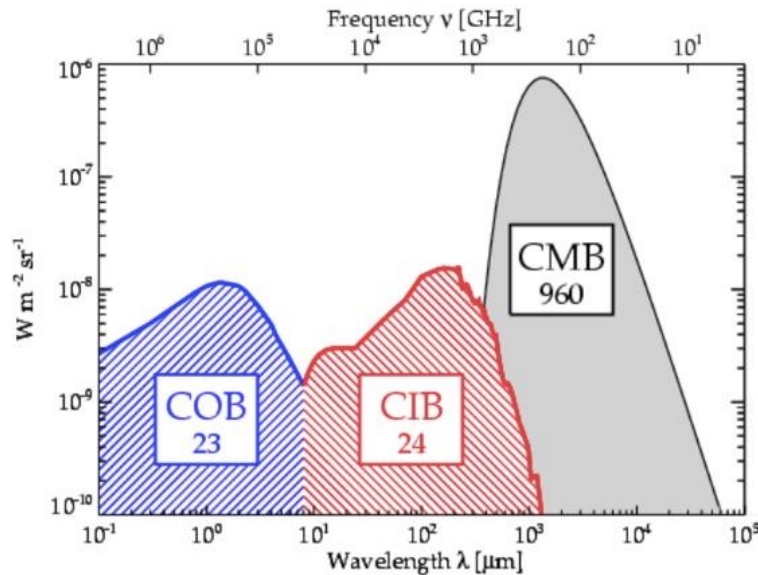


Figure 1.1: Spectral energy distributions of the extragalactic background (blue is cosmic optical background, red is cosmic infrared background and grey is cosmic microwave background) (Dole *et al.*, 2008)

The cosmic infrared background (CIB) is the emission at sub-mm wavelengths of the formation and evolution of galaxies, including active galactic nuclei (AGN) and star-forming systems (Puget *et al.*, 1996). The spectral energy distribution of the CIB peaks near 1 THz and accounts for approximately 50% of the energy in the optical/infrared extragalactic background.

The birth and much of the growth of galaxies, stars and planets occurs in regions hidden by a thick blanket of dust, which is opaque at optical wavelengths. Thus, a more complete

physical understanding of many processes that occur in the Universe is only possible with sensitive observations at infrared emissions, which can penetrate dust and reveal the details of star and planet formation in galaxies.

In general, observations at different wavelengths provide information about different physical and chemical processes in the universe, where different observation methods are required, depending on which band is being observed. Certain features that are visible in one part of the electromagnetic spectrum through their emissions become transparent in others. This is illustrated in Figure 1.2 below, which shows Messier 16 (‘Eagle nebula’).



Figure 1.2: M16 as viewed at visible, near infrared, far-infrared, mid-infrared, millimetre and sub-millimetre waves and X-rays (sci.esa.int, 2012)

The image taken at visible wavelengths shows the shadow of dark dust clouds, while at near-IR wavelengths, the dust becomes almost transparent. In the far-IR, the emission from the cool gas and dust can be observed, with each wavelength band representing a different temperature. Observations in the sub-millimetre band reveal the inner structure of the nebula. In the X-ray region, observations show hot young stars. Detecting radiation at these wavelengths and combining the data is essential in order to build a more complete picture of the interior structure of this star forming region. The same is true for many different physical processes including star formation and galaxy evolution.

Observations with previous space missions in the far-infrared have improved our knowledge of such processes. We shall now consider the Herschel Space Observatory (HSO) (Pilbratt, 2003) (see Figure 1.3), which was an ESA operated space observatory. Herschel was an infrared telescope with a primary mirror of 3.5 m and instruments capable of operating in the far-infrared and sub-millimetre wavelength range (55 – 672 μm), which, to date, is the only space facility ever developed to cover the far-infrared to submillimeter parts of the spectrum. It opened up parts of the spectrum which were almost unexplored and could not be observed from ground due to atmospheric effects. The telescope itself is a Cassegrain design with a primary mirror of 3.5 m in diameter, passively cooled to 80 K (sci.esa.int, 2010). It was launched on the 14th of May, 2009 along with ESA's Planck satellite on board an Ariane 5 rocket. The HSO continued observations of the sky for almost 4 years, until it ran out of coolant on the 29th of April, 2013.



Figure 1.3: Herschel Space Observatory (sci.esa.int, 2010)

The three scientific instruments aboard the craft were: HIFI (Heterodyne Instrument for the Far Infrared), PACS (Photodetector Array Camera and Spectrometer), SPIRE (Spectral and Photometric Imaging Receiver). HIFI was a high resolution heterodyne spectrometer, PACS was an imaging photometer / medium resolution grating spectrometer and SPIRE was an imaging photometer / imaging Fourier transform spectrometer.

The key science questions answered by Herschel include how galaxies formed in the early universe, issues related to interstellar medium physics, star formation and also

phenomena associated with cometary and planetary atmospheres. We now consider the significance of each one of the areas:

- (i) **Star formation and its interaction with the interstellar medium:** Star formation is the process by which dense regions within large molecular clouds of gas and dust collapse under gravity and fragment, becoming denser and hotter. When the pressure and density become sufficiently large, nuclear fusion in which hydrogen is converted into helium takes place (protostar formation). Observation of newly formed protostars is important for the investigation of the processes involved with star and planet formation. Newborn stars emit radiation at UV and visible wavelengths, approximately half of which is absorbed by the neighbouring dust grains and re-radiated at longer wavelengths (mid-IR, far-IR and sub-mm) (Carroll and Ostlie, 2007: 398). Observations in the far-IR and sub-mm bands of the spectrum thus can reveal protostars (and protoplanetary disks also). Moreover, circumstellar dust and gas making up the disks also emit at these wavelengths.
- (ii) **Galaxy formation in the early universe and the evolution of galaxies:** Redshifted wavelengths of distant objects cause the peak of the dust emission to move from far-IR to sub-mm wavelengths, and, since Herschel covered both of these parts of the spectrum, the observations complement one another, allowing for the study of star formation in both nearby and distant galaxies in the early universe. Herschel allowed astronomers to resolve the CIB radiation into individual active star forming galaxies at an epoch where star formation was roughly ten times greater on average than it is now.
- (iii) **Molecular chemistry of planetary, cometary and satellite atmospheres:** Data compiled by HIFI was used to investigate the role of water in the Universe. Absorption lines corresponding to the lowest energy (ground) state of water vapour are found in the far-IR sub-mm parts of the spectrum. Due to its spectral resolution, HIFI was sensitive to ~40 different transitions of the water molecule.

Figure 1.4 below shows a comparison of the view of M51 (Whirlpool Galaxy) in the Far Infrared (160 μm) as imaged by Spitzer (infrared space telescope launched by NASA) and Herschel.

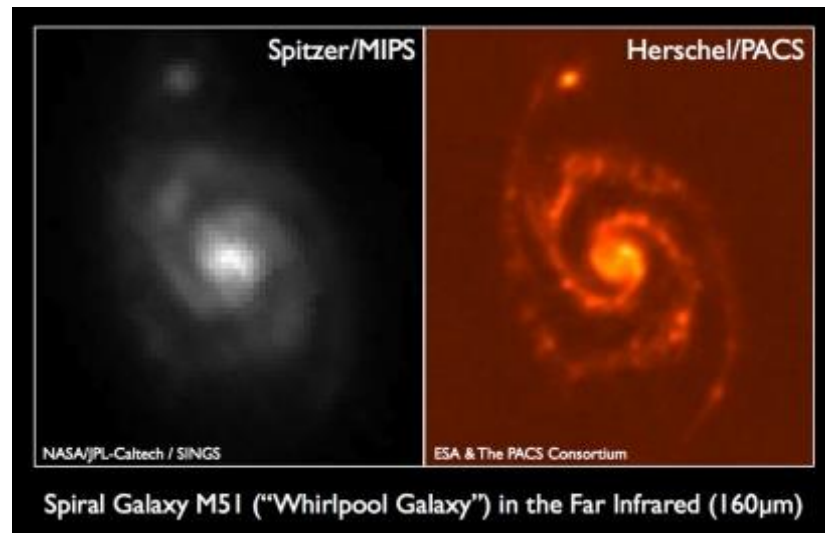


Figure 1.4: M51 as viewed by Spitzer (left) and Herschel (right) at 160 μm (sci.esa.int, 2009)

The advantage of the 3.5 m primary mirror of Herschel to the 0.85 m of Spitzer is clearly evident here as Herschel reveals structures that cannot be detected by Spitzer due to the improved resolution and sensitivity.

1.4 SPICA Space Observatory

Future far-infrared space missions, such as SPICA, aim to build on the work carried out by previous missions (such as Herschel), by looking deeper into space than their predecessors. The Space Infrared telescope for Cosmology and Astrophysics (SPICA) is a proposed space based infrared telescope (see Figure 1.5), aiming for launch in the latter part of the 2020s, with a mission duration of 3 years (nominally 5 years). It is a joint project between JAXA (Japan Aerospace Exploration Agency) and ISAS (Institute of Space and Astronautical Science) of Japan, and ESA. It will have a primary mirror of 2.5 m diameter (current design (spica-mission.org, 2017)) and will be cooled below 8 K. The three scientific instruments aboard will be: SMI (SPICA Mid Infrared Instrument), SAFARI/SPEC (SPICA Far-IR Instrument: spectrometer), SAFARI/POL (SPICA Far-IR Instrument: polarimeter).

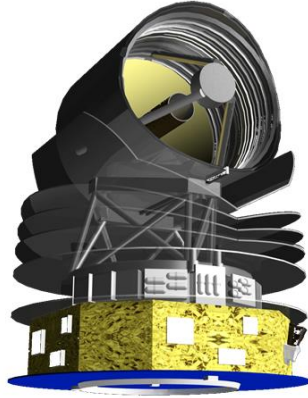


Figure 1.5 : SPICA space observatory (spica-mission.org, 2017)

The instrument on SPICA of most relevance to this thesis is SAFARI (SpicA FAR-Infrared instrument), which is a grating spectrometer covering a wavelength range of 34 – 210 μm . The proposed SAFARI instrument will use the mid- / far-infrared portion of the electromagnetic spectrum in order to study the evolution of galaxies.

In order to carry out new investigations with SPICA that were not possible previously, high sensitivity and spatial resolution are required. For high spatial resolution, a large primary mirror is needed. Due to the high sensitivities also required however, the mirror must be cooled to low temperatures, which is challenging due to the size of the mirror. Therefore, in the case of SPICA, making use of the cryogenically cooled primary mirror (at 4.5 K (spica-mission.org, 2017)) of the telescope, the goal is to achieve a sensitivity such that it could detect infrared sources two orders of magnitude fainter than the detection capability of Herschel.

SPICA will build on previous work carried out by Herschel by extending the frequency range to cover the full far-IR band and will complement future work of the Atacama Large Millimeter Array (ALMA) and the James Webb Space Telescope (JWST). It will close the gaps between the low frequency of the near-IR bands of the JWST and the upper frequency limit of the sub-mm bands of ALMA.

The primary goal of SPICA will be to understand how galaxies, stars and planets form and evolve as well as to investigate the interaction between the astrophysical processes that have led to the formation of our own Solar system. It will target young gas giant planets, protoplanetary disks, galactic and extragalactic star forming regions, luminous

IR galaxies, AGN and starburst galaxies at high redshift as well as performing deep cosmological surveys (spica-mission.org, 2017).

SPICA's highest resolution modes will be used to quantify gas disk dispersal processes such as jets, and winds and then link this to various disk geometries/structures such as gaps, holes and asymmetries. The high sensitivity and resolution of SMI will allow for the determination of accretion and disk winds from proto-planetary disks and establish the lifetime of primordial gas in the disk.

Having access to many diagnostic infrared lines, SPICA will help to analyse the mechanism driving galaxy evolution. It will also provide insight on the connection between the peak in star formation and black hole growth at redshift $z \sim 2$ and measure obscured starbursts and AGN out to $z = 4$.

SPICA will also probe the history of metal and dust production over the age of the universe and improve the understanding of magnetic fields and turbulence in the process of star formation.

SAFARI Instrument

The SAFARI instrument is an imaging spectrometer consisting of an infrared camera with approximately 3300 pixels. Fourier transform spectroscopy is used to obtain spectral information allowing for the determination of the chemical composition of the sources being observed.

The detectors consist of a multimode horn feeding a cavity containing a superconducting absorbing layer which is used with a transition edge sensor (TES) coupled bolometer to measure the absorbed power (as in Figure 1.6). The proposed cavity is hemispherical, which will retain any power that was not absorbed by the absorber and cause it to make further passes of the absorber, increasing the total amount of absorbed power.

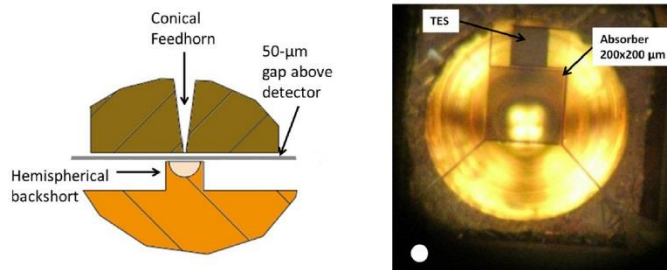


Figure 1.6: Single SAFARI pixel (Audley, 2014)

SAFARI will operate over the following wavelength bands: S-band (34-60 μm), M-band (60-110 μm) and L-band (110-210 μm). Each band requires a large number of high sensitivity pixels challenging existing detector technology (Audley, 2014).

The SAFARI instrument will use the mid- / far-infrared portion of the electromagnetic spectrum. It will analyse the radiation from the processes that drive galactic evolution, which are obscured by dust that is opaque at other frequencies, making the mid/far infrared so powerful when these processes are required to be studied.

1.5 The Planck Satellite and the Cosmic Microwave Background

The Cosmic Microwave Background (CMB), is the electromagnetic remnant of the very early dense, hot Universe. At approximately 380,000 years old, the early Universe had cooled to a temperature of about 4000 K and contained a primordial soup of free nuclei, electrons and photons. The mean free path of the photons was short since they interacted strongly with free electrons via Thomson scattering. As the universe expanded and cooled further, the photons lost energy until they were no longer able to ionise any atoms that formed in a process is known as recombination (Carroll and Ostlie, 2007: 1181) The photons were now free to travel essentially subject only to the effects of cosmological redshift. This ‘background’ radiation, expanding with the universe, continues to fill all space. The photons today appear to originate from a spherical surface, with a radius equal to their travel distance since last scattering, at approximately 380,000 years after the big bang (known as the last scattering surface) and is known as the Cosmic Microwave Background radiation as the wavelength of the photons has been redshifted onto the microwave/millimetre wave part of the electromagnetic spectrum.

The CMB was discovered by Arno Penzias and Robert Wilson in 1964 when they were working to re-purpose a Bell Laboratories horn antenna (see Figure 1.7) in New Jersey. They were unable to find the source of the noise from their microwave antenna signal encountered at a level of approximately 3.5 ± 1.0 K (Penzias and Wilson, 1965).

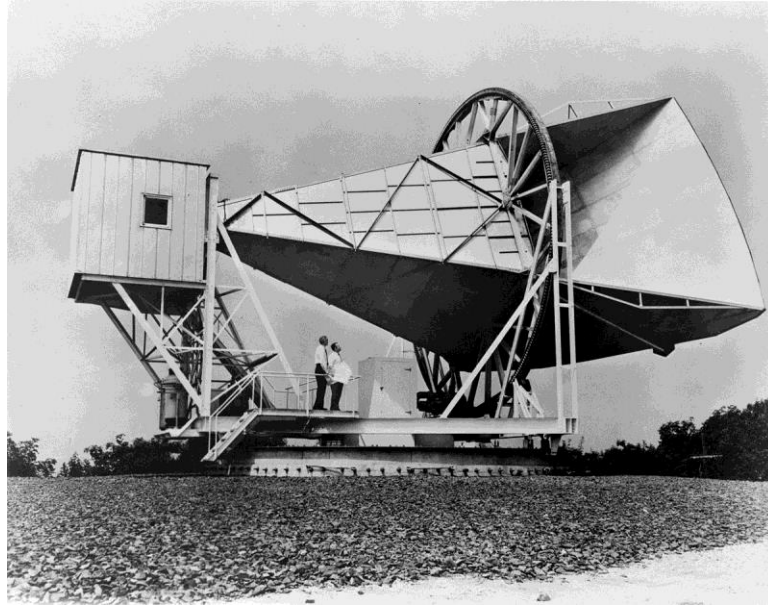


Figure 1.7: Holmdel Horn Antenna where the CMB was first detected (Carroll and Ostlie, 2007)

Having ruled out other possible sources they concluded that this noise must be coming from outside our own galaxy. They were put in touch with Robert Dicke who realized they had detected the CMB radiation from the Big Bang (Dicke *et al.*, 1965).

Since its discovery by Penzias and Wilson, numerous observations of the CMB have been made by both ground based and space based experiments. Ground based observations are limited in the number of frequency bands which can be viewed from Earth due to atmospheric absorption. For example, in the far-infrared range the atmosphere is opaque. This attenuation of the far-infrared signals due to the Earth's atmosphere would limit the accuracy of the detection of faint B – mode (faint features of the CMB polarisation) signals. Space based missions are better suited to study the CMB in greater detail as they can achieve the required sensitivity, frequency and sky coverage required.

Measurable properties of the CMB

Any observer who is at rest with respect to the Hubble flow, which describes the motion of galaxies solely due to the expansion of the universe, will observe the CMB spectrum with the same intensity in all directions (isotropic CMB). There exists a Doppler shift of the CMB which is caused by an observer's peculiar velocity through space (relative to Hubble flow).

After the dipole anisotropy has been subtracted from the CMB, the remaining background radiation is highly isotropic with the intensity being almost equal in all directions. However, sensitive instruments have revealed that the CMB has hotter and cooler areas. Multipole moments are useful for describing the CMB anisotropies, which can be described as a sum of spherical harmonic multipoles (Liddle, 2003: 152).

$$\frac{\Delta T}{T}(\theta, \phi) = \sum_{lm} a_{lm} Y_m^l(\theta, \phi) \quad (1.1)$$

where $Y_m^l(\theta, \phi)$ are the multipole moments. The largest possible angular scale measurement corresponds to a multipole moment of $l=0$ (360° , or the entire sky). At this scale, the CMB is isotropic. At $l=1$ (equivalent angular scale of 180°), the dipole fluctuation can be observed. At $l=2$ (quadrupole anisotropy) the polarisation of the CMB photons arises.

The polarisation of the CMB photons, which comes from the Thompson scattering of the CMB photons by free electrons in the photon-baryon fluid, is extremely difficult to detect. The magnitude of the polarization signal is less than 1% of the size of the temperature fluctuations (Carroll & Ostlie, 2007: 1270). Complications, such as polarized foreground radiation due to galactic synchrotron and thermal dust emission, must be accounted for. The resultant field can be decomposed into scalar E -modes and tensor E -modes and B -modes, where E -modes have a vanishing curl and B -modes have vanishing divergence. In order to test inflationary models of the early Universe via the detection of B -modes, which are introduced by primordial gravitational waves, the study of the polarisation of the CMB with high sensitivity is required.

Previous CMB missions

In 1989, NASA launched its first CMB mission, the Cosmic Background Explorer (COBE) (Boggess *et al.*, 1992). The purpose of this mission was to map the CMB emission over the whole sky and measure the temperature anisotropies (small fluctuations of the temperature of the CMB, imprinted on the sky). COBE contained the following instruments: the Differential Microwave Radiometer (DMR), the Far-InfraRed Absolute Spectrophotometer (FIRAS) and Diffuse InfraRed Background Experiment (DIRBE). The DMR was responsible for measuring the anisotropy (Smoot, 1992). The data from

COBE was used to produce the first full sky map of the anisotropies of the CMB of the order of $\frac{\Delta T}{T} = 1 \times 10^{-5}$ as in Figure 1.8.

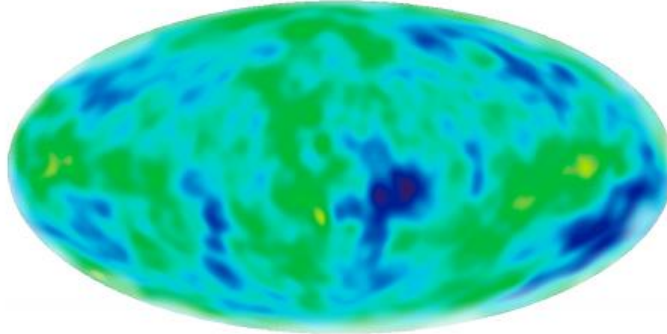


Figure 1.8: COBE map of anisotropies (science.nasa.gov, 2016)

In June 2001, NASA launched the Wilkinson Microwave Anisotropy Probe (WMAP). One of the goals of this mission was to measure the temperature anisotropies discovered by COBE with higher spatial resolution to obtain higher order multipoles. Observations were carried out in five different frequency bands: K-band, Ka-band, Q-band, V-band and W-band, covering a frequency range of 22 – 90 GHz, to allow separation of galactic foreground signals from the CMB. The receivers were polarization sensitive differential radiometers measuring the temperature difference between two points on the sky rather than measuring absolute temperatures. Figure 1.9 (left) below shows the full sky WMAP CMB anisotropy map and Figure 1.9 (right) show the CMB polarisation measurements as a composite of the five frequency bands. Figure 1.9 (right) shows the WMAP measurements of the angular power spectrum (TT), temperature / E-mode correlation (TE), E-mode polarization (EE) and upper limit B-mode polarization (BB) as evidence for B-modes was not found.

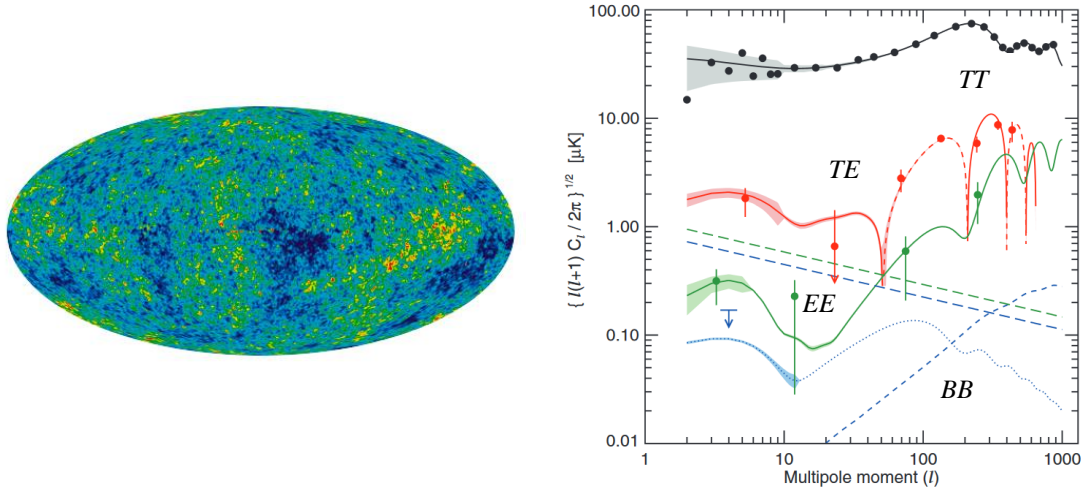


Figure 1.9: Anisotropy measurements carried out by WMAP (map.gsfc.nasa.gov, 2017)

The Planck satellite, launched by ESA in 2009, had several scientific aims. They include the measurement of the temperature and polarisation of the CMB with sensitivity, angular resolution and frequency range that were not achieved by previous missions (Planck mapped the sky (Figure 1.10) with an angular resolution that was 2.5 times that of WMAP). The larger number of frequency bands (9) observed by Planck, allows for the removal of diffuse and compact foregrounds, whose emission obscures the CMB. The payload consists of an off-axis tilted Gregorian telescope with a primary mirror measuring $1.9 \text{ m} \times 1.5 \text{ m}$ and a secondary of $1.1 \text{ m} \times 1.0 \text{ m}$ which fed two instruments: the Low Frequency Instrument (LFI) and High Frequency Instrument (HFI), providing a frequency coverage of 27 GHz to 1 THz.

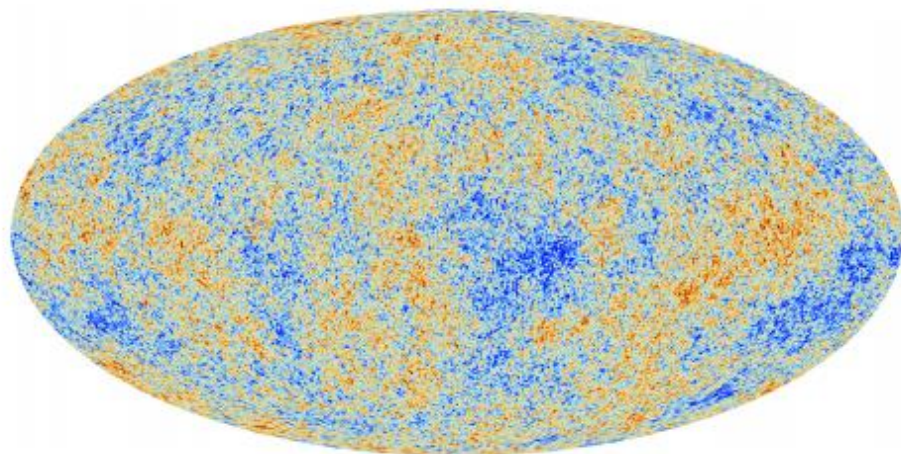


Figure 1.10: Planck map of anisotropies (Planck Collaboration, 2014(I))

In addition to making measurements of temperature anisotropies, both WMAP and Planck also recorded the polarisation characteristics of the CMB photons incident on the

detectors, which is important in order to understand the nature of the early Universe, when structure first formed. The polarisation fluctuations are several orders of magnitude lower than that of temperature fluctuations and polarised foregrounds must be removed, requiring extremely high sensitivity. For the case of Planck, one of the goals of the mission was to test inflationary models of the early universe via the detection of a component of the CMB (*B*-modes), which required study of the polarisation of the CMB with high sensitivity.

1.6 Foreground Sources

As a ‘by-product’, observations made by Planck provided information about the interstellar medium as seven types of unresolved foregrounds must be removed or controlled for CMB analysis. These include: dust thermal emission, dust anomalous emission, CO rotational emission lines, free-free emission, synchrotron emission, the Cosmic Infrared Background and Sunyaev-Zeldovich secondary CMB distortion (Planck Collaboration, 2014(I)). The regions of emission from these sources mentioned are shown as a function of frequency in Figure 1.11.

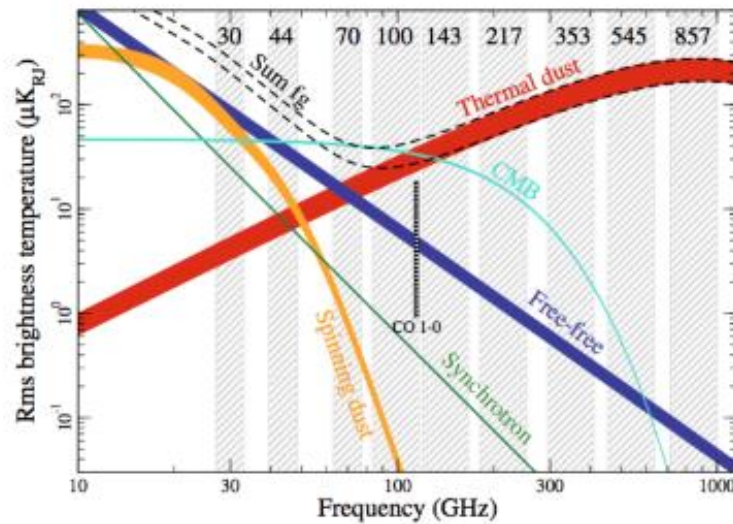


Figure 1.11: Plot of the contributions of the foreground sources in terms of brightness temperature at various frequencies (Planck Collaboration, 2014 (I))

Dust emission, which arises from the re-radiation of absorbed interstellar light, is the dominant foreground at HFI frequencies, with the contribution rising towards 1 THz. This can be seen in the all sky maps (Figure 1.12) produced by each frequency channel

on Planck, especially at the three highest frequency channels, 353 GHz, 545 GHz and 857 GHz, which show much more diffuse backgrounds.

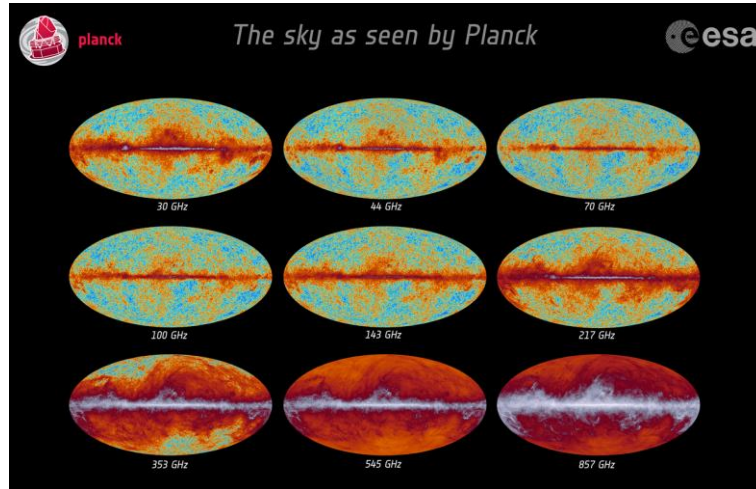


Figure 1.12: Planck all-sky maps at the three LFI and six HFI bands (sci.esa.int, 2013)

In the highest frequency bands of the HFI (353, 545 and 857 GHz), the cosmic infrared background (CIB), a signal which occurs in regions of high activity and density, can be observed. CIB anisotropies are expected to trace large-scale structures and probe the clustering properties of galaxies, constraining the relationship between dusty, star-forming galaxies and the dark matter distribution (Planck Collaboration, 2014 (I)).

The data from the three highest frequency channels on the HFI, along with data from the Infrared Astronomical Satellite (IRAS) mission (Neugebauer *et al.*, 1984) at 100 μm , were also used to produce all-sky maps of dust optical depth, temperature and spectral index over a frequency range of 353 – 3000 GHz (Planck Collaboration, 2014 (XI)). The high resolution of the Planck-IRAS product results in a more detailed mapping of column density structure, particularly in the denser regions of the ISM.

The three highest bands of the HFI have also been combined with IRAS to produce an all-sky catalogue of Galactic Cold Clumps (PGCC), containing 13,188 Galactic sources spread across the whole sky (Planck Collaboration, 2016 (XXXVIII)). Figure 1.13 shows the distribution of the GCC sources overlaid on the 857 GHz Planck map.

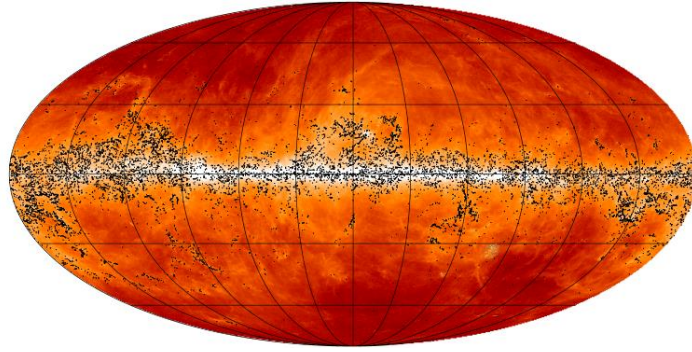


Figure 1.13: All-sky distribution of PGCC sources (Planck Collaboration, 2016(XXXVIII))

Cold dust clumps are mainly associated with dense regions within molecular clouds. Observing cold dust is relevant for the study of the earliest stages of star formation. The highest frequency channels of the HFI, 545 GHz and 857 GHz will also be analysed later in this thesis (Chapter 5).

1.7 Detector Technology

In this section, the detector technology used for astronomical observations in the terahertz band will be summarized, including bolometers, transition edge sensors and kinetic induction detectors.

The terahertz (THz) region is at the transition from microwaves to the infrared. Due to the historic lack of developed technologies, this range of frequencies is known as the ‘terahertz gap’, referring to the underutilization of this region in the past because of the limited availability of detectors. These sources, even with modern development, still tend to be expensive as a result of the technologies being used being a challenging combination of those at microwave and visible wavelengths. In comparison to microwaves, higher imaging resolution is typically obtained at THz frequencies on medium – sized telescopes and optical systems. In comparison to visible wavelengths, millimetre and sub-millimetre wavelengths can penetrate many materials opaque at visible wavelengths. Optical spectroscopy can provide information on the atomic composition, whereas THz spectroscopy can provide information on the molecular concentration as well as the physical condition of an object (heat, pressure *etc.*) (Dexheimer, 2008: 3).

Analysis software, which relies on geometrical optics and ray tracing, is fast and traditionally used at shorter wavelengths. The results of these methods are not always

reliable in sub-millimetre systems, mostly due to diffraction effects. At the longer wavelengths, full electromagnetic analysis is required and is more reliable, but suffers from long computation times. This results in multiple programs being used together.

For sub-millimetre wavelengths, bolometers are commonly used. A bolometer absorbs the power of the incoming radiation and is a detector whose resistance is sensitive to changes in temperature. The absorbing layer itself is made from a semiconductor material (such as silicon (Downey *et al.*, 1984)) which is connected to a thermal reservoir through a weak thermal link. Any photon incident on the detector raises the temperature of the detector to that above the thermal reservoir, making a detection possible. The sensor itself functions by recording the Joule heating of the material by using a detector which is either a resistive thermometer or it directly measures the resistance of the absorber. Normally, bolometers are operated at cryogenic temperatures in order to increase their sensitivity. An important aspect of any detector technology is the noise equivalent power (NEP) which is a measure of signal power that a detector can distinguish. Notable examples of the use of bolometers as detectors used in astronomy include the High Frequency Instrument on the Planck satellite. Planck HFI made use of two types of bolometric detectors, spider-web bolometers (SWB) and polarisation sensitive bolometers (PSB). SWB were used on the unpolarised channels of the high frequency instrument (HFI) on Planck, which work by absorbing the radiation on a web-like surface. The temperature change is detected by a thermistor located in the centre of the web (as in Figure 1.14 (left)). The web itself consists of a 1 μm layer of silicon nitride (Si_3N_4), coated with gold (Lamarre, 2010). PSBs were used in the polarisation sensitive channels of the HFI, where a pair of PSBs perpendicular to one another were placed in a cavity so that the two orthogonal polarisations could be detected. The temperature sensors were located at the upper edge of the PSB (see Figure 1.14 (right)).

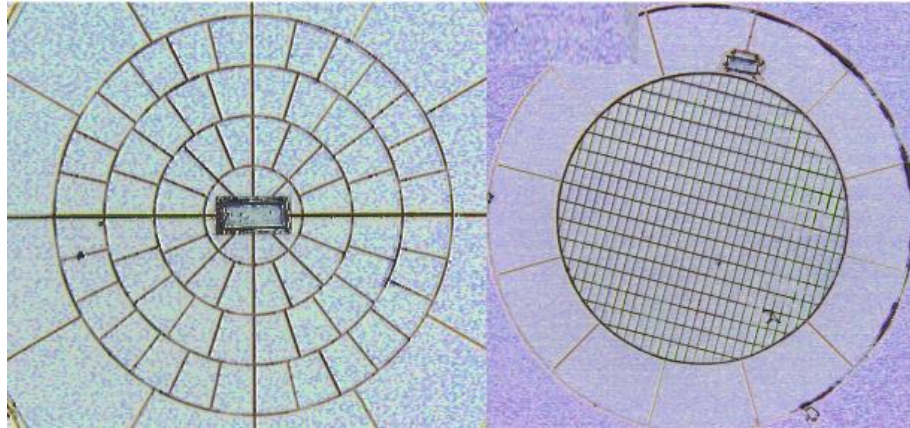


Figure 1.14: *Left*: Spider-Web bolometer of the 143 GHz horn on Planck with the temperature sensor in the middle *Right*: Polarisation-Sensitive bolometer of the 217 GHz channel on Planck with the sensor at the upper edge (Lamarre, 2010)

More recently, TES devices have been developed. A transition edge sensor (TES) is made from a material that exhibits superconducting behaviour. The transition between a superconducting and normal state can be used as a sensitive measure of temperature. The material is held at its transition temperature by a bias voltage, where a small increase in temperature causes a large increase in resistance. Transition edge sensors have been demonstrated to work well in close packed array format, which will be required for the SAFARI instrument. The SAFARI detector arrays will contain a total of ~ 3300 TES bolometers using Ti/Au superconducting bilayers in thin, thermally isolated silicon nitride islands. The detectors sit in a free space gap between the feed horns and reflecting backshorts and incoming radiation will be absorbed by a 7 nm thick Ta film (Audley *et al.*, 2016).

Kinetic Inductance Detectors (KIDs) function on the basis of splitting a Cooper pair into two quasi-particles (electrons). The detector material experiences a change in inductance if a photon is absorbed. This inductance is combined with a capacitor to form a microwave resonator whose resonant frequency changes with the absorption of photons. KIDs are being developed for a range of astronomy applications, including mm and sub-millimetre wave detection. KIDs also need to be kept at cryogenic temperatures. The big advantage of KIDs is that they can be multiplexed easier than TES detectors, for example, since they require a single readout line for one array. Lumped element KIDs represent one possible technology which can satisfy the requirements of producing large arrays for sensitive detectors for astronomy as they are relatively simple to fabricate (Doyle, 2008).

Receivers for high resolution spectroscopy in the mm- and sub-mm band most commonly use heterodyne receiver configurations. A heterodyne receiver, which operates under the principle of taking a high frequency signal and translating it into a lower frequency signal, making it easier to process than the original carrier frequency.

1.8 Thesis Overview

A brief overview of each chapter will be given here

Chapter 2

In chapter two, the details of the mode matching technique for the electromagnetic analysis of waveguide and horn structures is presented. The mode matching technique was implemented in the GAMMA (Generalised Absorber Mode Matching Analysis) software, developed in-house. The software allows one to probe the performance of various horn and waveguide structures, both cylindrical and rectangular. Modelling the presence of an absorber in the waveguide structure is also presented. The required modifications for the inclusion of an absorber in the software are also detailed. An overview of CST, a commercial software package based on finite element analysis (an alternative to mode matching) is also given in this chapter. CST was used for software verification and comparison with results produced by GAMMA for electrically small systems.

Chapter 3

Chapter 3 is concerned with beam propagation through optical systems including telescopes. The Gaussian Beam Mode Analysis of quasi-optical systems is outlined along with a more rigorous physical optics approach using the GRASP9 commercial software.

The application of mode matching for the design of a 4 mm wave receiver for the 20 m telescope in Onsala Space Observatory (OSO) is discussed in which a corrugated horn was used to feed the detector with high efficiency. The design was carried out using the in-house mode matching software.

The beam was also propagated through the front end optics and the 20 m telescope using GRASP9 to produce accurate farfield patterns on the sky at some spot frequencies across

the designed band. A tolerance analysis was also carried out for the manufacture of the horn and the resulting impact on the beam on the sky was also investigated.

Chapter 4

In this Chapter we report on the work carried out to investigate cavity effects on the signal coupling to a bolometer for particular examples where a finite element method approach would have been very difficult. This is particularly important for application to the SAFARI instrument proposed for SPICA. As well as predicting the beam pattern more precisely, we have also investigated the cavity configuration for optimizing power absorption by offsetting the axis of the waveguide feeding the cavity thus trapping power and also by varying the position, size and surface resistance of the absorber in the cavity. We have also developed an extension to the GAMMA software which allowed an absorber of arbitrary shape to be modelled, in particular investigating the case where the absorber sheet was square and the cavity was cylindrical.

Chapter 5

In this Chapter we discuss the application of some of the innovations made to the GAMMA waveguide mode matching approach to the 857 GHz and 545 GHz multimode channels on the Planck HFI instrument, particularly in order to improve on the agreement between previously reported predictions with both laboratory measurements and in-flight measurements. A more rigorous model was considered in the mode matching software and resulting broadband beams of the horns were compared with laboratory measurements. The beam was then propagated through the telescope and farfield beams on the sky were obtained and compared with the azimuthally and band averaged beam derived from observations of planets that appeared in the literature on the Planck results.

Chapter 6

In this Chapter we investigate the effect on the optical efficiency of detectors when a free space gap is present as will be the case for the proposed SAFARI pixels which will use arrays of detectors manufactured on a single chip. We have extended the mode matching approach (GAMMA) to include the case where a free space gap is present in the waveguide configuration with an open cavity in which an absorber can be placed.

Chapter 7

In Chapter 7 we draw the overall conclusion from the work in this thesis and consider future developments.

2 Single Mode and Multimode Horn Antennas

2.1 Introduction

In this chapter, we present an introduction to the mode matching technique and its application in the GAMMA (Generalised Absorber Mode Matching Analysis) software, developed in-house by the author of this thesis and written in Python. GAMMA is based on and extended the modelling capability of CylindricalSCATTER, which was written in Mathematica. The Python code was written to speed up the computations. GAMMA allows the performance of various horn and waveguide structures and absorbers to be predicted, it needs to be noted that CylindricalSCATTER was also able to handle absorbers, however, there were some pre-existing issues with the code which were addressed in GAMMA. A waveguide is a structure (or part of a structure) that causes a wave to propagate in a chosen direction with at least some measure of confinement in the planes transverse to the direction of propagation. Waveguides of various cross-sectional shapes exist and in particular rectangular and cylindrical waveguides are used extensively in millimetre and sub-millimetre wave detector feed systems. Furthermore, a horn antenna can be regarded as a kind of flared waveguide. Rectangular waveguide modes may be used to describe the electric and magnetic fields over a horn or waveguide with a rectangular cross-section. Similarly, cylindrical waveguide modes may be used to describe the fields when the structure has a circular cross-section (Ramo *et al.*, 1994: 423).

Usually, a horn antenna is said to be single mode when the waveguide feeding it only allows the fundamental mode to propagate (TE_{11} for the case of a cylindrical waveguide and TE_{10} for the case of a rectangular waveguide) and thus this provides good control of the radiation characteristics of the horn. If the waveguide feeding a horn antenna is oversized then potentially higher order waveguide modes as well as the fundamental mode are capable of coupling signal power to the detector. The beam pattern then depends on the relative efficiencies with which the modes couple to the detector (which could be a coherent detector, such as a mixer, or an incoherent detector, such as a bolometer). As a result, the beam pattern is thus less predictable. These effects will be seen on the beam

patterns of the Planck multimode horns (545 GHz and 857 GHz channels), to be discussed in Chapter 5. However, the advantage in this case is that more signal power can be coupled to the detector, although a disadvantage, of course, in imaging applications on telescopes is that there is necessarily reduced spatial resolution, assuming the multimode horn throughput is matched to the optics coupled to it. This is because the throughput, given by $A\Omega = n\lambda^2$ where n is the number of independent modes present, is higher than for the single mode case thus leading to larger beams on the sky (assuming of course the detector feed horn is well matched to the telescope so the number of modes is not attenuated). However, generally when a multimode waveguide is used to feed a horn antenna it is coupled to an incoherent detector. In the case of a coherent detector, such as a mixer, only one mode can ever effectively be coupled and therefore, normally, only a fundamental mode waveguide would be used.

The beam patterns of waveguide-horn fed systems with standard cross sections can in theory be modelled using an efficient mode matching scattering matrix approach, in which the horn is thought of as a series of waveguide sections of standard cross-section and varying size. This approach can similarly be applied to corrugated cylindrical waveguide and conical horn structures. The scattering matrix description of the propagation is based on tracking the scattering between the waveguide modes at discontinuities in the structure. Then when the sections are cascaded together, the complete waveguide-horn is recreated. In fact, a smooth walled horn is approximated as a large series of small steps while a corrugated waveguide and horn can be regarded as a large sequence of cascaded smooth walled sections with a finite step in radius between the corrugation slots and fins (Olver et. al., 1994: 106).

Waveguides (including horns) in fact support two orthogonal mode sets: ‘transverse magnetic’ (*TM*) modes with $H_z = 0$ and ‘transverse electric’ (*TE*) modes with $E_z = 0$. The number of propagating modes depends on the size of the cross-section of the waveguide structures (each mode is supported above its cut-off frequency) and an infinite number of evanescent modes can also exist in the guide but only propagate short distances over which they decay in amplitude. One of the issues in any numerical analysis is how many evanescent modes to include in the analysis to maintain accuracy but not to slow computations too much. This will be discussed in later chapters of this thesis (Ramo et. al., 1994: 424).

In this chapter, we summarize the scattering matrix approach for both cylindrical and rectangular structures, and the in-house GAMMA software, developed by the author of this thesis, will be used to model a rectangular back-to-back horn antenna to produce the scattering matrices and farfield patterns.

In Section 2.9 of this chapter, we discuss the results obtained from a measurement campaign which was undertaken in the millimetre-wave measurement laboratory in Maynooth University in order to verify multimode propagation theory.

2.2 Cylindrical Waveguide Modes

In general, waveguides and horn antennas of circular cross-section can propagate TE_{nm} and TM_{nm} modes (where n is the azimuthal order and m is the radial order). Each waveguide mode has a cut-off frequency associated with it, below which propagation is not possible (Ramo *et. al.*, 1994: 424). Smooth walled waveguide sections are able to transmit both polarisation orientations of the cylindrical modes (two orthogonal degenerate fields which exist for each mode of azimuthal order $n > 0$), and thus they are efficient feeds for bolometric systems (discussed in Chapter 4). In general, by contrast, rectangular waveguides are often used in a single mode operation with the ratio of the width to height of the guide adjusted so only a single polarization TE_{10} mode can propagate and in fact these would typically be used to feed a coherent detector (such as a mixer).

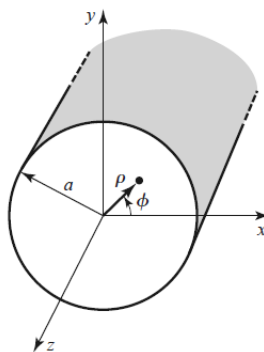


Figure 2.1: Cylindrical co-ordinate system for circular waveguides (Pojar, 2012: 121)

The co-ordinate system for cylindrical waveguides is defined as in Figure 2.1, so that the cross-section lies in the x - y plane and the radiation propagates in the z direction. The

transverse field components, expressed in cylindrical co-ordinates, for a dielectric assumed to be linear, homogeneous and isotropic, can be expressed in terms of the axial fields E_z and H_z as (Ramo *et. al.*, 1994 : 423)

$$E_r = -\frac{j}{k_c^2} \left[\beta \frac{\partial E_z}{\partial r} + \frac{\omega\mu}{r} \frac{\partial H_z}{\partial \phi} \right], \quad (2.1)$$

$$E_\phi = \frac{j}{k_c^2} \left[-\frac{\beta}{r} \frac{\partial E_z}{\partial \phi} + \omega\mu \frac{\partial H_z}{\partial r} \right], \quad (2.2)$$

$$H_r = \frac{j}{k_c^2} \left[\frac{\omega\varepsilon}{r} \frac{\partial E_z}{\partial \phi} - \beta \frac{\partial H_z}{\partial r} \right], \quad (2.3)$$

$$H_\phi = -\frac{j}{k_c^2} \left[\omega\varepsilon \frac{\partial E_z}{\partial r} - \frac{\beta}{r} \frac{\partial H_z}{\partial \phi} \right], \quad (2.4)$$

with,

$$k_c^2 = \gamma^2 + k^2 = k^2 - \beta^2, \quad (2.5)$$

where k_c is the cut-off wavenumber, γ is the propagation constant ($\gamma = j\beta$ for a propagating wave), β is the waveguide wavenumber and the field is assumed to have a z dependency of $e^{-\gamma z}$. Normally we will in fact assume the dielectric is replaced by free space so that $\varepsilon = \varepsilon_0$ and $\mu = \mu_0$.

TM modes

Using the separation of variables technique (Ramo *et al.*, 1994: 423), E_z may be expressed as

$$E_z = A_{nm} J_n(k_c r) \begin{pmatrix} \cos n\phi \\ \sin n\phi \end{pmatrix}, \quad (2.6)$$

where n is the azimuthal order and m is the radial order, J_n is a Bessel function of the first kind of order n and A_{nm} is a constant to satisfy the electric field boundary conditions. At $z = a$ the Bessel function $J_n(k_c a) = 0$ which implies $k_c a = p_{nm}$ where p_{nm} is the m^{th} zero of the Bessel function $J_n(z)$, *i.e.*, ($J_n(p_{nm}) = 0$). Using Equations (2.1) to (2.4), the transverse component of the electric and magnetic fields for TM modes of azimuthal order n and radial order m can then be expressed as (Gleeson, 2004: 57)

$$\mathbf{e}_{nm} = \sqrt{\frac{(2-\delta_{n0})}{\pi a^2 J_{n+1}^2(p_{nm})}} \left(J'_n \left(p_{nm} \frac{r}{a} \right) \begin{pmatrix} \cos n\phi \\ \sin n\phi \end{pmatrix} \hat{\mathbf{r}} + \frac{n J_n \left(p_{nm} \frac{r}{a} \right)}{p_{nm} \frac{r}{a}} \begin{pmatrix} -\sin n\phi \\ \cos n\phi \end{pmatrix} \hat{\phi} \right) \quad (2.7)$$

$$\mathbf{h}_{nm} = \sqrt{\frac{(2-\delta_{n0})}{Z_{TM_{nm}}^2 \pi a^2 J_{n+1}^2(p_{nm})}} \times \left(-\frac{n J_n \left(p_{nm} \frac{r}{a} \right)}{p_{nm} \frac{r}{a}} \begin{pmatrix} -\sin n\phi \\ \cos n\phi \end{pmatrix} \hat{\mathbf{r}} + J'_n \left(p_{nm} \frac{r}{a} \right) \begin{pmatrix} \cos n\phi \\ \sin n\phi \end{pmatrix} \hat{\phi} \right) \quad (2.8)$$

where $Z_{TM_{nm}}$ is the characteristic waveguide impedance of a TM mode given by

$$Z_{TM_{nm}} = Z_0 \sqrt{1 - \left(\frac{p_{nm}}{\omega a \sqrt{\mu \epsilon a}} \right)^2}. \quad (2.9)$$

In order to model horn antennas, it is convenient to re-write the transverse field expressions for TM modes in Cartesian components (\hat{i} and \hat{j}) (x and y directions). We define the "x-co-polar" field of the degenerate pair of fields of a mode as the one for which the electric field lines are polarised in the x -direction along the $\phi=0$ direction. By contrast, for the "y-co-polar" fields, the field lines are orthogonal to the x -axis (have y -component only) in the $\phi=0$ direction.

In Cartesian components, these fields are

$$e_x^{TM} = \sqrt{\frac{(2-\delta_{n0})}{4\pi a^2 J_{n+1}^2(p_{nm})}} \times \left(J_{n-1} \left(p_{nm} \frac{r}{a} \right) \begin{pmatrix} \cos(n-1)\phi \\ -\sin(n-1)\phi \end{pmatrix} - J_{n+1} \left(p_{nm} \frac{r}{a} \right) \begin{pmatrix} \cos(n+1)\phi \\ -\sin(n+1)\phi \end{pmatrix} \right), \quad (2.10)$$

$$e_y^{TM} = -\sqrt{\frac{(2-\delta_{n0})}{4\pi a^2 J_{n+1}^2(p_{nm})}} \left(J_{n-1} \left(p_{nm} \frac{r}{a} \right) \begin{pmatrix} \sin(n-1)\phi \\ \cos(n-1)\phi \end{pmatrix} + J_{n+1} \left(p_{nm} \frac{r}{a} \right) \begin{pmatrix} \sin(n+1)\phi \\ \cos(n+1)\phi \end{pmatrix} \right), \quad (2.11)$$

$$h_x^{TM} = \sqrt{\frac{(2-\delta_{n0})}{4Z_{TM_{nm}}^2 \pi a^2 J_{n+1}^2(p_{nm})}} \left(J_{n-1} \left(p_{nm} \frac{r}{a} \right) \begin{pmatrix} \sin(n-1)\phi \\ \cos(n-1)\phi \end{pmatrix} + J_{n+1} \left(p_{nm} \frac{r}{a} \right) \begin{pmatrix} \sin(n+1)\phi \\ \cos(n+1)\phi \end{pmatrix} \right), \quad (2.12)$$

$$h_y^{TM} = \sqrt{\frac{(2 - \delta_{n0})}{4Z_{TM_{nm}}^2 \pi a^2 J_{n+1}^2(p_{nm})}} \left(J_{n-1} \left(P_{nm} \frac{r}{a} \right) \begin{pmatrix} \cos(n-1)\phi \\ -\sin(n-1)\phi \end{pmatrix} - J_{n+1} \left(P_{nm} \frac{r}{a} \right) \begin{pmatrix} \cos(n+1)\phi \\ -\sin(n+1)\phi \end{pmatrix} \right) \quad (2.13)$$

In Equations (2.10) to (2.13) $\begin{pmatrix} \cos n\phi \\ \sin n\phi \end{pmatrix}$ etc. refer to the ‘x-co-polar’ field (upper entry) and ‘y-co-polar’ field (lower entry).

Figure 2.2 to Figure 2.4 show the intensity plots with the electric field lines (left) and magnetic field lines (right) for azimuthal order $n = 0, 1, 2$ for both polarisations. For the case of $n = 0$ the first two radial orders $m = 1, 2$ are shown.

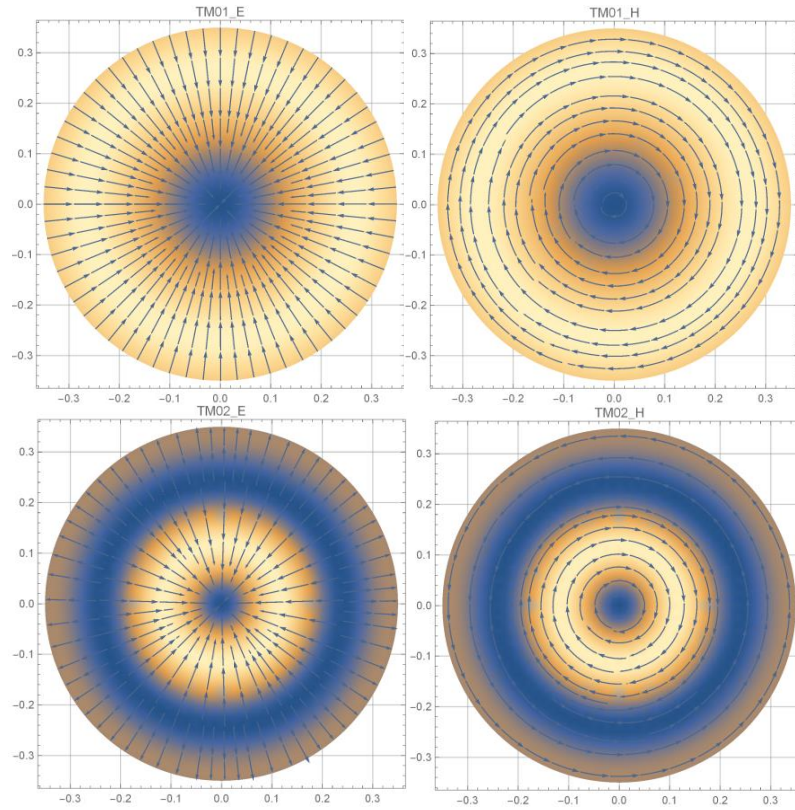


Figure 2.2: Density of electric field lines (left) and magnetic field lines (right) of radial orders $m = 1, 2$ for TM modes with azimuthal order $n=0$

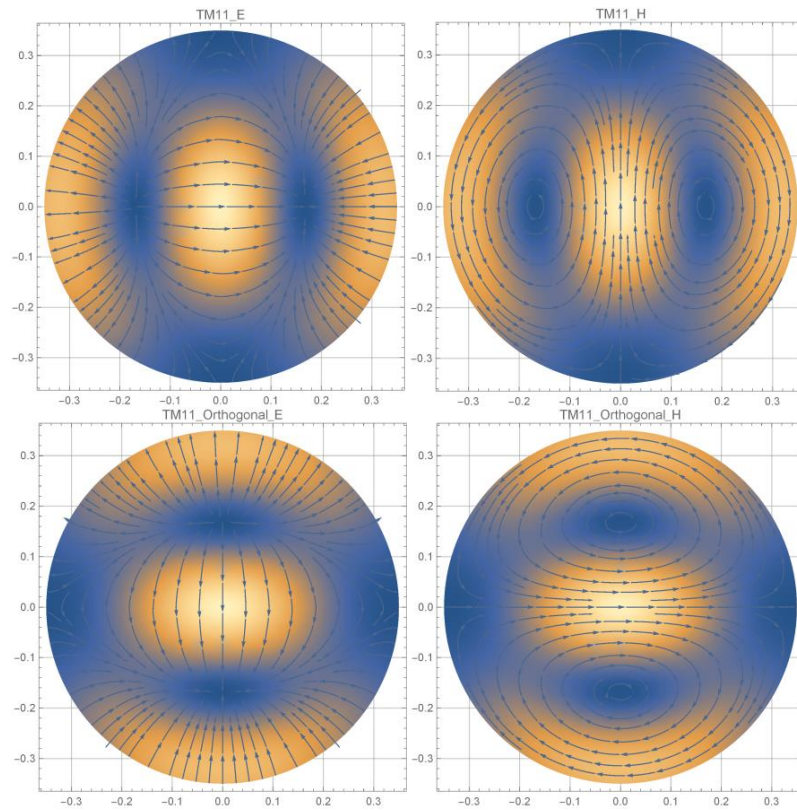


Figure 2.3: Density of electric field lines (left) and magnetic field lines (right) of a TM_{11} mode (both polarisations)

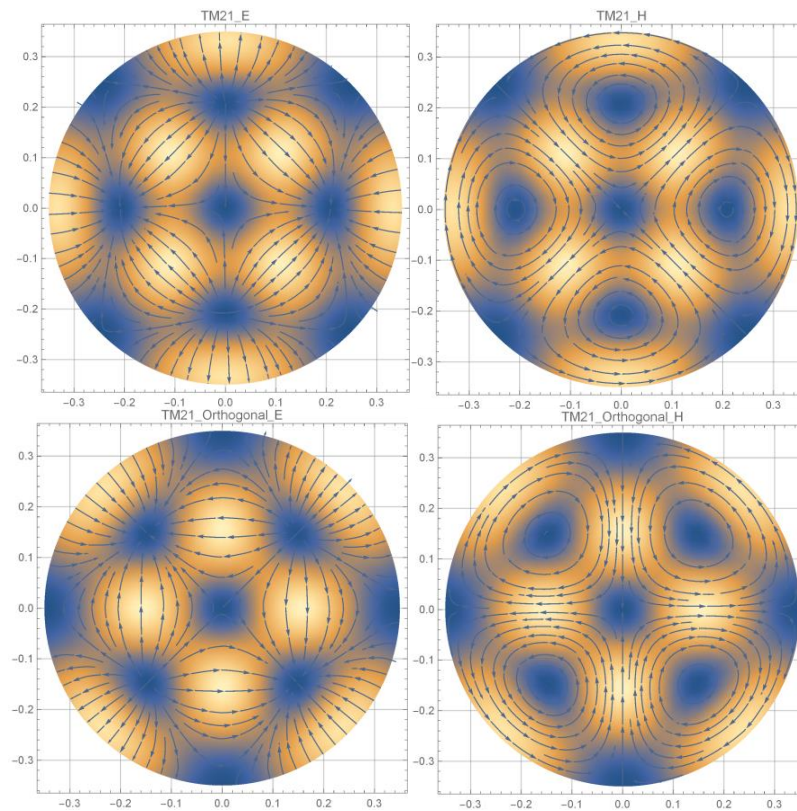


Figure 2.4: Density of electric field lines (left) and magnetic field lines (right) of a TM_{21} mode (both polarisations)

TM modes of azimuthal order $n > 0$ exhibit a $\pi/(2n)$ symmetry between the orthogonal (x-co-polar and y-co-polar) degenerate pairs of modes (i.e. the y-co-polar fields correspond to the x-co-polar fields rotated by $\pi/(2n)$).

TE modes

Using the separation of variables technique (Ramo *et. al.*, 1994: 423), H_z may be expressed as

$$H_z = B_{nm} J_n(k_c r) \begin{pmatrix} \cos n\phi \\ \sin n\phi \end{pmatrix}, \quad (2.14)$$

where n is the azimuthal order and m is the radial order, J_n is a Bessel function of the first kind of order n and B_{nm} is a constant to satisfy the magnetic field boundary conditions. At $z = a$ the Bessel derivative $dJ_n/dz(k_c a) = 0$ which implies $k_c a = p'_{nm}$ where p'_{nm} is the m^{th} zero of the derivative of the Bessel function $J_n(z)$ i.e. $(dJ_n/dz(p'_{nm}) = 0)$.

The transverse component of the electric and magnetic fields for TM modes of azimuthal order n and radial order m can be expressed as (Gleeson, 2004:59)

$$\mathbf{e}_{nm} = \sqrt{\frac{(2 - \delta_{n0})}{4\pi a^2 \left(1 - \left(\frac{n}{p'_{nm}}\right)^2\right) J_n^2(p'_{nm})}} \times \begin{pmatrix} \frac{n J_n\left(p'_{nm} \frac{r}{a}\right)}{p'_{nm} \frac{r}{a}} \begin{pmatrix} \cos n\phi \\ -\sin n\phi \end{pmatrix} \hat{\mathbf{r}} - J'_n\left(p'_{nm} \frac{r}{a}\right) \begin{pmatrix} \sin n\phi \\ \cos n\phi \end{pmatrix} \hat{\phi} \end{pmatrix}, \quad (2.15)$$

$$\mathbf{h}_{nm} = \sqrt{\frac{(2 - \delta_{n0})}{Z_{TE_{nm}}^2 \pi a^2 \left(1 - \left(\frac{n}{p'_{nm}}\right)^2\right) J_n^2(p'_{nm})}} \times \begin{pmatrix} J'_n\left(p'_{nm} \frac{r}{a}\right) \begin{pmatrix} \sin n\phi \\ \cos n\phi \end{pmatrix} \hat{\mathbf{r}} + \frac{n J_n\left(p'_{nm} \frac{r}{a}\right)}{p'_{nm} \frac{r}{a}} \begin{pmatrix} \cos n\phi \\ -\sin n\phi \end{pmatrix} \hat{\phi} \end{pmatrix} \quad (2.16)$$

where $Z_{TE_{nm}}$ is the characteristic waveguide impedance of a TE mode, given by

$$Z_{TE_{nm}} = \frac{Z_0}{\sqrt{1 - \left(\frac{p'_{nm}}{\omega a \sqrt{\mu \epsilon a}} \right)^2}}. \quad (2.17)$$

Again, re-expressing these fields in terms of Cartesian components,

$$e_x^{TE} = \sqrt{\frac{(2 - \delta_{n0})}{4\pi a^2 \left(1 - \left(\frac{n}{p'_{nm}} \right)^2 \right)}} J_n^2(p'_{nm}) \times \left(J_{n-1} \left(p'_{nm} \frac{r}{a} \right) \begin{pmatrix} \cos(n-1)\phi \\ -\sin(n-1)\phi \end{pmatrix} + J_{n+1} \left(p'_{nm} \frac{r}{a} \right) \begin{pmatrix} \cos(n+1)\phi \\ -\sin(n+1)\phi \end{pmatrix} \right), \quad (2.18)$$

$$e_y^{TE} = -\sqrt{\frac{(2 - \delta_{n0})}{4\pi a^2 \left(1 - \left(\frac{n}{p'_{nm}} \right)^2 \right)}} J_n^2(p'_{nm}) \times \left(J_{n-1} \left(p'_{nm} \frac{r}{a} \right) \begin{pmatrix} \sin(n-1)\phi \\ \cos(n-1)\phi \end{pmatrix} - J_{n+1} \left(p'_{nm} \frac{r}{a} \right) \begin{pmatrix} \sin(n+1)\phi \\ \cos(n+1)\phi \end{pmatrix} \right), \quad (2.19)$$

$$h_x^{TE} = \sqrt{\frac{(2 - \delta_{n0})}{4 Z_{TE_{nm}}^2 \pi a^2 \left(1 - \left(\frac{n}{p'_{nm}} \right)^2 \right)}} J_n^2(p'_{nm}) \times \left(J_{n-1} \left(p'_{nm} \frac{r}{a} \right) \begin{pmatrix} \sin(n-1)\phi \\ \cos(n-1)\phi \end{pmatrix} - J_{n+1} \left(p'_{nm} \frac{r}{a} \right) \begin{pmatrix} \sin(n+1)\phi \\ \cos(n+1)\phi \end{pmatrix} \right), \quad (2.20)$$

$$h_y^{TE} = \sqrt{\frac{(2 - \delta_{n0})}{4 Z_{TE_{nm}}^2 \pi a^2 \left(1 - \left(\frac{n}{p'_{nm}} \right)^2 \right)}} J_n^2(p'_{nm}) \times \left(J_{n-1} \left(p'_{nm} \frac{r}{a} \right) \begin{pmatrix} \cos(n-1)\phi \\ -\sin(n-1)\phi \end{pmatrix} + J_{n+1} \left(p'_{nm} \frac{r}{a} \right) \begin{pmatrix} \cos(n+1)\phi \\ -\sin(n+1)\phi \end{pmatrix} \right), \quad (2.21)$$

Similarly, in Equations (2.18) to (2.21) $\begin{pmatrix} \cos n\phi \\ \sin n\phi \end{pmatrix}$ etc. refer to the ‘x-co-polar’ field (upper entry) and ‘y-co-polar’ field (lower entry).

Figure 2.5 to Figure 2.7 show the density regions with the electric field lines (left) and magnetic field lines (right) for azimuthal orders $n = 0, 1, 2$ for both polarisations. For the case of $n = 0$ the first two radial orders $m = 1, 2$ are shown.

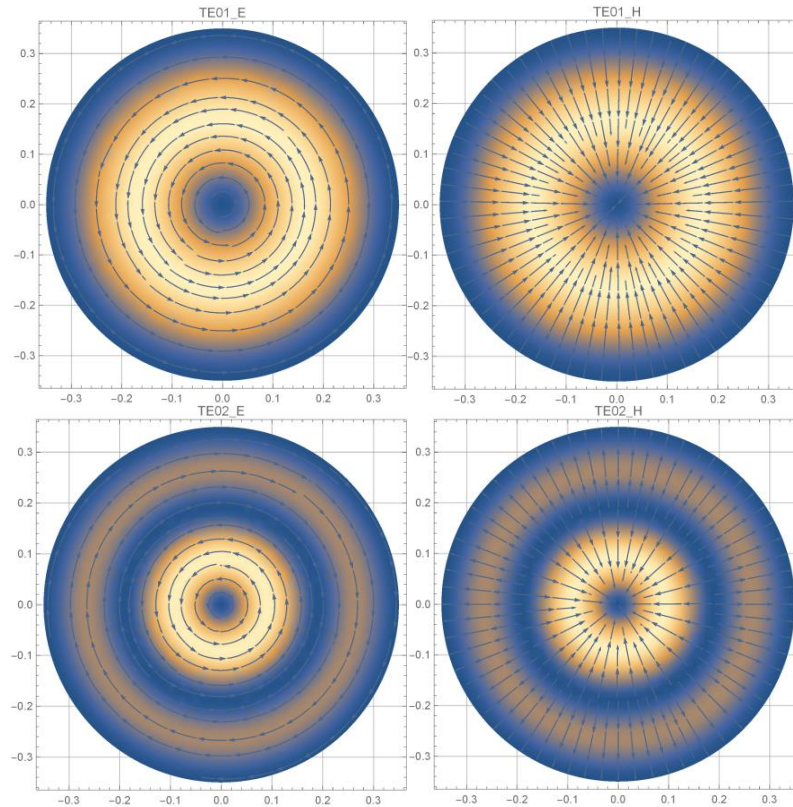


Figure 2.5: Density of electric field lines (left) and magnetic field lines (right) of radial orders $m = 1, 2$ for TE modes with azimuthal order $n=0$

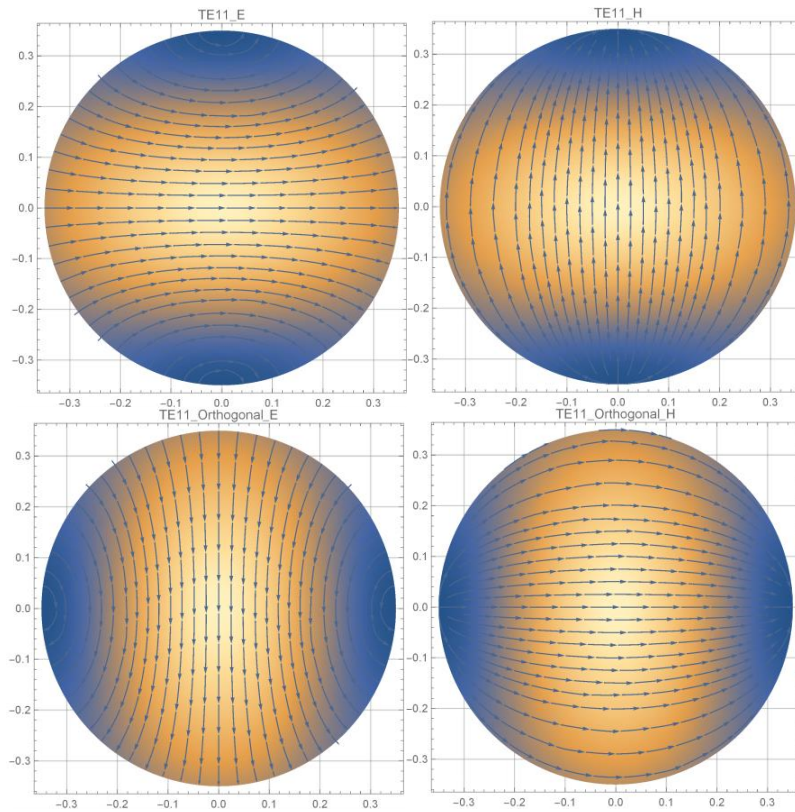


Figure 2.6: Density of electric field lines (left) and magnetic field lines (right) of a TE_{11} mode (both polarisations)

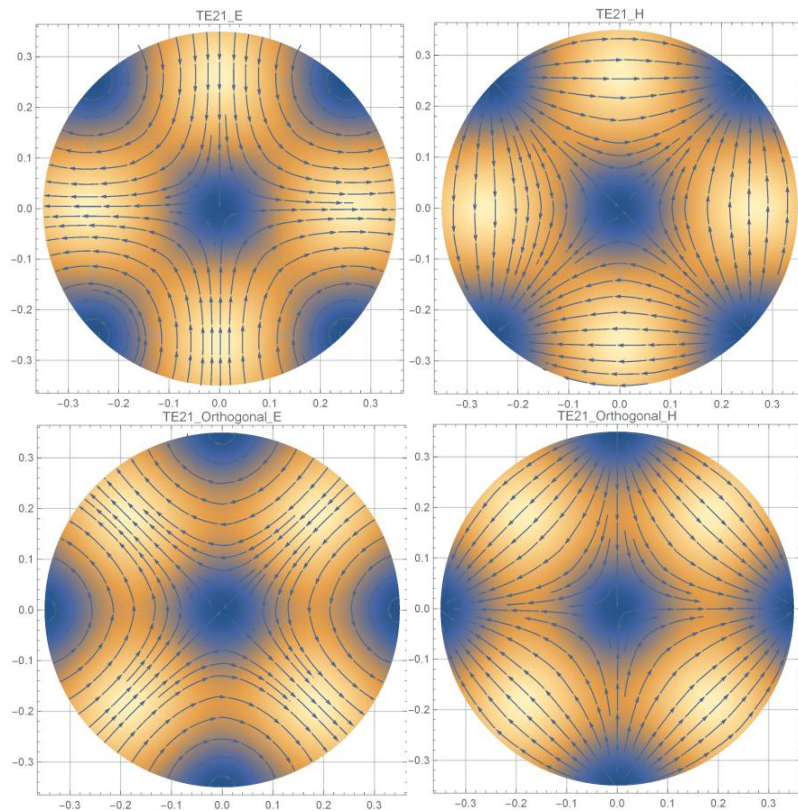


Figure 2.7: Density of electric field lines (left) and magnetic field lines (right) of a TE_{21} mode (both polarisations)

TE modes of azimuthal order $n > 0$ exhibit a $\pi/(2n)$ symmetry between the orthogonal (x-co-polar and y-co-polar) degenerate pairs of modes (*i.e.* the y-co-polar fields correspond to the x-co-polar fields rotated by $\pi/(2n)$).

2.3 Mode Matching in Cylindrical Waveguides

For horn structures with simple geometries, the solutions to the waveguide equation are simple functions of spherical waves which can be written as a waveguide mode field with a spherical phase front whose phase centre is at the apex of the horn. This method works well when the fields are stable along the horn. However, there are two restrictions: (i) it does not predict the fields at discontinuities along the horn, which leads to the excitation of multiple modes at either the waveguide end (throat) or the free space end (mouth) and can also be applied to waveguides with step discontinuities, and (ii) no information on the impedance properties of the horn is given. Thus the modal-matching technique has been developed in order to overcome these restrictions.

A modal method of studying the electromagnetic propagation in the internal region of a waveguide structure is to determine the amplitudes of the modes into which the fields can be decomposed and then propagate the field as a sum of modes, *eg.* $\mathbf{E} = \sum_n A_n \mathbf{e}_n$, where \mathbf{e}_n represents the modal field and A_n is known as the mode coefficient. Cylindrical waveguide modes can be used to study the propagation characteristics of horns with circular cross-sections, which may in fact have either smooth or corrugated internal walls. The aim is to predict the electromagnetic fields in the horn aperture treating the horn as being made up of a sequence of short waveguide sections which approximate the horn.

At a waveguide discontinuity, the interface between two segments is known as a junction which is where the change in guide radius occurs. At a junction (as in Figure 2.8), some of the incident power carried by the individual modes is scattered into other forward propagating modes and some is also scattered (reflected) into backward propagating modes. The reflected mode power propagates backwards in the first guide segment (LHS of a junction) while the forward power propagates in the second guide segment (RHS of a junction) (Gleeson *et al.*, 2005).

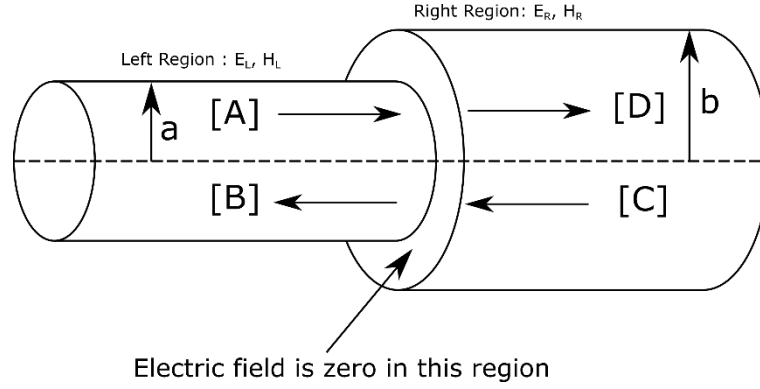


Figure 2.8: Junction discontinuity where the radius changes from a to b

The power coupling between modes is given by $\int \mathbf{e}_{n,left} \times \mathbf{h}_{m,right} \cdot d\mathbf{A}$ where $\mathbf{e}_{n,left}$ is the transverse electric field on the left hand side of the junction, $\mathbf{h}_{m,right}$ is the magnetic field on the right hand side of the junction and $d\mathbf{A}$ is the surface element on the transverse plane. The modes are then propagated through the length of waveguide section to the next scattering junction where the overlap integral between the modal components is performed again. The relationship between the input and output coefficients for the modes is described by a scattering matrix. These matrices are then cascaded for each section to obtain an overall scattering matrix for the horn structure. For perfectly aligned waveguide segments, scattering only occurs between modes of the same azimuthal order because of the circular symmetry, and thus scattering matrices are computed separately for each azimuthal order.

At each junction, we assume power may be incident from the left and the right. Thus power may be transmitted from left to right, right to left, reflected from left to left and right to right. Figure 2.9 shows a schematic of the matrix scattering. We assume that the incident field can be written as a sum of modes of the form $\mathbf{E}_{in} = \sum A_n \mathbf{e}_n$ or $\sum C_n \mathbf{e}_n$ and $\mathbf{H}_{in} = \sum A_n \mathbf{h}_n$ or $\sum C_n \mathbf{h}_n$.

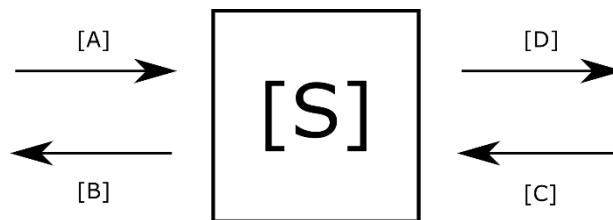


Figure 2.9: Schematic of scattering matrix representation

The mode coefficients A_n , B_n , C_n and D_n are organised into column matrices. In matrix form, the scattering of the incident field may then be represented as (Olver *et al.*, 1994:108)

$$\begin{bmatrix} [B] \\ [D] \end{bmatrix} = [S] \begin{bmatrix} [A] \\ [C] \end{bmatrix}, \quad (2.22)$$

where $[A]$ and $[C]$ are column vectors of mode coefficients of the incident field from the left and the right, and $[B]$ and $[D]$ are the resulting fields travelling to the left in the left waveguide and to the right in the right waveguide, respectively. The matrix $[S]$ may be broken down into sub-matrix components, $[S_{11}]$, $[S_{12}]$, $[S_{21}]$ and $[S_{22}]$, which describe the scattering of the transmitted and reflected modes at the input and output sides of the junction, given by

$$[S] = \begin{bmatrix} [S_{11}] & [S_{12}] \\ [S_{21}] & [S_{22}] \end{bmatrix}. \quad (2.23)$$

Thus,

$$[B] = [S_{11}][A] + [S_{12}][C], \quad (2.24)$$

$$[D] = [S_{21}][A] + [S_{22}][C], \quad (2.25)$$

Assuming no reflection at the horn aperture, the column matrix $[C]$ is set to zero, however, $[C]$ is non-zero for any other waveguide section.

The same number of modes ($N/2 \times TE$ modes and $N/2 \times TM$ modes) on either side of the junction are included so that the $[S]$ matrix consists of $2N \times 2N$ elements, with each of the sub-matrices $[S_{11}]$, $[S_{12}]$, $[S_{21}]$ and $[S_{22}]$ consisting of $N \times N$ elements. It is actually not necessary that there be the same number of modes on either side of the junction, but it was the arrangement chosen for the development of the GAMMA software code.

If the horn is fed by a single-mode waveguide, only the TE_{11} mode exists within the input guide and the input amplitude coefficient matrix ($[A]$) may be represented as a column matrix with one non-zero entry corresponding to the excited mode

$$[A] = \begin{bmatrix} 1 \\ 0 \\ 0 \\ \dots \\ \dots \end{bmatrix}. \quad (2.26)$$

The number of elements in $[A]$ represents the number of modes included, *i.e.* the column matrix contains N elements. The first row of $[A]$ represents the TE_{11} mode and the $(N+1)^{th}$ row represents the TM_{11} mode. This is clearly an approximation as strictly speaking an infinite number of modes should be used. The actual number of modes used has to be carefully determined to minimize any error resulting.

Consider a step discontinuity, where the diameter of the waveguide increases from a to b . As the diameter of a waveguide section changes, the number of propagating modes also changes, as each mode has its own cut-off frequency and associated guide wavelength. However, it is also important to include a sufficient number of evanescent modes. The transverse components of the electric and magnetic fields at the junction discontinuity are given by

$$\mathbf{E}_L = \sum_{n=1}^N \{A_n e^{-j\beta_n z} + B_n e^{j\beta_n z}\} \mathbf{e}_{nL}, \quad (2.27)$$

$$\mathbf{H}_L = \sum_{n=1}^N \{A_n e^{-j\beta_n z} - B_n e^{j\beta_n z}\} \mathbf{h}_{nL}, \quad (2.28)$$

$$\mathbf{E}_R = \sum_{n=1}^N \{D_n e^{-j\beta_n z} + C_n e^{j\beta_n z}\} \mathbf{e}_{nR}, \quad (2.29)$$

$$\mathbf{H}_R = \sum_{n=1}^N \{D_n e^{-j\beta_n z} - C_n e^{j\beta_n z}\} \mathbf{h}_{nR}, \quad (2.30)$$

where n denotes the mode number (not the azimuthal order in this case), N denotes the total number of modes, $\mathbf{e}_{nL,nR} e^{\pm j\beta_n z}$ and $\mathbf{h}_{nL,nR} e^{\pm j\beta_n z}$ denote the transverse fields to the left or right of a junction for the n^{th} mode with the positive phase term corresponding to the modes propagating to the left. A_n and B_n are the forward and reflected coefficients of the n^{th} mode on the left side of the junction. Similarly, C_n and D_n are the forward and reflected coefficients of the n^{th} mode on the right side of the junction.

Without loss of generality, we can place the junction at $z = 0$. The transverse electric and magnetic fields must be continuous at the junction, so that the modes must satisfy

$$\sum_{n=1}^N (A_n + B_n) \mathbf{e}_{nL} = \sum_{n=1}^N (D_n + C_n) \mathbf{e}_{nR} \quad (2.31)$$

$$\sum_{n=1}^N (A_n - B_n) \mathbf{h}_{nL} = \sum_{n=1}^N (D_n - C_n) \mathbf{h}_{nR} \quad (2.32)$$

This implies that

$$\sum_{n=1}^N (A_n + B_n) \int_{S_L} \mathbf{e}_{nL} \times \mathbf{h}_{mR}^* \cdot d\mathbf{S} = \sum_{n=1}^N (D_n + C_n) \int_{S_L} \mathbf{e}_{nR} \times \mathbf{h}_{mR}^* \cdot d\mathbf{S} \quad (2.33)$$

where S_L refers to the cross-sectional area on the left side of the junction (as in Figure 2.10).

The orthogonality relation (with $d\mathbf{S}$ pointing in the z-direction) for modes where $n \neq m$

$$\int_S \mathbf{e}_{nL} \times \mathbf{h}_{mL}^* \cdot d\mathbf{S} = 0 \quad (2.34)$$

$$\int_S \mathbf{e}_{nR} \times \mathbf{h}_{mR}^* \cdot d\mathbf{S} = 0 \quad (2.35)$$

The integral over S_L on LHS (see Figure 2.10) may be transformed into an integral over S_R where this is for the case of stepping into a waveguide with larger radius ($b > a$).

Thus since,

$$\sum_{n=1}^N (D_n + C_n) \mathbf{e}_{nR} = 0 \quad (2.36)$$

at the conducting wall, S_W (where $S_W = S_R - S_L$), in order to satisfy the boundary condition that the transverse electric field in the larger waveguide outside the common free space region between the guides is zero, this implies

$$\sum (D_n + C_n) \int_{S_L} \mathbf{e}_{nR} \times \mathbf{h}_{n'R}^* \cdot d\mathbf{S} = \sum (D_n + C_n) \int_{S_R} \mathbf{e}_{nR} \times \mathbf{h}_{n'R}^* \cdot d\mathbf{S}. \quad (2.37)$$

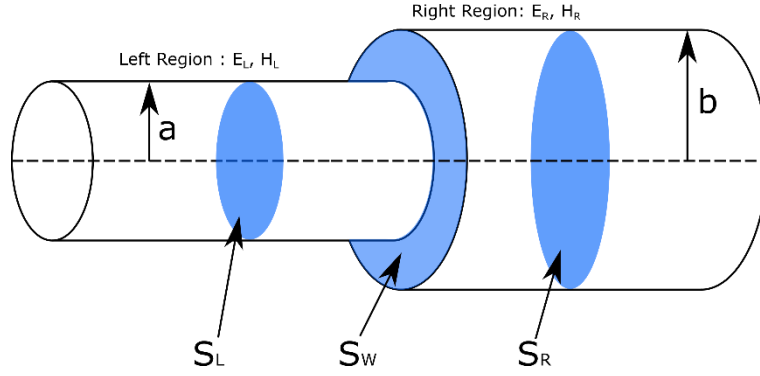


Figure 2.10: Fields at a junction between two horn sections

Equation (2.33) may then be re-expressed as

$$\sum_{n=1}^N (A_n + B_n) P_{n'n} = \sum_{n=1}^N (D_n + C_n) Q_{n'n}, \quad (2.38)$$

or, in matrix form

$$[P][[A]+[B]] = [Q][[C]+[D]], \quad (2.39)$$

where

$$P_{n'n} = \int_{S_L} \mathbf{e}_{nL} \times \mathbf{h}_{n'R} \cdot dS, \quad (2.40)$$

and

$$Q_{n'n} = \left(\int_{S_R} \mathbf{e}_{nR} \times \mathbf{h}_{n'R} \cdot dS \right) \delta_{n'n}. \quad (2.41)$$

The $[P]$ matrix contains the power coupled between modes on the LHS to modes on the RHS of the discontinuity and the $[Q]$ matrix represents the self-coupling power between modes on RHS of the discontinuity.

Similarly, we obtain a result for the continuity of the magnetic fields at a junction

$$\sum_{n=1}^N (A_n^* - B_n^*) \int_{S_L} \mathbf{e}_{n'L} \times \mathbf{h}_{nL}^* \cdot dS = \sum_{n=1}^N (D_n^* - C_n^*) \int_{S_L} \mathbf{e}_{n'L} \times \mathbf{h}_{nR}^* \cdot dS \quad (2.42)$$

which may be also expressed as

$$\sum_{n=1}^N (A_n^* - B_n^*) R_{m'} = \sum_{n=1}^N (D_n^* - C_n^*) P_{m'}, \quad (2.43)$$

or, in matrix form taking the complex conjugate on both sides

$$[R]^* [[A] - [B]] = [P]^+ [[D] - [C]], \quad (2.44)$$

where

$$R_{m'} = \left(\int_{S_L} \mathbf{e}_{n'L} \times \mathbf{h}_{nL}^* \cdot d\mathbf{S} \right) \delta_{n'n}. \quad (2.45)$$

The $[R]$ matrix represents the self-coupling power between modes on the LHS of the junction. The cross-coupling integral $[P]$ and the self-coupling integrals $[Q]$ and $[R]$ are evaluated using the surface integral relation

$$\int_S \mathbf{e}_n \times \mathbf{h}_{n'}^* \cdot d\mathbf{S} = \int_0^{2\pi} \int_0^a (E_r H_\phi^* - E_\phi H_r^*) r dr d\phi \quad (2.46)$$

$\mathbf{e} \times \mathbf{h}^*$ has the form of a Poynting vector giving the magnitude and direction of energy flow density at any point in the waveguide. The self-coupling integrals are real for propagating modes and imaginary for evanescent modes.

The scattering matrices at a junction can be derived using Equations (2.23), (2.24), (2.35) and (2.40) and are given by (Olver 1994: 112):

$$[S_{11}] = [[R^*]^+ + [P]^+ [Q]^{-1} [P]]^{-1} [[R] - [P]^+ [Q]^{-1} [P]] \quad (2.47)$$

$$[S_{12}] = 2 [[R^*]^+ + [P]^+ [Q]^{-1} [P]]^{-1} [P]^+ \quad (2.48)$$

$$[S_{21}] = 2 [[Q] + [P][R^*]^{-1} [P]^+]^{-1} [P] \quad (2.49)$$

$$[S_{22}] = -[[Q] + [P][R^*]^{-1} [P]^+]^{-1} [[Q] - [P][R^*]^{-1} [P]^+] \quad (2.50)$$

Between the junctions where a step in the radius occurs, the fields clearly propagate through uniform waveguide sections. Although no scattering occurs within the uniform waveguide section, nevertheless, the modes do suffer a phase delay. The ‘scattering’ matrices for these sections are thus diagonal and of the form

$$[S_{11}] = [S_{22}] = [0], \quad (2.51)$$

$$[S_{12}] = [S_{21}] = [V], \quad (2.52)$$

where $[V]$ is a diagonal matrix containing the propagation terms

$$[V] = [e^{-j\beta_n L}], \quad (2.53)$$

where β_n is the waveguide wavenumber (real for propagating modes and imaginary for evanescent modes) and L is the length of the waveguide section (the first section of the structure in this case) (Olver, 1994: 110,115). Each propagation term is given by

$$V_{nn} = e^{-j\beta_n L} \delta_{nn}. \quad (2.54)$$

By cascading the scattering matrix for the current discontinuity being considered with the scattering matrix for the horn and waveguide up this current junction (step discontinuity) in an iterative process, the complete scattering matrix for the horn and waveguide feed as a whole is obtained. This is illustrated schematically in Figure 2.11.

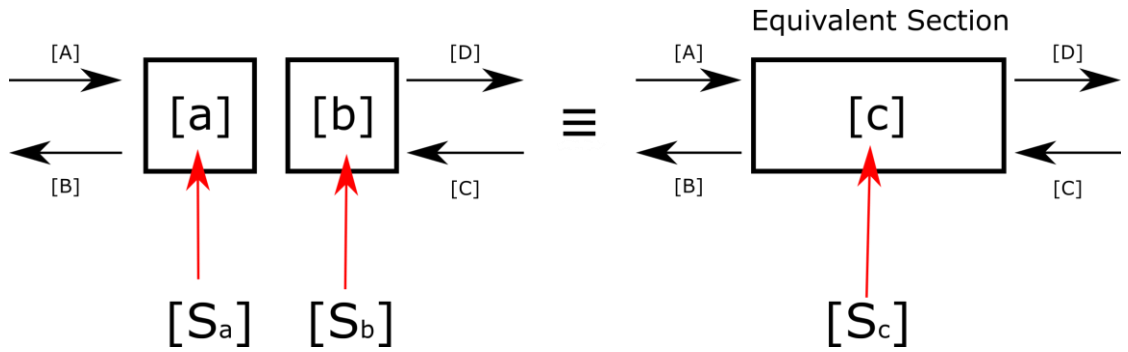


Figure 2.11: Schematic for cascading matrices for two consecutive sections

Thus, consider two consecutive waveguide sections with scattering matrices $[S^a]$, followed by $[S^b]$, which give the following cascaded matrix (Olver et.al., 1994 : 109):

$$[S^c] = \begin{bmatrix} [S_{11}^c] & [S_{12}^c] \\ [S_{21}^c] & [S_{22}^c] \end{bmatrix}. \quad (2.55)$$

The cascaded matrix elements are given by (Olver *et. al.*, 1994: 109)

$$[S_{11}^c] = [S_{12}^a] [[I] - [S_{11}^b] [S_{22}^a]]^{-1} [S_{11}^b] [S_{21}^a] + [S_{11}^a], \quad (2.56)$$

$$[S_{12}^c] = [S_{12}^a] [[I] - [S_{11}^b] [S_{22}^a]]^{-1} [S_{12}^b], \quad (2.57)$$

$$[S_{21}^c] = [S_{21}^b] \left[[I] - [S_{22}^a] [S_{11}^b] \right]^{-1} [S_{21}^a], \quad (2.58)$$

$$[S_{22}^c] = [S_{21}^b] \left[[I] - [S_{22}^a] [S_{11}^b] \right]^{-1} [S_{22}^a] [S_{12}^b] + [S_{22}^b], \quad (2.59)$$

where the index a refers to the scattering matrix for the horn up to the current junction and b refers to the scattering matrix for the current junction.

A smooth walled horn can be regarded as a large series of steps which approximate a tapered waveguide profile. Corrugated horns are regarded as a large series of short waveguide sections corresponding to the corrugation slots and fins (Olver *et al.*, 1994: 106).

The mutual power coupling integrals P_{ij} between the left and right hand waveguides are given in (Olver, 1994: 114) and (Gleeson, 2004: 134) as

$$P_{TM,n,l'-TM,n,l} = \frac{(1 + \delta_{n0}) \pi C_{nl}(a) C_{n'l'}(b) a \left(\frac{p_{n'l'}}{b} \right) J'_n(p_{nl}) J_n \left(\frac{p_{nl} a}{b} \right)}{Z_{TM,n,l'}^{b*} \left(\left(\frac{p_{n'l'}}{b} \right) + \left(\frac{p_{nl}}{a} \right) \right)^2}, \quad (2.60)$$

$$P_{TE,n,l'-TE,n,l} = \frac{-(1 + \delta_{n0}) \pi D_{nl}(a) D_{n'l'}(b) p'_{n'l'} J_n(p'_{n'l'}) J'_n \left(\frac{p'_{n'l'} a}{b} \right)}{Z_{TE,n,l'}^{b*} \left(\left(\frac{p'_{n'l'}}{b} \right) - \left(\frac{p'_{nl}}{a} \right) \right)^2}, \quad (2.61)$$

$$P_{TE,n,l'-TM,n,l} = \frac{\pi D_{nl}(a) C_{n'l'}(b)}{2 Z_{TM,n,l'}^{b*}} J_n(p_{nl}) J'_n \left(\frac{p'_{n'l'} a}{b} \right), \quad (2.62)$$

$$P_{TM,n,l'-TE,n,l} = 0, \quad (2.63)$$

where a and b refer to the left hand (smaller) and right hand (larger) waveguides, n is the azimuthal order, l is the radial order associated with the waveguide of radius a and l' is the radial order associated with the waveguide of radius b . The C_{nl} and D_{nl} terms are defined as

$$C_{nl}(a) = \sqrt{\frac{(2 - \delta_{n0}) |Z_{TM,n,l}^a|}{\pi a^2 J_{n+1}^2(p_{nl})}}, \quad (2.64)$$

$$D_{nl}(a) = \sqrt{\frac{(2 - \delta_{n0}) |Z_{TE,n,l}^a|}{\pi a^2 (1 - (n/p'_{nl})) J_n^2(p'_{nl})}} \quad (2.65)$$

and the characteristic waveguide impedances Z_{TE} and Z_{TM} for TE and TM modes are defined as (with $Z_0 = \sqrt{\mu/\varepsilon}$) in Equations (2.9) and (2.17).

2.4 Mode Matching in Cylindrical Waveguides when Absorber is Included

This mode matching approach can be extended to model waveguide cavities containing resistive sheet absorbers (see Figure 2.12). The absorber at a particular location within the structure can be approximated as a 2-dimensional resistive current sheet if it is not thick compared to the wavelength in free space. Furthermore, we assume that the electric field remains constant across the sheet while the magnetic field must change because of the current flowing in the sheet (Amperes Law) (Griffiths, 1999: 332). Thus considering the input (left side) and output (right side) faces of the absorber (see Figure 2.12), applying the usual boundary conditions at an interface (Griffiths, 1999 : 332) the electric and magnetic fields must satisfy: $\mathbf{E}_L = \mathbf{E}_R$ and $\mathbf{H}_L = \mathbf{H}_R - \mathbf{K} \times \hat{\mathbf{k}}$ where the induced surface current, \mathbf{K} , (driven by the electric field) is given by: $\mathbf{K} = \mathbf{E}_L/R_S = \mathbf{E}_R/R_S$ and $\hat{\mathbf{k}}$ is a unit vector in the direction of propagation (z). R_S is the surface resistance of the absorber and it is defined in units of Ohms per square (Ω/\square).

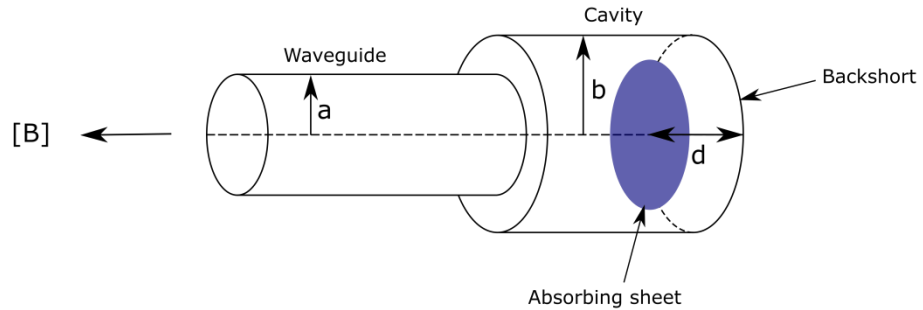


Figure 2.12: Waveguide-fed sealed cavity containing a circular absorber sheet

Consider the case of an absorber in a waveguide cavity with the exit port closed. Positioning the absorber at $z=0$ the electric and magnetic fields are given by Equations (2.27) to (2.30) as before.

Since for the electric fields on both sides of the absorber $\mathbf{E}_L = \mathbf{E}_R$ over the whole waveguide diameter (including the absorber) this implies that (since $\mathbf{e}_{nL} = \mathbf{e}_{nR} = \mathbf{e}_n$ and $\mathbf{h}_{nL} = \mathbf{h}_{nR} = \mathbf{h}_n$ as there is no step in the waveguide, so the waveguide modes on either side of the absorber are the same) and following a similar approach to that used for deriving the $P_{m'n'}$ elements of the $[P]$ matrix (Equation (2.33)) we obtain:

$$\sum_{n=1}^N \{A_n + B_n\} R_{n'n} = \sum_{n=1}^N \{C_n + D_n\} Q_{n'n} \quad (2.66)$$

while $\mathbf{H}_L = \mathbf{H}_R - \mathbf{K} \times \hat{k}$ implies

$$\begin{aligned} \sum_{n=1}^N \{A_n^* - B_n^*\} Q_{m'n'} = \\ \sum_{n=1}^N \{D_n - C_n\} Q_{m'n'} - \sum_{n=1}^N \{A_n + B_n\} \int_0^a \int_\phi^{2\pi} \mathbf{e}_{n'} \times \left(\frac{\mathbf{e}_n^*}{R_S(r, \phi)} \times \hat{k} \right) \cdot \hat{k} r dr d\phi \end{aligned} \quad (2.67)$$

Note that the absorber is allowed to have an arbitrary shape and even a varying surface resistance by introducing $R_S(r, \phi)$ and such that where there is no absorber $R_S(r, \phi) = \infty$.

Then, clearly since $[R_{m'n'}] = [Q_{m'n'}]$ (no step) this implies that

$\sum_{n=1}^N \{A_n + B_n\} Q_{m'n'} = \sum_{n=1}^N \{C_n + D_n\} Q_{m'n'}$ which we can write in matrix notation as:

$$[Q][A] + [Q][B] = [Q][C] + [Q][D] \quad (2.68)$$

Similarly letting $T_{n'n} = -\int_0^a \int_\phi^{2\pi} \mathbf{e}_{n'}^* \times \left(\frac{\mathbf{e}_n}{R_S(r, \phi)} \times \hat{k} \right) r dr d\phi = \int_0^a \int_\phi^{2\pi} \frac{\mathbf{e}_{n'}^* \cdot \mathbf{e}_n}{R_S(r, \phi)} r dr d\phi$, we

have that: $\sum_{n=1}^N \{A_n - B_n\} Q_{m'n'}^* = \sum_{n=1}^N \{D_n - C_n\} Q_{m'n'}^* + \sum_{n=1}^N \{A_n + B_n\} T_{n'n}^*$ which can be

written in matrix form as:

$$[Q]^*[A]-[Q]^*[B]=[Q]^*[D]-[Q]^*[C]+[T][A]+[T][B] \quad (2.69)$$

This allows us to solve for $[B]$ and $[D]$ for given input $[A]$ and $[B]$ (incident field amplitude vectors). Since $[Q]$ always has an inverse, this implies that:

$$[A]+[B]=[C]+[D], \quad (2.70)$$

and

$$[A]-[B]=[D]-[C]+[Q^*]^{-1}[T][A]+[Q^*]^{-1}[T][B], \quad (2.71)$$

This yields, after some matrix manipulation and simple algebra, that:

$$[B]=\left[[Q^*]^{-1}+\frac{1}{2}[T]\right]^{-1}[Q^*][C]-\left[[Q^*]^{-1}+\frac{1}{2}[T]\right]^{-1}\frac{1}{2}[T][A] \quad (2.72)$$

$$[D]=\left[[Q^*]^{-1}+\frac{1}{2}[T]\right]^{-1}[Q^*][A]-\left[[Q^*]^{-1}+\frac{1}{2}[T]\right]^{-1}\frac{1}{2}[T][C] \quad (2.73)$$

The relationships derived above allow for the derivation of the required scattering matrices for the case when the absorber is partially, or completely, filling the surrounding waveguide or cavity cross-section. The power carried by the modes making up the propagating fields may be either reflected or transmitted at a discontinuity at the two surfaces of an absorber, thus giving rise to the usual four scattering matrices. The appropriate scattering matrices for an absorber in a waveguide are therefore:

$$[S_{11}]=[S_{22}]=-\left[[Q^*]+\frac{1}{2}[T]\right]^{-1}\frac{1}{2}[T] \quad (2.74)$$

$$[S_{12}]=[S_{21}]=\left[[Q^*]+\frac{1}{2}[T]\right]^{-1}[Q^*] \quad (2.75)$$

where $[S_{11}]$, $[S_{12}]$, $[S_{21}]$ and $[S_{22}]$ represent the usual scattering matrices at a discontinuity. Because of the symmetry of the problem, clearly $[S_{21}]=[S_{12}]$ and $[S_{22}]=[S_{11}]$. These matrices can then be cascaded with the scattering matrices for the rest of the structure in the usual manner for waveguides to determine the overall behaviour of the structure.

In cylindrical polar coordinates for the case where the absorber has a coaxial disc shape of radius R , and uniform surface resistance R_S it is possible to derive analytical forms for the $[T]$ matrix. These will have very similar forms to the coupling integrals for the power coupling integrals between modes in cylindrical waveguide with a step discontinuity.

2.5 Mode Coupling at a Circular Absorber in a Circularly Symmetric System

For a uniform concentric absorber of radius R , $T_{mn'}$ is given by

$$T_{mn'} = \int_{r=0}^a \int_{\phi=0}^{2\pi} \frac{(\mathbf{e}_n \cdot \mathbf{e}_{n'})}{R_S(r, \phi)} \cdot r dr d\phi = \frac{1}{R_S} \int_{r=0}^R \int_{\phi=0}^{2\pi} (\mathbf{e}_n \cdot \mathbf{e}_{n'}) \cdot r dr d\phi \quad (2.76)$$

In this section, n represents the azimuthal order and i and j represent the radial order of modes on LHS and RHS of the absorber (*i.e.* n in the previous section is now replaced by ni and nj).

For the case where both \mathbf{e}_i and \mathbf{e}_j are TM modes of the same azimuthal order n , and also both modes have the same polarisation dependence on ϕ , then (using Equation (2.7)) it can be written as

$$T_{n,ij}(TM \rightarrow TM) = \alpha_{ni} \cdot \alpha_{nj} (1 + \delta_{n0}) \pi \int_{r=0}^R \left\{ J_n' \left(p_{ni} \frac{r}{a} \right) J_n' \left(p_{nj} \frac{r}{a} \right) + \frac{n J_n(p_{ni} r/a) n J_n(p_{nj} r/a)}{p_{ni} r/a \quad p_{nj} r/a} \right\} r dr, \quad (2.77)$$

where

$$\alpha_{ni} = \frac{1}{a^2 |J_{n+1}(p_{ni})| |J_{n+1}(p_{nj})|}. \quad (2.78)$$

Then using the Bessel function relationships which state that $2J_n'(z) = J_{n-1}(z) - J_{n+1}(z)$ and also that $2nJ_n(z)/z = J_{n-1}(z) + J_{n+1}(z)$ we can then write for the term in the integral that:

$$\left\{ J_n'(z) J_n'(z) + \frac{n J_n(z) n J_n(z)}{z \quad z} \right\} = \{ J_{n-1}(z) J_{n-1}(z) + J_{n+1}(z) J_{n+1}(z) \} \quad (2.79)$$

Also as $a \neq b$ we have that:

$$\int J_n(az)J_n(bz)z dz = \frac{z}{a^2 - b^2} \left\{ \pm aJ_{n\pm 1}(az)J_n(bz) \mp bJ_{n\pm 1}(bz)J_n(az) \right\} \quad a \neq b \quad (2.80)$$

and this in turn implies that

$$\begin{aligned} & \int \{J_{n-1}(az)J_{n-1}(bz) + J_{n+1}(az)J_{n+1}(bz)\} z dz = \\ & \frac{z}{a^2 - b^2} \{aJ_n(az)J'_n(bz) - bJ_n(bz)J'_n(az)\} \quad a \neq b \end{aligned} \quad (2.81)$$

while for the case where $a = b$ the appropriate integral is:

$$\int J_n(az)^2 z dz = \frac{z^2}{2} \{J_n(az)^2 - J_{n-1}(bz)J_{n+1}(az)\} \quad a = b. \quad (2.82)$$

This then implies

$$\begin{aligned} & \int \{J_{n+1}(az)^2 + J_{n-1}(az)^2\} z dz = \\ & \frac{z^2}{2} \{J_{n+1}(az)^2 + J_{n-1}(az)^2 - J_n(bz)J_{n+2}(az) - J_n(bz)J_{n-2}(az)\}. \end{aligned} \quad (2.83)$$

Thus for the T_{ij} matrix elements where both modes are TM :

$$\begin{aligned} T_{TM, TM_j} &= \frac{2Ra\alpha_{ni}^* \alpha_{nj}}{R_s} \\ & \times \frac{\left(p_{ni}J_n\left(p_{ni}\frac{R}{a}\right)J'_n\left(p_{nj}\frac{R}{a}\right) - p_{nj}J'_n\left(p_{ni}\frac{R}{a}\right)J_n\left(p_{nj}\frac{R}{a}\right) \right)}{p_{ni}^2 - p_{nj}^2} \quad \text{for } i \neq j \end{aligned} \quad (2.84)$$

and for the case where $i = j$ we obtain:

$$\begin{aligned} T_{TM, TM_i} &= \frac{R^2\alpha_{ni}^2}{2R_s} \times \\ & \left(\left\{ J_{n-1}\left(p_{ni}\frac{R}{a}\right) \right\}^2 + \left\{ J_{n+1}\left(p_{ni}\frac{R}{a}\right) \right\}^2 - J_n\left(p_{ni}\frac{R}{a}\right) \left\{ J_{n-2}\left(p_{ni}\frac{R}{a}\right) + J_{n+2}\left(p_{ni}\frac{R}{a}\right) \right\} \right). \end{aligned} \quad (2.85)$$

Following the same procedure for TE modes we get

$$\mathbf{e}_{n,i,TE} = \chi_{ni} \cdot \left[\frac{nJ_n(q_{ni}r/a)}{p'_{ni}r/a} \begin{Bmatrix} \sin n\phi \\ -\cos n\phi \end{Bmatrix} \hat{\mathbf{r}} + J'_n\left(p'_{ni}\frac{r}{a}\right) \begin{Bmatrix} \cos n\phi \\ \sin n\phi \end{Bmatrix} \hat{\boldsymbol{\phi}} \right] \quad (2.86)$$

where

$$\chi_{ni} = \left[a^2 J_n(p'_{ni})^2 \left| 1 - (p'_{ni}/a k_0)^2 \right| \left(1 - (n/p'_{ni})^2 \right) \right]^{-1/2} \quad (2.87)$$

and consequently,

$$T_{ij}(TE \rightarrow TE) = \chi_{ni}^* \chi_{nj} (1 + \delta_{n0}) \pi \int_{r=0}^R \left\{ \frac{n J_n(p'_{ni} r/a)}{p'_{ni} r/a} \frac{n J_n(p'_{nj} r/a)}{p'_{nj} r/a} + J'_n \left(p'_{ni} \frac{r}{a} \right) J'_n \left(p'_{nj} \frac{r}{a} \right) \right\} r dr, \quad (2.88)$$

which has a very similar form as was the case for both modes being TM.

Therefore, we can write down the appropriate terms for *TE* modes:

$$T_{TE_i TE_j} = \frac{2 R a \chi_{ni} \chi_{nj}}{R_s} \times \frac{\left(p'_{ni} J'_n \left(q_{nj} \frac{R}{a} \right) J_n \left(p'_{ni} \frac{R}{a} \right) - p'_{nj} J'_n \left(p'_{ni} \frac{R}{a} \right) J_n \left(p'_{nj} \frac{R}{a} \right) \right)}{p_{ni}^2 - p_{nj}^2} \quad \text{for } i \neq j \quad (2.89)$$

and for $i = j$:

$$T_{TE_i TE_i} = \frac{R^2 \chi_{ni}^2}{2 R_s} \left(\left\{ J_{n-1} \left(p'_{ni} \frac{R}{a} \right) \right\}^2 + \left\{ J_{n+1} \left(p'_{ni} \frac{R}{a} \right) \right\}^2 - J_n \left(p'_{ni} \frac{R}{a} \right) \left\{ J_{n-2} \left(p'_{ni} \frac{R}{a} \right) + J_{n+2} \left(p'_{ni} \frac{R}{a} \right) \right\} \right) \quad (2.90)$$

For the case where one mode is TE and the other TM we obtain:

$$T_{ij}(TM \rightarrow TE) = \alpha_{ni}^* \chi_{nj} (1 + \delta_{n0}) \pi \int_{r=0}^R \left\{ J'_n \left(p_{ni} \frac{r}{a} \right) \frac{n J_n(q_{nj} r/a)}{q_{nj} r/a} + \frac{n J_n(p_{ni} r/a)}{p_{ni} r/a} J'_n \left(q_{nj} \frac{r}{a} \right) \right\} r dr. \quad (2.91)$$

$$T_{ij}(TE \rightarrow TM) = \chi_{ni}^* \alpha_{nj} (1 + \delta_{n0}) \pi \int_{r=0}^R \left\{ \frac{n J_n(q_{ni} r/a)}{q_{ni} r/a} J'_n \left(p_{nj} \frac{r}{a} \right) + J'_n \left(q_{ni} \frac{r}{a} \right) \frac{n J_n(p_{nj} r/a)}{p_{nj} r/a} \right\} r dr. \quad (2.92)$$

These integrals are of the form: $\int \left\{ J'_n(az) \frac{J_n(bz)}{bz} + \frac{J_n(az)}{az} J'_n(bz) \right\} z dz = \frac{1}{ab} J_n(az) J_n(bz)$

which immediately gives:

$$T_{TM_i TE_j} = \frac{2na^2 \alpha_{ni} \chi_{nj}}{R_s} \times \frac{J_n\left(p_{ni} \frac{R}{a}\right) J_n\left(p'_{nj} \frac{R}{a}\right)}{p_{ni} p'_{nj}} \quad (2.93)$$

$$T_{TE_i TM_j} = \frac{2na^2 \chi_{ni} * \alpha_{nj}}{R_s} \times \frac{J_n\left(p'_{ni} \frac{R}{a}\right) J_n\left(p_{nj} \frac{R}{a}\right)}{p'_{ni} p_{nj}}. \quad (2.94)$$

The analytical expressions between mode coupling at the absorber will be used in chapter 4 for software verification, in chapter 5 when modelling the Planck HFI multimode 545 and 857 GHz channels, and in chapter 6 when analysing absorbers placed in free space gaps.

2.6 Rectangular Waveguide Modes

In this section we consider how to apply the mode matching technique to rectangular horns and waveguides. Square horns in particular are being proposed for terahertz systems such as SAFARI. The rectangular waveguides can propagate TE_{mn} and TM_{mn} modes (where m and n are the mode numbers associated with the variations in the field in the x and y directions respectively). Each waveguide mode has a cut-off frequency associated with it, below which propagation is not possible. For the case of a rectangular waveguide of width a and height b , the cutoff wavenumber for both TE and TM modes is given by Equation (2.95) below

$$k_c^2 = \left(\frac{m\pi}{a} \right)^2 + \left(\frac{n\pi}{b} \right)^2. \quad (2.95)$$

The origin of the axes is defined in Figure 2.13 below

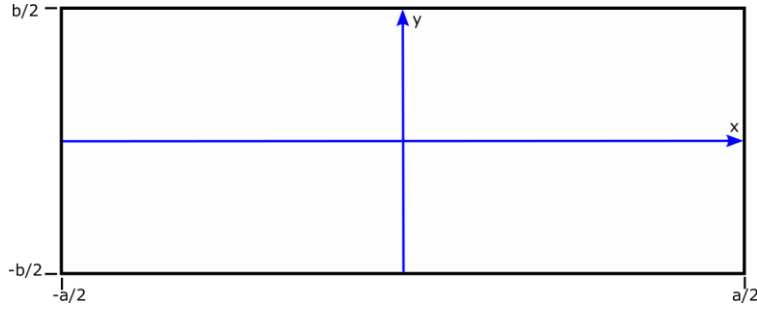


Figure 2.13: Axes origin

Assuming fields of the form $f(x, y) \cdot \exp(-i\beta k_0 z + i\omega t)$ the transverse fields can be derived from the z components as follows (Balanis, 2012: 353, 361)

$$\begin{aligned} E_x &= -\frac{1}{k_0^2(1-\beta^2)} \left(j\beta k_0 \frac{\partial E_z}{\partial x} + j\omega\mu \frac{\partial H_z}{\partial y} \right), \\ &= \frac{k_0}{k_x^2 + k_y^2} \left(-j\beta \frac{\partial E_z}{\partial x} - jZ_0 \frac{\partial H_z}{\partial y} \right) \end{aligned} \quad (2.96)$$

$$\begin{aligned} H_y &= -\frac{1}{k_0^2(1-\beta^2)} \left(j\omega\varepsilon \frac{\partial E_z}{\partial x} + j\beta k_0 \frac{\partial H_z}{\partial y} \right), \\ &= \frac{k_0}{k_x^2 + k_y^2} \left(-j \frac{1}{Z_0} \frac{\partial E_z}{\partial x} - j\beta \frac{\partial H_z}{\partial y} \right) \end{aligned} \quad (2.97)$$

$$\begin{aligned} E_y &= \frac{1}{k_0^2(1-\beta^2)} \left(-j\beta k_0 \frac{\partial E_z}{\partial y} + j\omega\mu \frac{\partial H_z}{\partial x} \right), \\ &= \frac{k_0}{k_x^2 + k_y^2} \left(-j\beta \frac{\partial E_z}{\partial y} + jZ_0 \frac{\partial H_z}{\partial x} \right) \end{aligned} \quad (2.98)$$

$$\begin{aligned} H_x &= \frac{1}{k_0^2(1-\beta^2)} \left(j\omega\varepsilon \frac{\partial E_z}{\partial y} - j\beta k_0 \frac{\partial H_z}{\partial x} \right), \\ &= \frac{k_0}{k_x^2 + k_y^2} \left(j \frac{1}{Z_0} \frac{\partial E_z}{\partial y} - j\beta \frac{\partial H_z}{\partial x} \right) \end{aligned} \quad (2.99)$$

Note that β is dimensionless, and $k_z = k_0 \beta$ (wavenumber in the z – direction).

TM Modes

We now apply these equations to rectangular waveguide modes in a rectangular waveguide. They have the form for TM modes ($H_z = 0$) in order to satisfy the boundary conditions on the perfectly conducting walls (depending on whether m is even or odd and whether n is even or odd):

$$H_x = -\frac{2}{\sqrt{|Z_0|\beta|}} \frac{n}{b} \sqrt{\frac{ab}{b^2 m^2 + a^2 n^2}} \sin\left(\frac{m\pi}{a}x - \frac{m\pi}{2}\right) \cos\left(\frac{n\pi}{b}y - \frac{n\pi}{2}\right) \quad (2.100)$$

$$H_y = \frac{2}{\sqrt{|Z_0|\beta|}} \frac{m}{a} \sqrt{\frac{ab}{b^2 m^2 + a^2 n^2}} \cos\left(\frac{m\pi}{a}x - \frac{m\pi}{2}\right) \sin\left(\frac{n\pi}{b}y - \frac{n\pi}{2}\right) \quad (2.101)$$

$$E_z = 2 \frac{\pi i}{k_0} \sqrt{\frac{|Z_0|}{|\beta|}} \left(\frac{m^2}{a^2} + \frac{n^2}{b^2}\right) \sqrt{\frac{ab}{b^2 m^2 + a^2 n^2}} \sin\left(\frac{m\pi}{a}x - \frac{m\pi}{2}\right) \sin\left(\frac{n\pi}{b}y - \frac{n\pi}{2}\right) \quad (2.102)$$

$$E_x = Z_0 \beta H_y \quad \text{and} \quad E_y = -Z_0 \beta H_x.$$

Expanding the terms in 2.100-2.102 we obtain

$$H_x = -\frac{2}{\sqrt{|Z_0|\beta|}} \frac{n}{b} \sqrt{\frac{ab}{b^2 m^2 + a^2 n^2}} \times \begin{pmatrix} \sin\left(\frac{m\pi}{a}x\right) \cos\left(\frac{n\pi}{b}y\right) & -\sin\left(\frac{m\pi}{a}x\right) \sin\left(\frac{n\pi}{b}y\right) \\ \cos\left(\frac{m\pi}{a}x\right) \cos\left(\frac{n\pi}{b}y\right) & -\cos\left(\frac{m\pi}{a}x\right) \sin\left(\frac{n\pi}{b}y\right) \end{pmatrix} \quad (2.103)$$

$$H_y = \frac{2}{\sqrt{|Z_0|\beta|}} \frac{m}{a} \sqrt{\frac{ab}{b^2 m^2 + a^2 n^2}} \times \begin{pmatrix} \cos\left(\frac{m\pi}{a}x\right) \sin\left(\frac{n\pi}{b}y\right) & \cos\left(\frac{m\pi}{a}x\right) \cos\left(\frac{n\pi}{b}y\right) \\ -\sin\left(\frac{m\pi}{a}x\right) \sin\left(\frac{n\pi}{b}y\right) & -\sin\left(\frac{m\pi}{a}x\right) \cos\left(\frac{n\pi}{b}y\right) \end{pmatrix} \quad (2.104)$$

$$E_z = 2 \frac{i}{\pi k_0} \sqrt{\frac{|Z_0|}{|\beta|}} \left(\frac{m^2 \pi^2}{a^2} + \frac{n^2 \pi^2}{b^2}\right) \sqrt{\frac{ab}{b^2 m^2 + a^2 n^2}} \times \begin{pmatrix} \sin\left(\frac{m\pi}{a}x\right) \sin\left(\frac{n\pi}{b}y\right) & \sin\left(\frac{m\pi}{a}x\right) \cos\left(\frac{n\pi}{b}y\right) \\ \cos\left(\frac{m\pi}{a}x\right) \sin\left(\frac{n\pi}{b}y\right) & \cos\left(\frac{m\pi}{a}x\right) \cos\left(\frac{n\pi}{b}y\right) \end{pmatrix} \quad (2.105)$$

and as before: $E_y = -Z_0 \beta H_x$, $E_x = Z_0 \beta H_y$ and the terms in the brackets of (2.103) – (2.105) are arranged in the following manner

$$\begin{pmatrix} \text{even}(m) - \text{even}(n) & \text{even}(m) - \text{odd}(n) \\ \text{odd}(m) - \text{even}(n) & \text{odd}(m) - \text{odd}(n) \end{pmatrix} \quad (2.106)$$

with $H_x = -\left(\frac{\beta}{Z_0}\right) E_y$ and $H_y = \left(\frac{\beta}{Z_0}\right) E_x$. Thus, the 4 terms in the 2×2 matrix in brackets in each equation represent the 4 possibilities for the fields where m and n are either even or odd. For example, the x-component of the magnetic field of the TM_{58} mode is given by $H_x = -\frac{2}{\sqrt{Z_0|\beta|}} \frac{8}{b} \sqrt{\frac{ab}{25b^2 + 64a^2}} \times \left[\cos\left(\frac{5\pi}{a}x\right) \cos\left(\frac{8\pi}{b}y\right) \right]$. The field distribution of some rectangular waveguide TM modes is given in Figure 2.14 below.

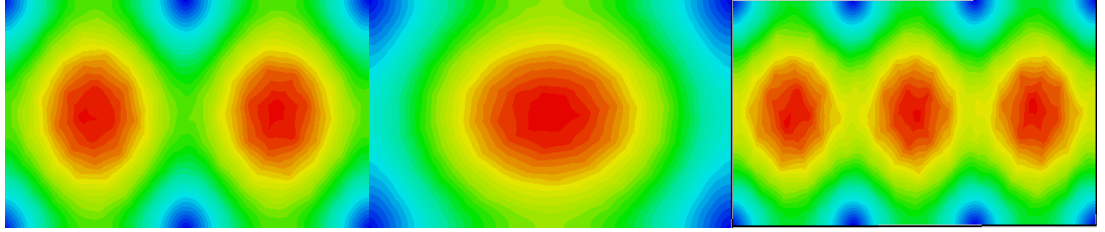


Figure 2.14: Electric field of TM21 (left), TM11 (middle) and TM31 (right) rectangular waveguide modes produced by CST

TE Modes

In order to satisfy the boundary conditions on the perfectly conducting walls the TE modes in a rectangular waveguide have the form:

$$E_x = 2 \sqrt{\frac{Z_0}{|\beta|}} \frac{n}{b} \sqrt{\frac{ab}{b^2 m^2 + a^2 n^2}} \cos\left(\frac{m\pi}{a}x - \frac{m\pi}{2}\right) \sin\left(\frac{n\pi}{b}y - \frac{n\pi}{2}\right) \quad (2.107)$$

$$E_y = -2 \sqrt{\frac{Z_0}{|\beta|}} \frac{m}{a} \sqrt{\frac{ab}{b^2 m^2 + a^2 n^2}} \sin\left(\frac{m\pi}{a}x - \frac{m\pi}{2}\right) \cos\left(\frac{n\pi}{b}y - \frac{n\pi}{2}\right) \quad (2.108)$$

and $H_x = -\left(\frac{\beta}{Z_0}\right) E_y$, $H_y = \left(\frac{\beta}{Z_0}\right) E_x$ and, since $\text{div } \mathbf{H} = 0$, we can derive H_z as

$$H_z = \frac{2}{j\pi k_0} \sqrt{\frac{1}{Z_0|\beta|}} \left(\frac{m^2\pi^2}{a^2} + \frac{n^2\pi^2}{b^2} \right) \sqrt{\frac{ab}{b^2 m^2 + a^2 n^2}} \cos\left(\frac{m\pi}{a}x - \frac{m\pi}{2}\right) \cos\left(\frac{n\pi}{b}y - \frac{n\pi}{2}\right) \quad (2.109)$$

Expanding the terms in Equations (2.107) to (2.109) we obtain (again depending on whether m is even or odd and whether n is even or odd)

$$E_x = 2 \sqrt{\frac{Z_0}{|\beta|}} \frac{n}{b} \sqrt{\frac{a b}{b^2 m^2 + a^2 n^2}} \times \begin{pmatrix} \cos\left(\frac{m \pi}{a} x\right) \sin\left(\frac{n \pi}{b} y\right) & -\cos\left(\frac{m \pi}{a} x\right) \cos\left(\frac{n \pi}{b} y\right) \\ \sin\left(\frac{m \pi}{a} x\right) \sin\left(\frac{n \pi}{b} y\right) & -\sin\left(\frac{m \pi}{a} x\right) \cos\left(\frac{n \pi}{b} y\right) \end{pmatrix}, \quad (2.110)$$

$$E_y = 2 \sqrt{\frac{Z_0}{|\beta|}} \frac{m}{a} \sqrt{\frac{a b}{b^2 m^2 + a^2 n^2}} \times \begin{pmatrix} -\sin\left(\frac{m \pi}{a} x\right) \cos\left(\frac{n \pi}{b} y\right) & -\sin\left(\frac{m \pi}{a} x\right) \sin\left(\frac{n \pi}{b} y\right) \\ \cos\left(\frac{m \pi}{a} x\right) \cos\left(\frac{n \pi}{b} y\right) & \cos\left(\frac{m \pi}{a} x\right) \sin\left(\frac{n \pi}{b} y\right) \end{pmatrix}, \quad (2.111)$$

$$H_z = \frac{2}{\pi j k_0} \sqrt{\frac{1}{Z_0 |\beta|}} \left(\frac{m^2 \pi^2}{a^2} + \frac{n^2 \pi^2}{b^2} \right) \sqrt{\frac{a b}{b^2 m^2 + a^2 n^2}} \times \begin{pmatrix} \cos\left(\frac{m \pi}{a} x\right) \cos\left(\frac{n \pi}{b} y\right) & \cos\left(\frac{m \pi}{a} x\right) \sin\left(\frac{n \pi}{b} y\right) \\ \sin\left(\frac{m \pi}{a} x\right) \cos\left(\frac{n \pi}{b} y\right) & \sin\left(\frac{m \pi}{a} x\right) \sin\left(\frac{n \pi}{b} y\right) \end{pmatrix}, \quad (2.112)$$

where the terms in the brackets of Equations (2.110) to (2.112) are arranged as in Equation (2.106) and $H_x = -\left(\frac{\beta}{Z_0}\right) E_y$ and $H_y = \left(\frac{\beta}{Z_0}\right) E_x$. The field distribution of some rectangular waveguide TE modes is given in Figure 2.15 below.

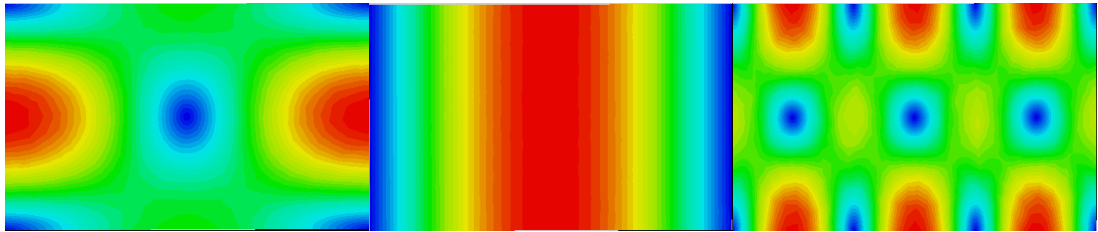


Figure 2.15: Electric field of TE₁₁ (left), TE₁₀ (middle) and TE₃₁ (right) rectangular waveguide modes produced by CST

2.7 Mode Matching in Rectangular Waveguides

In this section, we discuss the significant differences between mode matching in cylindrical waveguides and mode matching in rectangular waveguides, since the underlying physics in both cases is similar. While Bessel functions are used to describe the basis set for cylindrical modes, in the rectangular case it is the *sin* and *cos* functions that represent the basis set for rectangular modes.

The solutions to the modal cross-coupling integral, $[P]$, at a symmetric junction are outlined in Equations (2.113) to (2.116) below, where m and n refer to the mode numbers on the LHS of the junction and a and b refer to the dimensions of the step on the LHS of the junction. Similarly md , nd , ad and bd refer to the mode numbers and dimensions of the RHS of the junction as in Figure 2.16

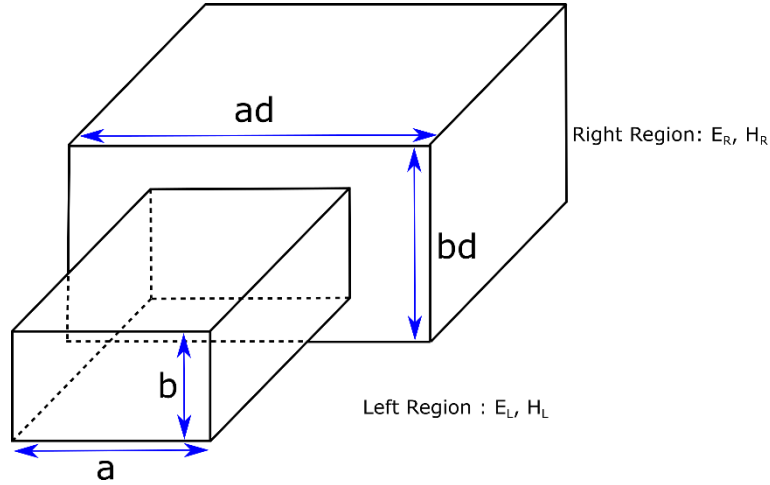


Figure 2.16: Rectangular waveguide junction

$$\begin{aligned}
 P_{TE \rightarrow TE} &= \frac{\beta d^*}{\sqrt{|\beta|} |\beta d|} \times \frac{16 md nd}{\pi^2 \sqrt{(\Gamma + \delta_{m0})} \sqrt{(\Gamma + \delta_{n0})}} \times \\
 &\sqrt{\frac{ab}{ad bd}} \times \sqrt{\frac{m^2 b^2 + n^2 a^2}{md^2 bd^2 + nd^2 ad^2}} \times \frac{ad^2}{md^2 a^2 - m^2 ad^2} \times \frac{bd^2}{nd^2 b^2 - n^2 bd^2} \times \\
 &\begin{pmatrix} (-1)^{(m+n)/2} \sin\left(\frac{md \pi a}{ad} \frac{a}{2}\right) \sin\left(\frac{nd \pi b}{bd} \frac{b}{2}\right) & (-1)^{(m+n+1)/2} \sin\left(\frac{md \pi a}{ad} \frac{a}{2}\right) \cos\left(\frac{nd \pi b}{bd} \frac{b}{2}\right) \\ (-1)^{(m+n+1)/2} \cos\left(\frac{md \pi a}{ad} \frac{a}{2}\right) \sin\left(\frac{nd \pi b}{bd} \frac{b}{2}\right) & (-1)^{(m+n+2)/2} \cos\left(\frac{md \pi a}{ad} \frac{a}{2}\right) \cos\left(\frac{nd \pi b}{bd} \frac{b}{2}\right) \end{pmatrix}
 \end{aligned} \tag{2.113}$$

$$\begin{aligned}
 P_{TM \rightarrow TM} &= \frac{\beta d}{\sqrt{|\beta||\beta d|}} \frac{16 mn}{\pi^2} \sqrt{\frac{ad bd}{ab}} \sqrt{\frac{md^2 bd^2 + nd^2 ad^2}{m^2 b^2 + n^2 a^2}} \times \\
 &\quad \frac{a^2}{md^2 a^2 - m^2 ad^2} \frac{b^2}{nd^2 b^2 - n^2 bd^2} \times \\
 &\quad \left(\begin{array}{cc} (-1)^{(m+n)/2} \sin\left(\frac{md \pi a}{ad \ 2}\right) \sin\left(\frac{nd \pi b}{bd \ 2}\right) & (-1)^{(m+n+1)/2} \sin\left(\frac{md \pi a}{ad \ 2}\right) \cos\left(\frac{nd \pi b}{bd \ 2}\right) \\ (-1)^{(m+n+1)/2} \cos\left(\frac{md \pi a}{ad \ 2}\right) \sin\left(\frac{nd \pi b}{bd \ 2}\right) & (-1)^{(m+n+2)/2} \cos\left(\frac{md \pi a}{ad \ 2}\right) \cos\left(\frac{nd \pi b}{bd \ 2}\right) \end{array} \right)
 \end{aligned} \tag{2.114}$$

$$\begin{aligned}
 P_{TE \rightarrow TM} &= \frac{1}{\sqrt{|\beta||\beta d|}} \times \frac{16}{\pi^2 \sqrt{(\Gamma + \delta_{m0})} \sqrt{(\Gamma + \delta_{n0})}} \times \\
 &\quad \sqrt{\frac{ab}{m^2 b^2 + n^2 a^2}} \times \sqrt{\frac{ad bd}{md^2 bd^2 + nd^2 ad^2}} \times \frac{(n^2 a^2 md^2 bd^2 - m^2 b^2 nd^2 ad^2)}{(md^2 a^2 - m^2 ad^2)(nd^2 b^2 - n^2 bd^2)} \times \\
 &\quad \left(\begin{array}{cc} (-1)^{(m+n)/2} \sin\left(\frac{md \pi a}{ad \ 2}\right) \sin\left(\frac{nd \pi b}{bd \ 2}\right) & (-1)^{(m+n-1)/2} \sin\left(\frac{md \pi a}{ad \ 2}\right) \cos\left(\frac{nd \pi b}{bd \ 2}\right) \\ (-1)^{(m+n-1)/2} \cos\left(\frac{md \pi a}{ad \ 2}\right) \sin\left(\frac{nd \pi b}{bd \ 2}\right) & (-1)^{(m+n-2)/2} \cos\left(\frac{md \pi a}{ad \ 2}\right) \cos\left(\frac{nd \pi b}{bd \ 2}\right) \end{array} \right)
 \end{aligned} \tag{2.115}$$

$$P_{TM \rightarrow TE} = 0 \tag{2.116}$$

where the terms in the brackets are arranged as before (in Equation (2.106)).

For the case of a TM_{mn} mode, the mode number coefficients cannot be zero. However, for the case of a TE_{mn} , it is possible for one of the coefficients to be zero. Thus, for example if a TE_{0n} mode on the LHS of a junction scatters into a TE_{0nd} mode on the RHS of a junction, then Equation (2.113) becomes indeterminate. Thus, for the case when the m and md mode numbers are both zero we obtain the following expression

$$\begin{aligned}
 P_{TE \rightarrow TE} &= \frac{4}{\pi} \times \frac{\beta d^*}{\sqrt{|\beta||\beta d|}} \times \sqrt{\frac{ab}{ad bd}} \times \frac{nb d^2}{nd^2 b^2 - n^2 bd^2} \times \\
 &\quad \left(\begin{array}{cc} (-1)^{n/2} \sin\left(\frac{nd \pi b}{bd \ 2}\right) & (-1)^{(n+1)/2} \cos\left(\frac{nd \pi b}{bd \ 2}\right) \\ 0 & 0 \end{array} \right),
 \end{aligned} \tag{2.117}$$

where the terms in the brackets of Equation (2.117) are arranged as in Equation (2.106).

Similarly, if a TE_{m0} mode on the LHS of a junction scatters into a TE_{md0} mode on the RHS of a junction, then Equation (2.113) becomes indeterminate. Thus, for the case when the n and nd numbers are both zero we obtain the following expression

$$P_{TE \rightarrow TE} = \frac{4}{\pi} \frac{\beta d^*}{\sqrt{|\beta|} |\beta d|} \sqrt{\frac{ab}{ad bd}} \frac{mad^2}{md^2 a^2 - m^2 ad^2} \quad (2.118)$$

$$\times \begin{pmatrix} (-1)^{m/2} \sin\left(\frac{md \pi a}{ad 2}\right) & 0 \\ (-1)^{(m+1)/2} \cos\left(\frac{md \pi a}{ad 2}\right) & 0 \end{pmatrix},$$

where the terms in the brackets of Equation (2.118) are arranged as before (in Equation (2.106)).

The power coupling matrix $[P]$ is arranged as displayed in Figure 2.17 below. The matrix is divided into four quadrants, which represent coupling from TE to TE and TM modes and from TM to TM and TE modes. Modal scattering is only possible for certain combinations of modes because of the symmetry, which are highlighted in Figure 2.17 below (blue squares represent possible scattering combinations for TE to TE modes, red represent TM to TM power coupling and green represent TE to TM power coupling).

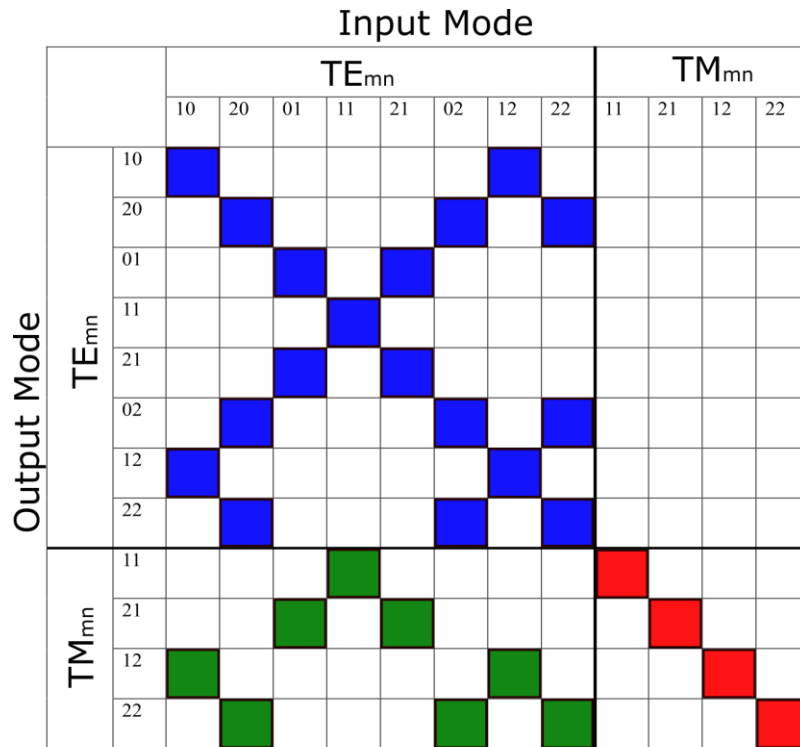


Figure 2.17: Example of the elements of the power coupling matrix, $[P]$, for rectangular geometries. The maximum mode order here is 2

When applying mode matching for the cylindrical case it was observed that only modes with the same azimuthal order could couple to one another, provided the symmetry was not broken. In the cylindrical case, the scattering matrices were separated for every azimuthal order in order to avoid unnecessary computations and to only evaluate the coupling integral for modes of the same order. In the rectangular case, modal scattering is possible between different mode orders. It is thus necessary to have just one large scattering matrix representing the scattering between all of the different mode orders (the same applies to the cross-coupling and self-coupling matrices). In terms of deriving the scattering matrix for rectangular geometries, the same set of equations were used for both the cylindrical and rectangular geometries (Equations (2.47) to (2.50)), keeping all of the mode orders together in the rectangular case. Figure 2.18 below shows the arrangement of each scattering submatrix ($[S_{11}]$, $[S_{12}]$, $[S_{21}]$ and $[S_{22}]$) for a rectangular geometry where modes up to order 2 are being considered. The matrix is divided into four quadrants, which represent coupling from TE to TE and TM modes and from TM to TM and TE modes as for the $[P]$ matrix. Modal scattering in this case is only possible for certain combinations of modes, which are highlighted in Figure 2.18 below (blue squares represent possible scattering combinations for TE to TE modes, red represent TM to TM modal scattering, green represent TE to TM modal scattering and yellow represent TM to TE modal scattering.). Note that in this case there are entries for the TM to TE modes as is clear from Equations (2.47) to (2.50).

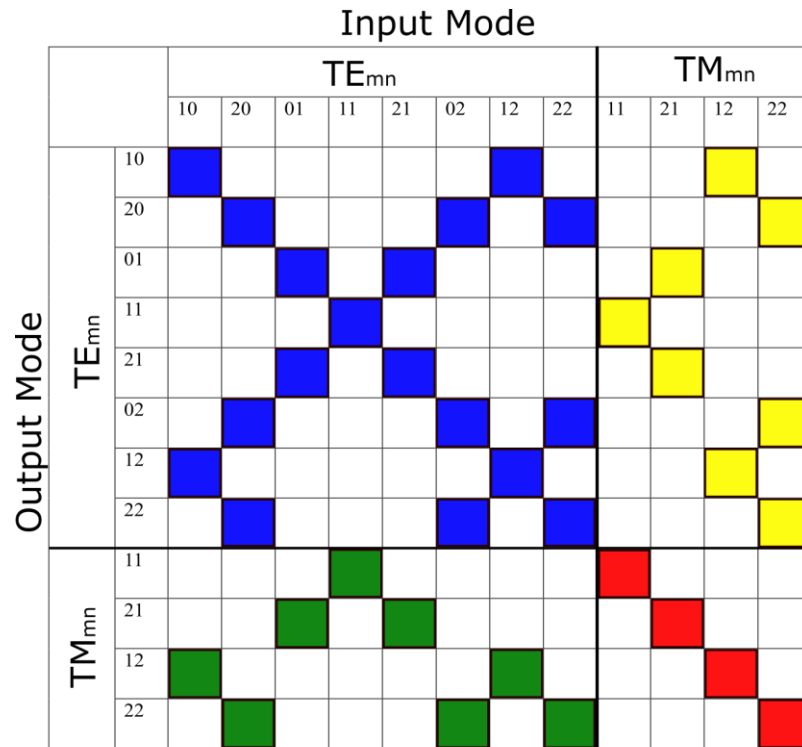


Figure 2.18: Example of a scattering matrix for rectangular geometries.

In summary, the mode matching approach for obtaining an overall scattering matrix for both cylindrical and rectangular matrices is very similar. However, in the cylindrical case, the final scattering matrices can be separated for the different azimuthal orders. There is only one resulting large scattering matrix for a rectangular structure due to the fact that the different orders can scatter into each other when working out the scattering matrices at an individual junction.

2.8 Other Electromagnetic Analysis Techniques

As well as the mode matching approach, other electromagnetic analysis techniques are available, particularly those based on finite element analysis. CST (Computer Simulation Technology) (cst.com, 2017) Microwave Studio, for example, is a commercial software for Electromagnetic simulation of high frequency components which enables analysis of high frequency devices by calculating scattering parameters, electromagnetic field distributions, radiation patterns and other relevant parameters. Other FEM packages include for example HFSS and COMSOL, which use a similar approach. CST was the software package used throughout this thesis and thus will be described in detail.

CST is a computer aided design (CAD) based program which utilises finite integration techniques (FIT) to probe the performance of the structure (for example a horn antenna) being considered. Once the structure has been constructed in CST using the available CAD tools, it is then divided into mesh cells where the integral form of Maxwell's equations is solved for each individual mesh geometry. In order to solve the equations numerically, a calculation domain needs to be defined and a mesh is implemented to divide this domain into grid cells. Using the 'Mesh View' option, the mesh can be visualised in CST. Internally, a second mesh is set up orthogonal to the first one (as in Figure 2.19) and the spatial discretisation of Maxwell's equations is performed on the two orthogonal grid systems.

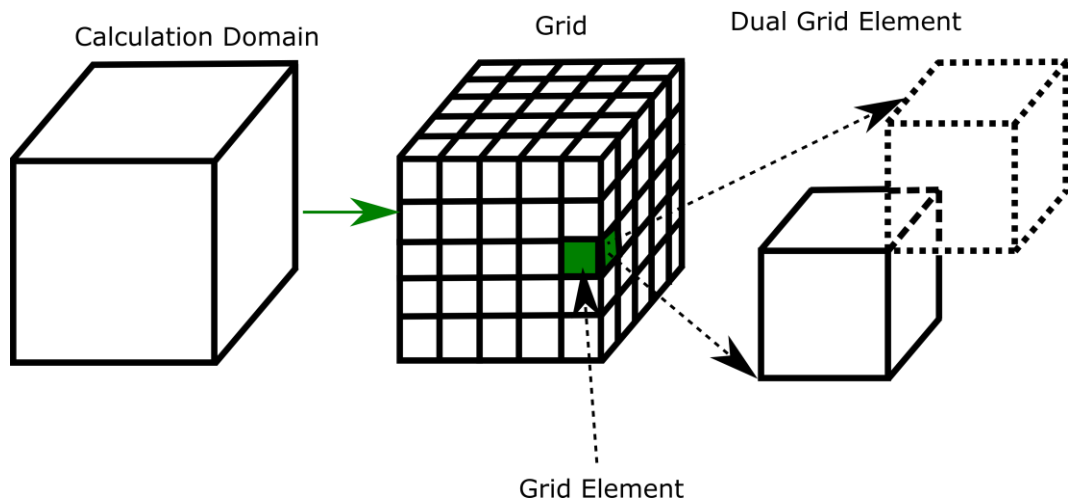


Figure 2.19: The CST mesh system

As well as being applied to orthogonal hexahedral grids, FIT can also be used with tetrahedral grids.

Solver Types

The finite element approach is implemented by means of three separate solvers available in CST: frequency domain, time domain and eigenmode solvers. The choice of solver used is determined by the type of structure being considered. For the applications considered in this thesis only the frequency domain and time domain solvers were used.

The frequency domain solver can be used together with both grid types available for mesh generation: hexahedral and tetrahedral, depending on what kind of structure is being considered. This solver is ideally suited for narrow band applications since every frequency considered requires a separate iteration. This solver does not compute fields,

but it is fast compared to other solvers as it is equipped with specialised modules for fast S-parameter calculations.

The time domain solver allows for the simulation of a structure's behaviour (full set of S-parameters and beam patterns) over a wide frequency band, where all frequencies considered are calculated in one computation. This solver type is compatible with the hexahedral grid mesh only. One limitation of this solver type is encountered when dealing with highly resonant structures (for example cavities), where the initial excitation may result in instabilities in the system, thus producing unphysical results. One way to overcome this would be to increase the time interval over which the structure is being examined. However, this is computationally intensive and will result in lengthy calculation times, even for electrically small structures.

Materials and Resistive Sheets

The two basic materials provided by CST are perfect electric conductors (PECs) and vacuums. CST also contains an extensive library of properties for various metals and dielectrics. Some of the more complex material types include conducting materials, lossy metals as well as coated and thermally dependent materials. The work presented in this thesis made use of PECs, vacuums and resistive sheet models.

When defining a resistive sheet in CST, two options were available: (i) the 'Ohmic Sheet' model, and (ii) the 'Tabulated Surface Impedance' model. For the work presented in this thesis, the Ohmic Sheet model was used. The ohmic sheets have the property that the electric field on both sides is the same. The resistance and reactance was specified by the user at a reference frequency, thus when using the frequency domain solver, the resistance and reactance remained constant across the investigated band.

CST for multimode structures

Throughout this thesis, CST will be used as a verification tool for the predictions made by the in-house mode matching software. The reflection and transmission characteristics were compared for waveguide and cavity structures, which are electrically small. CST was not applied to model the characteristics of a horn antenna due to the computational intensity of a calculation for an electrically large structure. As an example, the Planck 857

GHz receiver pixel is $\sim 400 \lambda$ in length (as will be described in Chapter 5), and since CST is designed to deal with much smaller structures, it would not be feasible to accurately model a structure of this large geometrical design in CST. Thus, CST was applied to electrically small (in terms of wavelength) structures, such as a few-moded waveguide fed cavity.

When analyzing a multimode structure in CST, all of the modes need to be defined at the excitation port. Consider the example shown in Figure 2.20, where a multimode waveguide is housing an absorber.

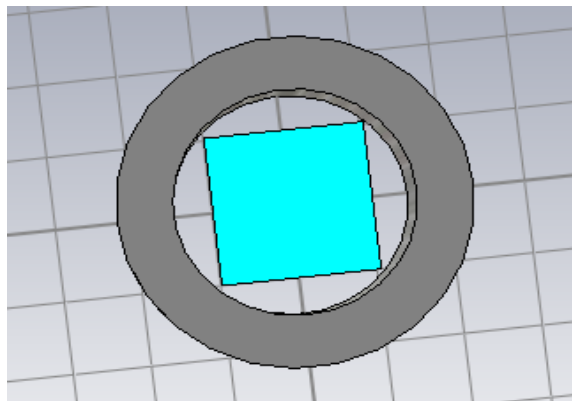


Figure 2.20: Example of a waveguide containing an absorber in CST

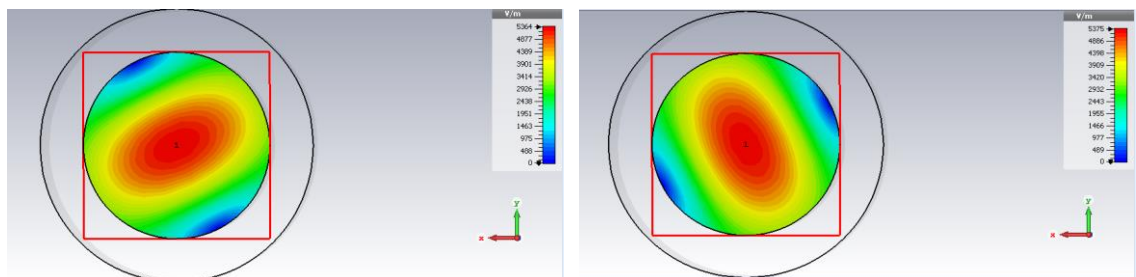


Figure 2.21: TE₁₁ Co-polar and TE₁₁ Orthogonal mode at the excitation port

There exists polarization orientation angle difference of $\pi/2$ radians between the TE_{11} co-polar and TE_{11} orthogonal mode. In the mode matching software these modes are assumed to be aligned with the x – axis and y – axis whereas in CST they are at angles of $\pm \pi/4$ radians with respect to the x -axis (as shown in Figure 2.21). This would not cause any issues for a symmetric system (for example a cylindrical waveguide housing a circular absorber), but once the symmetry is broken (as in the example in Figure 2.20), it is important to define polarization directions to be consistent with the mode matching software.

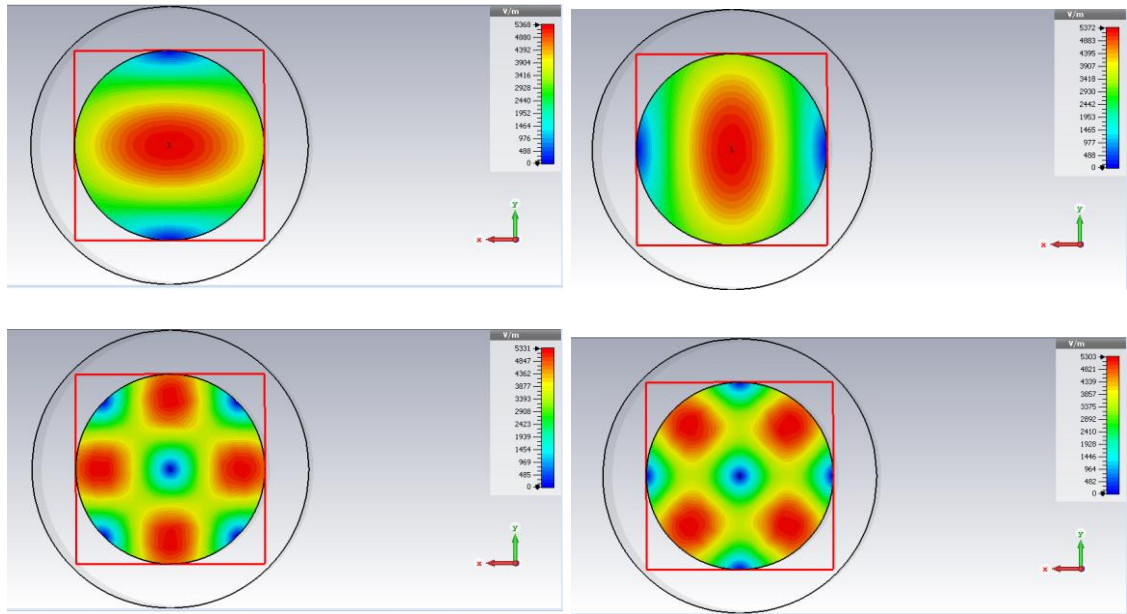


Figure 2.22: TE_{11} Co-polar, TE_{11} Orthogonal, TE_{21} Co-polar and TE_{21} Orthogonal modes at the excitation port

With the polarisation angle defined as 0° with respect to the x -axis (as in Figure 2.22), the $\pi/(2n)$ (where n is the azimuthal order) symmetry between co-polar and orthogonal modes is still present and this definition is consistent with the modes defined in GAMMA so that a direct comparison between the softwares is possible.

2.9 Experimental Verification of Multimode Propagation

In order to verify multimode propagation theory in waveguide-horn antenna structures, a measurement campaign was undertaken at the millimetre-wave measurement laboratory at Maynooth University. The laboratory is equipped with a Vector Network Analyser (VNA) and beam scanning system capable of making measurements between 75 GHz and 110 GHz. In this section we discuss the measurements carried out on a rectangular back-to-back horn antenna using the millimetre wave measurement testbed in Maynooth University.

2.9.1 Vector Network Analyser

The millimetre wave testbed uses a Rohde and Schwarz ZVA-24 (4 port) VNA. The VNA is designed to operate between 10 MHz and 24 GHz. However, by means of two ZV-110 frequency converter heads, measurements are possible in the W-band (75-110 GHz). The VNA allows for the measurement of the complex amplitude of the transmitted signal by comparing the received signal with the source that was originally used to create it, meaning that both the magnitude and phase of the electric field can be recovered.

The parameters commonly measured by the VNA are the S-parameters. The two port configuration used in Maynooth measures the transmission and reflection coefficients of each port. Figure 2.23 below shows an example of a two port system and the scattering parameters of a device under test as well as the incident waves from each port essentially the same as the scattering matrix representation for waveguides as illustrated in Figure 2.9 and Equation (2.23). The radiation from each port is linked by the scattering parameters. The relationship between the incident waves and reflected waves is outlined in Equation (2.22), which is in the section that discusses mode matching (Section 2.3).

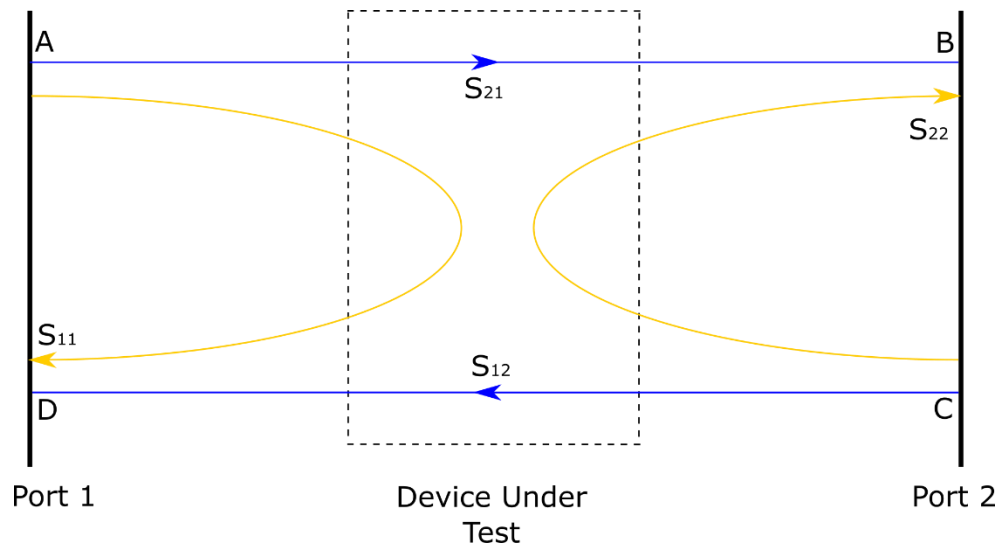


Figure 2.23: Scattering parameters for device under test for a two port system

Both frequency extension heads are able to simultaneously act as emitters and receivers. Thus, when studying a beam transmitted from an antenna, one of the ports is considered to be the emitter (port 2) and the other the receiver (port 1). The transmitter is kept stationary while the receiver is mounted on an xy scanner, thus resulting in a grid of data points which allows one to recover the beam properties.

Another stepper motor driven translation stage is also in use, which allows for the possibility of adjusting the distance from the transmitter to the receiver. The receiver is mounted on the z -translation stage.

2.9.2 Experimental Setup

In order to verify the predicted propagation of higher order modes in a rectangular horn fed by an overmoded waveguide the setup shown in Figure 2.24 was used. The measurement campaign was carried out in collaboration with Dr. Marcin Grądziel. However, the analysis was carried out by the author of this thesis. A symmetric back-to-back horn configuration was used in order to illuminate the radiating horn. The back-to-back overmoded structure could be rotated in order to vary power carried by the higher order modes in the waveguide. The measurement setup also consisted of a WR-10 waveguide probe on port 2 (xy scanner), a conical corrugated horn with a transition to a WR-10 waveguide on port 1 (z -translation stage), with the device under test (the rectangular back-to-back horn) placed on a rotational stage between port 1 and port 2. Figure 2.24 below shows the measurement setup.

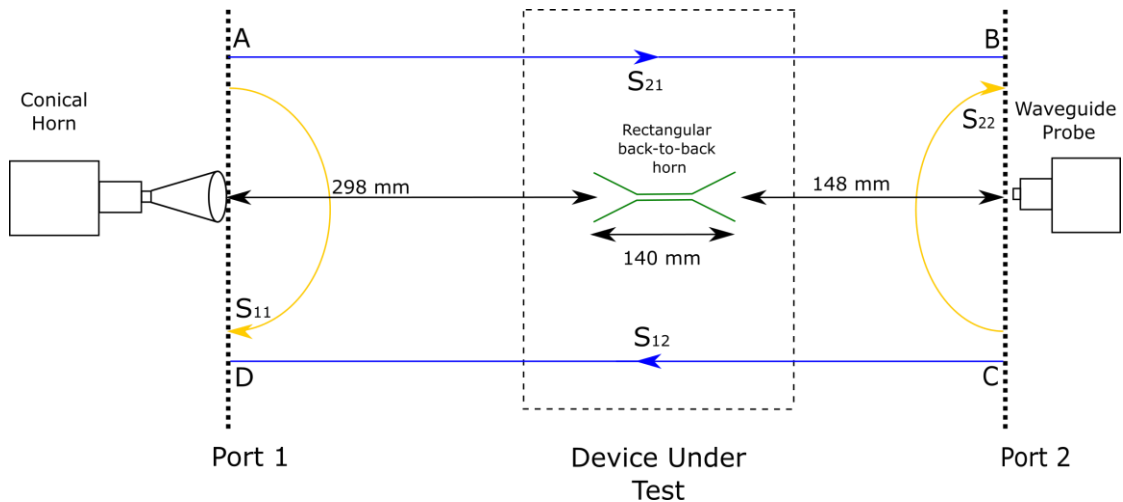


Figure 2.24: Measurement setup

The receiver converter head with the WR-10 waveguide probe was mounted on the xy scanner which allowed a two-dimensional grid of data to be produced containing information on the beam evolution. The resolution of the scan was set to be 0.5 mm both in the x -axis and the y -axis. During this measurement, the distance between the emitter and the receiver was constant at 446 mm. The rectangular back-to-back horn was mounted

on a rotational stage, which allowed the device under test to be rotated through a range of angles from -10 to 10 degrees in steps of 0.5 degrees. At each angle, a 40 mm by 40 mm xy grid of data was produced.

The dimensions of the rectangular back-to-back horn aperture and throat section are detailed in Figure 2.25 and Table 2.1 shows the supported modes (and when they cut-on) across the investigated band.

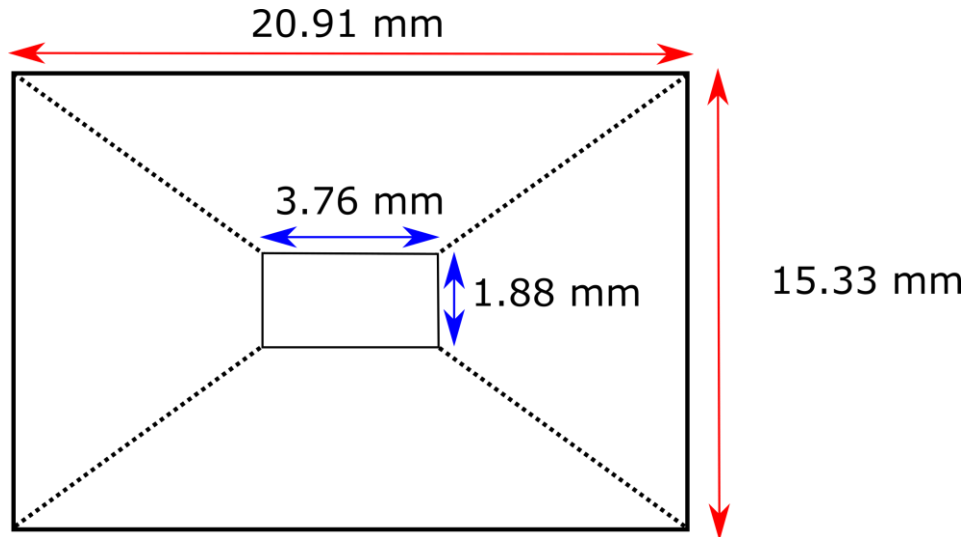


Figure 2.25: Dimensions of rectangular horn aperture and throat section

	75	80	85	90	95	100	105	110
TE₁₀	✓	✓	✓	✓	✓	✓	✓	✓
TE₂₀		✓	✓	✓	✓	✓	✓	✓
TE₀₁		✓	✓	✓	✓	✓	✓	✓
TE₁₁				✓	✓	✓	✓	✓

Table 2.1: Supported modes across the investigated band

2.9.3 Comparison of Measurements with Theoretical Predictions

In this section, the results of the measurements outlined in Section 2.9.2 will be presented, with the setup seen in Figure 2.26. The modifications made to GAMMA to allow for horn illumination by an off-axis input wave will also be discussed. In the standard version of GAMMA for rectangular geometries, it is assumed that all modes are excited equally with unity power at the input port (*i.e.* an ideal cavity mounted bolometer system), with the smallest section (generally this is the throat of the horn) filtering out any higher order modes that do not propagate.

In this case clearly the modes will not all carry the same power in the waveguide feeding the (front) radiating horn. The modification required includes the generation of an input

amplitude coefficient matrix ($[A]$), allowing for a wave to be incident on the excitation aperture at some user-defined angle (as in Figure 2.27).



Figure 2.26: Measurement setup showing the back-to-back horn and the scanner before and after including ecosorb to minimise reflections

If the back-to-back horn structure is rotated through some angle α then the incident radiation from the waveguide probe will appear to arrive at an angle β , as illustrated in Figure 2.27 below.

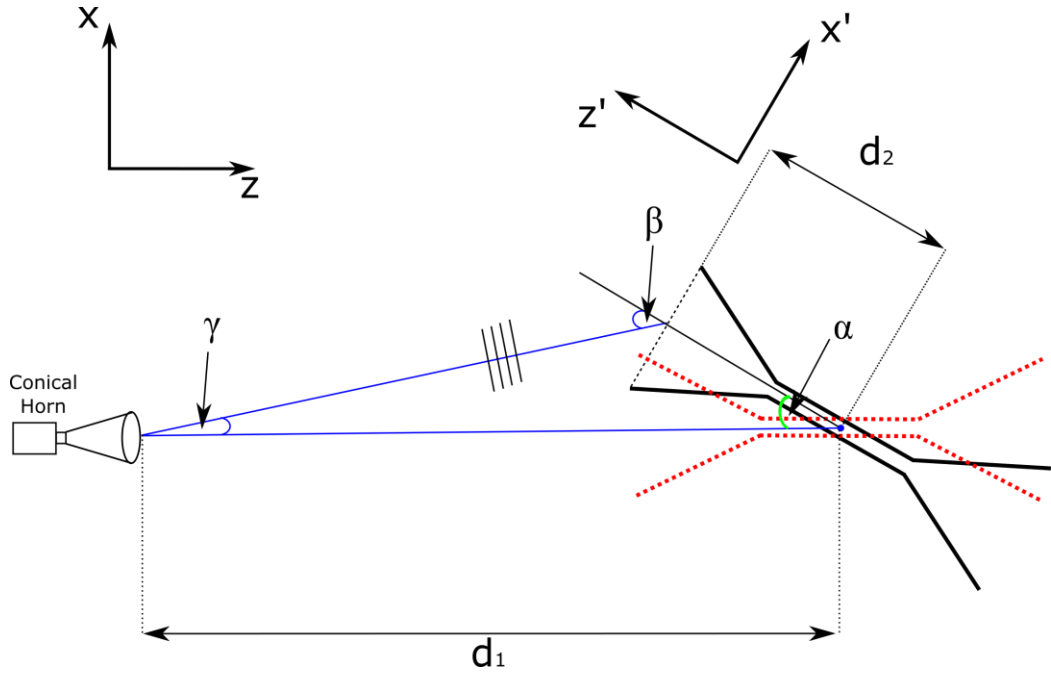


Figure 2.27: Measurement setup with angles

Clearly the angle of incidence of the wave on the excitation aperture is given by

$$\beta = \gamma + \alpha = \tan^{-1}\left(\frac{d_2 \sin(\alpha)}{d_1 - d_2 \cos(\alpha)}\right) + \alpha. \quad (2.119)$$

Making the approximation that the incident radiation locally is a plane wave arriving at an off-axis angle β with respect to the axis of the horn, then the amplitude of the waveguide modes excited in the horn aperture (mode coefficients) is given by

$$A_n = \int_{Ap} E_0 e^{ikx' \sin(\beta)} \hat{n} \cdot \mathbf{e}_n(x', y') dx' dy', \quad (2.120)$$

where the integral is taken over the horn aperture and the aperture defines the (x', y') plane as illustrated in the Figure 2.27. The polarization direction of the incident wave \hat{n} depends on the VNA waveguide orientation for the input beam source. But the A_n are related to the Fourier transform of the modal fields (*i.e.* the farfield of the modes) which are

$$\mathbf{e}_{n,ff}(k_x, k_y) = \int_{Ap} e^{-i(k_x x' + k_y y')} \mathbf{e}_n(x', y') dx' dy'. \quad (2.121)$$

where

$$k_x = k_0 \sin \theta \cos \phi, \quad (2.122)$$

and

$$k_y = k_0 \sin \theta \sin \phi. \quad (2.123)$$

where θ and ϕ are the spherical polar angular co-ordinates of the far-field point with respect to the axis of the system.

If the incident field is polarized in the y -direction (out of the plane of the page) then clearly

$$A_n^{(\alpha)} = \mathbf{e}_{n,ff} (k \sin(\beta), 0) \cdot \hat{j}. \quad (2.124)$$

We can then operate with $[S_{21}]$ on the column vector of the mode coefficients $[A]$ to determine the mode coefficients at the aperture of the radiating horn

$$[B] = [S_{21}][A]. \quad (2.125)$$

We can thus predict the farfield of the radiating horn at the scan plane (assumed farfield)

$$\mathbf{e}_{ff} = \sum B_n \mathbf{e}_{n,ff} (k_x, k_y). \quad (2.126)$$

The farfield will clearly be displaced on the scan plane by an amount $d_3 \tan(\alpha)$ which needs to be taken into account when comparing theory with experiment. d_3 is the distance from the centre of rotation of the horn to the scan plane.

The analysis results (both simulation and measurement) are presented in Figure 2.28 to Figure 2.34. The off-axis angles of $\alpha = -8^\circ, -5^\circ, 0^\circ, 5^\circ, 8^\circ$ are presented at frequencies of 75 GHz, 95 GHz and 110 GHz. The back-to-back rectangular horn was rotated around the centre point as it was more convenient mechanically.

The beams in Figure 2.28 are contour plots of measurements (top) and simulation (bottom) for an on-axis ($\alpha = 0^\circ$) incoming beam at 75 GHz, 95 GHz and 110 GHz. The back-to-back horn is single mode at 75 GHz supporting only the TE_{10} mode and multimode at 95 GHz and 110 GHz supporting the TE_{10} , TE_{20} , TE_{01} and TE_{11} modes. It can be seen that the modes couple strongly to the on-axis incoming wave as the farfield

pattern has on-axis power. Good agreement can be seen between the contour beams of measurements and simulation, providing some validation of the code implementation.

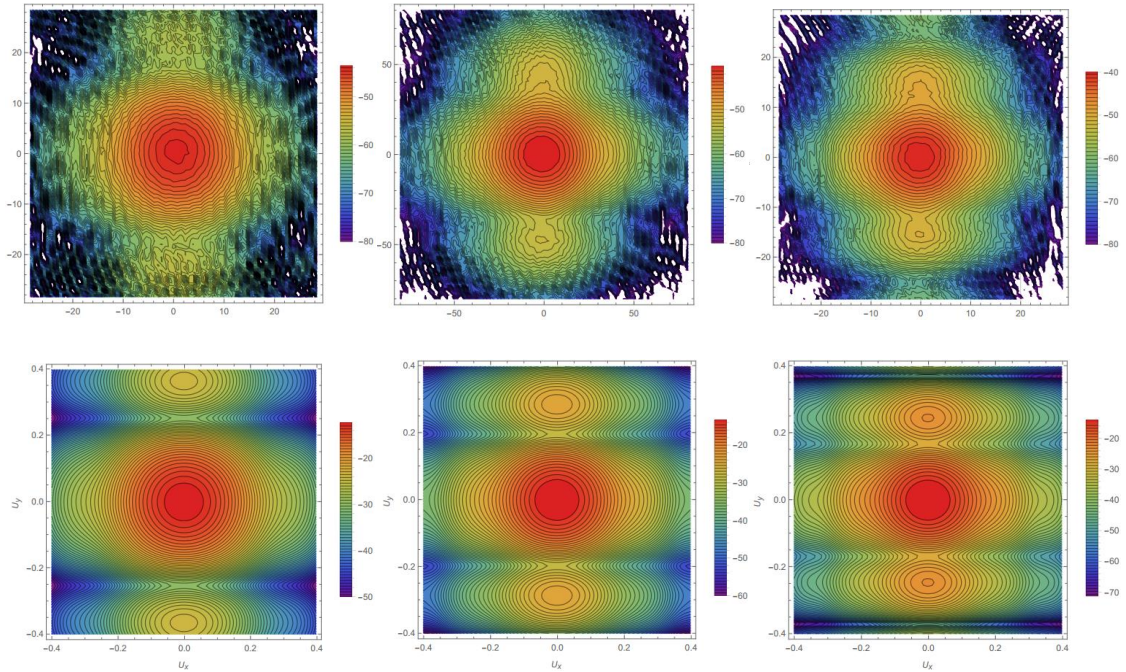


Figure 2.28: Contour plots of measurements (top) and simulated beams (bottom) for the incoming beam on-axis at 75 GHz (left), 95 GHz (middle) and 110 GHz (right)

The beams in Figure 2.29 show the measured and simulated contour beam with the angle of illumination $\alpha = -5^\circ$ on the left and $\alpha = 5^\circ$ on the right for an incoming beam at 75 GHz. Both measurements and simulations result in a field that still has on-axis power. This is as expected, since at this frequency, only the fundamental mode propagates in the waveguide filter section of the back-to-back rectangular horn. Figure 2.30 below shows the cuts of both the measured and simulated data at 75 GHz, taken from the contour beams in Figure 2.29. The cuts of the measurement data are taken along the $y = 0$ direction and the cuts of the simulated data are taken along the $U_y = 0$ direction (where $U_x = k_x/k_0$ and $U_y = k_y/k_0$ contain the spherical polar and azimuthal angles θ and ϕ as indicated in Equations (2.122) and (2.123)).

The aperture size of the measurement probe ($2.54 \text{ mm} \times 1.27 \text{ mm}$) was much less than the typical sizes of the structures of the measured far-field beams ($S \sim 25 \text{ mm}$) and therefore the approximation was made that deconvolution was not necessary for revealing the main features of the beam pattern.

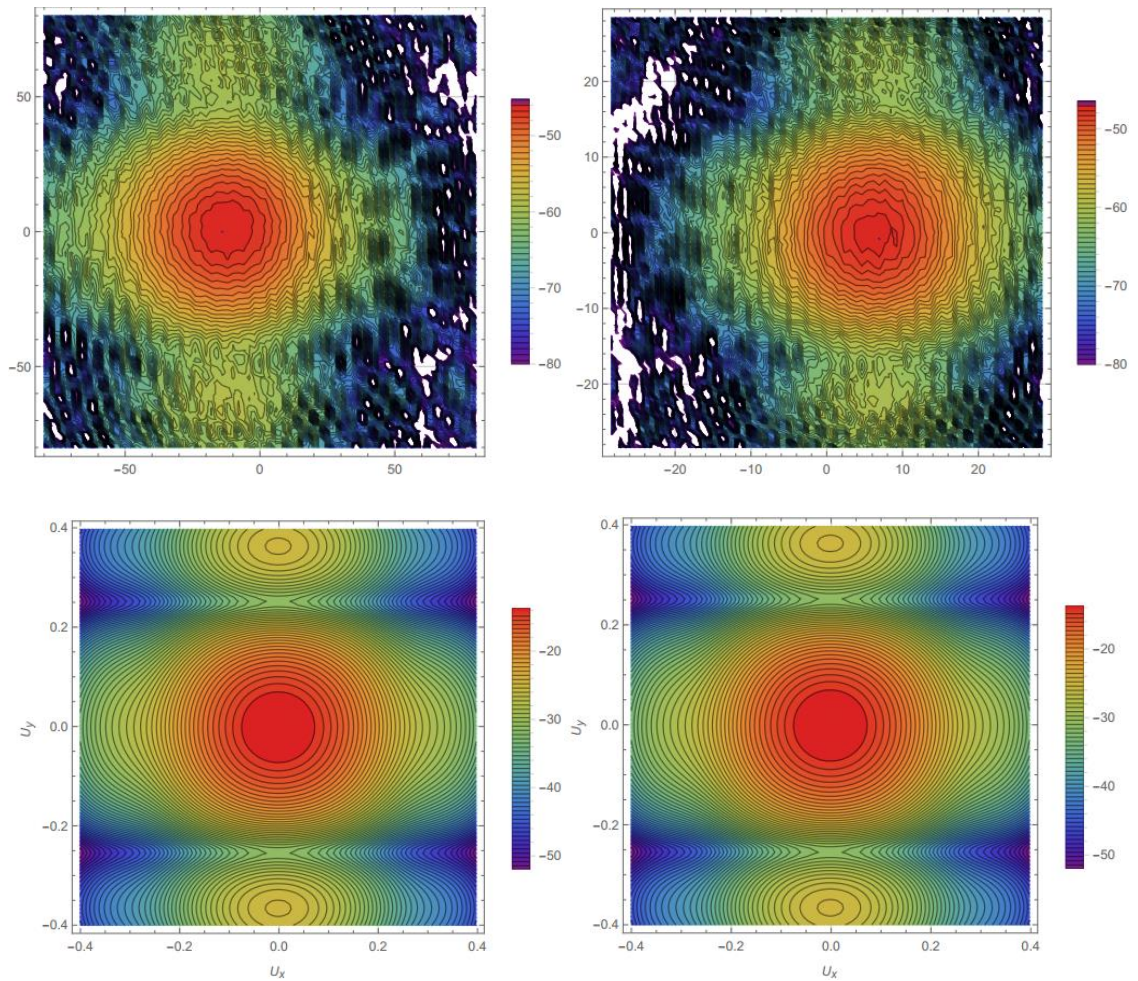


Figure 2.29: Contour plots of measurements (top) and simulated beams (bottom) at 75 GHz for the incoming beam off-axis at $\alpha = -5^\circ$ on the left and $\alpha = 5^\circ$ right

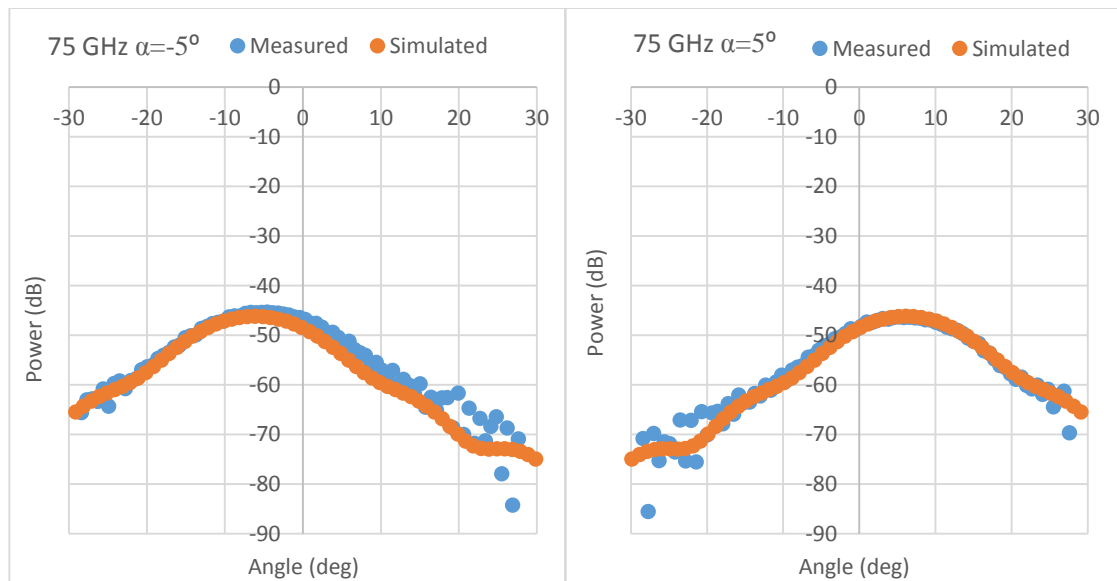


Figure 2.30: Cut of contour plots in Figure 2.29 of measured and simulated data for the incoming beam at 75 GHz off-axis at $\alpha = -5^\circ$ on the left and $\alpha = 5^\circ$ right

The beams in Figure 2.31 show the measured and simulated contour beam with the angle of illumination $\alpha = -8^\circ$ on the left and $\alpha = 8^\circ$ on the right for an incoming beam at 95 GHz. A double peak structure separated by a deep off-axis null is observed in the simulations whereas the null was shallower in the measurements, implying that the higher order modes dominate for this angle of illumination. This can be explained by the fact that the measurement probe was of the same size as the null feature and therefore was insensitive to it. Also the measurements were taken not at infinity (true far-field) but at a distance of 148 mm ($\sim 49\lambda$) from the radiating horn and therefore some Fresnel diffraction effects may be still present that fill the null. Deconvolution (using phase and amplitude measurements) would reveal whether there is a discrepancy, but this was beyond the scope of this work due to time constraints. The TE_{10} , TE_{20} , TE_{01} and TE_{11} modes can propagate at 95 GHz and 110 GHz. However, due to the symmetry only the TE_{10} and TE_{20} are excited, the other two modes are not excited due to their field polarization. The double peak structure indicates that the TE_{20} mode couples to the incoming plane with a higher degree than the fundamental TE_{10} mode (*i.e.* relative balance between the modes has shifted). Figure 2.32 below shows the cuts of both the measured and simulated data at 95 GHz, taken from the contour beams in Figure 2.31. The cuts of the measurement data are taken along the $y = 0$ direction and the cuts of the simulated data are taken along the $U_y = 0$ direction.

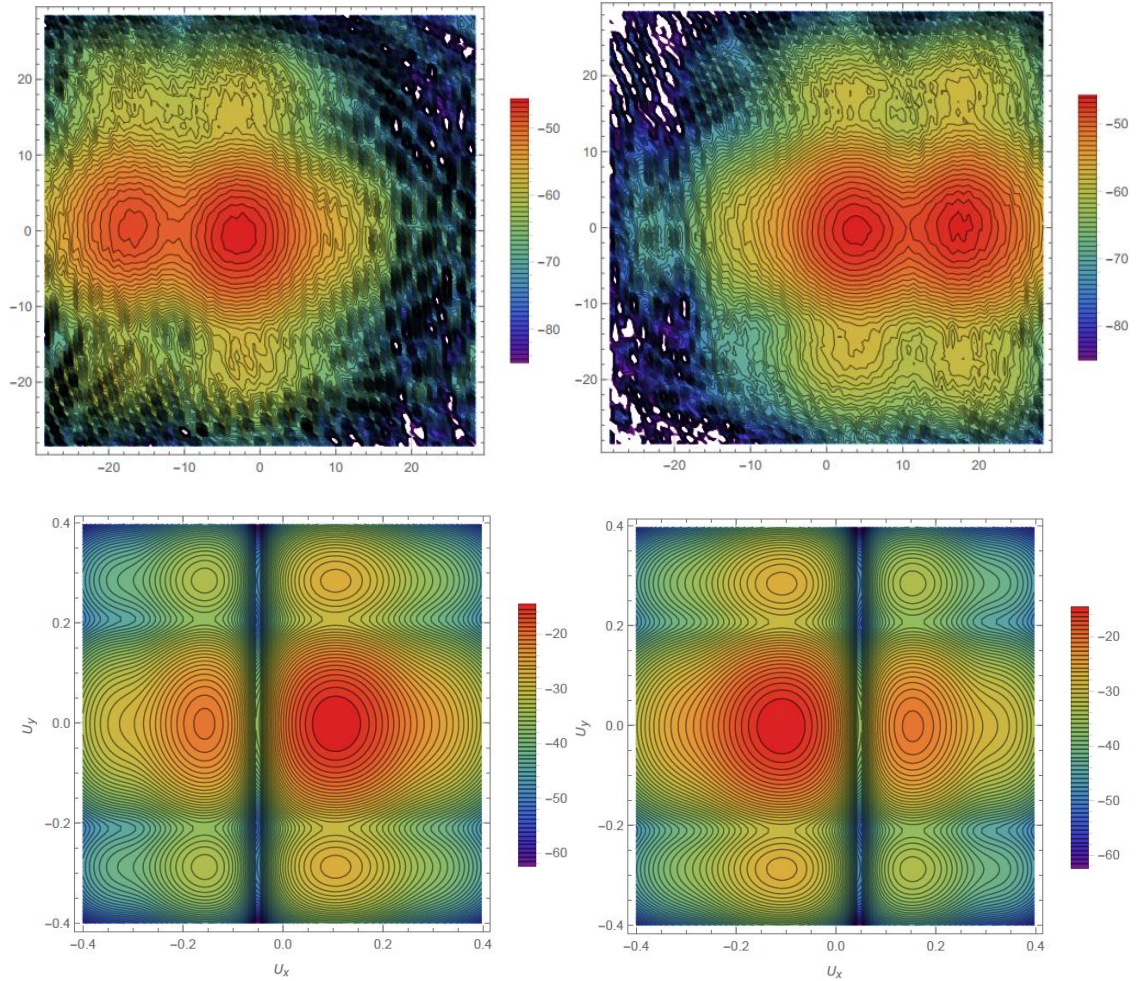


Figure 2.31: Contour plots of measurements (top) and simulated beams (bottom) at 95 GHz for the incoming beam off-axis at $\alpha = -8^\circ$ on the left and $\alpha = 8^\circ$ on the right

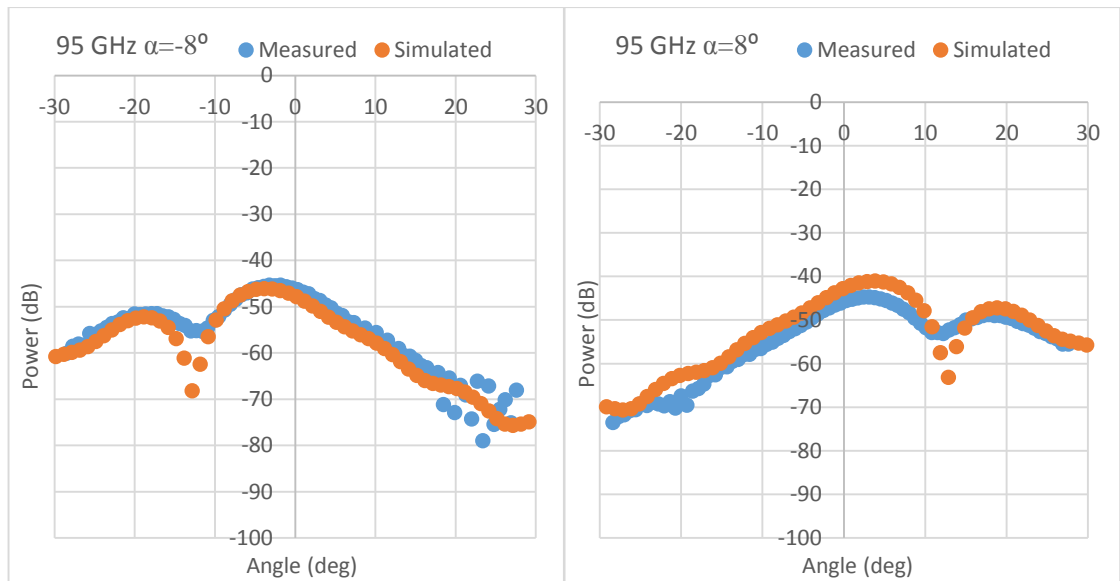


Figure 2.32: Cut of contour plots in Figure 2.31 of measured and simulated data for the incoming beam at 95 GHz off-axis at $\alpha = -8^\circ$ on the left and $\alpha = 8^\circ$ right

The beams in Figure 2.33 show the measured and simulated contour beam with the angle of illumination $\alpha = -8^\circ$ on the left and $\alpha = 8^\circ$ on the right for an incoming beam at 110 GHz. Again a double peak structure separated by a significant off-axis null is observed for this case, in both the measurements and simulations, implying that the higher order modes dominate for this angle of illumination. Figure 2.34 below shows the cuts of both the measured and simulated data at 110 GHz, taken from the contour beams in Figure 2.33. The cuts of the measurement data are taken along the $y = 0$ direction and the cuts of the simulated data are taken along the $U_y = 0$ direction. Comparing the cuts of the beams in Figure 2.32 and Figure 2.34, it can be seen that the null between the two peaks (maxima) is not as clearly defined at 110 GHz as it is for the 95 GHz frequency, still indicating that the relative balance between the modes has shifted, with the off-axis mode not dominating to the same level it did at 95 GHz.

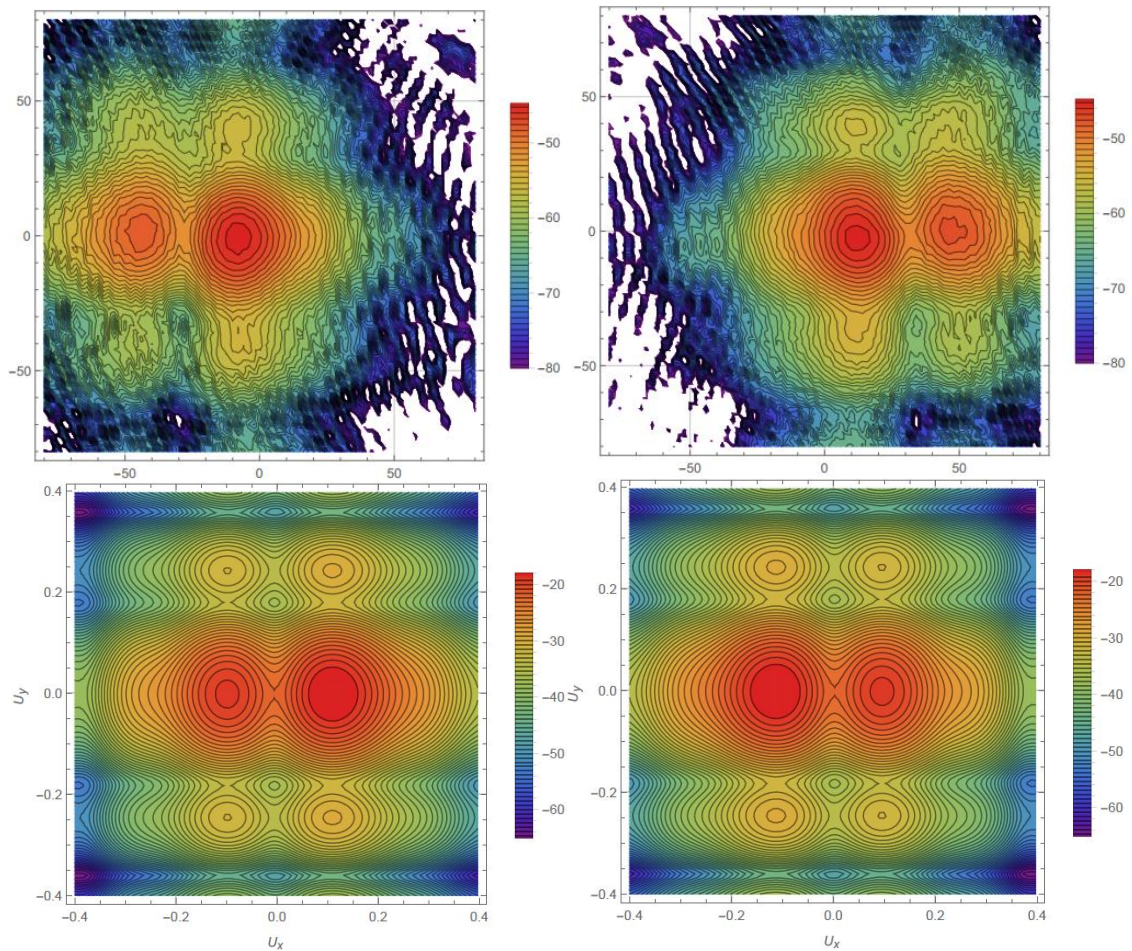


Figure 2.33: Contour plots of measurements (top) and simulated beams (bottom) at 110 GHz for the incoming beam off-axis at $\alpha = -8^\circ$ on the left and $\alpha = 8^\circ$ on the right

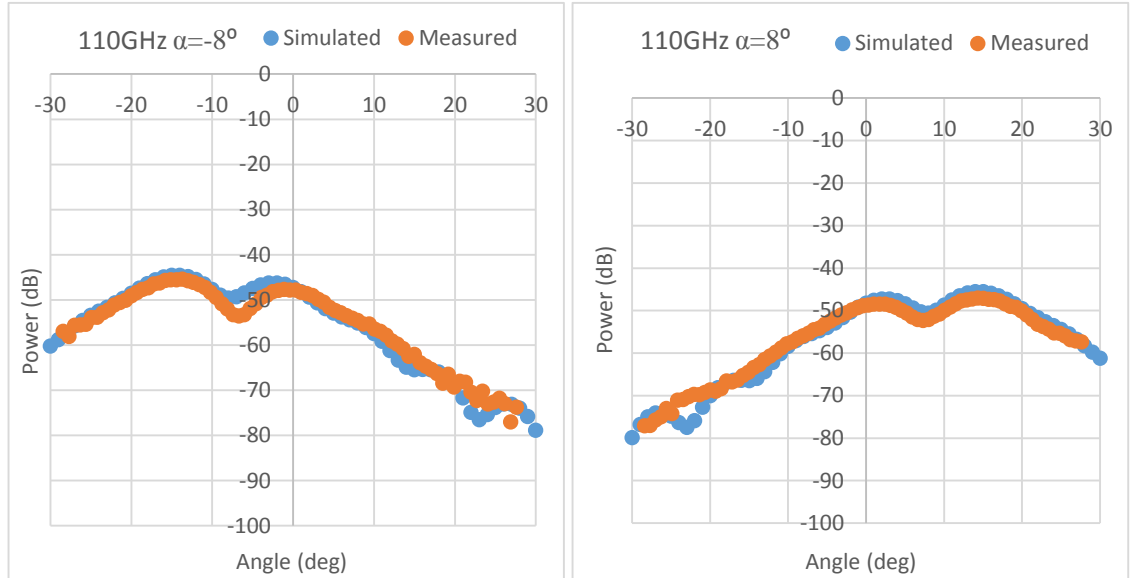


Figure 2.34: Cut of contour plots in Figure 2.33 of measured and simulated data for the incoming beam at 110 GHz off-axis at $\alpha = -8^\circ$ on the left and $\alpha = 8^\circ$ right

For the various angles of off-axis illumination presented above, it was seen that the relative balance with which the modes couple to the incoming plane changes as a function of the angle of illumination, with the off-axis (higher order) modes beginning to influence the overall farfield pattern, as was indicated by the off-axis null. The measurements do of course indicate clear multimode operation. Table 2.2 displays the absolute values of the mode amplitudes (from Equation (2.125)) for the cases considered in Figure 2.28 to Figure 2.34.

	$\alpha = -8^\circ$	$\alpha = -5^\circ$	$\alpha = 0^\circ$	$\alpha = 5^\circ$	$\alpha = 8^\circ$
75 GHz <i>(TE₁₀)</i>	0.236	0.313	0.374	0.313	0.236
95 GHz <i>(TE₁₀)</i>	0.176	0.260	0.340	0.260	0.176
95 GHz <i>(TE₂₀)</i>	0.274	0.241	0.107	0.241	0.274
110 GHz <i>(TE₁₀)</i>	0.143	0.223	0.313	0.223	0.143
110 GHz <i>(TE₂₀)</i>	0.238	0.234	0.113	0.234	0.238

Table 2.2: Absolute values of the mode amplitudes for the investigated frequencies and rotation angles

2.10 Conclusion

In this chapter, waveguide modes and mode matching were introduced for systems of both rectangular and circular cross sections. The basic implementation of the mode matching technique into a Generalised Absorber Mode Matching and Analysis (GAMMA) software, developed in-house by the author of this thesis, has also been discussed. An overview of the theory behind implementation of absorbers in waveguide structures was also given, which will be applied to specific examples in the later chapters of this thesis. We will discuss the various extensions to GAMMA which will be used to analyse the systems in Chapters 4, 5 and 6.

An overview of CST was also provided, which will be used as a benchmark simulation tool to verify the further development of GAMMA (offset absorbing cavities, absorbers of arbitrary shape, *etc.*) for electrically small systems. It will be shown that when the systems become large in terms of wavelength, mode matching proves to be more efficient both in terms of time and computational power needed.

We also provided the details of a measurement campaign which was undertaken at the millimetre-wave measurement laboratory at Maynooth University by the thesis author for experimental verification of multimode propagation. Multimode back-to-back rectangular horn measurements were carried out across a frequency range of 60 – 120 GHz and across a range of angles (-10° to 10° rectangular back-to-back horn rotation) with some results presented in this chapter. At the higher frequencies (95 GHz and 110 GHz) the ratio with which the modes are excited at the mode aperture varies as a function of illumination angle, while at the lower frequency of 75 GHz the pattern contained on-axis power since the waveguide filter section only allowed for the propagation of the fundamental mode.

An equivalent system was also modelled in GAMMA and agreement was observed between measurements and simulations, thus in a sense providing verification for both the experimental and the software approach. A method of simulating an off-axis incoming beam in GAMMA was also discussed, with this extension allowing for direct comparison of measurement and simulation results.

3 Quasi-Optical Propagation and the Design of a 4mm Receiver for the Onsala Space Observatory

3.1 Introduction

One of the critical issues for receiver systems on astronomical telescopes is coupling to the feed horn antenna, which feeds a detector as discussed in the previous chapter, with the telescope for optimizing the aperture efficiencies of the combined system (so that both the resolution and sensitivity are optimised). In this chapter, we introduce two approaches that can be used to achieve this: Gaussian Beam Mode Analysis and Physical Optics. Gaussian Beam Mode Analysis was used for determining the basic design of the horn and Physical Optics was used to provide accurate beam on the sky. Given the pre-set GBM parameters the horn was designed by the author of this thesis to match the receiver optics.

One of the goals of this chapter is to also illustrate the design and analysis process for the specific example of a new 4 mm receiver on the Onsala Space Observatory 20 m telescope, in particular looking also at tolerancing issues. This involves both the consideration of the design of the horn antenna for the receiver and the analysis of the optical relay system and the telescope to predict the farfield beams on the sky.

The Onsala Space Observatory (OSO) is the Swedish national facility for radio astronomy (chalmers.se, 2013). Among the radio telescopes located at Onsala are the 20 and 25 m radio telescopes. The 25 m decimetre-wave telescope is equipped with receivers up to 7 GHz and mainly used for astronomical VLBI (Very-long-baseline interferometry) observations (such as star formation and AGN) and is occasionally used as a single dish for interstellar molecule observation. The 20 m millimetre-wave telescope is protected by a radome and equipped with receivers up to 116 GHz. It is used for observations of millimetre-wave emission from molecules in the interstellar medium (ISM) and for the study of comets. Currently, the telescope is equipped with the following receivers (see Table 3.1):

Frequency Range	Receiver Temperature
2.2 – 2.4 GHz	60 K
8.2 – 8.4 GHz	80 K
18.0 – 26.0 GHz	30 K
26.0 – 36.0 GHz	50 K
36.0 – 49.8 GHz	50 K
67.0 – 87.0 GHz ('4 mm')	50 – 60 K
85.0 – 116.0 GHz ('3 mm')	50 – 60 K

Table 3.1: Frequency channels present on the 20 m OSO telescope (chalmers.se, 2018a)

The Terahertz Space Optics group in the Maynooth Experimental Physics department undertakes research in the area of millimetre-wave and terahertz optics and technology for astronomical instrumentation. As a result of expertise in this research area present in the department, the group was invited to design the optical system for the new proposed 4 mm system for the 20 m telescope. The author's contribution was the design of the corrugated feed horn. A critical component of the front end optics is a corrugated horn with a low focal ratio to feed the detector with high efficiency via the front end optics. The performance requirements of the horn were as follows: it had to operate over a frequency band of 67 GHz to 86 GHz, have a beam power coupling to a best-fit Gaussian field (Gaussicity) of 98.1%, low cross-polarisation levels, low return loss and have most of the power in the HE_{11} hybrid waveguide mode (Clarricoats, 1984:7). A similar performance was achieved in the case of the 3 mm receiver. The new 4 mm receiver was installed on the telescope in October 2015 in parallel with the existing 3 mm receiver channel. With the two millimetre-wave receivers, the main interest is to obtain good quality data to determine the concentrations and dynamics of molecules in astronomical sources, especially including CO, CN and HCN (chalmers.se, 2018b). Figure 3.1 shows spectra from some early commissioning observations carried out with the 4 mm receiver.

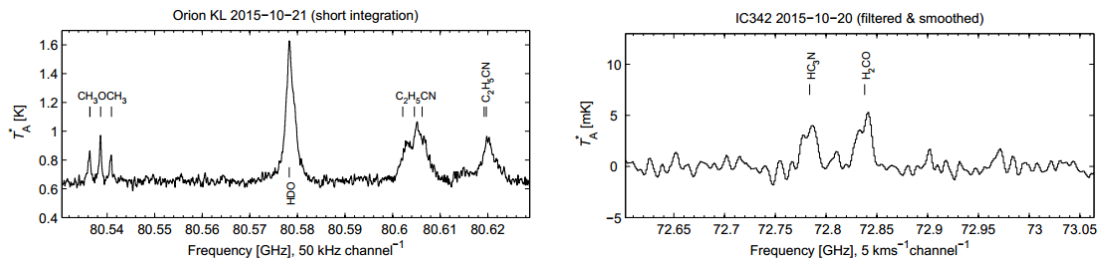


Figure 3.1: Spectrum with observations of HDO and other molecules in Orion KL (Left). Spectrum with observations of two spectral lines in the galaxy IC 342 (Right). (chalmers.se, 2018a)

Three corrugated horns were considered for the design. Two of them are standard conical corrugated horns (one with an aperture of 30 mm and the other of 18.8 mm) and the other is a compact design horn which optimises the aperture efficiency of the horn while reducing its length. Each horn considered contains a flared waveguide section, with corrugations perpendicular to the axis of propagation of the horn. The purpose of the corrugations is to force the boundary conditions for electric and magnetic fields to be the same, resulting in a symmetric beam pattern for the horn with low cross-polarization levels.

The design was carried out mainly using the original ‘CylindricalSCATTER’ mode matching code and the GAMMA software (as explained in Chapter 2). Maximum Gaussicity was achieved by adjusting the corrugated horn parameters (beam width and phase curvature) to excite the HE_{11} amplitude and to minimize the excitation of HE_{12} and higher order modes. The HE_{11} and the HE_{12} are so called hybrid modes (mix of TE and TM modes) that satisfy the boundary conditions in corrugated horns.

A manufacturing tolerance analysis of the horn was also carried out where the radii of the sections making up the horn were altered with random error values ranging from $\pm 15 \mu m$ to $\pm 100 \mu m$. In particular, the co-polar and cross-polar beam patterns were investigated for any deterioration in predicted performance for the different tolerance limits.

A brief outline of the optics of the 4 mm receiver channel design will also be presented. The optical design was carried out by George Walker and a more detailed specification of the optics is given in Walker (2016). In this chapter as indicated above we will mainly focus on the design of the corrugated horn antenna and on propagating its beam through the front end optics and the 20 m Onsala telescope to produce the farfield pattern of the beam on the sky at a number of spot frequencies across the band. The main focus here will be to establish a tolerance limit on the horn manufacture.

3.2 Gaussian Beam Mode Analysis

To understand the propagation of an electromagnetic beam through an optical system at sub-mm wavelengths a quasi-optical approach can be used. Geometrical optics is an effective analysis tool for optical systems when the wavelength is small compared to the

size of the components in the optical system. However, it breaks down for systems in which the components are only a few wavelengths in diameter as diffraction effects become important (Goldsmith, 1998: 26) As a result, an alternative approach, Gaussian Beam Mode Analysis (GBMA), is a technique that has been developed to more accurately describe quasi-optical propagation taking into account Fresnel diffraction effects, particularly for coherent beams (Lesurf, 1990: 8). This technique allows for the analysis of much more compact optical systems (relative to the wavelength). However, for a full analysis of polarization properties, Physical Optics is required as will be discussed in Section 3.3.

The solution to the paraxial wave equation forms the basis for Gaussian beam propagation. This Gaussian beam solution is given by (Goldsmith, 1998: 25)

$$E_G(r, z) = \sqrt{\frac{2}{\pi W(z)^2}} \times \exp\left[-\frac{r^2}{W(z)^2}\right] \times \exp\left[-jk\left(z + \frac{r^2}{2R(z)}\right) + j\phi_0(z)\right], \quad (3.1)$$

where the z -axis is the axis of propagation and the origin is located on the plane at $z=0$ where the beam is narrowest (has a waist) as in Figure 3.2. The beam width parameter $W(z)$, the phase curvature $R(z)$ and the phase slippage term $\phi_0(z)$ all vary with z and determine the beam propagation properties. Thus at $z = z$, they are given by (Goldsmith, 1998:25)

$$W^2(z) = W_0^2 \left(1 + \left[\frac{\lambda z}{\pi W_0^2} \right]^2 \right), \quad (3.2)$$

$$R(z) = z \left(1 + \left[\frac{\pi W_0^2}{\lambda z} \right]^2 \right), \quad (3.3)$$

$$\phi(z) = \tan^{-1} \left(\frac{\lambda z}{\pi W_0^2} \right). \quad (3.4)$$

where W_0 is the beam waist (the value W has at $z=0$ and where the radius of curvature is infinite) and the beam propagation distance is measured relative to the waist and λ is the wavelength. The relationships given in (3.2) – (3.4) are fundamental for Gaussian beam propagation as this simple set of equations describes the behaviour of the beam

parameters at all distances from the beam waist. The beam width at any point is given by Equation (3.2) and Figure 3.2 shows how it is changing with propagation.

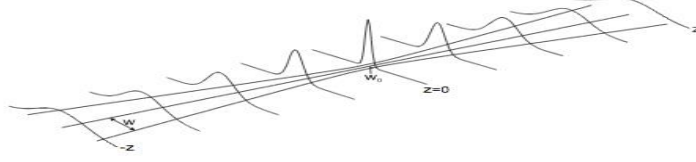


Figure 3.2: Illustration of how the beam width and radius of curvature of a propagating Gaussian beam is changing.

Although the fundamental Gaussian beam mode solution is important in quasi-optical analysis, higher order modes are required to increase the accuracy of the analysis. In cylindrical co-ordinates, these higher order modes have the Laguerre polynomials modulating the fundamental beam mode Gaussian profile (Murphy and Egan, 1993). These higher order modes have the property that the beam radius and the radius of curvature take on the same value as for the fundamental mode, but their phase shifts are different.

$$\begin{aligned} \psi_n(r, z) = & \sqrt{\frac{2}{\pi W^2}} L_n \left[2 \left(\frac{r^2}{W^2} \right) \right] \times \exp \left[- \left(\frac{r^2}{W^2} \right) \right] \\ & \times \exp \left[-jk \left(z + \frac{r^2}{2R} \right) + j(2n+1) \times \tan^{-1} \left(\frac{\pi W^2}{\lambda R} \right) \right] \end{aligned} \quad (3.5)$$

A general beam therefore represented by $E(r, z)$ is considered to be made up of a linear sum of independently propagating modes $\psi_n(r, \phi, z)$, meaning that at any point the field may be expressed as

$$E(r, z) = \sum_{nl} A_{nl} \psi_{nl}(r, z) \quad (3.6)$$

where A_n are the mode coefficients, and ψ_n (in cylindrical co-ordinates for azimuthally symmetric modes) is the Laguerre-Gaussian function.

The mode coefficients, A_n , are given by

$$A_n = \int E(r, z) \psi_n^* dA, \quad (3.7)$$

provided that the higher order modes are normalized so that $\int \psi_n^* \psi_n dA = 1$. The power contained in a mode (assuming it's normalized) is given by $|A_n|^2$, so that the field may be reconstructed by using Equation (3.7).

Furthermore, it is possible to model the propagation of a beam through an optical system of lenses or curved mirrors using the ABCD matrix approach as described in Goldsmith. However, for a more accurate description when cross-polarisation levels are of interest, a more accurate Physical Optics approach is required and will be discussed in the following section.

3.3 GRASP9 Software Description

In order to undertake a physical optics (PO) analysis of the OSO receiver system the software package GRASP9 (Generalised Reflector Antenna Software Package) was used. GRASP9 is a specialist software package developed by TICRA for the analysis of reflector antenna systems. It consists of three main components: (i) A pre-processor (to assist the user in visualising the system and setting up the problem geometry), (ii) Analysis module (to perform the electromagnetic analysis), and (iii) Post-processor (to perform data processing and plots, which can be in the form of cuts and contours). It predicts the beam patterns of telescope systems by calculating (or reading in) the field from a source feed and propagating it through the reflector system to a detection grid in the far- (or near-) field of the telescope. It can also be used for any optical system consisting of reflecting curved mirrors.

GRASP9 was developed using the Fortran 90 language and makes use of object-oriented programming techniques (Pontoppidan, 2005). Reflector and feed systems defined in GRASP9 are described in terms of objects belonging to different classes. The three main object classes in GRASP9 are Geometrical Objects, Electrical Objects and Plot Objects.

In this section, we will discuss Geometrical Objects and Electrical Objects. Physical Optics (PO) calculations will also be discussed (Geometrical Optics (GO) / Geometrical Theory of Diffraction (GTD) and Method of Moments (MoM) were not used and will not be discussed).

Geometrical Objects

In GRASP9, scattering structures (reflectors) are contained in the *Scatterer* group. The *Reflector* class is used to specify a *Scatterer*. A reflector needs to have a minimum of three components to be defined, including a surface object, a rim object and a co-ordinate system. Afterwards, depending on the system being analysed, the reflector may have a central hole (the radius of which can be defined), or it may contain surface distortions (which may also be added to the reflector surface).

The *Coordinate Systems* class is used to specify the position of a co-ordinate system either with respect to a global co-ordinate system or to another user-defined co-ordinate system. The co-ordinate system can be defined in terms of *xyz* components, *Euler Angles* or *GRASP Angles*.

The *Surface Object* class describes the surface of a reflector. It contains built in reflector surfaces, such as paraboloid, hyperboloid, ellipsoid, *etc.* More complex surface can also be generated by providing a second order polynomial to define the surface, this is found under *Other Quadrics*. The second order polynomial is defined by (GRASP9 Reference Manual, 2010) as follows

$$A_{xx}x^2 + A_{xy}xy + A_{yy}y^2 + A_x x + A_y y + A_c = A_{zz}z^2 + A_z z + A_{xz}xz + A_{yz}yz, \quad (3.8)$$

where the surface is defined in the same co-ordinate system as the corresponding reflector object.

The *Rim Object* describes the bounding rim of a reflector. The following types of edges are available: elliptical, rectangular and triangular. A polynomial definition of the rim can also be used in the class *Tabulated Rim*. In each case, the edge is specified in a plane which is orthogonal to the *z*-axis of the co-ordinate system specifying the reflector. For the case of *Tabulated Rim* being used, the values are tabulated either in Cartesian (*x,y*) or polar (*r,φ*) co-ordinates.

Electrical Objects

The four required components to carry out PO analysis found in the *Electrical Objects* menu are: *Frequency*, *Feed*, *PO (standard)* and *Field Storage*. The class *Other Sources* will also be discussed as items in this class were used to produce beams on the sky of the telescope systems analysed in this thesis.

The frequency (or frequencies) at which the calculations need to be carried out can be specified as a list in *Frequency List*. A range of frequencies can also be specified in *Frequency Range* by providing the minimum and maximum frequencies and the number of samples. Alternatively, a list or range of wavelengths may also be used.

Feeds are radiation sources used as the starting point in the PO analysis. The *Feed* menu contains simple and general sources, the models of which are collected in the following groups: *Pattern*, *Horn*, *Tabulated Feed*, *Planar Feed* and *Helix* or *Dipole*. A beam pattern fulfilling certain criteria can be defined in *Pattern*. For the case of a single mode conical corrugated horn the beam pattern at the aperture may be represented by a Gaussian, by defining a beam radius ($W(z)$) and radius of curvature ($R(z)$).

If the geometry of the radiation source is well known, various horn geometries can be read in by the *Horn* class. Examples include: conical horn, fundamental mode circular waveguide, Potter horn, hybrid mode conical horn, rectangular horn and hexagonal horn. The aperture radius (or width and height for the case of rectangular horns) and flare length need to be supplied. Based on the supplied information, GRASP9 creates a beam at the aperture, which may be propagated through the optical system.

The *PO (standard)* class is used to store the induced currents on a reflector surface. This is a useful feature when modelling systems containing multiple reflectors, as the currents stored in the object can then be used as a source in later calculations.

The *Field Storage* is used to determine the output points at which the field will be determined. It contains the following classes: *Cut*, *Grid* and *Tabulated uv-Points*. Cuts and grids can be of type spherical, planar or cylindrical, taken at the field upon a surface in space, or surface grids or cuts at a scatterer. In each case a co-ordinate system for the cut and/or grid needs to be defined. *Tabulated uv-points* are defined by irregularly distributed points in the farfield pattern, where the points themselves are defined in a file and given in *uv*-coordinates (which themselves are defined in terms of the spherical polar and azimuthal angles θ and φ).

The *Other Sources* class may be used where the aperture field of the horn has already been calculated. If this is the case, it can be read in by GRASP9 as a *Tabulated Planar Source*. In-house mode matching software ‘CylindricalSCATTER’ and ‘GAMMA’ (for the case of the 4 mm OSO horn) and ‘GAMMA’ (for the case of the Planck 857 GHz and

545 GHz horns, discussed in Chapter 5) was used to generate the aperture fields of the horns, specified in a file containing relevant GRASP9 header data (dimensions and sampling of the field). The tabulated planar source files were then used as input to GRASP9 for propagation of the beam through the system and to the sky (Sections 3.7 for the 20 m telescope coupled to the 4 mm receiver optics, Section 5.6 and Section 5.8 for the case of the Planck 857 and 545 GHz channels).

Commands

For the purposes of the examples discussed in this thesis the *Get Currents* and *Get Fields* commands were used to perform the electromagnetic analysis calculations. *Get Currents* activates the computation of the currents at the reflector. The source illuminating the scatterer (tabulated planar source for the case of the examples outlined in this thesis) is what generates the currents which are calculated and stored in a physical optics object, which may be used as the source for any further calculations to be made. The *Get Field* command was then used to obtain the field from a source at the points specified in the field storage object.

Physical Optics

GRASP9 can perform scattering simulations using a number of different methods, with PO being the method that is most commonly used (Pontoppidan, 2005) and is of interest to us here. The term ‘physical’ is used to indicate that it is a more physical approach to optics than ray tracing techniques employed by geometrical optics so that track can be kept of physical electric and magnetic fields, \mathbf{E} and \mathbf{H} , and thereby the polarized field.

It is true for any scattering problem that the goal is to calculate the radiated field. In order to do so, the incident field needs to be known, as well as the electrical properties of the scatterer in question. The following description relates the fields by

$$\mathbf{E}_{total} = \mathbf{E}_{incident} + \mathbf{E}_{scattered} \quad (3.9)$$

A three-step process describes the analysis to solve a scattering problem: (i) the currents induced on a scattering surface need to be calculated, (ii) the field radiated by the induced surface currents needs to be calculated, and (iii) the incident and the scattered field need to be added to obtain the total field.

Step (i) is the most complex and would commonly employ the MoM technique for non-ideal surfaces. However, it is very computationally intense for electrically large scatterers. PO provides an approximation to the surface currents, assuming a perfectly conducting scatterer surface which is large in terms of wavelength. It is also assumed that the surface current at a specific point on a curved (but perfectly conducting) surface is the same as the surface current on an infinite planar surface. Each current element can then be related to the incident magnetic field, \mathbf{H}_{inc} , by

$$\mathbf{J} = 2 \hat{n} \times \mathbf{H}_{inc}, \quad (3.10)$$

where \hat{n} is the unit vector normal to the surface of the scatterer and \mathbf{H}_{inc} is the incident magnetic field.

The incident magnetic field itself is the result of radiation from a previous surface, S' , with currents J' given by

$$\mathbf{H}_{inc} = \frac{1}{\mu} \nabla \times \frac{\mu}{4\pi} \int_{S'} \mathbf{J}' \frac{e^{jkr}}{r} dS'. \quad (3.11)$$

where r is the distance to dS' .

No further approximations are made in step (ii) since the surface currents may be computed using high precision numerical integration. However, the PO approximation, strictly speaking, cannot be used precisely at an edge. In that case Physical Theory of Diffraction (PTD) is required to obtain the field near the edge of a surface. PTD integrates equivalent edge currents along the edge of the reflector surface, calculated using an approximation based on a perfectly conducting infinite half plane (Johansen, 1996). PTD acts as a correction factor to PO, thus the scattered field is expressed as

$$\mathbf{E}_{scattered} = \mathbf{E}_{PO} + \mathbf{E}_{PTD} \quad (3.12)$$

GRASP9 was used in the analysis of the OSO 4 mm receiver for predicting beams on the sky and in the multimode channels of the Planck HFI with the input modal fields provided by GAMMA.

3.4 Design Parameters of Corrugated Horns

The variety of antenna applications where a corrugated horn is used are listed in Table 3.2 which details the types of horn used and lists some example applications. A corrugated horn is usually used as a feed for a reflector antenna for coherent transmitters or receivers (single mode), although it can occasionally be used on its own (for example, Penzias' and Wilson's experiment of first CMB detection (Penzias and Wilson, 1965)).

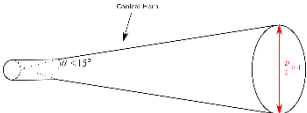
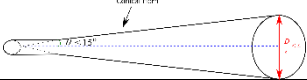
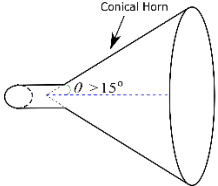
Types of Horn	Typical uses	Types of Horn	Typical uses
Large aperture, narrow flare angle $\left(\frac{D}{\lambda} > 4\right), (\theta < 15^\circ)$ 	Large Cassegrain antennas Earth stations, Radio Astronomy antennas	Multimode* horns (where multimode refers to the fact that more than one mode is excited in the horn, but the waveguide is still single mode)	Radars Prime focus reflectors Offset reflectors
Small aperture, narrow flare angle $\left(\frac{D}{\lambda} < 4\right), (\theta < 15^\circ)$ 	Spacecraft antennas Prime focus	Very broad band horns	Electronic warfare
Wide flare angle $(\theta > 15^\circ)$ Conical Horn 	Prime focus reflectors Gain standard Low frequency	Multifrequency Compact horns	Multifrequency communication channels Spacecraft antennas

Table 3.2: Different types and applications of horn antennas where D refers to the aperture diameter of the horn and θ refers to the opening angle of the horn (Clarricoats and Olver, 1984 : 98)

Millimetre wave antennas are often not directly placed at the reflector antenna focus, but rather some optical components (typically re-focussing mirrors) are used to match the millimetre wave horn to the telescope in order to optimize aperture efficiency. The corrugated horn designs considered for the OSO 4 mm receiver channel are large aperture and narrow flare angle horns. This design is most commonly used in corrugated horns since the large aperture diameter ensures the horns are less sensitive to cross-polarisation.

In any type of corrugated horn four important sections (see Figure 3.3) can be identified for design purposes (Clarricoats, 1984: 99): (i) the aperture diameter and flare angle, (ii) the corrugations, (iii) the flare section and (iv) the throat section

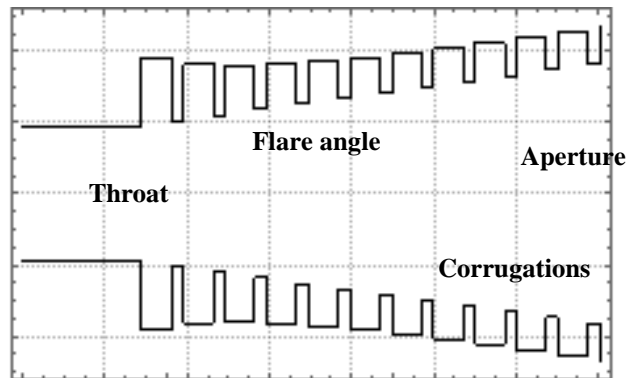


Figure 3.3: Corrugated Horn showing the sections relevant for design

The aperture diameter and flare angle determine the co-polar beamwidth, while the corrugations determine the beam pattern symmetry and cross-polarisation levels. The flare section determines the mode conversion along the horn and the position of the phase centre. The throat section determines both the impedance match into the waveguide sections behind the horn and also which modes are generated that can propagate in the horn (Clarricoats and Olver, 1984: 73). The narrow flare angle ($\theta < 15^\circ$) gives a physically long horn resulting in the phase centre of the horn varying less with frequency, and the large aperture diameter simplifies the analysis by enabling further approximations to be made.

In single mode horns, the cross-polar field can be regarded as the orthogonal component of the field relative to the dominant (co-polar) field direction. The cross-polar field is generally a maximum at $\phi = 45^\circ$ and $\phi = 135^\circ$, the power of which can be attributed to: (i) the intrinsic cross-polarisation of corrugations, (ii) higher order modes generated by throat region, (iii) higher order mode conversion along the horn (such as the EH_{12}), and (iv) direct radiation from flange (only of concern for small horns) with significant currents around the aperture area (Clarricoats and Olver, 1984: 114). Standard conical corrugated horns are favoured over standard smooth walled conical horns because the latter tend to have significantly higher cross-polarisation levels and asymmetric beams. This is undesirable in an astronomical receiver system such as the 4 mm OSO receiver, due to cross-polarisation introduced by the receiver channel mirrors.

When designing the flared section of the horn, one needs to consider: (i) the mechanical constraints of the length, (ii) the position and movement of the phase centre (point on the axis of the horn which is the centre of curvature of the phase front) across the operating band, and (iii) mode conversion along the flared section. The throat section is one of the most difficult parts of the feed to design correctly for optimum performance, particularly for wide band operation, because any mismatch between the waveguide modes and the modes in the throat section of the horn, will lead to the generation of higher order modes which cause increased cross-polarisation as well as reflections back into the feed waveguide (Clarricoats and Olver, 1984: 128). It is reported in the literature that the optimum corrugation depth for minimal cross-polarisation is $\lambda/2$ slowly transitioning to $\lambda/4$ at the throat, but it introduces a frequency dependent factor and does not answer the question as to what is the best design away from the central frequency. A certain amount of trial and error is required to reach the performance goals.

3.5 4 mm OSO Channel Design

As mentioned previously, three different horn designs were initially considered for the receiver feed: two standard conical corrugated horns (one with a wider 30 mm aperture and one with a narrower 18.8 mm aperture) and one compact profiled design (Maffei *et al.*, 2004) horn. In the end, due to the difficulty in manufacturing the profiled horn option it was not chosen for the design. Thus it will not be discussed to the same level of detail as the two other standard corrugated horns. Both standard conical corrugated horns have a large aperture and a narrow flare angle. The physical specifications of both of these horns can be seen in Table 3.3.

	Wider	Narrower
Aperture Diameter	30 mm	18.8 mm
Flare Angle	8.53°	4.88°
Slant Length	100 mm	110 mm
Axial Length	87 mm	93 mm

Table 3.3: Specifications of horns considered for design

3.5.1 Corrugated horn with 30 mm aperture (wider aperture)

The horn shown in Figure 3.4 (left) contains corrugations which are perpendicular to the axis of propagation. The Mathematica version of the CylindricalSCATTER software was used to obtain the scattering matrices for the horn, as well as the aperture fields. Figure 3.4 (right) shows the beam at the aperture produced by the mode matching software showing the cuts at azimuthal angles $0^\circ / 180^\circ$, $90^\circ / 270^\circ$ and $45^\circ / 225^\circ$.

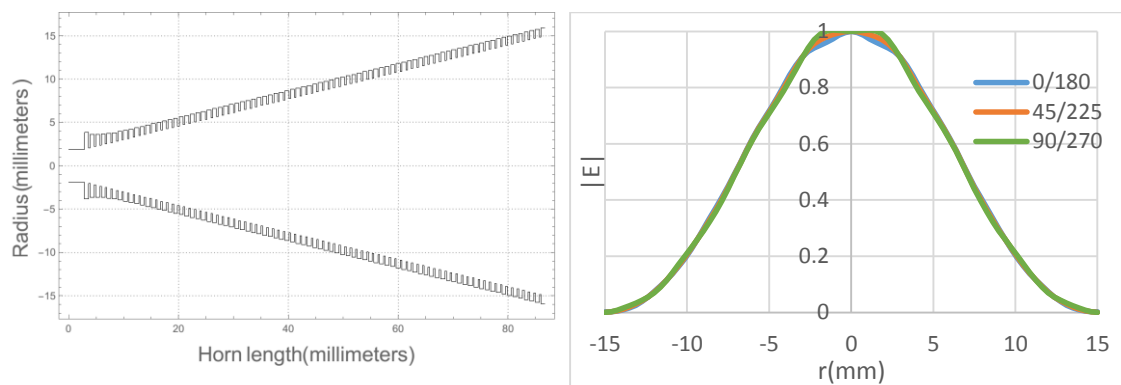


Figure 3.4: Corrugated Horn with 30 mm aperture plotted in Mathematica (Left). The aperture fields at 76 GHz taken at various cuts (Right) (blue line corresponds to a cut taken at $\phi = 0^\circ / 180^\circ$, green at $\phi = 90^\circ / 270^\circ$ and orange at $\phi = 45^\circ / 225^\circ$)

The farfield patterns were produced by CylindricalSCATTER using the expressions for farfield of the waveguide modes at the aperture. The beam patterns were produced at 67 GHz, 76 GHz and 86 GHz, where the frequencies effectively correspond to the lower edge, middle and upper edge of the band. Both the co-polar and cross-polar patterns are displayed in Figure 3.5 below. The cross-polar cut is taken at $\phi = 45^\circ / 225^\circ$ where the cross-polarisation is maximum (the level is zero in the $\phi = 0^\circ / 180^\circ$ and the $\phi = 90^\circ / 270^\circ$ directions).

The cross-polar pattern is at a very low level right across the operating band, and the different cuts of the co-polar pattern line up well, indicating that the beam is highly symmetric across the band. At the design frequency the cross-polar levels are considerably lower than at the band edges by about 10 dB, indicating excellent performance across the band by the wider aperture horn.

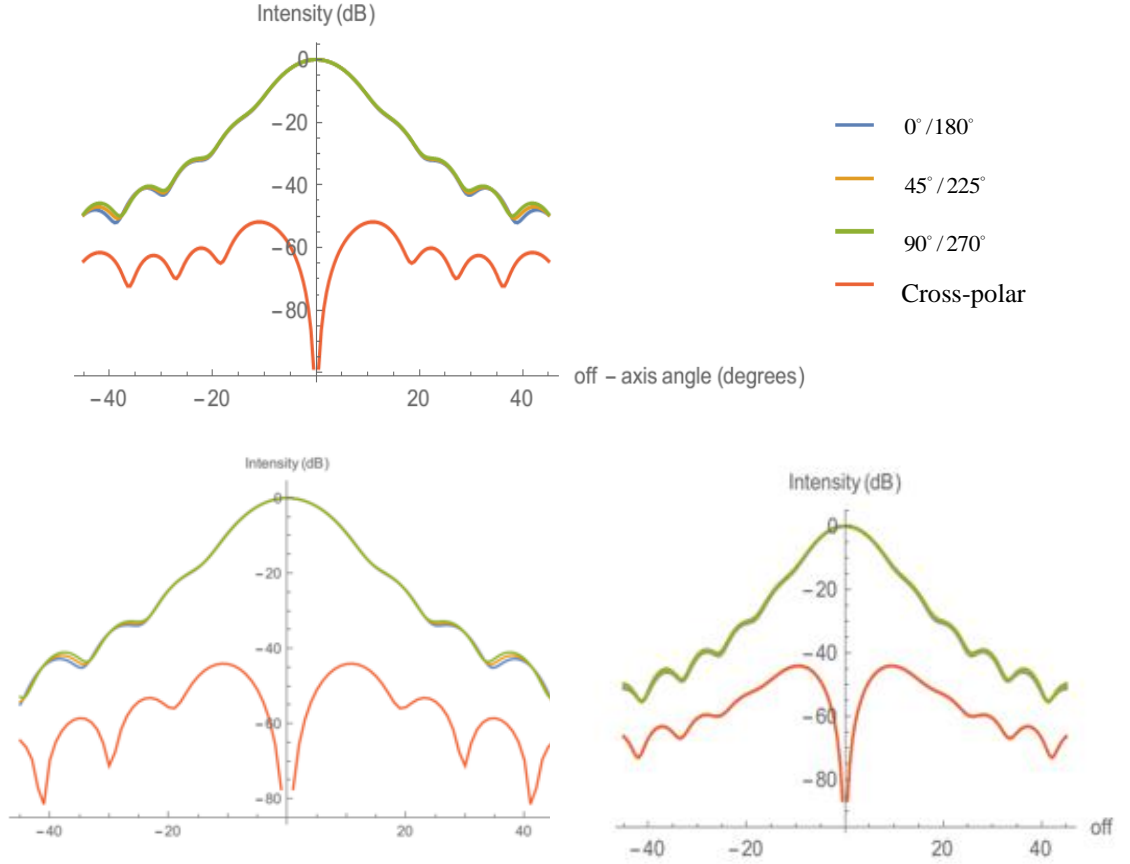


Figure 3.5: Farfield co-polar and cross-polar radiation pattern cuts at $\phi = 0^\circ / 180^\circ$, $45^\circ / 225^\circ$ and $90^\circ / 270^\circ$ at 67 GHz (bottom left), 76 GHz (top) and 86 GHz (bottom right) for the wider (30 mm) aperture conical horn

The Gaussicity of a field E_F is defined as (O’Sullivan and Murphy, 2012: 70)

$$K_G = \frac{\left| \int_0^{2\pi} \int_0^a \psi_G^*(W, R) E_F r dr d\phi \right|^2}{\int_0^{2\pi} \int_0^a |E_F|^2 r dr d\phi \times \int_0^\infty |\psi_G(W, R)|^2 2\pi r dr} \quad (3.13)$$

where $\psi_G(W, R)$ is the best-fit Gaussian to the beam and $|E_F|$ is the co-polar field component. Gaussicity is a parameter used to determine how well the beam couples to a Gaussian. Generally, the more a beam can be approximated as a Gaussian field the better, especially to minimize any truncation and diffraction effects. Component sizes can be minimized as there are no sidelobes carrying power off-axis and single quasi-optical design parameters based on Gaussian beams can be used (Goldsmith, 1998: 162).

When fitting a Gaussian beam profile to the horn, the Gaussian parameters, W_a (the beam radius at the aperture) and R (the radius of curvature) are varied to maximise Gaussicity. The fit that produced the maximum Gaussicity was taken as the best fit.

The beam radius was first estimated visually (as indicated in Figure 3.6 below), *i.e.* by plotting the field amplitude $|E_F|$ at $\phi = 0^\circ / 180^\circ$ and by comparing it with the amplitude of the Gaussian field (Equation (3.14))

$$\psi_0(r, z, W, R) = \sqrt{\frac{2}{\pi W^2}} \times \exp\left[-\left(\frac{r^2}{W^2}\right)\right], \quad (3.14)$$

with $W(z)$ as a variable.

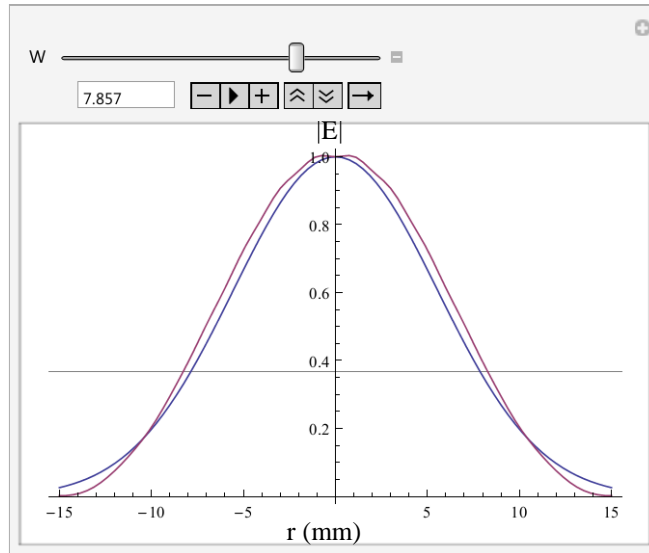


Figure 3.6: The red line corresponds to the absolute value of the aperture field at $\phi=0^\circ$ and the blue line is the fundamental Gaussian field varying with W

The radius of curvature parameter, R , was found in a similar manner (as in Figure 3.7), using the phase of the field. This is achieved using the argument of the complex aperture field was plotted along with the phase term of the complex exponential term of the Gaussian beam (essentially $k r^2 / 2R$).

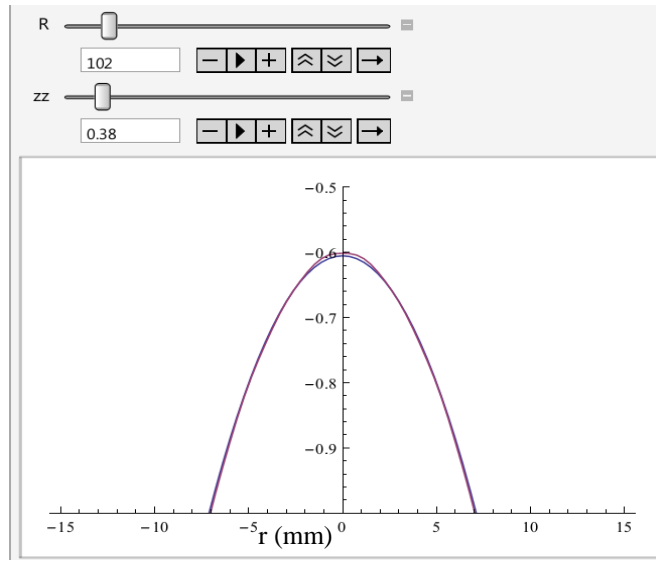


Figure 3.7: The red line corresponds to the argument of the aperture field at $\phi=0^\circ$ and the blue line corresponds to the argument of the fundamental Gaussian field varying with R and z.

Using the method above, approximate values of W and R were obtained. The ‘*Manipulate*’ command in Mathematica was used in order to estimate a range of approximate values for the beam radius ($W(z)$). ‘*Manipulate*’ was used to generate a plot of Equation (3.14) above, with added controls allowing for interactive manipulation of the beam radius value. Once an approximate range of the beam radius was quickly established by eye, integration was used to get a more precise value of $W(z)$, thus reducing the overall computation time.

The coupling coefficient, K_G (given by Equation (3.13)), was calculated for a smaller range of $W(z)$ and $R(z)$ values. The precise values of $W(z)$ and $R(z)$ resulted in maximum coupling of the aperture field to a Gaussian (with $K_G = 1$ indicating a perfect Gaussian). In fact, in the literature (Goldsmith, 1998: 163) states that at the horn aperture, the best-fit Gaussian was given by $W_a = 0.6435 \times a$, so that W_0 (the beam waist) and z (the beam waist position behind the horn aperture) are given by (Wylde and Martin, 1993)

$$W_0 = \frac{0.6435 \times a}{\sqrt{1 + \left(\frac{\pi W_{ap}^2}{\lambda L} \right)^2}}, \quad (3.15)$$

$$\Delta z = \frac{L}{1 + \left(\frac{\lambda L}{\pi W_{ap}^2} \right)^2}, \quad (3.16)$$

provided ψ_0 is normalized. L is the slant length and a is the aperture radius of the horn.

An identical procedure was followed to obtain the Gaussian Beam Mode parameters at the upper and lower edges of the frequency band and the results are given in Table 3.4.

Frequency	W (mm)	R (mm)	W₀ (mm)	z (mm)	λ (mm)
76 GHz	9.69	100	7.76	35.9	3.94
67GHz	9.7	99	8.07	30.5	4.47
86GHz	9.72	98	7.34	42.2	3.49

Table 3.4: Gaussian Beam Mode parameters at the centre, upper and lower edges of the frequency band

Once all of the Gaussian Beam Mode parameters were known, the Gaussicity was calculated to be 98.2% at the central band frequency when $W(z)$ was optimized.

The field at the horn aperture can be reconstructed using Gaussian Beam Mode Analysis by including the higher order modes as well as the fundamental Gaussian in the analysis. At the horn aperture the field can be considered as a sum of HE and EH hybrid modes made up of a coherent sum of TE and TM waveguide modes. If the TE and TM waveguide modes have equal phase the resulting hybrid mode is HE and if the modes are out of phase by 180° the hybrid mode is EH will naturally couple to Laguerre-Gaussian mode sets. The mode coefficients are listed in Table 3.5 and the reconstructed fields are shown in Figure 3.8. The W used is for the real horn as simulated by CylindricalSCATTER rather than assuming the W for a perfect HE_{11} mode at the horn aperture.

Chapter 3:
Quasi-Optical Propagation and the Design of a 4mm Receiver for the Onsala Space Observatory

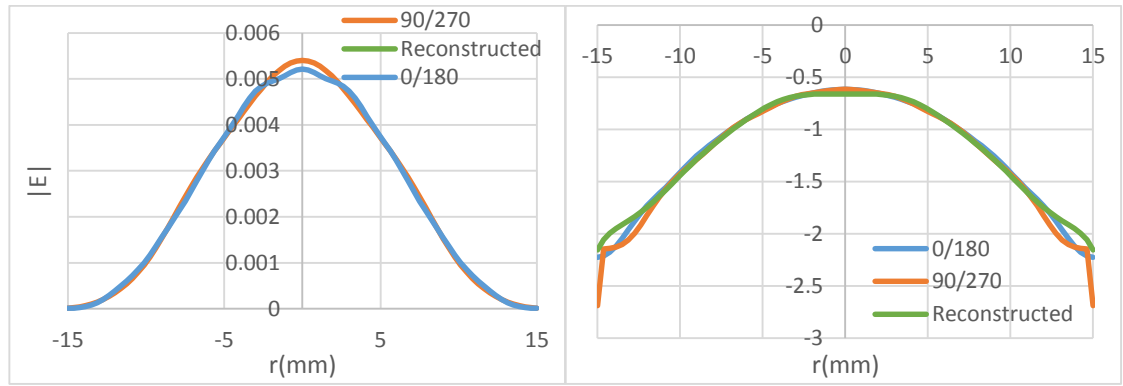


Figure 3.8: Comparison of the reconstructed (green) amplitude ($|E|$) (left) and phase (right) with CylindricalSCATTER predictions of the amplitude and phase at the horn aperture at angles $0^\circ / 180^\circ$ (blue) and $90^\circ / 270^\circ$ (orange) at 76 GHz

n	A_n (67 GHz)	A_n (76 GHz)	A_n (86 GHz)	n	A_n (67 GHz)	A_n (76 GHz)	A_n (86 GHz)
0	0.9909	0.9910	0.9911	5	0.0317	0.0322	0.0328
1	0.0079	0.0014	0.0021	6	0.0189	0.0175	0.0174
2	0.1160	0.1157	0.1153	7	0.0014	0.0014	0.0020
3	0.0430	0.0390	0.0378	8	0.0110	0.0124	0.0176
4	0.0172	0.0203	0.0215	9	0.0133	0.0138	0.0145

Table 3.5: Modal Coefficients at some spot frequencies across the band

The fundamental mode (A_0^2) contains 98.2% of the power indicating a good approximation to the main beam. Similarly, the fundamental mode (A_0^2) contains 98.1% of the power at the lower edge and 98.2% at the upper edge of the band, indicating a good approximation to the main beam away from the central frequency.

One of the performance specifications was for the horn to operate over a frequency band from 67 GHz to 86 GHz. Therefore the beam was also reconstructed at the horn aperture using Gaussian Beam Mode Analysis at the band edges (as in Figure 3.9 and Figure 3.10).

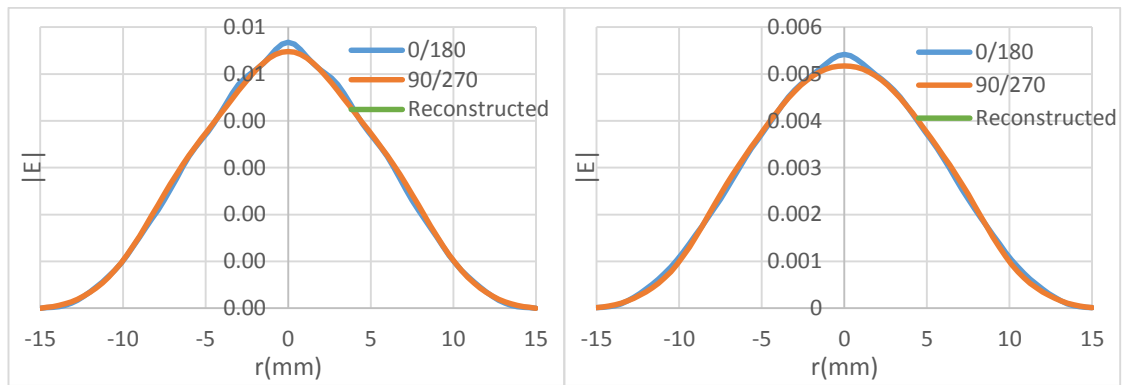


Figure 3.9: Comparison of the reconstructed amplitude ($|E|$) (green) with CylindricalSCATTER predictions of the amplitude at the horn aperture at angles $0^\circ/180^\circ$ (blue) and $90^\circ/270^\circ$ (orange) at 67 GHz (left) and 86 GHz (right)

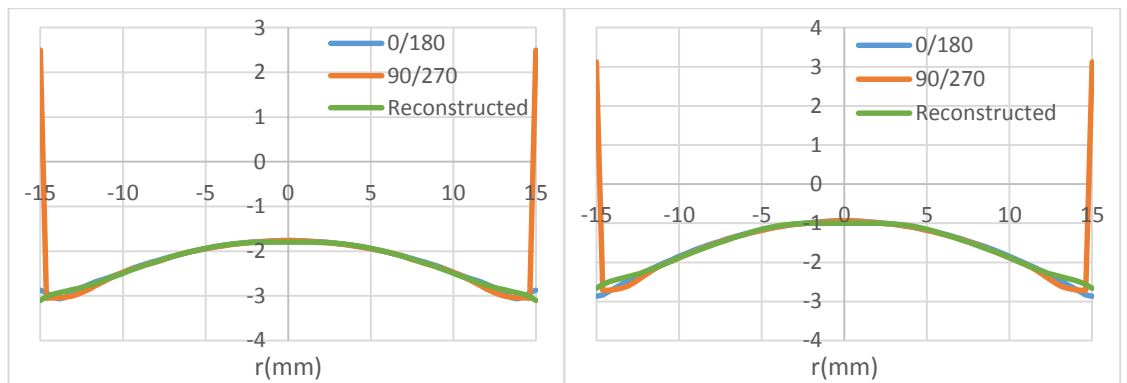


Figure 3.10: Comparison of the reconstructed phase (green) with CylindricalSCATTER predictions of the amplitude at the horn aperture at angles $0^\circ/180^\circ$ (blue) and $90^\circ/270^\circ$ (orange) at 67 GHz (left) and 86 GHz (right)

It is interesting to note that the field at the aperture of a corrugated horn antenna can be approximated by a zero order Bessel function $J_0(\alpha r)$ (in fact, this is the HE_{11} hybrid mode) truncated at its first zero ($r = a$) provides a good fit to the field (Wylde and Martin, 1993). Figure 3.11 shows the co-polar radiation patterns in the farfield for the centre of the band as well as a plot of the equivalent truncated Bessel beam. However, in any simulation of the optical system using GRASP9, GAMMA and CylindricalSCATTER were used for the horn fields, although a truncated Bessel beam clearly could have also been used.

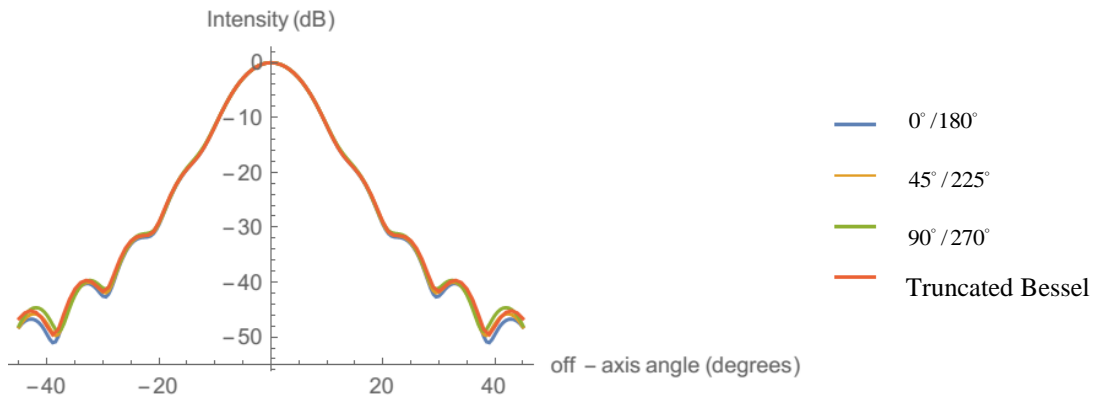


Figure 3.11: Farfield co-polar radiation pattern cuts at $\phi = 0^\circ / 180^\circ$, $45^\circ / 225^\circ$ and $90^\circ / 270^\circ$ at 76 GHz with a truncated Bessel Beam

3.5.2 Corrugated horn with 18.8 mm aperture (narrower aperture)

As was done previously, the Mathematica version of the mode matching software (CylindricalSCATTER) was applied to the narrower aperture horn (shown in Figure 3.12 (left)) design. Figure 3.12 (right) shows the beam at the aperture produced by the mode matching software showing the cuts at azimuthal angles $0^\circ / 180^\circ$, $90^\circ / 270^\circ$ and $45^\circ / 225^\circ$.

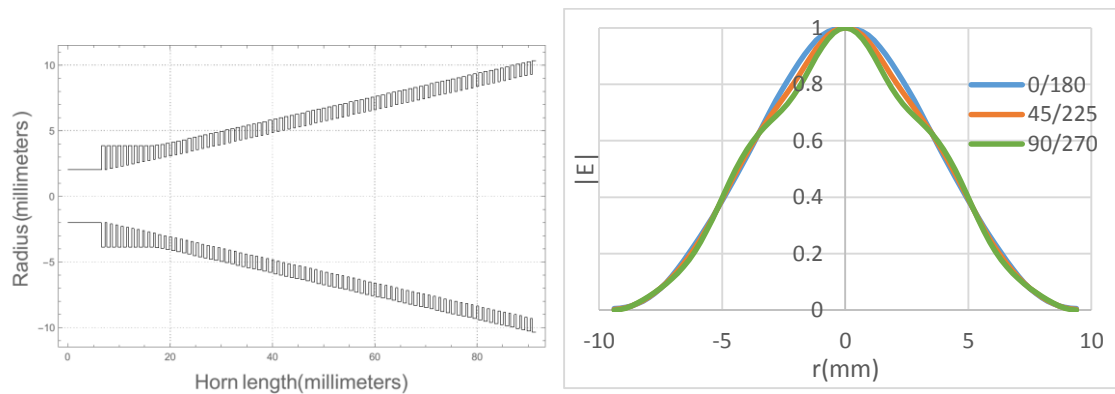


Figure 3.12: Corrugated Horn with 9.3 mm aperture plotted in Mathematica (Left). The aperture fields at 76 GHz taken at various cuts (Right) (blue line corresponds to a cut taken at $\phi = 0^\circ / 180^\circ$, green at $\phi = 90^\circ / 270^\circ$ and orange at $\phi = 45^\circ / 225^\circ$)

Figure 3.13 displays the co-polar and cross-polar radiation patterns in the farfield at the lower and upper edge of the band, as well as in the centre of the band. The cross-polar pattern is at a very low level across the operating band (-47 dB relative to the on-axis co-polar power at 67 GHz and 76 GHz, and -36 dB at 86 GHz), and the cuts at the different

azimuthal angles of the co-polar pattern line up well, indicating that the beam is symmetric.

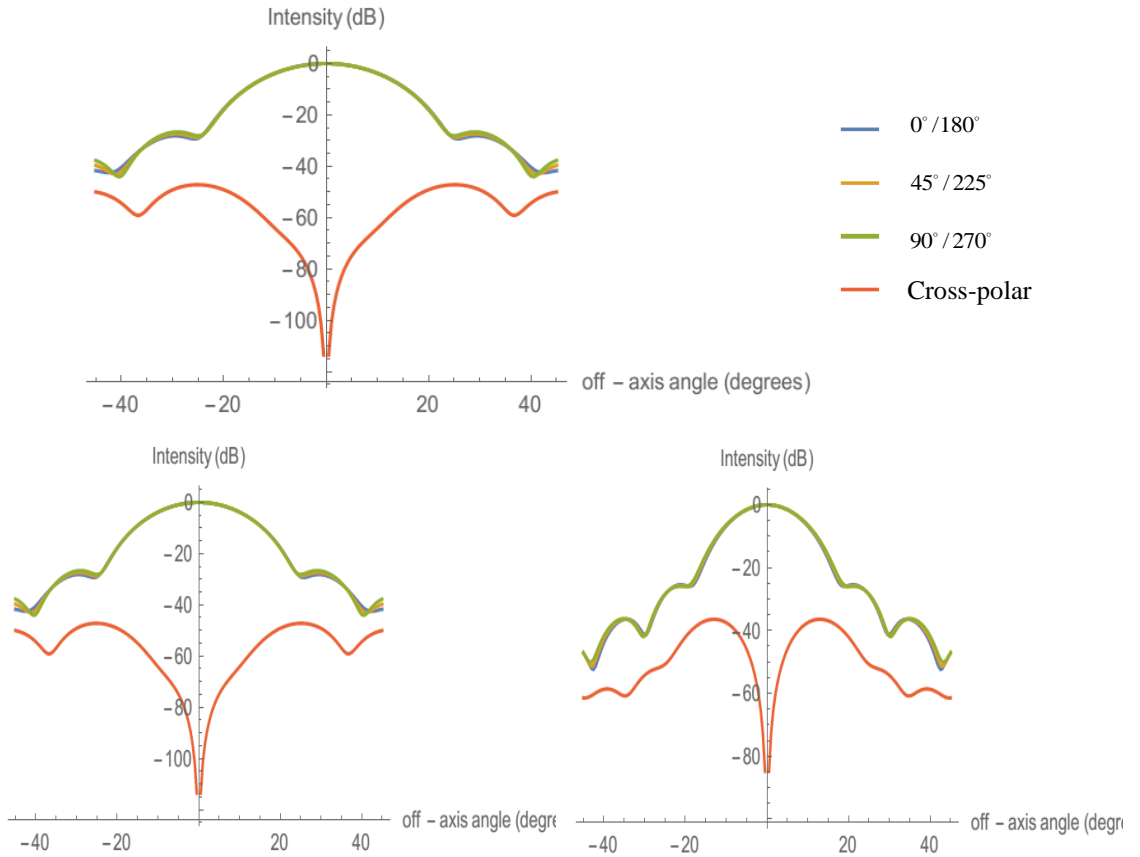


Figure 3.13: Farfield co-polar and cross-polar radiation pattern cuts at $\phi = 0^\circ/180^\circ, 45^\circ/225^\circ, 90^\circ/270^\circ$ at 67 GHz (bottom left), 76 GHz (top) and 86 GHz (bottom right) for the narrower aperture (18.8 mm) corrugated horn

The beam radius was first estimated visually (as outlined in the design procedure for the horn with wider aperture), *i.e.* by plotting the absolute value squared of the aperture field at $\phi = 0^\circ/180^\circ$ and by plotting the amplitude term of the Laguerre-Gaussian beam mode set, which is given by Equation (3.14) in Section 3.5.1. The radius of curvature parameter, $R(z)$, was also found using the same procedure as outlined for the horn with wider aperture.

The precise values of $W(z)$ and $R(z)$ at the horn aperture were again found by performing the overlap integral between the best-fit Gaussian field and the aperture field. Once all of the Gaussian Beam Mode parameters were known, the Gaussicity was calculated to be 98.2% at the centre of the band. Again, it was found that at the horn aperture, the best-fit Gaussian agreed with $W_a = 0.6435 \times a$ as given in the literature (Goldsmith, 1998: 163),

so that W_0 (the beam waist) and z (the beam waist position behind the horn aperture) are also given by Equations (3.15) and (3.16). The Gaussian Beam Mode parameters at the upper and lower edges of the band were also found by using the same procedure as for the wider aperture horn and are given in Table 3.6.

Frequency	W(mm)	R(mm)	W ₀ (mm)	z(mm)	λ(mm)
76 GHz	6.13	110	5.92	7.6	3.94
67GHz	6.07	113	5.92	5.6	4.47
86GHz	6.18	111	5.90	9.7	3.49

Table 3.6: Gaussian Beam Mode parameters at the centre, upper and lower edges of the frequency band

Again, a Gaussian Beam Mode Analysis of the field at the horn aperture was undertaken and the mode coefficients are listed below in Table 3.7.

n	A _n (67 GHz)	A _n (76 GHz)	A _n (86 GHz)	n	A _n (67 GHz)	A _n (76 GHz)	A _n (86 GHz)
0	0.9911	0.9907	0.9900	5	0.0267	0.0319	0.0349
1	0.0044	0.0032	0.0019	6	0.0163	0.0172	0.0202
2	0.1167	0.1178	0.1197	7	0.0041	0.0011	0.0004
3	0.0406	0.0398	0.0412	8	0.0124	0.0110	0.0123
4	0.0163	0.0199	0.0211	9	0.0119	0.0111	0.0149

Table 3.7. Modal coefficients at the centre of the band

The fundamental mode (A_0^2) contains 98.1% of the power indicating a good approximation to the main beam. Similarly, the fundamental mode (A_0^2) contains 98.2% of the power at the lower edge and 98.0% at the upper edge of the band indicating a good approximation to the main beam away from the central frequency.

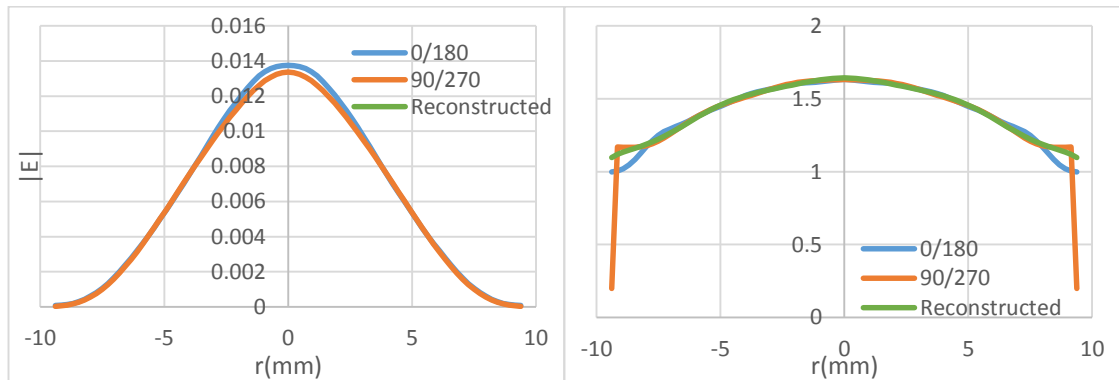


Figure 3.14. Comparison of the reconstructed (green) amplitude ($|E|$) (left) and phase (right) with CylindricalSCATTER predictions of the amplitude and phase at the horn aperture at angles $0^\circ / 180^\circ$ (blue) and $90^\circ / 270^\circ$ (orange) at 76 GHz

The beam was also reconstructed using Gaussian Beam Mode Analysis at 67 GHz and 86 GHz as shown in Figure 3.15 and Figure 3.16

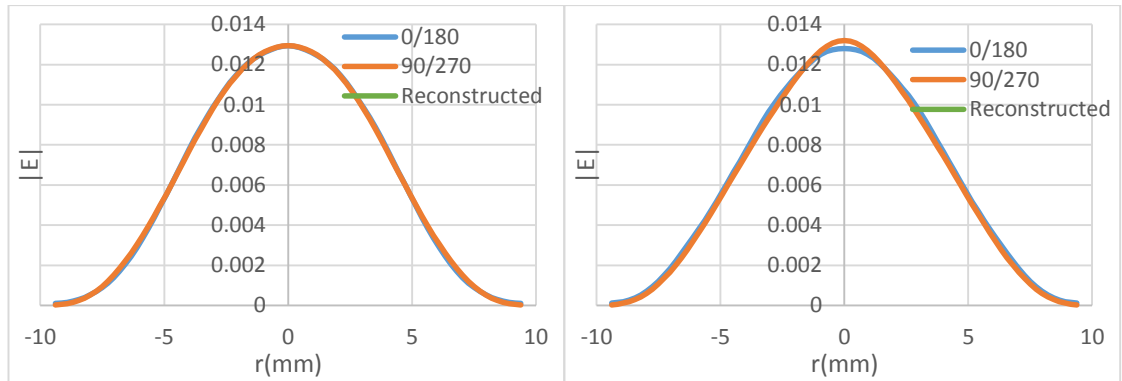


Figure 3.15: Comparison of the reconstructed amplitude ($|E|$) (green) with CylindricalSCATTER predictions of the amplitude at the horn aperture at angles $0^\circ/180^\circ$ (blue) and $90^\circ/270^\circ$ (orange) at 67 GHz (left) and 86 GHz (right)

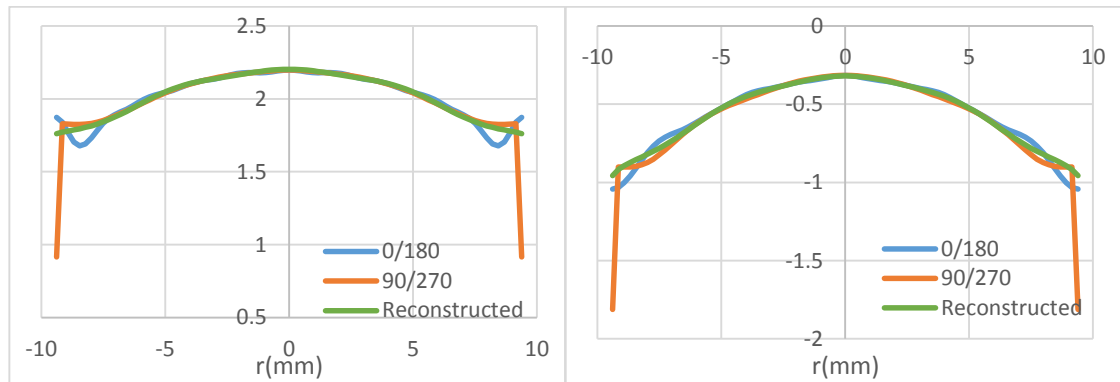


Figure 3.16: Comparison of the reconstructed phase (green) with CylindricalSCATTER predictions of the amplitude at the horn aperture at angles $0^\circ/180^\circ$ (blue) and $90^\circ/270^\circ$ (orange) at 67 GHz (left) and 86 GHz (right)

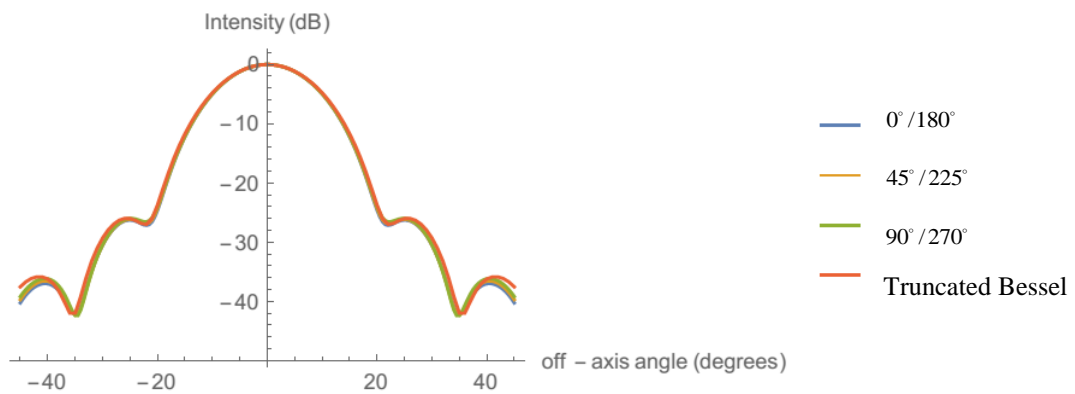


Figure 3.17: Farfield co-polar radiation pattern cuts at $\phi = 0^\circ, 45^\circ, 90^\circ$ at 76 GHz with a truncated Bessel beam.

Figure 3.17 contains the co-polar radiation patterns in the farfield for the centre of the band as well as a plot of an equivalent truncated Bessel beam.

3.5.3 Profiled horn design

The compact horn design that was chosen for investigation was based on a Winston-cone profile as developed for the 150 GHz channel on the CLOVER B-mode CMB experiment by B.Maffei (Maffei, 2000). The profile was re-scaled for 75 GHz and is shown in Figure 3.18(left).

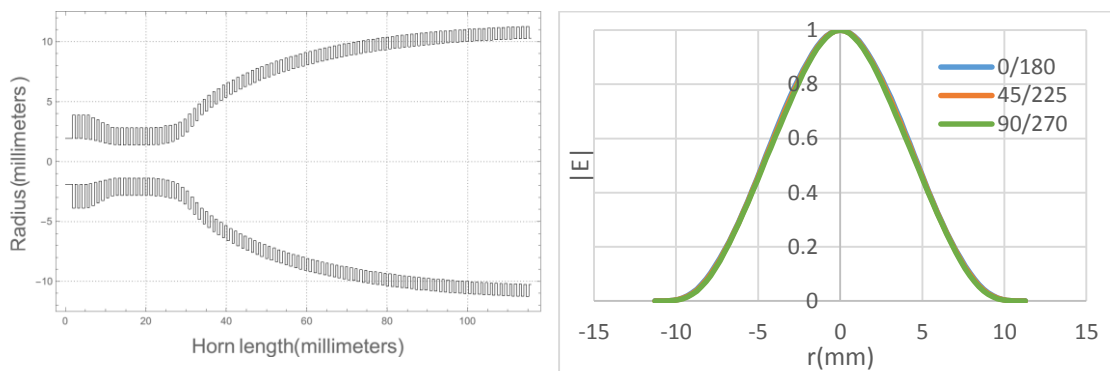


Figure 3.18. CLOVER Horn at 75GHz (Left). The aperture fields taken at various cuts (Right) (blue line corresponds to a cut taken at $\phi = 0^\circ/180^\circ$, green at $\phi = 90^\circ/270^\circ$ and orange at $\phi = 45^\circ/225^\circ$)

As before, the mode matching software (CylindricalSCATTER) was used to model the system and produce plots of the aperture field at various azimuthal cuts. Figure 3.18 (right) shows the beam at the aperture at 75 GHz as produced by the mode matching software. Figure 3.19 displays the co-polar and cross-polar radiation patterns at 75 GHz.

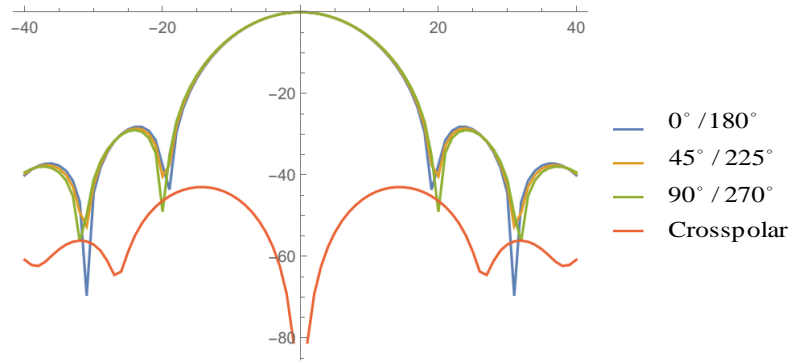


Figure 3.19: Farfield co-polar and cross-polar radiation pattern cuts at $\phi = 0^\circ/180^\circ, 45^\circ/225^\circ, 90^\circ/270^\circ$ at 75GHz

The beam radius was first estimated using the visual method (as outlined in the design procedure for the wider aperture horn). The Gaussian beam mode parameters at 75 GHz are given in Table 3.8 below. It can be seen that the waist of the beam lies very close to the horn aperture

Frequency	W (mm)	R (mm)	W ₀ (mm)	z (mm)	λ (mm)
75GHz	6.69	670	6.68	1.84	4.00

Table 3.8: Gaussian Beam Mode parameters

Table 3.9 shows the higher-order mode content in terms of symmetric Laguerre-Gaussian beam modes.

n	0	1	2	3	4	5	6
A(n)	0.9913	0.0025	0.1145	0.0387	0.0196	0.0320	0.0185

Table 3.9: Modal coefficients at the centre of the band

The fundamental mode (A_0^2) contains 98.2% of the power indicating a good approximation to the main beam. Once all of the Gaussian Beam Mode parameters were known, the Gaussicity was calculated to be 98.2%. The fields were then reconstructed using Gaussian Beam Mode Analysis. The amplitude and phase were reconstructed at 75 GHz and are shown in Figure 3.20.

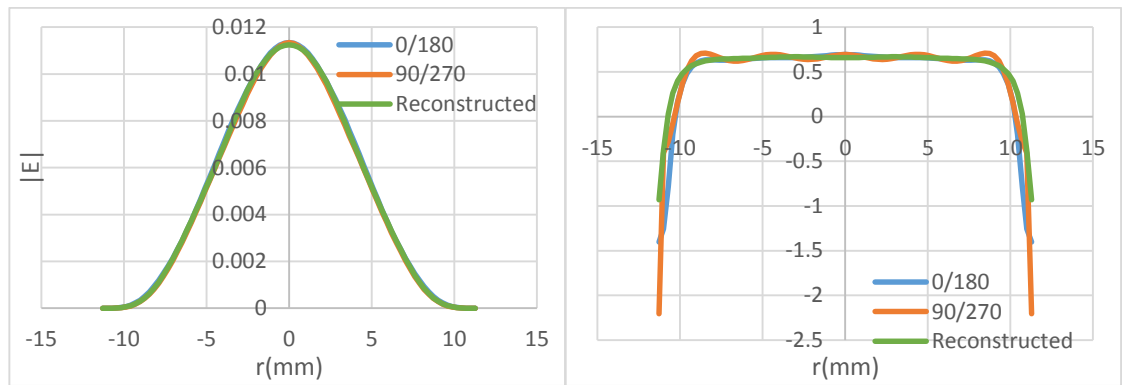


Figure 3.20: Comparison of the reconstructed (green) amplitude ($|E|$) (left) and phase (right) with CylindricalSCATTER predictions of the amplitude and phase at the horn aperture at angles $0^\circ / 180^\circ$ (blue) and $90^\circ / 270^\circ$ (orange) at 76 GHz

Table 3.10 below summarises the performance of the corrugated horns at 76 GHz for the case of the standard corrugated horns and at 75 GHz for the profiled horn.

	Wider	Narrower	Profiled
Gaussicity	98.1992%.	98.1589%.	98.2467%.
Power in fundamental mode	97.995%	98.075%	98.096%
Cross-polarisation	-56 dB	-47 dB	-43 dB

Table 3.10: Summary of corrugated horn performance

The main advantage of the Winston profile is that it should be more compact.

3.6 Tolerance Analysis

In this section, we investigate the possibility of how imperfections arising from the manufacturing process would affect the beam patterns. This study was carried out for both wider and narrower aperture conical corrugated horns described in Section 3.5. The horns were manufactured by electroforming on a mandril (negative shape of horn) milled on a lathe.

Deviations from the ideal design in the radii of the sections making up the horn were investigated as this was most likely to be the source of error although the long wavelength

of design operation meant these were not relatively large. A random number generator was used to generate the random errors between a given positive and negative tolerance value. Thus, with each tolerance value, a new geometry file for the horn was created. The tolerance values were used to investigate the co-polar and cross-polar farfield beam patterns at a number of spot frequencies across the operating band of the horn (67 GHz, 76 GHz and 86 GHz).

Figure 3.21 to Figure 3.24 show the effect of tolerance errors of $\pm 15 \mu\text{m}$, $\pm 30 \mu\text{m}$, $\pm 50 \mu\text{m}$ and $\pm 100 \mu\text{m}$ applied to the radii of the horns. This effect was investigated for the two standard corrugated horns but not the compact design profiled horn (as this was not chosen for further investigation due to the complexity of manufacture).

Corrugated horn with wider aperture (30 mm)

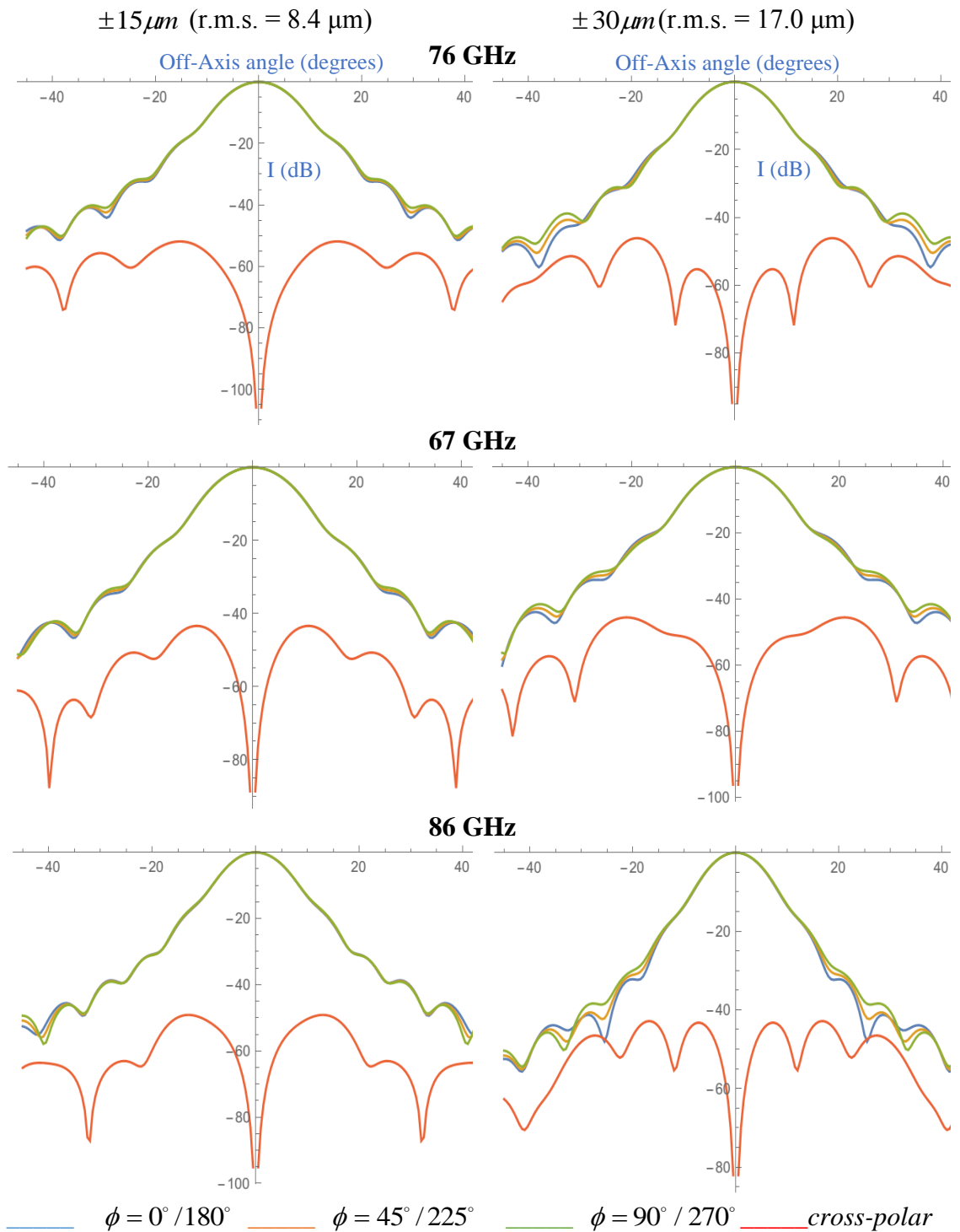


Figure 3.21: Co-polar and cross-polar farfield patterns at 76 GHz (top), 67 GHz (middle) and 86 GHz (bottom) with a tolerance of $\pm 15 \mu\text{m}$ (left) and $\pm 30 \mu\text{m}$ (right)

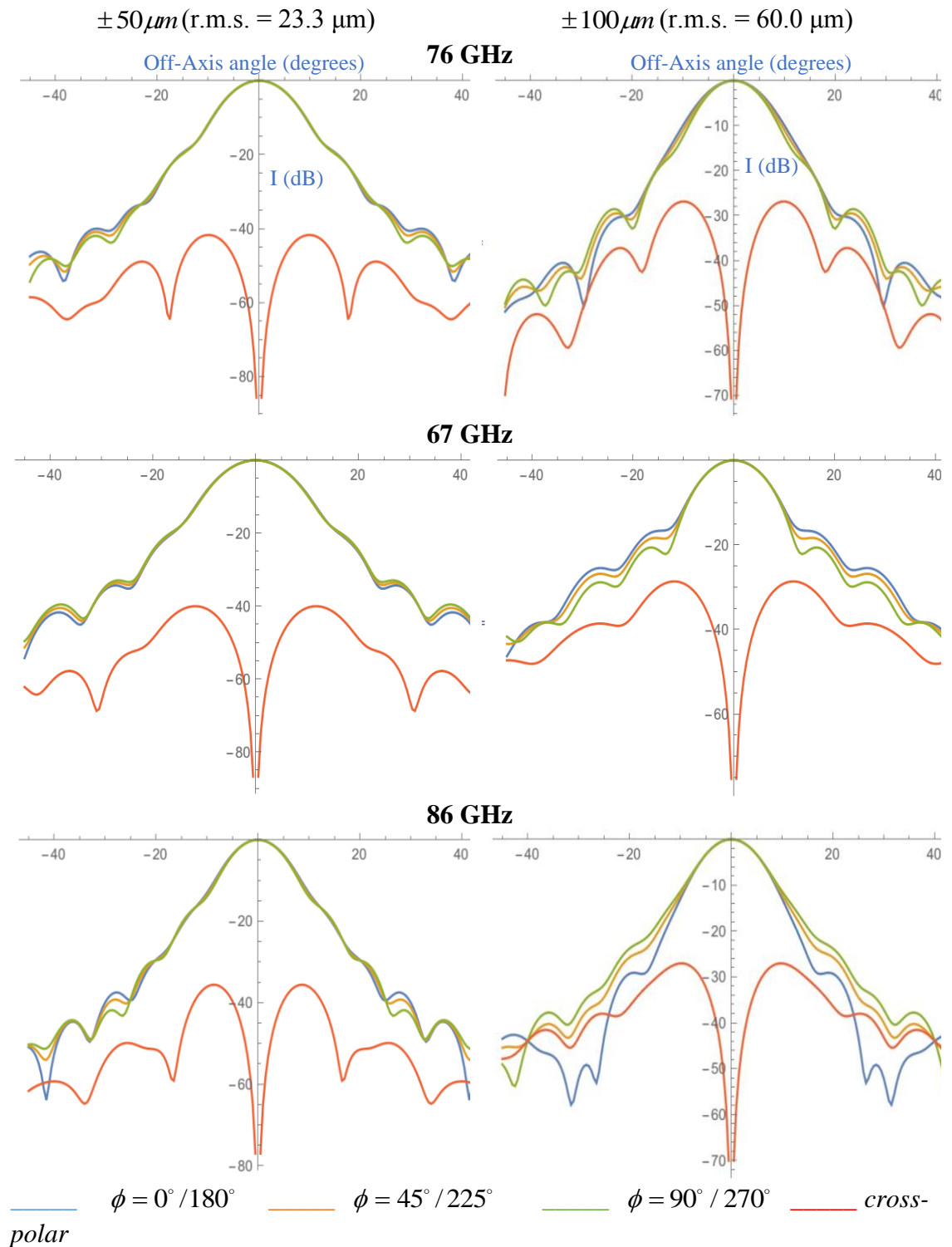


Figure 3.22: Co-polar and cross-polar farfield patterns at 76 GHz (top), 67 GHz (middle) and 86 GHz (bottom) with a tolerance of $\pm 50 \mu\text{m}$ (left) and $\pm 100 \mu\text{m}$ (right)

Table 3.11 summarises the results of the tolerance analysis in terms of the cross-polar power. The maximum cross-polarisation level below the co-polar maximum is displayed for the three spot frequencies at every tolerance value as well as the values produced by the original design.

	67 GHz	76 GHz	86 GHz
Original	-44 dB	-56 dB	-45 dB
± 15 µm	-44 dB	-52 dB	-48 dB
± 30 µm	-45 dB	-46 dB	-43 dB
± 50 µm	-40 dB	-42 dB	-36 dB
± 100 µm	-29 dB	-27 dB	-27 dB

Table 3.11: Maximum cross-polarisation resulting from deviations in horn section radii

In terms of the co-polar beam patterns, the beam remains highly symmetric for tolerancing errors between $\pm 15 \mu\text{m}$ and $\pm 30 \mu\text{m}$. At $\pm 50 \mu\text{m}$ we begin to notice some asymmetries in the sidelobes at 86 GHz and at $\pm 100 \mu\text{m}$ we begin to see asymmetries in the main beam at 76 GHz, and at -10 dB for 67 GHz and 86 GHz. However, the effects on the beam are negligible.

Corrugated horn with narrower aperture (18.8 mm)

Following the same procedure as for the wider aperture horn, the tolerance values were used to investigate the co-polar and cross-polar farfield beam patterns at some spot frequencies across the band (67 GHz, 76 GHz and 86 GHz) of the 18.8 mm aperture radius horn. The resulting beams are shown in Figure 3.23 and Figure 3.24.

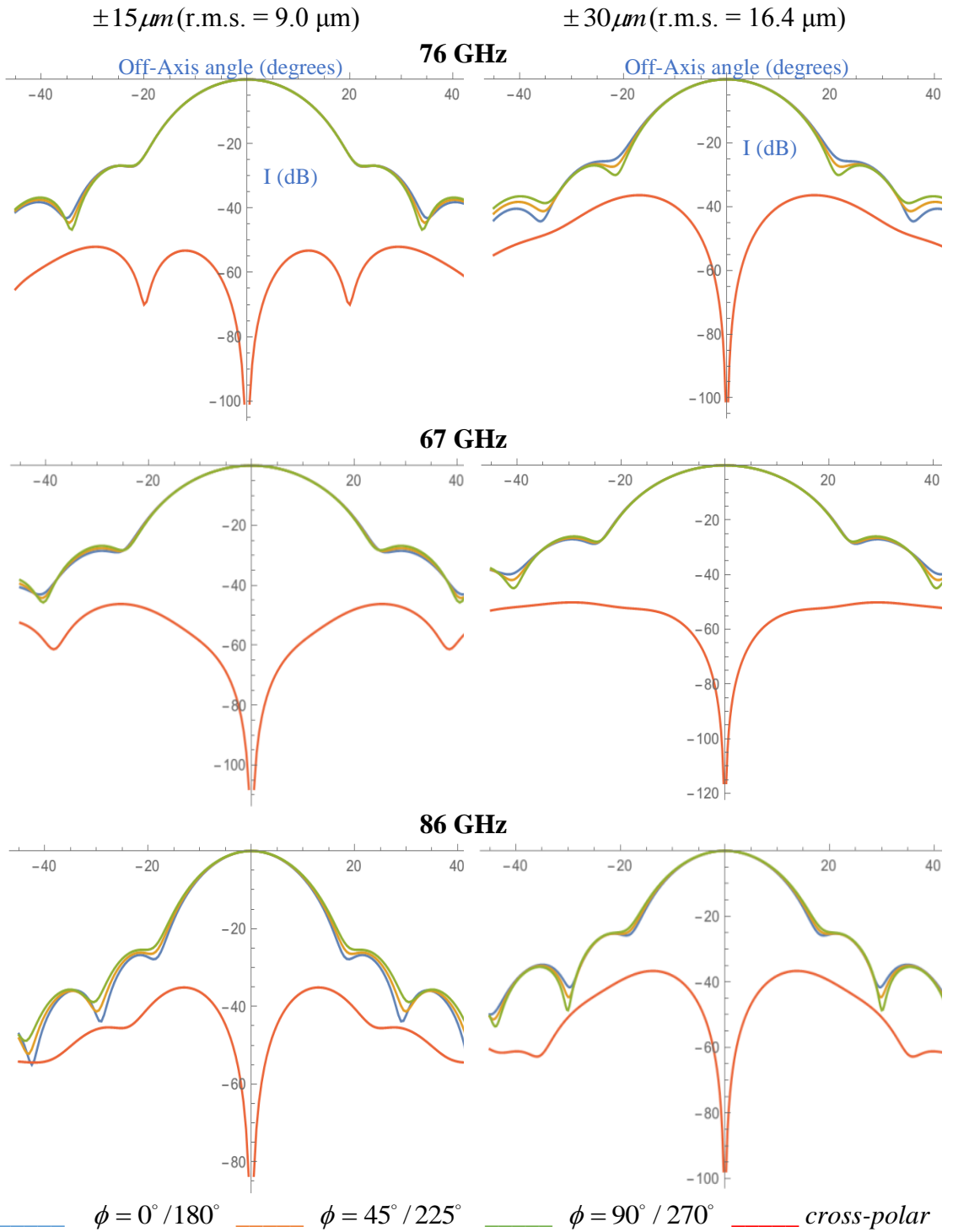


Figure 3.23: Co-polar and cross-polar farfield patterns at 76 GHz (top), 67 GHz (middle) and 86 GHz (bottom) with a tolerance of $\pm 15 \mu\text{m}$ (left) and $\pm 30 \mu\text{m}$ (right)

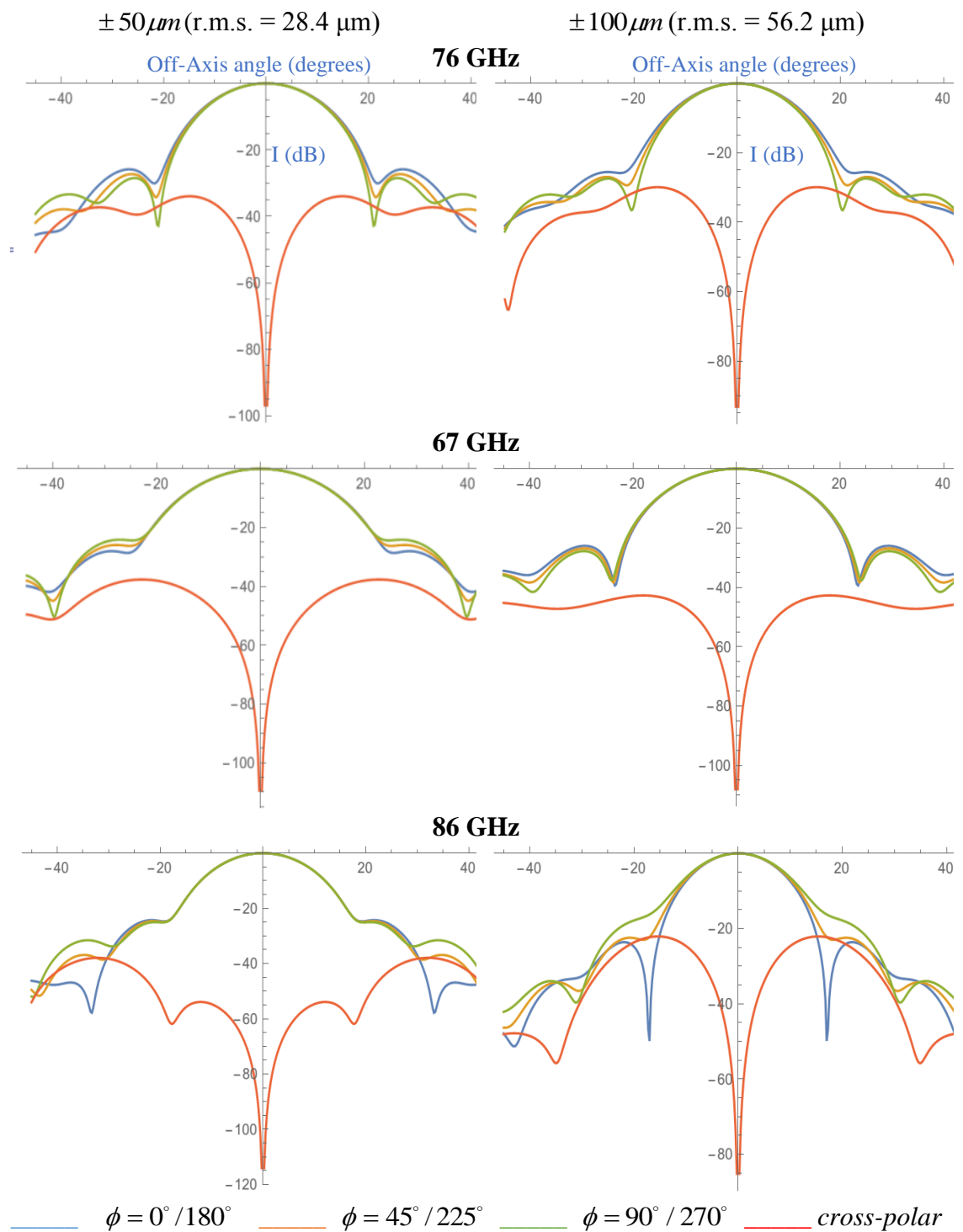


Figure 3.24: Co-polar and cross-polar farfield patterns at 76 GHz (top), 67 GHz (middle) and 86 GHz (bottom) with a tolerance of $\pm 50 \mu\text{m}$ (left) and $\pm 100 \mu\text{m}$ (right)

Table 3.12 summarises the results of the tolerance analysis in terms of the cross-polar power. The maximum cross-polarisation below the on-axis co-polar level is displayed for the three spot frequencies at the various tolerancing values as well as the levels for the original design.

	67 GHz	76 GHz	86 GHz
Original	-47 dB	-47 dB	-36 dB
± 15 µm	-46 dB	-52 dB	-35 dB
± 30 µm	-51 dB	-36 dB	-36 dB
± 50 µm	-37 dB	-34 dB	-38 dB
± 100 µm	-43 dB	-30 dB	-23 dB

Table 3.12: Maximum cross-polarisation resulting from deviations in horn section radii

In terms of the co-polar beam patterns, the beam remains highly symmetric for tolerancing errors between $\pm 15 \mu\text{m}$. At $\pm 30 \mu\text{m}$ we begin to notice some asymmetries in the sidelobes at 76 GHz with the beam remaining symmetric at 67 GHz and 86 GHz. At $\pm 50 \mu\text{m}$ the asymmetry in the sidelobes can be seen at all three spot frequencies. At $\pm 100 \mu\text{m}$, we begin to see asymmetries at -10 dB for 76 GHz and 86 GHz while it is more symmetric at 67 GHz.

In general, we can conclude that the tolerancing issues will have a minimal effect on the co-polar beam patterns for both the wider and narrower aperture horn. This confirms the insensitivity of the beam patterns to manufacturing errors at this millimetre wavelength. There is an effect on the cross-polar beam pattern particularly at the band edges, although these levels are all quite low anyway.

3.7 Modelling of the OSO 4 mm Receiver Channel in GRASP9

The 4 mm receiver channel was installed in parallel to a pre-existing 3 mm receiver channel on the OSO 20 m telescope. The cryostat housing both receiver channels is located near the focal point of the telescope (see Figure 3.25 (left) and Figure 3.26 (left)). The proposed optical design of the relay optics to couple the receiver horn to the telescope makes use of two off-axis ellipsoidal mirrors. Figure 3.25 (right) below shows the proposed design of the 4 mm receiver within the cryostat unit.

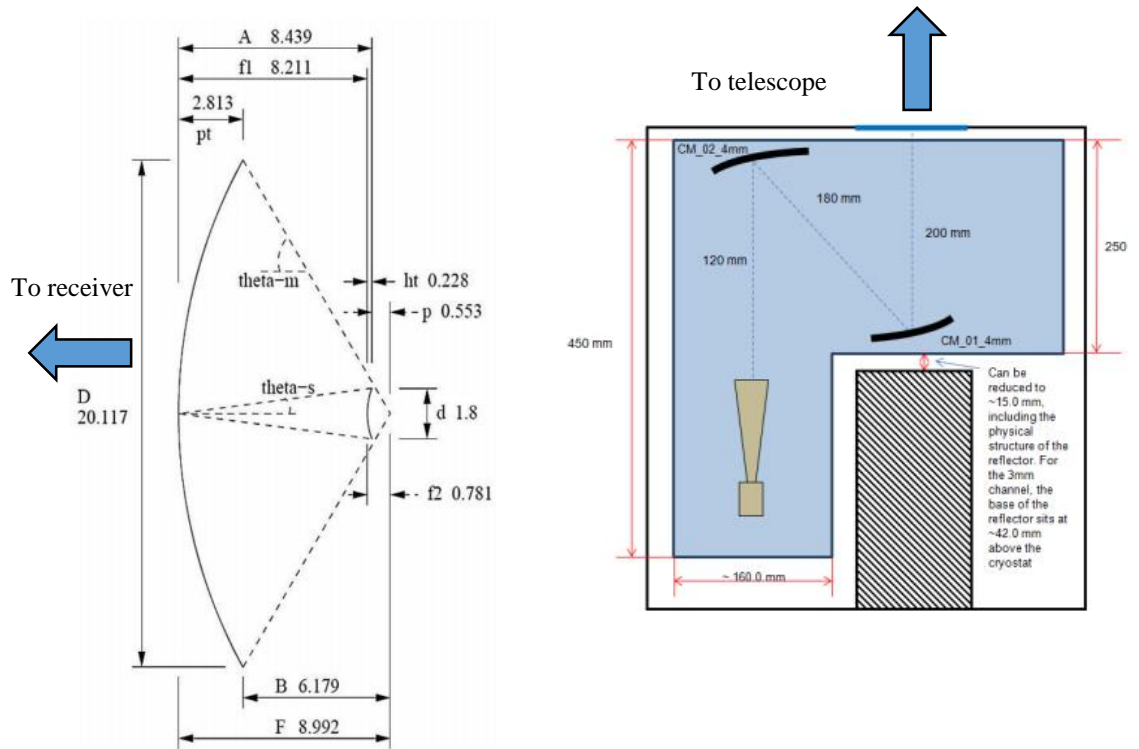


Figure 3.25: Schematic of the 20 m telescope in OSO with the dimensions given in metres (Left) (Nystrom, 2011). 4 mm receiver system within the cryostat (Right) (Walker, 2016)

In order to calculate the beam on the sky we need to propagate the horn aperture field through the receiver relay optics and the telescope. This could be done using Gaussian beam mode analysis but for accurate beams on the sky Physical Optics is more appropriate and it includes the effects of aberrations in the optics and provides accurate cross-polarisation predictions. It is also possible to calculate the aperture efficiency of the horn by doing an overlap integral of the GRASP9 beams at the telescope aperture and an incoming plane wave.

We also consider the impact of the various potential manufacturing tolerance levels for the feed horn on the predictions of the beam on the sky as discussed in the previous section. GRASP9 was used to carry out the simulations using Physical Optics modelling.

Since the aperture field at the horn is known, it was read in by GRASP9 as a tabulated planar source (as described in Section 3.3). The corrugated horn can propagate the HE_{11} mode and its orthogonal pair, however, the detector used is only sensitive to one

polarization. Thus, only the HE_{11} hybrid mode was propagated through the optical system and onto the sky.

A grid file to be read in by GRASP9 was created for the propagating mode. A Mathematica script was written to generate the grid files. The Mathematica script first reads in the scattering matrix, $[S_{21}]$, generated by the mode matching software.

The aperture field (appropriate sum of waveguide modes) is given by

$$\mathbf{e}_{ap}(r, \phi) = \sum_n [S_{21}](n, 1) \mathbf{e}_n(r, \phi), \quad (3.17)$$

which was then written in terms of Cartesian co-ordinates as

$$e_{nl}(r, \phi) \rightarrow e_{nl}\left(\sqrt{x^2 + y^2}, \tan^{-1}\left(\frac{y}{x}\right)\right), \quad (3.18)$$

taking care to ensure the software computing this transformation accounts for which quadrant the point (x,y) is in.

The radius at the aperture of the corrugated horn was 15 mm. As the grid to be read in by GRASP9 needs to be square or rectangular, and the horn aperture is circular, a mask was required to zero pad the region outside the aperture but inside the square.

The resulting patterns were specified in a file containing appropriate GRASP9 header data including the dimensions of the grid and the sampling interval of the fields, as well as the frequency and co-ordinate system being used. The source file had to be referenced to a co-ordinate system within GRASP9, where the source itself was located within the xy -plane and the horn aperture was located at the origin of the co-ordinate system. The input generated for the HE_{11} hybrid mode by the mode matching software was in the form of the E-field. The accuracy to which the field should be measured on the surface of interest was automatically specified in GRASP9 and was determined by the PO sampling.

The mirrors were specified as Physical Optics objects. The ‘Get Currents’ command triggered the computation of PO currents on the first ellipsoidal mirror from the illuminating source. These currents were then used as the source for calculating the currents on the second ellipsoidal mirror, which were in turn used as the source when calculating the currents on the hyperbolic secondary mirror of the 20 m telescope and finally the calculated currents on the secondary mirror were used as the source to calculate

the currents on the parabolic primary mirror. The ‘Get Field’ command was used to compute the fields from the given source at the points specified in the relevant ‘Field Storage’ object. Figure 3.26 shows the 4 mm receiver coupled to the 20 m telescope.

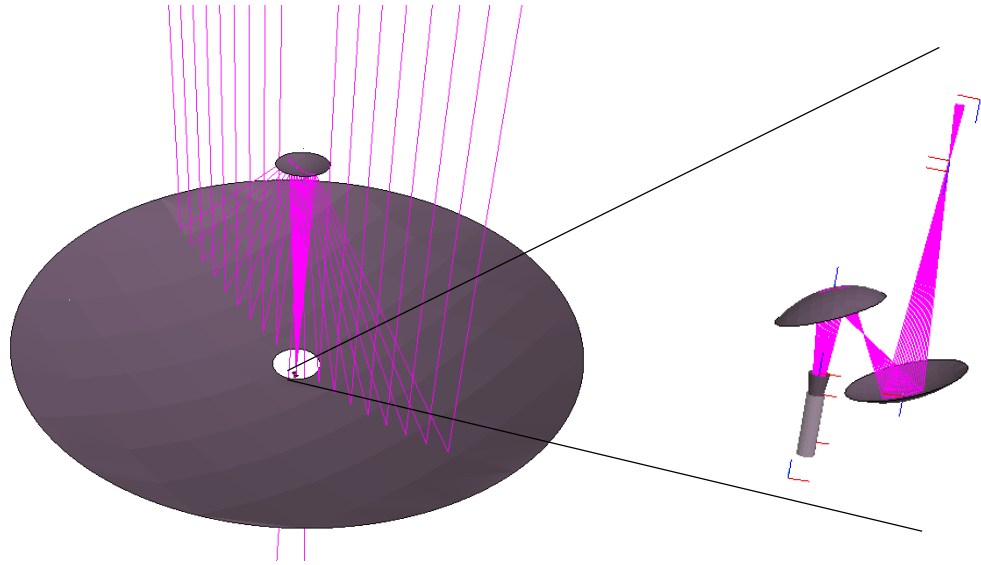


Figure 3.26: Primary and secondary mirrors of the OSO coupled to the 4 mm receiver (Left) and the 4 mm receiver channel (Right) in GRASP9

Figure 3.27 to Figure 3.30 show both the contours and azimuthal cuts of the co-polar and cross-polar beams on the sky at 67 GHz, 75 GHz and 86 GHz. The beam pattern at the aperture from the mode matching software (CylindricalSCATTER) was read in by GRASP9 as a tabulated planar source both for the original horn and the geometry of the horn with a tolerance error of $\pm 100 \mu\text{m}$ applied (the level which has a maximum effect on the horn beam). The contour beams of the co-polar pattern were normalized to 0 dB on-axis.

*Chapter 3:
Quasi-Optical Propagation and the Design of a 4mm Receiver for the Onsala Space
Observatory*

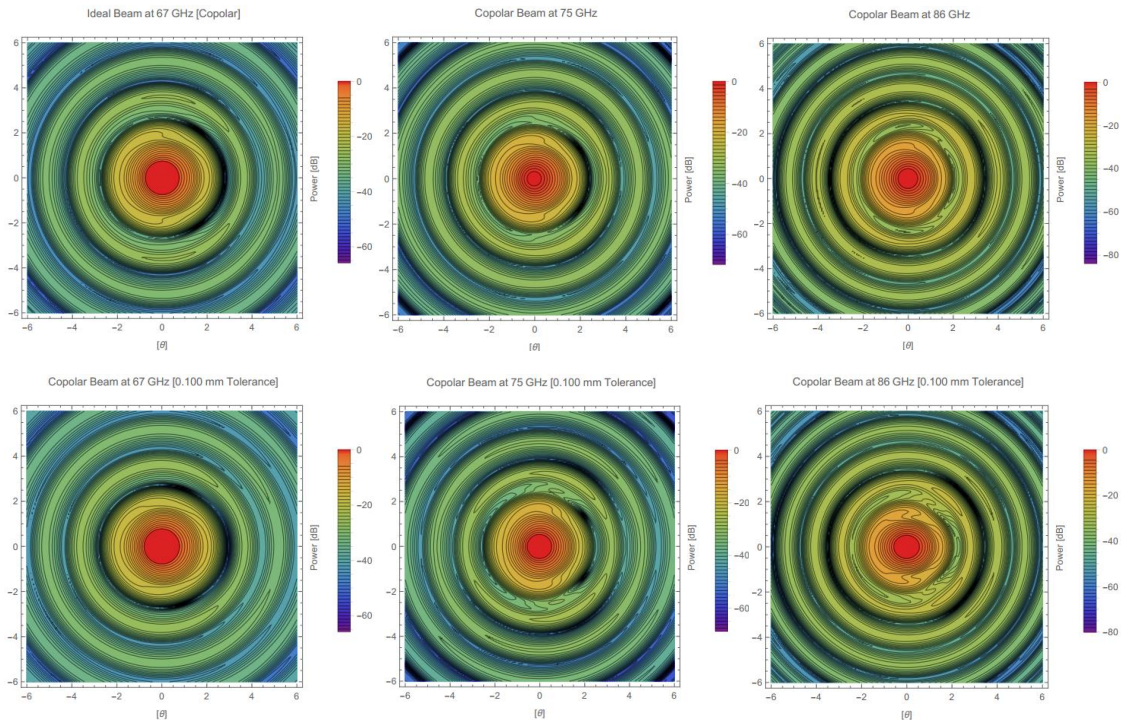


Figure 3.27: Co-polar beam on the sky at 67 GHz (left), 75 GHz (middle) and 86 GHz (right) for the case for the ideal case (top) and tolerance of $\pm 100 \mu\text{m}$ (bottom)

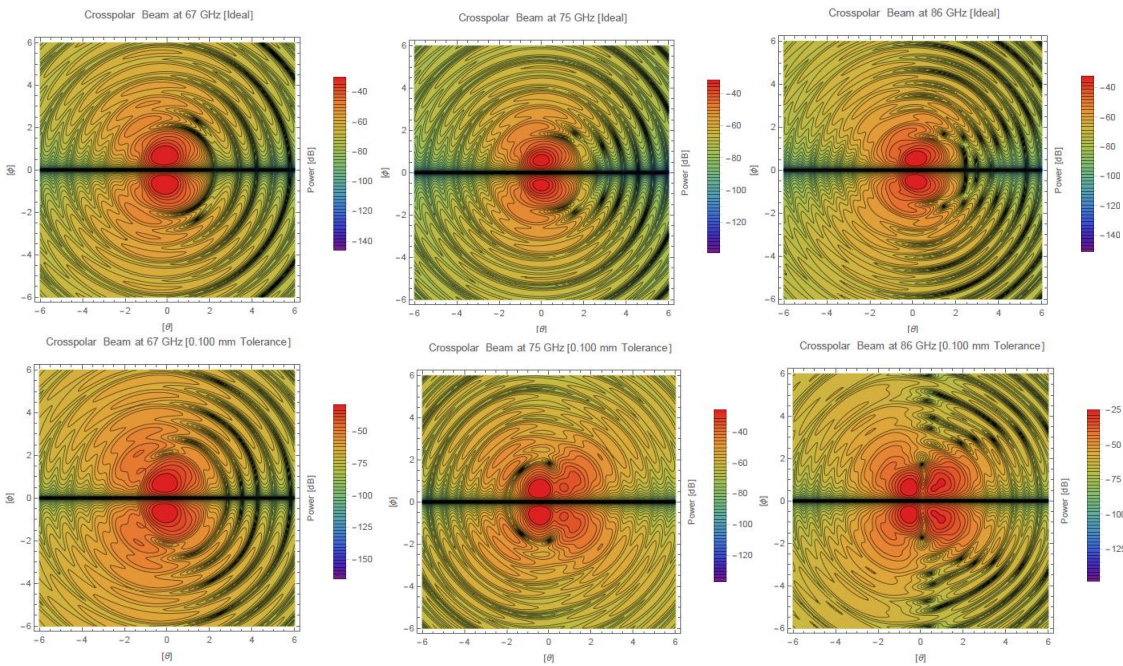


Figure 3.28: Cross-polar beam on the sky at 67 GHz (left), 75 GHz (middle) and 86 GHz (right) for the case for the ideal case (top) and tolerance of $\pm 100 \mu\text{m}$ (bottom)

Chapter 3:
Quasi-Optical Propagation and the Design of a 4mm Receiver for the Onsala Space Observatory

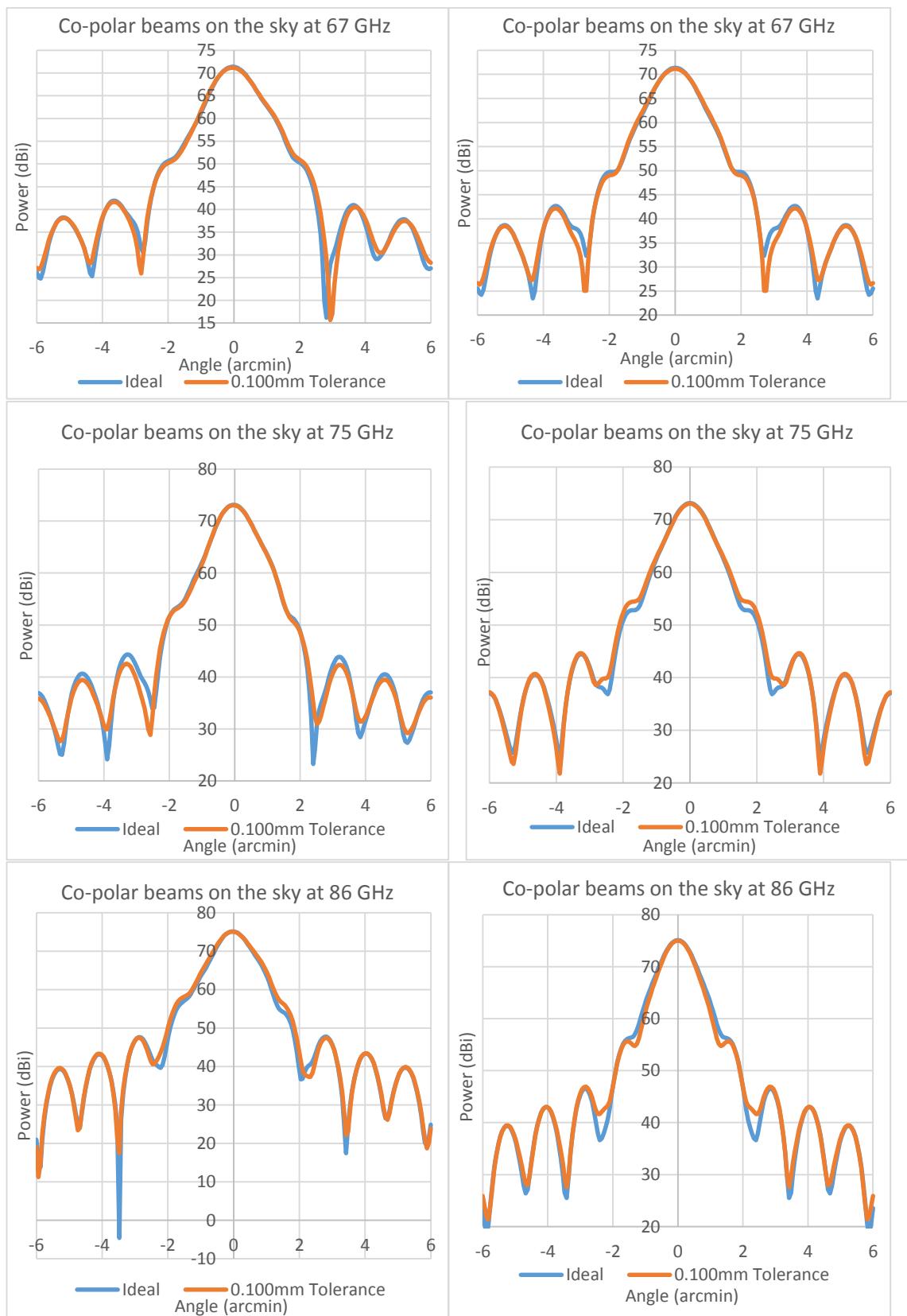


Figure 3.29: Cuts of co-polar beam on the sky at 67 GHz (top), 75 GHz (middle) and 86 GHz (bottom) for the ideal case and the case with a tolerance of $\pm 100 \mu\text{m}$. Cuts were taken along the H-plane (right) and along the E-plane (left) of both beams

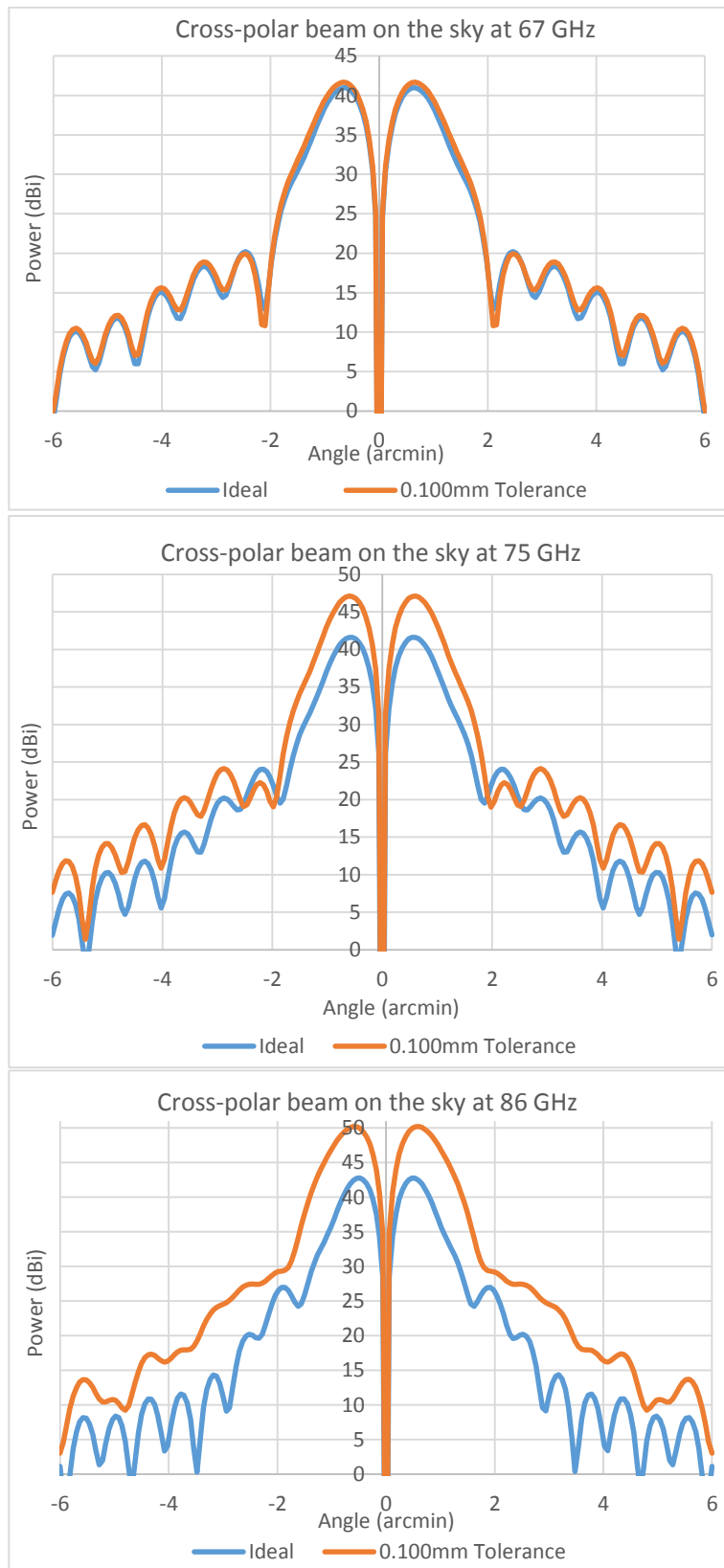


Figure 3.30: Cuts of cross-polar beam on the sky at 67 GHz (top), 75 GHz (middle) and 86 GHz (bottom) for the ideal case and the case with a tolerance of $\pm 100 \mu\text{m}$. Cuts were taken along the H-plane of both beams

As is seen in Figure 3.27 to Figure 3.30, the effects of the tolerance value of 100 μm are minimal. The cuts of the co-polar beam along both the E-plane and the H-plane show no change in terms of power levels and symmetry. Change was observed in the cross-polar pattern, particularly at 75 GHz and 86 GHz, both in terms of the shape of the beam and peak power levels. Taking a cut vertical through the beam where the cross-polar levels are a maximum and capturing the peak value, an increase of approximately 6 dB at 75 GHz and approximately 8 dB at 86 GHz is seen between the nominal and tolerance case. These effects are at effectively a negligible level. Other effects may be dominant, such as misalignments in the telescope and optical system.

3.8 Conclusion

In this chapter, we have discussed how the mode matching technique was applied for the design of a 4 mm wave receiver for the OSO 20 m millimetre-wave telescope. Three corrugated horns were considered for the design, and based on the analysis presented in Section 3.5, the conical corrugated horn with the wider aperture diameter of 30 mm was chosen for manufacture. The 4 mm receiver was installed on the 20 m OSO telescope in October 2015.

A tolerance analysis of the horn was also carried out where the radii of the sections making up the horn were altered with tolerance values ranging from $\pm 15 \mu\text{m}$ to $\pm 100 \mu\text{m}$. The co-polar and cross-polar beam patterns were investigated for the different tolerance limits. It was seen that due to the long wavelength of operation only large deviations in radii, $\pm 100 \mu\text{m}$, produce asymmetries in the co-polar beam pattern, while the effect on the cross-polarisation can be noticed even at lower tolerance values.

The beam was propagated through the 4 mm receiver and through the optics of the 20 m telescope and onto the sky using GRASP9. Far-field beam patterns were produced at some spot frequencies across the band. The beam on the sky was also investigated with tolerance values applied to the radii of the horn sections. It was observed that even with a significant tolerance value of $\pm 100 \mu\text{m}$, the co-polar beam on the sky was mostly unaffected while the cross-polar beam was affected, particularly at the higher frequency, with an increase in peak power levels

4 Modelling of Cavity Coupled Bolometers using Mode Matching Techniques

4.1 Introduction

Superconducting imaging arrays will form the basis of large format focal plane detectors for the next generation of space born missions building on the heritage of Planck and Herschel. In the next-generation mission, whether a millimetre-wave system focussed on the CMB (90-150 GHz) or one on the Far-IR part of the spectrum (1-10 THz), waveguide coupled bolometer devices can be used to achieve the sensitivity levels required. Thus placing, for example, a hyper sensitive transition edge sensor and its superconducting absorber layer within a waveguide cavity can maximise the optical efficiency of the device, ensuring the efficient detection of inherently weak astronomical signals. Although much development research has taken place in the recent past to enhance the technical readiness levels of these detectors, much more rigorous analysis techniques still need to be developed and verified through precise experimental measurements. As the waveguide structures are very large in terms of the wavelength of operation and are inherently multimode, and thus only partially coherent, there exist many challenges to model such structures accurately and in a computationally efficient manner.

If the waveguide feeding a horn antenna is oversized then potentially higher order waveguide modes as well as the fundamental mode are capable of coupling signal power to the detector. If that detector is a cavity coupled bolometer then these higher order modes essentially ensure increased throughput compared to single mode feeds (Murphy et. al. (2010)). A significant advantage of multimode horns over other types of horn antennas (such as planar antennas) is that they provide good control of the sidelobe characteristics of the beam pattern (as is the case for single mode feed horns). The feed patterns of systems with standard cross sections can in theory be modelled using efficient mode matching scattering matrix approaches. A disadvantage, of course, in imaging applications on telescopes is that there is necessarily reduced spatial resolution (assuming the multimode horn throughput is matched to the optics coupled to it). This is because the

throughput, given by $A\Omega = n \lambda^2$ where n is the number of modes present, is higher than for the single mode case, leading to larger beams on the sky.

Clearly, the efficiency with which the individual modes couple to the bolometer in the cavity will influence the overall beam pattern shape, as well as the aperture efficiency of the horn. In many cases it may be a reasonable approximation to assume that the cavity mounted bolometer acts as a perfect black body absorber (Murphy *et. al.*, (2001); Murphy *et. al.*, (2010)). Thus, for the purposes of modelling the system to obtain the horn beam patterns, we can apply reciprocity and assume that all modes are equally excited in the waveguide that directly feeds the bolometer cavity. Clearly, this is an approximation, particularly because of any impedance mismatches the modes may suffer at the entrance to the cavity (*i.e.* if there is a sudden step in the diameter of the structure), and furthermore the individual modes in the cavity may not perfectly couple to the bolometer/absorber. Thus, in certain cases the perfect blackbody assumption about feeding the radiating horn-waveguide structure could become a poor one, thus a more thorough approach to modelling the system is clearly required. Such horn-waveguide-cavity configurations could be modelled using finite element methods. However, multimode structures by their nature are electrically large, and therefore any simulations will be computationally intensive. On the other hand, one expects that a modal approach by its nature (*i.e.* using solutions to the propagating electromagnetic fields based on the symmetries of the system) should be much more efficient.

This chapter will focus on the work we have undertaken to investigate cavity effects on the signal coupling to the bolometer for particular examples where a finite element analysis would have been very difficult. In this case the radiation pattern of multi-mode horns can be most efficiently simulated using mode matching, typically with smooth walled waveguide modes as the basis and computing an overall scattering matrix for the horn-waveguide-cavity system.

One improvement to the accuracy of such mode matching simulations over the ideal black body radiator is to model the bolometer as a thin current sheet of finite surface resistance, in which lossy currents are induced by the fields at its surface (Murphy *et. al.*, (2012); Doherty (2012); Bracken (2015)). Then, any real power that is not reflected back into propagating modes in the horn plus waveguide feeding the cavity must have been converted into Joule heating of the effective power absorbing sheet. Thus, the beam

pattern of the horn can be determined from the strength of the coupling of the incident radiation from a point in the sky with those modes that are efficiently coupled to the absorbing cavity. Note that in this case we have not applied reciprocity, and instead treat the horn aperture as the input port to the full system. This approach however assumes no other loss of power, such as due to any gaps in the effective perfectly conducting walls of the feed system of the cavity. Such gaps could be present for the insertion of filters, for example as in Planck-HFI (discussed in Chapter 5), or in the case of an array system where a gap is necessary to prevent shorting of the detectors which are fabricated on a chip that necessarily straddles several detector elements. In such cases the power reflected at the horn aperture will be reduced because of extra losses due to radiation escaping through the gaps. Furthermore, because of reflections within the system we cannot easily disentangle the power absorbed in the cavity from such power losses through any gaps. In fact, it is better to invoke reciprocity as before, treating the cavity as an imperfect black body radiator as in that way we can more easily include the effects of any losses due to gaps in the waveguide structure. In this regard, we describe an approach based on the natural eigenfields of the absorbing cavity and some simple thermodynamic assumptions in chapter 5 for including an imperfect cavity in modelling the Planck HFI 545 and 857 GHz channels.

As well as predicting the horn beam pattern more precisely, it is also important to investigate the cavity configuration itself for optimizing power absorption. For example, the effects of offsetting the axis of a cylindrically symmetric absorbing cavity from that of a circular waveguide feeding it were investigated. This configuration might be expected to trap more power within the cavity which could then couple to the absorber/bolometer. Offsetting the cavity results in extra possibilities for power scattering between modes of different azimuthal orders, as well as also between the degenerate orthogonal pairs of modes (with the same radial field distributions) of a given azimuthal order. This has been implemented in the GAMMA code resulting in significantly larger scattering matrices over pure symmetric systems, including the requirement for a large number of numerical integrations. Efficient code written in Python was therefore developed to ensure workable computational times for typical overmoded waveguide-cavity systems. The code was verified using CST for electrically compact systems but is applicable to large multimode systems too, clearly.

Another contributing factor to power absorption might be the shape of the absorber itself. The mode matching software was extended to be able to model an absorber of arbitrary shape (for example a square absorber in a cylindrical cavity). Changing the shape of the absorber also results in more possibilities of power scattering between modes of different azimuthal orders. If the absorber itself is not symmetric, scattering between the degenerate orthogonal pairs of modes will also be observed. This configuration will also result in the requirement of a large number of integrations and significantly larger scattering matrices. The expectation is, however, that such absorbers will absorb more incident power because of mode scattering of higher order modes trapped in the absorber cavity.

4.2 Modelling of Absorbing Cavities

Mode matching code developed in Python was used to model a simple cavity consisting of a waveguide structure with one end sealed by a perfect electrical conducting (PEC) end wall. GAMMA code cannot deal with such a wall but we can still model an equivalently perfectly reflecting wall by stepping from the cavity guide down to a very narrow waveguide at the end wall. This makes use of the fact that at a given frequency, each waveguide mode has a critical value for the radius of a waveguide section, so that if the radius falls below this value the mode will no longer be supported and thus will not propagate. The radius for this section was selected to be well below than the value required for the fundamental TE_{11} mode and the waveguide thus acts like a (PEC) short circuit. To this end the radius was chosen to be of the order of 0.0001 mm and the length was chosen to be of order of a few λ . Since only evanescent modes can exist in this narrow waveguide at this wavelength and they decay over short distances, this effectively closes the cavity.

First consider the empty cavity shown in Figure 4.1. We define the input side on the cavity aperture port 1, and the 'pinched' (narrow) waveguide section port 2 the following is therefore observed: when the software is run as expected, since no modes are supported in the 'pinched' waveguide section, none of the incident power can propagate to port 1 or be reflected within the system and returned to port 2. Similarly, no modes can propagate to port 2 from port 1 with $[S_{12}]$, $[S_{22}]$ and $[S_{21}]$ being all zero matrices. Thus, by conservation of power, all of the power entering the cavity at port 1 that is not absorbed

by the bolometer, must be reflected back at port 1. This power can be extracted from the $[S_{11}]$ matrix for the cavity-waveguide system as a whole. Assuming that the cavity was made from a PEC material, the four matrices governing the behaviour of the cavity provide a valid model in terms of expected cavity behaviour. Figure 4.1 below illustrates an example case of an empty cavity with radius b .

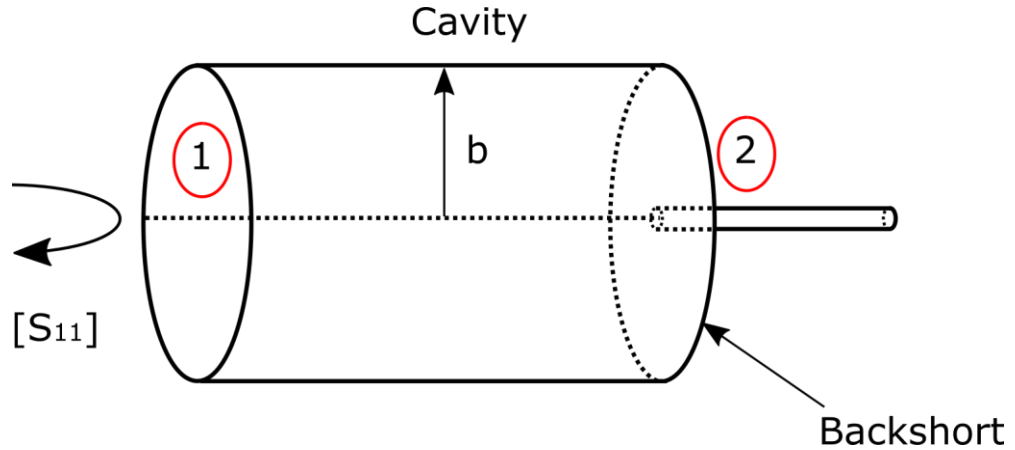


Figure 4.1: Empty cavity configuration

Consider a simple test case, consisting of a cavity of length 6 mm and radius 1.3 mm. We examine the reflected power of this configuration over a frequency range of 65 – 110 GHz. The fundamental TE_{11} mode begins propagating at 68 GHz and the second mode to cut on, the TM_{01} , begins propagating at 88 GHz. The result of this analysis can be seen in Figure 4.2 below.

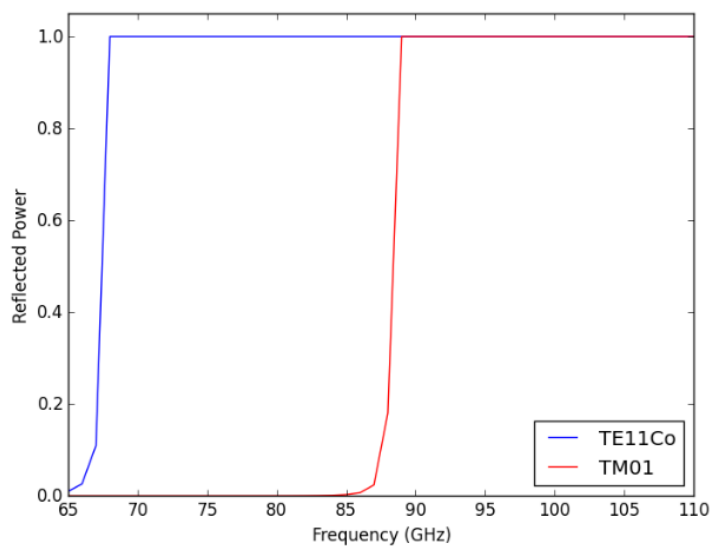


Figure 4.2: Reflected power of the TE_{11} and TM_{01} modes in an empty cavity

It can be seen that all of the power entering the empty cavity at port 1 is reflected back to port 1, once the modes are able to propagate.

When modelling an empty cavity, little modification was needed as it was just the geometry file that needed to be changed. However, in order to include an absorber in the existing GAMMA code, the software clearly had to be modified so that it could handle absorbers like the Scatter code. In fact, we assume the absorber can be approximated by a resistive sheet where it is assumed its surface resistance results in Joule heating, in the presence of an incident electromagnetic field, and thus power from the signal is absorbed. Such resistive sheets may be used to simulate bolometric detectors which contain an absorbing layer and are placed within optical systems used in Far-IR and Terahertz instrumentation, such as a typical TES detector for example. Since an absorbing cavity is generally closed at one end (backshort), radiation that was not absorbed when initially incident upon the detector, may be reflected from the back wall (backshort) of the cavity and absorbed by the detector on subsequent multiple passes. Since complex power is conserved, any radiation not eventually absorbed by the detector will be reflected back out to the entrance port of the cavity (feed waveguide).

A summary of the theory involved in modelling absorbing resistive sheets in waveguides was given in Sections 2.4 and 2.5. The author was involved in the implementation of the theory into a Generalised Absorber Mode Matching Analysis (GAMMA) software written in Python, but not in the development of the theory (Murphy *et. al.*, 2012). A verification analysis was carried out by using the GAMMA software, and some of the more interesting examples will be presented in the following sections of this chapter. CST was used for the verification of any code developed in Python. In fact, some pre-existing issues with in-house Mathematica code were solved during the implementation of the GAMMA software in Python.

The boundary conditions outlined in section 2.4 allow for the derivation of the required scattering matrices for the case when the absorber is partially (or completely) filling the surrounding waveguide or cavity cross-section. The power carried by the modes making up the propagating fields may be either reflected or transmitted at the two surfaces of an absorber (port 1 and port 2), thus giving rise to the usual four scattering matrices: (i) $[S_{11}]$, representing power from port 1 reflected back at port 1, (ii) $[S_{12}]$ representing power transmitted from port 2 to port 1, (iii) $[S_{21}]$ representing power transmitted from port 1 to port 2, and (iv) $[S_{22}]$ representing power from port 2 reflected back at port 2. These

scattering matrices for an absorber (resistive sheet) in a waveguide are given by Equations (2.74) and (2.75).

T is a matrix of coupling integrals of the form given by Equation (4.1) over the absorber surface. These matrices can then be cascaded with the scattering matrices for the rest of the structure in the usual manner for waveguides. An important matrix for the calculation is a matrix of electric field coupling integrals of the form:

$$T_{ij} = \int_{S_A} \vec{e}_i \cdot \vec{e}_j^* \cdot dS = \int_{S_A} \vec{e}_{i,r} \vec{e}_{j,r} + \vec{e}_{i,\phi} \vec{e}_{j,\phi} \cdot dS = \int_{S_A} \vec{e}_i \cdot \vec{e}_j \cdot dS \quad (4.1)$$

where T_{ij} are the coupling terms and e_i and e_j are the electric fields on both sides of the absorber.

4.3 Software Verification

In this section, the implementation and verification of the mode matching modelling approaches in GAMMA will be discussed. The results from the FEM approach (CST) will be used to verify the mode matching code. Three specific examples will be discussed, all of which include a concentric disk shaped absorber, so that the $[P]$ and $[T]$ matrices are calculated analytically as discussed in section 2.3. In the first example the cavity is few-moded and the radius of the absorber equals the cavity radius, in the second example the cavity is also few-moded but this time the absorber is only partially filling the cavity. In the third and final example we implement a waveguide feeding an absorber cavity, where the waveguide is highly overmoded and the absorber is partially filling the cavity. Here, we discuss the number of modes needed to accurately model the system when the diameter of the absorber changes from fully filling to partially filling the cavity housing it.

Absorber fully filling cavity

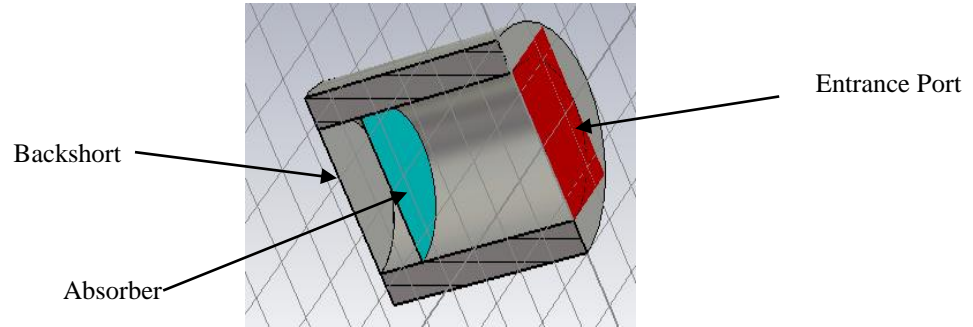


Figure 4.3: Absorber fully filling cavity

For the first example, a simple system consisting of a multimode waveguide with one end closed containing an absorber filling the guide (as in Figure 4.3) was investigated. The results of the GAMMA software were then compared with CST to verify the code implementation. In this case the absorber was filling the cavity structure ($R_{bolometer} = R_{cavity}$) and the investigated frequency range was 100 - 200 GHz, a wide band to investigate the effects of higher order modes. The length and radius of the cavity are 4.0 mm and 1.5 mm, respectively. λ_0 at the centre of the band (150 GHz) is 2.0 mm. The absorber was placed a distance of $\lambda_0/4$ mm from the cavity backshort (where λ_0 corresponds to the free-space wavelength at the centre of the band). The reflected power given by GAMMA and CST can be seen in Figure 4.4 (a) to (e) for the propagating modes in the cavity.

There is essentially perfect agreement between GAMMA and CST for the power absorbed for the incident waveguide excited with TE_{11} , TE_{01} , TE_{21} , TM_{01} and TM_{11} modes (see Figure 4.4 (a) to (e)). Depending on the system feeding the cavity, it was noted that for the case of the absorber fully filling the cavity structure, a small number of modes used in GAMMA gives good agreement with CST. This is due to the fact that there is no scattering between cross terms in the scattering matrix (for example, TE_{12} does not scatter into TE_{11} , etc.), *i.e.* the various matrices are diagonal.

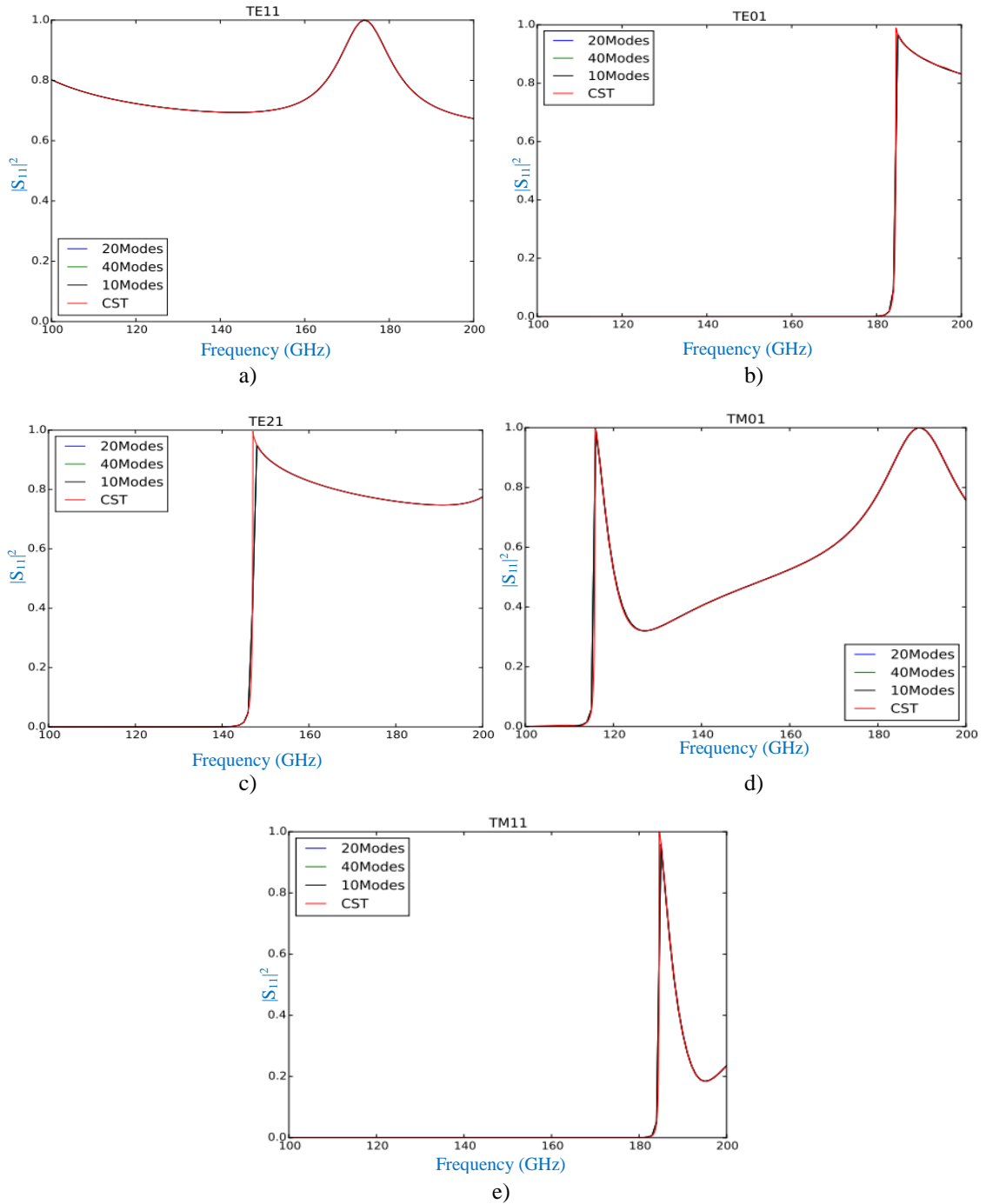


Figure 4.4: Comparison of reflected power between GAMMA and CST for a cavity coupled bolometer for different modes at input to waveguide

The reflected power can be extracted from the $[S_{11}]$ matrix ($|S_{11}|_{ij}$) where j represents the input mode and i represents the output mode (*i.e.* the mode travelling backwards toward the input port from the waveguide). Thus the total reflected power for mode j at the input is given by

$$W_{reflected}(j) = \sum_i |[S_{11}]_{ij}|^2 Q_{ii}, \quad (4.2)$$

where Q_{ii} (element of the self-coupling matrix) gives the power carried by the i^{th} propagating mode. If we are interested in the power absorbed, then this power must be real (Joule heating loss). In this case we need to extract the real part of the $W_{reflected}$. Thus the power absorbed is given by Equation (4.3), provided there is no other loss in the system.

$$W_{absorbed} = \text{Re}[W_{incident} - W_{reflected}] \quad (4.3)$$

The absorbed power for the j^{th} mode is then given by

$$W_{absorbed} = \text{Re} \left\{ \left[1 - \sum_i |[S_{11}]_{ij}|^2 \right] Q_{ii} \right\}, \quad (4.4)$$

where Q_{ii} is 1 for real modes and pure imaginary for evanescent modes (modes which are below cutoff).

Thus, it needs to be noted that if $[S_{11}]_{ij} = 0$ (as is partially present in Figure 4.4 (b) to (e)) below the cutoff frequency of the input mode, it does not necessarily mean that $W_{absorbed} = 1$, since the reflected power is imaginary for evanescent modes meaning the Q_{ii} term in Equation (4.4) will be imaginary.

Absorber partially filling cavity

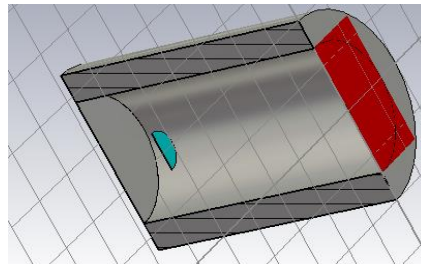


Figure 4.5: Absorber partially filling cavity

In the previous example the absorber filled the guide. We now consider the case where the absorber only partially fills the guide. Again, the example consists of a multimode waveguide with one end closed containing an absorber (as in Figure 4.5) and the results of the GAMMA analysis were compared with CST to verify the code implementation.

For this case the absorber radius was half that of the waveguide ($R_{bolometer} = 0.5 \times R_{cavity}$). The investigated frequency range was 100 - 200 GHz, the length and radius of the cavity are 4.0 mm and 1.5 mm, respectively. λ_0 at the centre of the band is 2.0 mm. The absorber was placed a distance of $\lambda_0/4$ mm from the cavity backshort (where λ_0 corresponds to the free-space wavelength at the centre of the band). The reflected power produced by both CST and GAMMA can be seen in Figure 4.6 (a) to (e) for the propagating modes.

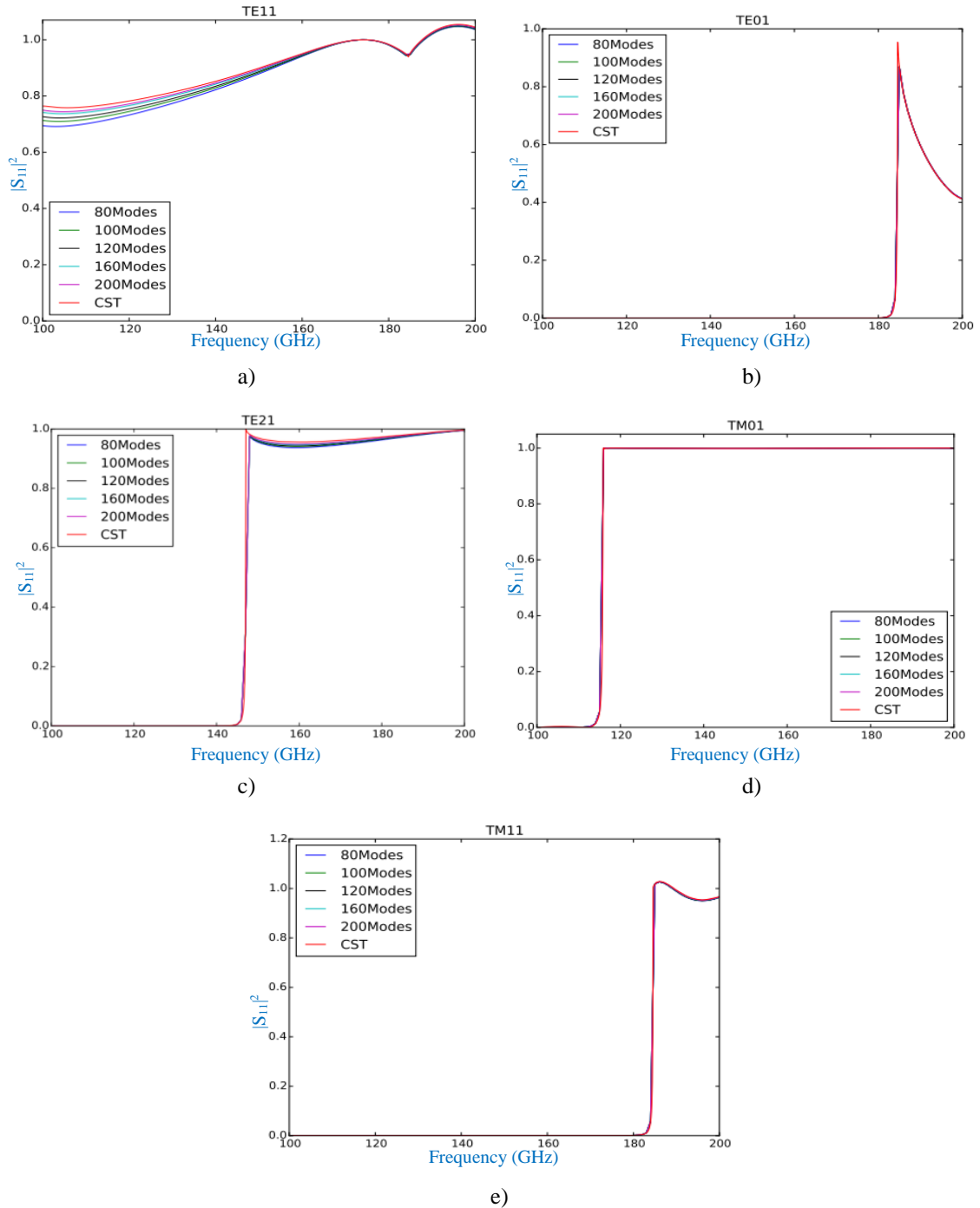


Figure 4.6: Comparison of reflected power between GAMMA and CST for a cavity coupled bolometer for different modes at input to waveguide

There is clearly good agreement between GAMMA and CST for the power absorbed for the incident waveguide excited with TE_{11} , TE_{01} , TE_{21} , TM_{01} and TM_{11} modes. The agreement becomes almost perfect when a large number of modes is considered in the analysis. This is to be expected as scattering occurs between cross terms in the scattering matrix (for example, TE_{12} does scatter into TE_{11} , etc.) and the T -matrix (see Section 2.5 or Section 4.2) contains a large number of significant off-diagonal terms.

Highly overmoded waveguide-cavity-absorber system

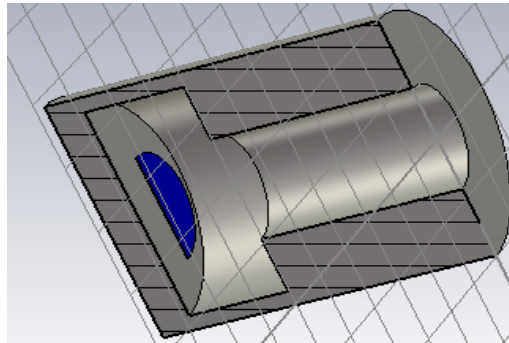


Figure 4.7: Highly overmoded waveguide feeding a cavity housing a partially filling absorber

An example of a highly overmoded cavity system was also considered, where the cavity is now fed by a multimoded waveguide with a significant change in the radius of the structure at the entrance to the cavity (as in Figure 4.7). The results of the GAMMA software were compared with CST to verify the code implementation. In this case the absorber was partially filling the cavity structure ($R_{bolometer} = 0.5 \times R_{cavity}$) and a waveguide fed the cavity, so that power is now trapped inside the structure. The investigated frequency range was 500 - 1500 GHz. The chosen frequency is higher than in the previous two examples illustrated in Figure 4.2 to Figure 4.6, although it would have also been possible to use a larger structure (rather than increasing the frequency) in order to observe multimode behaviour. The length and radius of the guide are 0.6 mm and 0.17 mm, respectively. The length and radius of the cavity are 0.3 mm and 0.35 mm respectively. λ_0 at the centre of the band is 0.3 mm. The absorber was placed a distance of $\lambda_0/4$ mm from the cavity backshort (where λ_0 corresponds to the free-space frequency at the centre of the band). The reflected power as predicted by GAMMA and CST can be seen in Figure 4.8 (a) to (g).

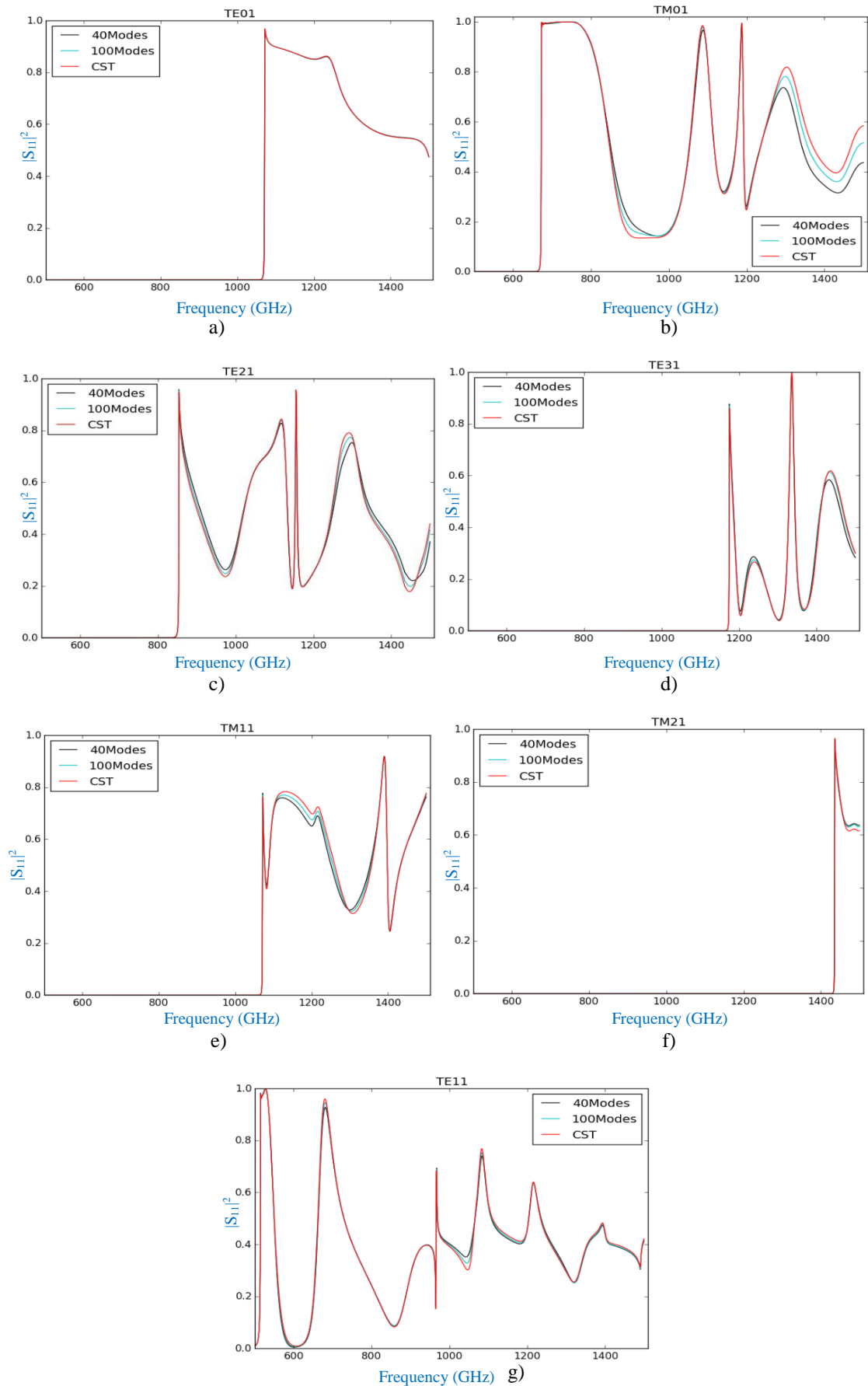


Figure 4.8: Comparison of reflected power between GAMMA and CST for a cavity coupled bolometer for different modes at input to waveguide

There is clearly excellent agreement between GAMMA and CST for the power absorbed for the incident waveguide excited with TE_{11} , TE_{01} , TE_{21} , TE_{31} , TM_{01} , TM_{11} and TM_{21} modes (see Figure 4.8 (a) to (g) and also Table 4.1). The agreement again becomes almost perfect when 100 modes per azimuthal order are included in the mode matching analysis. The time taken to carry out this analysis with GAMMA using 100 modes per azimuthal order was under 2 hours and the time taken using CST was approximately 24 hours.

	Frequency (GHz)	750	850	950	1050	1150	1250	1350	1450
TM_{01}	CST	0.999	0.470	0.135	0.467	0.323	0.586	0.587	0.426
	GAMMA	0.999	0.478	0.145	0.469	0.329	0.583	0.531	0.382
TE_{11}	CST	0.406	0.090	0.394	0.336	0.434	0.429	0.386	0.387
	GAMMA	0.404	0.090	0.392	0.307	0.428	0.433	0.380	0.383

Table 4.1: Reflected power as obtained by both GAMMA and CST at some spot frequencies across the investigated band

In a real system the waveguide might be connected to a horn antenna. In that case an input field will couple to the different modes with different amplitudes which will depend on the incident angle of the signal (to be discussed in Chapter 6).

4.4 Absorber of arbitrary shape

We now consider how GAMMA was extended to model absorbers of arbitrary shape in which case clearly the integrals T_{ij} (see section 4.2) at the absorber junction must be evaluated numerically. This is novel work which was not implemented previously in in-house software in Maynooth. It also implies that we can no longer apply the simplification that the azimuthal orders can be treated separately when calculating the scattering matrices for a cylindrically symmetric system. Nor can it be assumed that the scattering matrices are identical for the two orthogonal degenerate fields of each mode as there can be power scattered between them for asymmetrical systems. In fact, in the general case scattering is possible between any two modes, implying much larger scattering matrices are required rather than separate matrices for the different azimuthal orders.

An example is shown in Figure 4.9 below for the case of a cylindrical waveguide feeding a cylindrical cavity containing a square absorber.

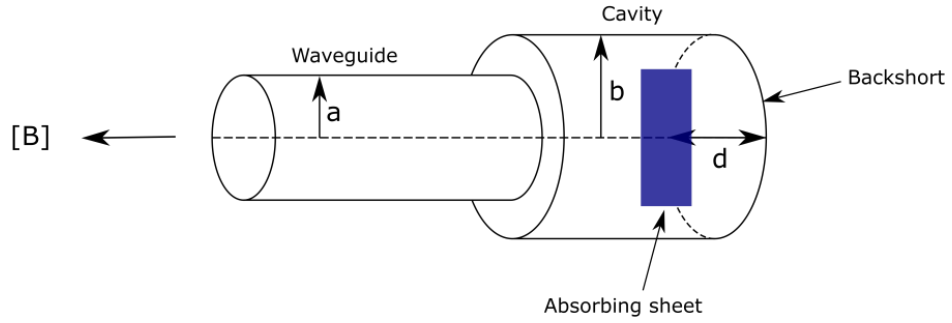


Figure 4.9: Waveguide fed sealed cylindrical cavity containing a square absorber sheet

The problem of defining the edges of a square absorber required for calculating the T_{ij} for a cylindrical waveguide or cavity structure is clearly less straightforward when using cylindrical co-ordinates as we integrate over the area of the absorber only. In order to implement this problem in GAMMA, a numerical approach was taken to define the area of the square. We define a grid of points in terms of r and ϕ where r corresponds to the radial component, limited by the boundary of the guide, and ϕ corresponds to the angular component. The r value extended from 0 (the centre of the waveguide structure) to r (the edge of the guide), the phi value extended from 0 to 2π radians. At each point on the grid a field contribution must be evaluated. The task at hand now is create a square ‘mask’ which would later be used to represent the absorber area. This was done by overlaying the mask with the circular fields. The mask was generated and populated with a constant value, a condition was then implemented, such that if a value was outside the absorber it was assigned a value of zero, if it was within the boundaries of the absorber, it was assigned a value of 1. The condition in Equation (4.5) defines the points (x,y) which lie inside a square of side length L_{Bol} , centered on the origin:

$$\left(\frac{2x}{L_{Bol}}\right)^N + \left(\frac{2y}{L_{Bol}}\right)^N = 1, \quad (4.5)$$

where L_{Bol} represents the length of the bolometric absorber edge and N is a large number (eg. 1000), depending on the number of samples in the grid.

An example of the radial grid may be seen in Figure 4.10.

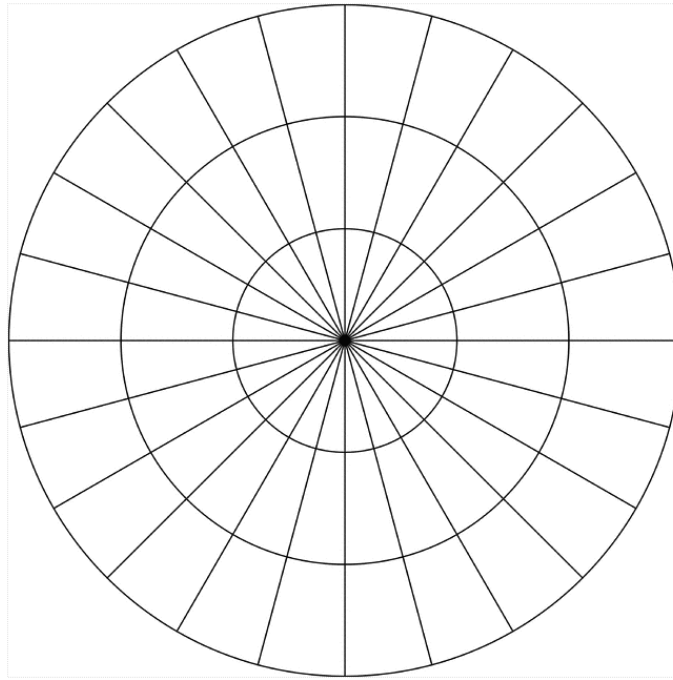


Figure 4.10: Radial grid of points

The relationship between Cartesian and Cylindrical co-ordinates on the plane of the absorber is given in Equation (4.6):

$$(x, y) \rightarrow (r \cos(\phi), r \sin(\phi)) \quad (4.6)$$

The resulting grid may be seen in Figure 4.11:

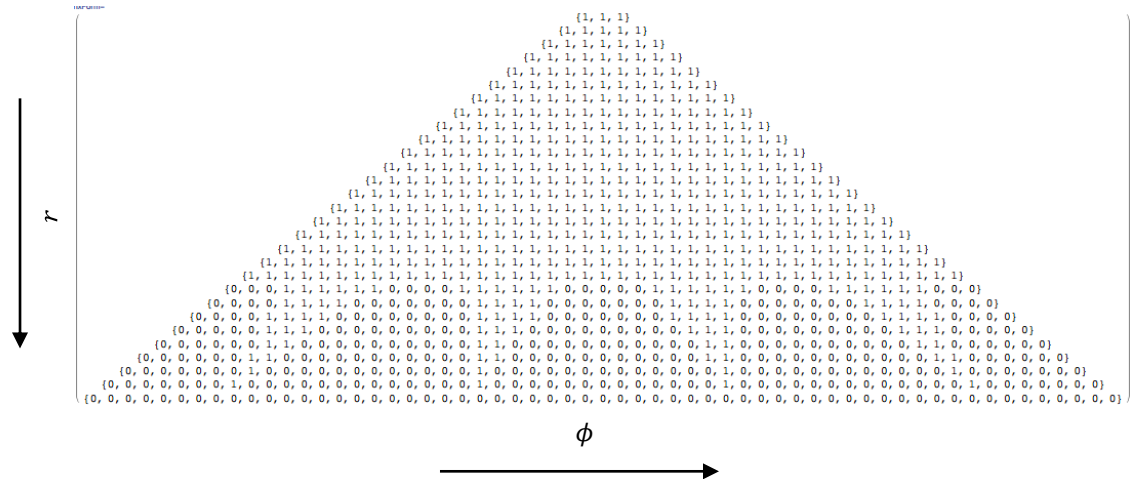


Figure 4.11: Example grid output using Cylindrical Polars

An issue that occurred in undertaking the $T_{ij} = \int e_i \cdot e_j^* dA$ for a square absorber was whether to use a Cartesian or a radial grid. Both approaches were investigated and it was found that the agreement between GAMMA (mode matching approach) and CST was

improved (for the same number of grid points) when a radial grid was used, even for absorbers which have obvious Cartesian symmetry, such as a square. This is presumably because of the modal structure, which obviously has radial/azimuthal structure in terms of the field variations.

Each row of the resulting grid ('mask') in Figure 4.11 represents an annulus where a value of 1 means that the field contribution from a mode is within the absorber boundaries and a value of 0 means that the contribution is not incident on the absorber and thus it will not be considered when calculating the T_{ij} .

Sampling in both r and ϕ needs to be chosen carefully to produce reliable results. Generally, when symmetry within a structure is broken, scattering between modes of different azimuthal orders will occur, we have to ensure that enough modes are considered, this is where the need for fine sampling in the radial direction plays an important role. For a mode where most of the power lies along the edge of the absorber (such as the TE_{21} orthogonal, TE_{31} co-polar, etc. modes for an absorber that nearly fills the guide), it is crucial to model the corners of the absorber accurately, thus if the sampling in the azimuthal direction is not accurate enough, the modes will 'miss' parts of the absorber and most likely they will be reflected back out of the cavity, producing an inaccurate result.

The process of determining the sample size is now presented. First, the maximum number of samples to be used in r was defined (Equation (4.7))

$$N_{\max} = \frac{r}{\Delta r}, \quad (4.7)$$

where r represents the radius of the structure and Δr represents the sampling in the radial direction. The upper limit on possible Δr is determined by the number of modes (radial orders) used. For example, if 30 modes were used, then Δr needs to be sufficiently small such that N_{\max} is at least 60 (similar to Nyquist sampling in Fourier transforms).

The sampling in the ϕ direction was determined by dividing each annulus into N_i segments as shown in Equation (4.8)

$$\Delta\phi = \frac{2\pi}{N_i} \quad (4.8)$$

The number of sample points contained in each annulus needs to be proportional to the radius

$$N_i(r) = \frac{r_i}{R_{cavity}} \times N_{max}, \quad (4.9)$$

where r_i represents the radial distance the i^{th} annulus from the origin and R_{cavity} is the radius of the cavity structure. This is to ensure that the ‘area’ associated with each sample point remains approximately constant.

For perfectly symmetric systems, the $[T]$ matrix for an individual azimuthal order as defined in GAMMA has the form

$$[T] = \begin{bmatrix} T_{TE-TE} & T_{TM-TE} \\ T_{TE-TM} & T_{TM-TM} \end{bmatrix} \quad (4.10)$$

where T_{TE-TE} represents power coupling between TE modes on the LHS with TE modes on the RHS of the absorber, T_{TM-TE} represents power coupling between TM modes on the LHS with TE modes on the RHS of the absorber, *etc.* When the absorber is of arbitrary shape (such as a square absorber in a cylindrical cavity), the system is no longer symmetric and scattering is observed between modes of different azimuthal orders as well as between co-polar and orthogonal modes.

An example of the form the $[T]$ matrix might take on when the absorber is of arbitrary is given in Equation (4.11):

$$[T]_{total} = \begin{bmatrix} T[0-0] & T[co-0] & T[orth-0] \\ T[0-co] & T[co-co] & T[orth-co] \\ T[0-orth] & T[co-orth] & T[orth-orth] \end{bmatrix} \quad (4.11)$$

So for a structure which supports 3 ($n = 0, 1, 2$) azimuthal orders the $[T]$ matrix will be much bigger as it now must include all azimuthal orders and in GAMMA it is given the typical form (for 3 azimuthal orders being considered)

$$[T]_{total} = \begin{bmatrix} [T_{00}] & [T_{10}]_{co} & [T_{20}]_{co} & [T_{10}]_{orth} & [T_{20}]_{orth} \\ [T_{01}]_{co} & [T_{11}]_{co-co} & [T_{21}]_{co-co} & [T_{11}]_{orth-co} & [T_{21}]_{orth-co} \\ [T_{02}]_{co} & [T_{12}]_{co-co} & [T_{22}]_{co-co} & [T_{12}]_{orth-co} & [T_{22}]_{orth-co} \\ [T_{01}]_{orth} & [T_{11}]_{co-orth} & [T_{21}]_{co-orth} & [T_{11}]_{orth-orth} & [T_{21}]_{orth-orth} \\ [T_{02}]_{orth} & [T_{12}]_{co-orth} & [T_{22}]_{co-orth} & [T_{12}]_{orth-orth} & [T_{22}]_{orth-orth} \end{bmatrix}, \quad (4.12)$$

where

$$[T_{12}]_{co-orth} = \begin{bmatrix} [T_{12}]_{TEco-TEortho} & [T_{12}]_{TMortho-TEco} \\ [T_{12}]_{TEco-TMortho} & [T_{12}]_{TMortho-TEco} \end{bmatrix}, \quad (4.13)$$

with

$$[T_{12}]_{TEco-TMortho} = \begin{bmatrix} T_{TE1\,1co-TM\,2\,1ortho} & T_{TE1\,2co-TM\,2\,1ortho} & T_{TE1\,3co-TM\,2\,1ortho} & \cdots \\ T_{TE1\,1co-TM\,2\,2ortho} & T_{TE1\,2co-TM\,2\,2ortho} & T_{TE1\,3co-TM\,2\,2ortho} & \cdots \\ T_{TE1\,1co-TM\,2\,3ortho} & T_{TE1\,2co-TM\,2\,3ortho} & T_{TE1\,3co-TM\,2\,3ortho} & \cdots \\ \cdots & \cdots & \cdots & \cdots \end{bmatrix}. \quad (4.14)$$

Thus, for example,

$$[T_{12}]_{co-orth} = \begin{bmatrix} [TE_{1\,1co} - TE_{2\,1ortho} & \cdots & TE_{1\,Lco} - TE_{2\,1ortho} \\ \vdots & \ddots & \vdots \\ TE_{1\,1co} - TE_{2\,Lortho} & \cdots & TE_{1\,Lco} - TE_{2\,Lortho} \\ & [TE - TM] & \\ & & [TM - TM] \end{bmatrix} \quad (4.15)$$

where the number of TE and TM modes considered in the analysis for the azimuthal orders concerned was L . The $TM - TE$, $TE - TM$ and $TM - TM$ matrix components are constructed in the same way as the $TE - TE$.

The power carried by the modes making up the propagating fields may be either reflected or transmitted at an absorber, which can be described in terms of the usual four scattering matrices (Equations (2.74) and (2.75)). For example, the overall scattering matrix $[S_{11}]$ representing power entering port 1 and being reflected back at port 1 is arranged in a similar way as the $[T]$ matrices (as follows for order n to order m):

$$[S_{11}]_{total} = \begin{bmatrix} S_{11}[0-0] & S_{11}[0-co] & S_{11}[0-orth] \\ S_{11}[co-0] & S_{11}[co-co] & S_{11}[co-orth] \\ S_{11}[orth-0] & S_{11}[orth-co] & S_{11}[orth-orth] \end{bmatrix} \quad (4.16)$$

As an example, if three azimuthal orders ($n = 0, 1, 2$) were considered, the scattering matrix has the form

$$[S_{11}]_{total} = \begin{bmatrix} S_{11}[00] & S_{11}[01]_{co} & S_{11}[02]_{co} & S_{11}[01]_{orth} & S_{11}[02]_{orth} \\ S_{11}[10]_{co} & S_{11}[11]_{co-co} & S_{11}[12]_{co-co} & S_{11}[11]_{orth-co} & S_{11}[12]_{orth-co} \\ S_{11}[20]_{co} & S_{11}[21]_{co-co} & S_{11}[22]_{co-co} & S_{11}[21]_{orth-co} & S_{11}[22]_{orth-co} \\ S_{11}[10]_{orth} & S_{11}[11]_{co-orth} & S_{11}[12]_{co-orth} & S_{11}[11]_{orth-orth} & S_{11}[12]_{orth-orth} \\ S_{11}[20]_{orth} & S_{11}[21]_{co-orth} & S_{11}[22]_{co-orth} & S_{11}[21]_{orth-orth} & S_{11}[22]_{orth-orth} \end{bmatrix}, \quad (4.17)$$

where each matrix entry is divided into four quadrants representing coupling from TE to TE and TM modes and from TM to TM and TE modes.

$$[S_{11}][12]_{co-co} = \begin{bmatrix} TE_{11co} - TE_{21co} & \cdots & TE_{11co} - TE_{2Lco} \\ \vdots & \ddots & \vdots \\ TE_{1Lco} - TE_{21co} & \cdots & TE_{1Lco} - TE_{2Lco} \\ & [TM - TE] & [TM - TM] \end{bmatrix}, \quad (4.18)$$

where the number of TE and TM modes are considered in the scattering was L . The $[S_{21}]$, $[S_{12}]$ and $[S_{22}]$ scattering matrices take on the same form.

For analysis of the performance of cavity structures only the $[S_{11}]$ is of interest. However, the individual elements making up the system may each have an associated non-zero set of $[S_{21}]$, $[S_{12}]$ and $[S_{22}]$ scattering matrices, of course and will be required for cascading.

Code Verification

In order to verify the technique, a straightforward example was set up in both GAMMA and CST, where the structure consists of a continuous cylindrical waveguide of radius 1.5 mm and length of 9 mm, with a square absorber placed symmetrically in the middle of the guide. The absorber was of dimensions 2 mm x 2 mm and had a surface resistance of 188.5 Ω / Sq. The example setup is shown in Figure 4.12 below.

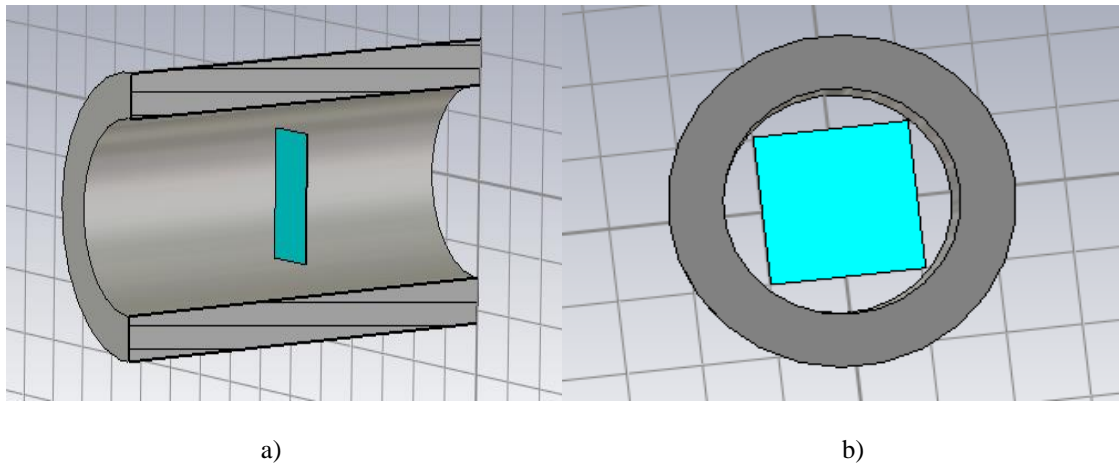
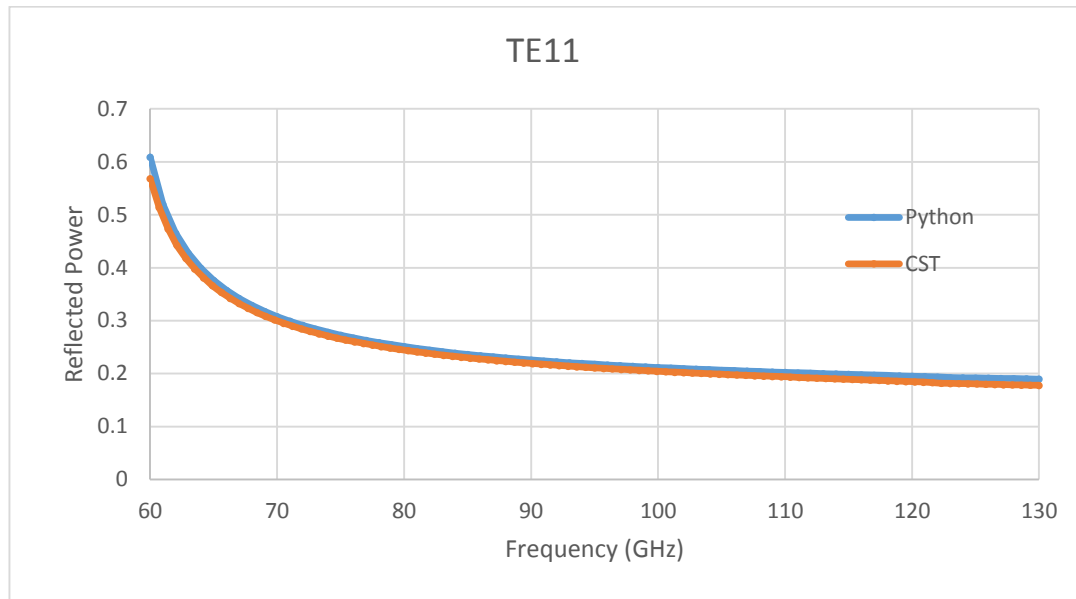


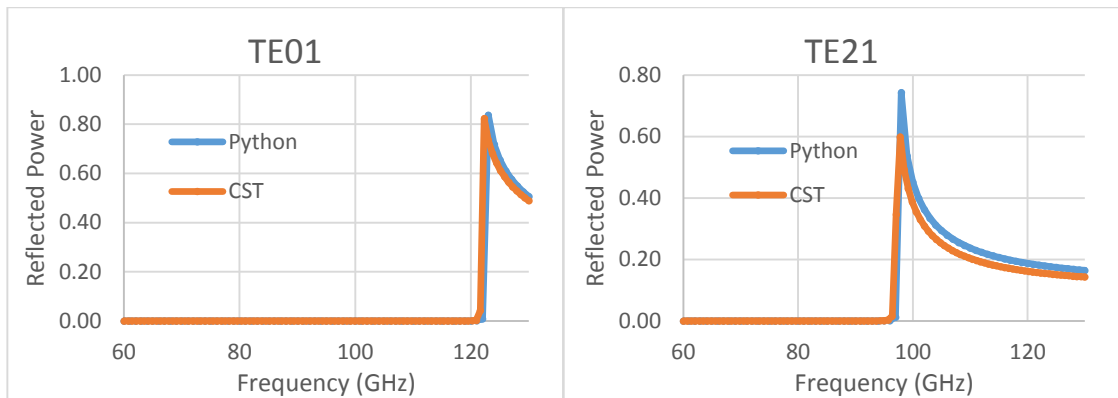
Figure 4.12: Waveguide fed sealed cylindrical cavity containing a square absorber sheet, (a) – side view, (b) front view

The frequency range investigated extends from 60 GHz to 130 GHz, with the TE_{01} , TE_{11} , TE_{21} , TM_{01} and TM_{11} modes (and their orthogonal pairs) propagating at the highest frequency. In this example, 40 modes per azimuthal order were used in GAMMA with the following sampling: $\Delta r = 0.025$ mm. To verify the GAMMA code this example was also analysed using CST. The results of the verification can be seen in Figure 4.13 and Figure 4.14. The square of the reflection matrix, $|S_{11}|^2$, obtained by both GAMMA and

CST can be seen in Figure 4.13 (a) to (e) and the square of the transmission matrix, $|S_{21}|^2$, obtained by both software techniques can be seen in Figure 4.14 (a) to (e).

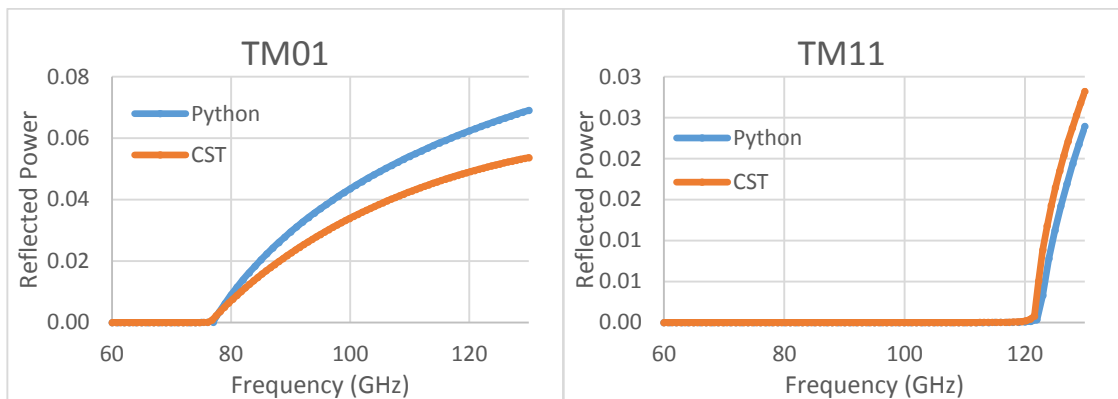


a)



b)

c)



d)

e)

Figure 4.13: $|S_{11}|^2$ for a waveguide containing a square absorber sheet

Good agreement is observed between GAMMA and CST in terms of the reflected power. A slight discrepancy can be seen in the TM_{01} mode (further discussed in Table 4.2).

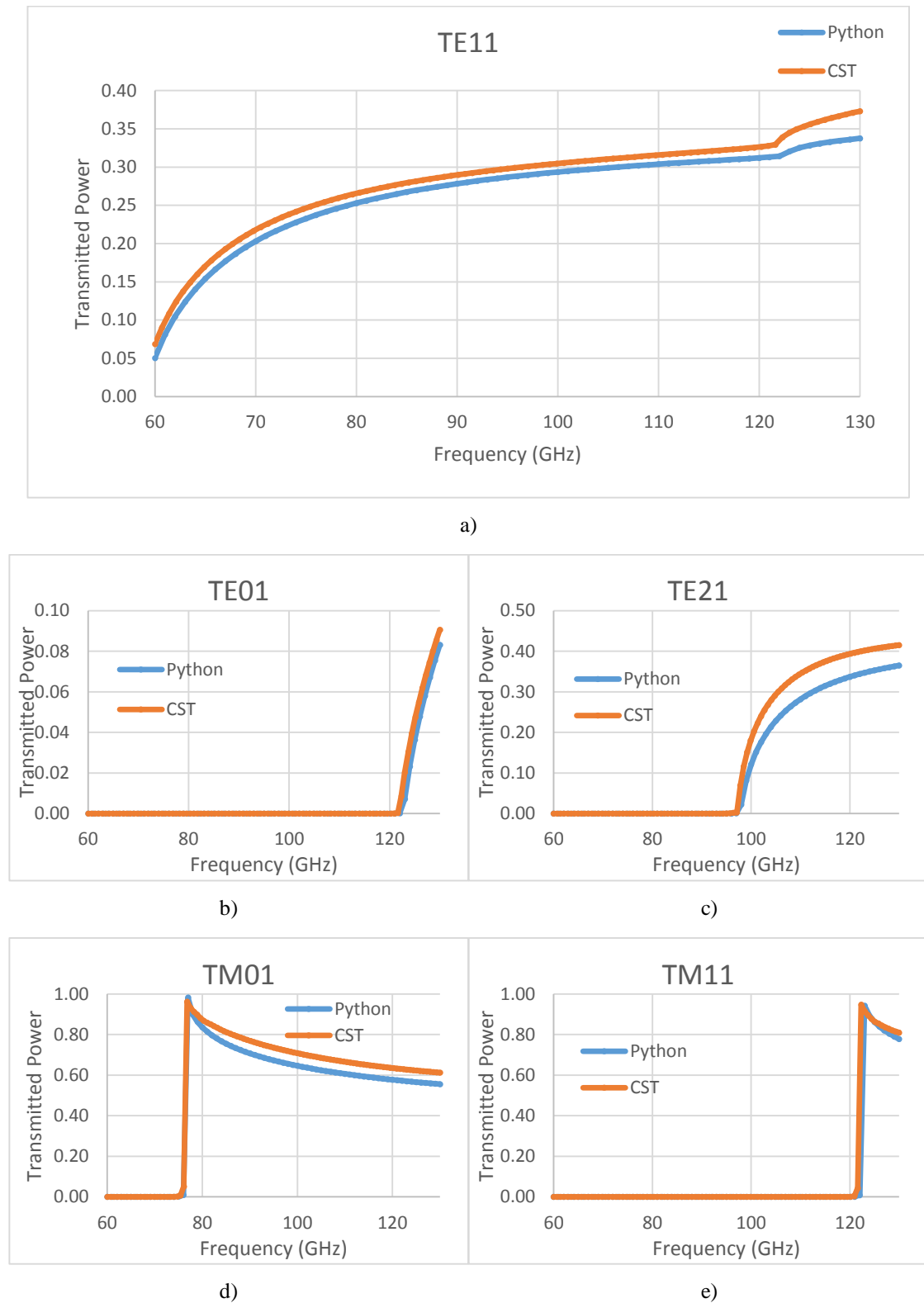


Figure 4.14: $|S_{21}|^2$ for a waveguide containing a square absorber sheet

Good agreement is also observed between GAMMA and CST in terms of the transmitted power. A relatively small discrepancy can be seen in the cases of the TM_{01} , TE_{21} and TE_{11} modes (illustrated in Table 4.2). This may be an indication that more modes need to be included in the analysis or that the sampling needs to be finer, at the moment the minimum requirement of $\Delta r = 0.025$ for 40 modes has been met. Another issue might be how GAMMA and CST treat evanescent modes, since extending the length of the feed waveguide in general results in better agreement between the two softwares. However, with the structures becoming several wavelengths long, they become difficult to model in CST.

Frequency (GHz)		60	70	80	90	100	110	120	130
TM_{01}	CST	0	0	0.007	0.023	0.034	0.042	0.049	0.054
	GAMMA	0	0	0.008	0.029	0.043	0.054	0.062	0.069
TE_{21}	CST	0	0	0	0	0.180	0.342	0.394	0.415
	GAMMA	0	0	0	0	0.121	0.282	0.337	0.365

Table 4.2: Reflections of the TM_{01} mode and transmissions of the TE_{21} mode as predicted by both GAMMA and CST at some spot frequencies across the band

Comparison of Square vs Circular Absorber

A comparison study was then carried out in GAMMA to compare the performance of a cylindrical and square absorber, where both absorbers occupy equal areas. In both cases, the frequency range extended from 60 GHz to 140 GHz. The square absorber contained an edge length of 2 mm and the circular absorber has a radius of 1.13 mm. The structure being investigated was a piece of waveguide of length 4 mm with one end closed, in both examples, the absorber was placed 1 mm from the closed end of the waveguide (3 mm from the entrance) so that it is $\lambda_0/3$ mm from the backshort (where λ_0 is the wavelength at the centre of the frequency band). The radius of the waveguide structure was chosen to be 1.5 mm in both examples. The dimensions of both configurations were created in CST for visualization and can be seen in Figure 4.15 (a) to (d).

The TE_{01} , TE_{11} , TE_{21} , TE_{31} , TM_{01} and TM_{11} modes (and their orthogonal pairs) propagate at the highest frequency. The result of this comparison can be seen in Figure 4.16 (a) to (f) where the absorbed power for the waveguide housing a square and circular absorber is displayed.

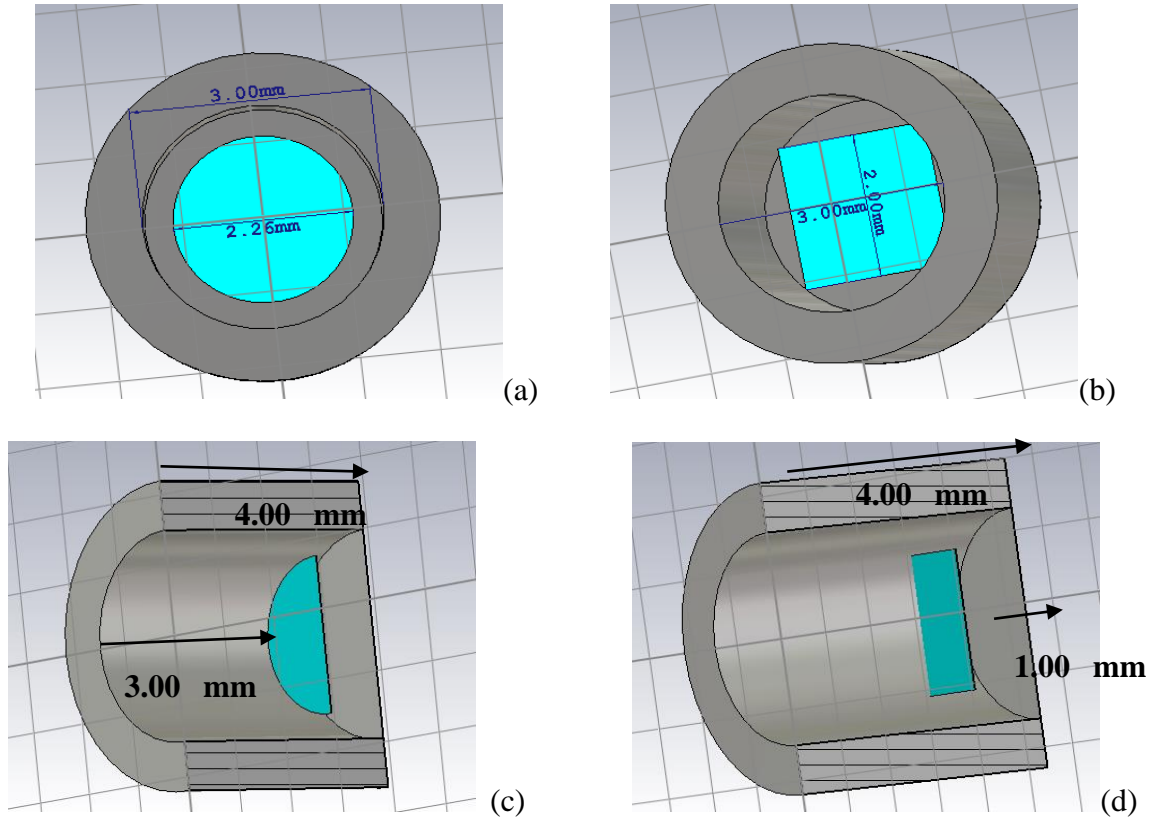


Figure 4.15: Configurations, including dimensions, used in analysis. (a) and (b) show the diameter of the waveguide used, with (a) also indicating the diameter of the absorber and (b) indicating the length of the absorber edge. The side-view is shown in (c) and (d), where in both cases the length of the guide is 4.00 mm and both absorbers are placed 1.00 mm from the back wall

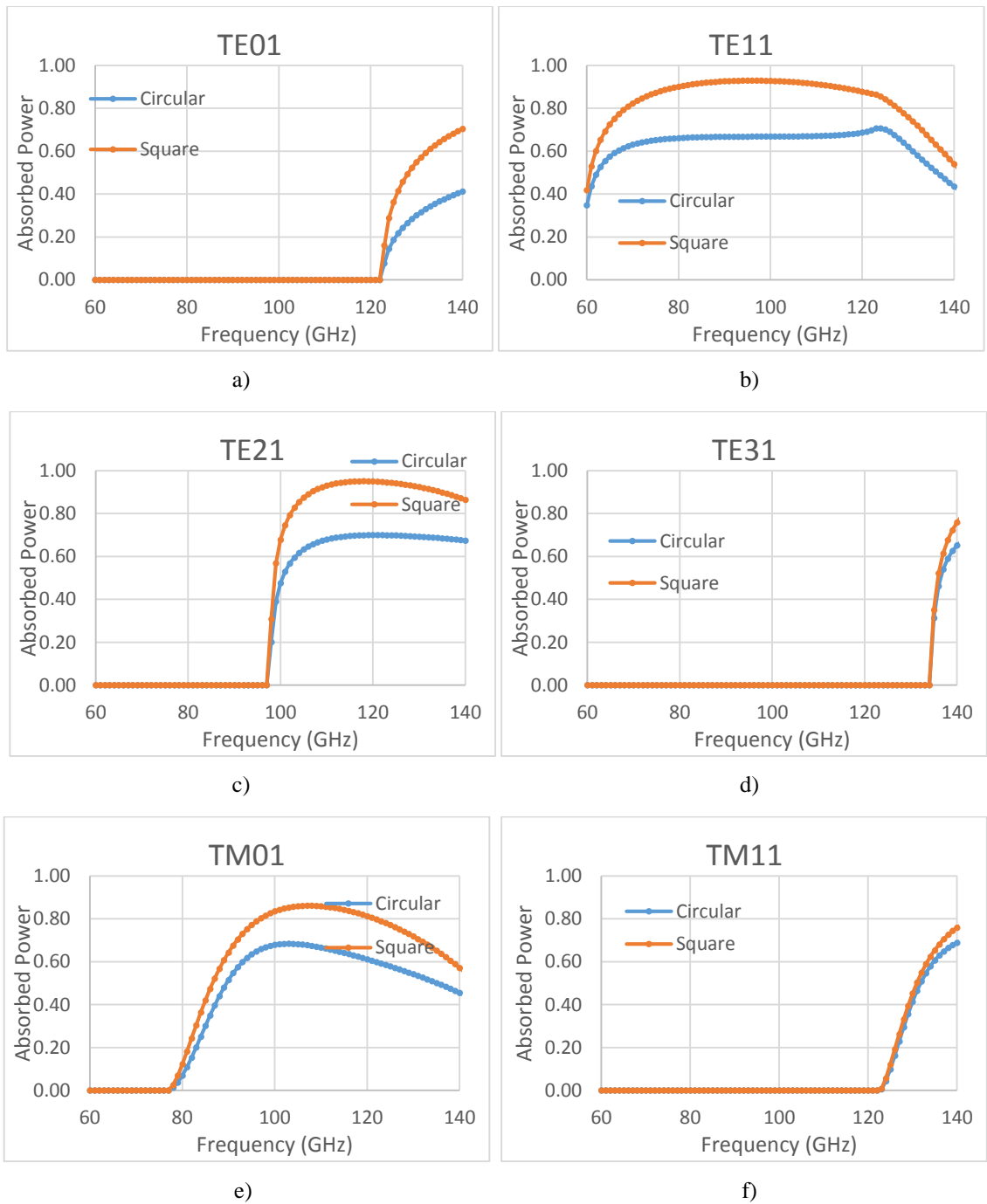


Figure 4.16: Comparison of absorbed power for a sealed cylindrical cavity containing a square absorber sheet and a sealed cylindrical cavity containing a circular absorber sheet where both absorbers occupy equal areas

It can be seen from Figure 4.16 (a) to (f) that the square absorber tends to have lower reflection than the circular absorber, indicating that more power is absorbed by the square absorber thus yielding better performance. This is to be expected of course, as more scattering occurs at the square absorber, since the symmetry is broken in this case. As discussed above, in asymmetrical structures, there is the possibility of scattering between

modes of different azimuthal orders (and polarisation orientations when the absorber itself is not symmetric), meaning that higher order modes could scatter into modes of lower azimuthal order at the absorber resulting in more power absorbed in the absorber.

In the development of detectors for future instruments we now have the capability to determine the amount of power absorbed for arbitrary shaped absorbers in cylindrical cavities. This will be an important factor for optimizing the absorbing efficiency of cavity coupled bolometers.

4.5 Offset absorbing cylindrical cavities

This section now describes another possible approach for optimising the power absorbed for cavity coupled bolometers. This is based on offsetting the axis of the cavity from that of the waveguide feeding it with the aim of trapping more power in the cavity. Thus the investigation of the effects of offsetting the axis of an absorbing cavity from that of the waveguide feeding it when both the cavity and waveguide are circularly symmetric will be discussed. In particular, we are interested in whether this offset would improve the absorption of a bolometric detector in a cavity particularly for broadband or multi-mode applications. For such applications tuning a $\lambda_0/4$ backshort (*i.e.* the gap behind the absorber) to match an absorber to a cavity will clearly only be optimal for a specific frequency or waveguide mode so there may be less power absorbed by the cavity. In particular, one of the usual drawbacks with a usual co-axial configuration is that reflected (*i.e.* unabsorbed) radiation from the absorber/bolometer might be efficiently coupled back into the feeding waveguide, resulting in poor optical efficiency. It is reasonable to expect that in such a circumstance if we offset the incident waveguide relative to the cavity axis more power would get trapped and be absorbed by the absorber.

In order to analyse this scenario one can use either CST (FEM approach) or a mode matching method again (GAMMA). As mentioned already CST has the disadvantage of being computationally intensive and therefore rather slow for electrically large structures (relative to the wavelength). The GAMMA software was developed further to be able to handle such cases (*i.e.* where a circular waveguide of radius a feeds another offset waveguide of radius b , with $a < b$, the second waveguide essentially being the cavity).

4.5.1 Implementing offsets in GAMMA

As discussed in Section 4.3, because of the symmetry in cylindrical systems GAMMA can utilize analytical expressions for the various power coupling integrals of the form $P_{ij} = \int \mathbf{e}_i^L \times \mathbf{h}_j^{R*} \cdot d\mathbf{S}$ (see Section 2.3), required for the mode matching method. However, for non-coaxial systems where the axes of the cavity and waveguide are offset from each other, clearly numerical integrations become necessary to calculate these P_{ij} .

The first task therefore was to modify the GAMMA code for such cases. We allow the axis of the smaller feed waveguide to be off-set by some displacement $d = \delta \hat{i} + \varepsilon \hat{j}$ with respect to the larger guide (cavity), where \hat{i} and \hat{j} refer to the usual Cartesian coordinates (unit vectors). This involved a number of modifications to the pre-existing mode matching code. The first important difference is that the power coupling integrals are now calculated numerically as analytical expressions do not exist for the case where there is a finite offset. Secondly, it is also now possible that there is power scattering at the junction of the two guides between modes of different azimuthal order and modes of different polarization orientation (the two degenerate fields exist for each mode of azimuthal order $n > 0$). This is similar to scattering of power at non cylindrically symmetric absorbers as discussed in Section 4.4. This means that we can no longer apply the simplification that the azimuthal orders can be treated separately when calculating the scattering matrices, nor that the scattering matrices are identical for the two orthogonal degenerate fields of each mode as there can be power scattered between them for non-symmetrical systems.

The modifications to the GAMMA software involved defining two Cartesian grids of points for the cross sections of two offset waveguides where the junction is located, at which the \mathbf{e}_n^{WG} (for the narrower feed waveguide) and \mathbf{h}_n^{cav} (for the cavity cross-section) transverse modal fields are calculated (these will be used for the numerical integrations of the power couplings between the two off-set guides). The sampling (Δx and Δy) should be fine enough that the displacement can be given by $\delta = m \Delta x$ and $\varepsilon = n \Delta y$ where m and n are integers.

Power scattered between modes is evaluated for all possible modal scattering combinations across the junction (*i.e.* the overlap region between the two guides). This is done numerically by calculating the cross product term $W_{mn} = \mathbf{e}_m^{wg} \times \mathbf{h}_n^{*cav}$ - for each

physical point. Because the displacement between the two guides is an integer times the sampling interval Δx and Δy , this ensures we have calculated the appropriate \mathbf{e}_n^{wg} and $\mathbf{h}_m^{\text{cav}}$ for a particular physical point. We displace one field grid with respect to the other before computing the W_{mn} so that the same actual physical point has a different grid coordinate for the two waveguides. We then assume the rectangular rule and integrate across the W_{mn} (so as to have the same structure as the arbitrary shaped absorber T matrix), yielding the power coupling coefficients and thus populating the $[P]$ matrix. To ensure a small rounding off error the grid size is picked to allow good coverage but still maintain computational efficiency. Clearly outside the overlap region we set the $W_{mn} = 0$ as the \mathbf{e}_m are not defined there in particular. The scattering matrices for the waveguide junction can then be cascaded with those for the absorbing cavity and waveguide to yield the scattering matrix for the system as a whole.

In order to get a feeling for the effects of a when waveguide sections are not in perfect alignment with one another power, couplings between different mode fields of different azimuthal orders were computed, remembering also that power can be scattered between the co-polar field of a mode and the orthogonal field of the same or a different mode (and vice versa).

In the computation of the $[P]$ matrix elements, it is convenient to re-write the transverse field expressions for TE and TM modes in Cartesian co-ordinates (otherwise the polarisation mismatch becomes complicated to model. As defined in Equations (2.10) to (2.13) and (2.18) to (2.21), for the "co-polar" field of the degenerate pair of fields of a mode the electric field lines are polarised in the x - direction along the $\phi = 0$ direction. By contrast, for the "orthogonal" fields, the field lines are orthogonal to the x - axis (have y - component only) in the $\phi = 0$ direction.

Now consider the case where we have a circular guide of radius a , feeding another circular guide (*i.e.* cavity) of radius b , where $a < b$ and the smaller guide is shifted with respect to the larger guide. A shift in the x - direction of δ with a shift in the y - direction of ε can be represented in cylindrical coordinates of the shifted guide as

$$\rho'(x, y) = \sqrt{(x - \delta)^2 + (y - \varepsilon)^2}, \quad (4.19)$$

so the angle ϕ' becomes

$$\phi'(x, y) = \tan^{-1}\left(\frac{y - \varepsilon}{x - \delta}\right). \quad (4.20)$$

Substituting $\rho(x, y)$ and $\phi(x, y)$, and $\rho'(x, y)$ and $\phi'(x, y)$ in Equations (2.10) to (2.13) and (2.18) to (2.21)) the cross-coupling may be computed from

$$P_{n'n} = \int_{S_L} e_n^L \times h_{n'}^{*R} \cdot dS = \int_{S_L} (e_{xn}^L \times h_{yn'}^{*R} - e_{yn}^L \times h_{xn'}^{*R}), \quad (4.21)$$

where S_L refers to the smaller left-hand waveguide, and L is for a mode on LHS of the junction and R a mode on RHS of the junction. Performing this integral over a surface gives a measure of the power flowing through that surface. $e_n^L \times h_{n'}^{*R}$ has the form of a Poynting vector and is real for propagating modes on the right and imaginary for evanescent modes on the right.

For perfectly symmetric systems, the $[P]$ matrix for an individual azimuthal order as defined in GAMMA has the form as represented in Equation (4.10) (replacing $[T]$ with $[P]$).

When the larger guide is shifted with respect to the smaller guide, the system is no longer symmetric and scattering is observed between modes of different azimuthal orders as well as between co-polar and orthogonal modes. An example of the form the $[P]$ matrix might take on when the junctions are offset is given in Equation (4.22):

$$[P]_{total} = \begin{bmatrix} P[0-0] & P[co-0] & P[orth-0] \\ P[0-co] & P[co-co] & P[orth-co] \\ P[0-orth] & P[co-orth] & P[orth-orth] \end{bmatrix}, \quad (4.22)$$

which is the same form as that for the $[T]$ matrix of an arbitrary shaped absorber.

The grids generated are rectangular, but the structure in question is cylindrical, thus a ‘mask’ was used as was discussed in Section 4.4. A kronecker delta condition was once again implemented, an example of this mask can be seen in Figure 4.17.

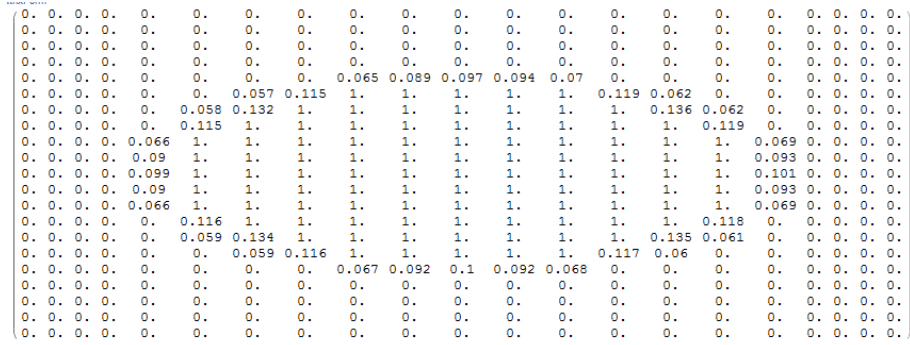


Figure 4.17: Example grid output for the mask used to convert the rectangular field to a circular modal field

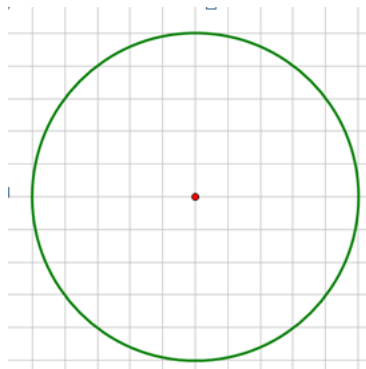


Figure 4.18: Circular area on a square grid

Because we use the rectangular/trapezoidal rule to evaluate the P_{ij} integrals, a significant number of samples are required to accurately represent the field. The problem that we are facing is illustrated by Figure 4.18. Sampling is critical to accurately represent the contribution to the P_{ij} integrals at the edges of the structure, the method outlined above assigns a value of $\Delta x \Delta y$ to the area of a square that's fully within the circle and a value of 0 to the contribution of a square where the sample point lies just outside the circle. The method can also account for the fact that some grid points only lie partially within the circle. Thus, the finer the sampling, the more accurate the method. This is particularly important for a mode where the maxima occur near the edges, such as the TE_{21} orthogonal mode or the TE_{31} co-polar mode, whose electric field line and intensity plot can be seen in Figure 4.19.

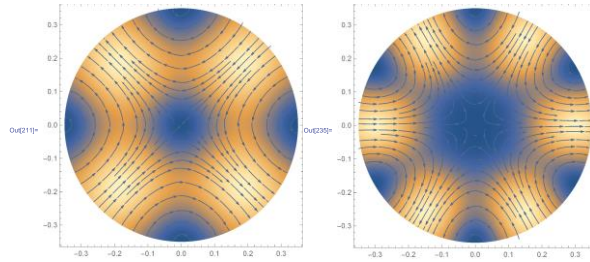


Figure 4.19: Electric field lines and intensity plot of a TE21 Orthogonal (left) and TE31 Co-polar (right) waveguide modes

Clearly, for the case of the modes in Figure 4.19, undersampling the grids will lead to inaccurate results. This was solved by adjusting the area of dA of the sample squares to take account of the area being less than $dx dy$ and use the mask shown in Figure 4.17.

Now, consider a junction where the smaller guide on the LHS has a radius of 1.89 mm and the larger guide on the RHS has a radius of 3.825 mm. Figure 4.20 shows the power coupling for some possible modal scattering combinations, while shifting the smaller guide relative to the larger guide by up to 1.80 mm in steps of 0.1 mm. Evaluating example integrals like these allowed us to probe when there will be scattering of power between modes and when they remained uncoupled (due to any residual symmetry).

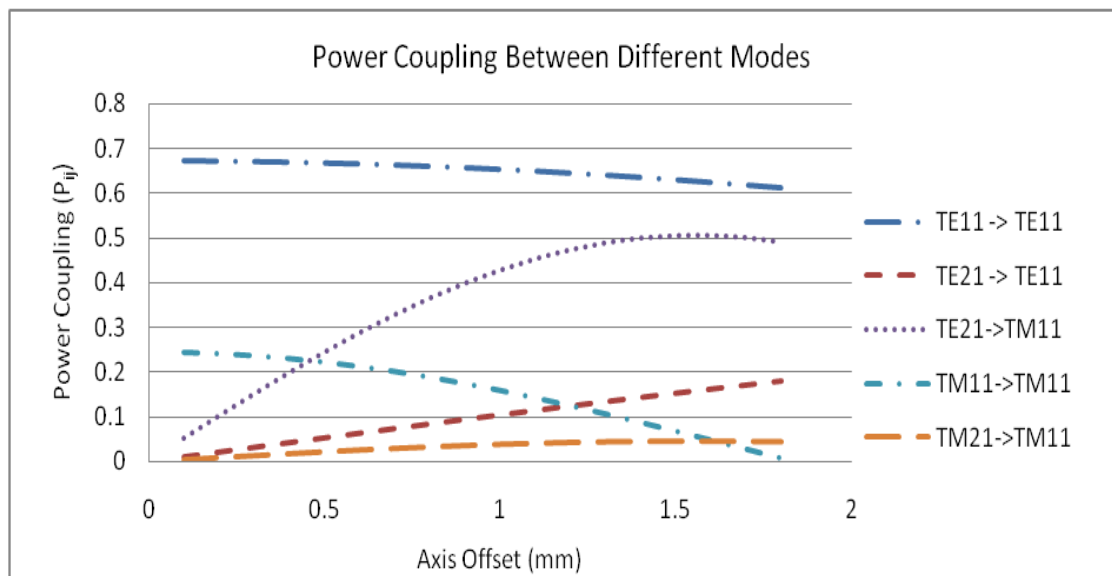


Figure 4.20: Power coupling between certain modes in the presence of an offset

Clearly the scattering between modes of different azimuthal orders needs to be accounted for as the power coupling between them is non-negligible.

The power carried by the modes making up the propagating fields may be either reflected or transmitted at a discontinuity, which can be described in terms of the usual four

scattering matrices (Equations (2.47) to (2.50)). For example, the overall scattering matrix $[S_{11}]$ representing power entering port 1 and being reflected back at port 1 is arranged in a similar way as the $[P]$ and $[T]$ matrices (as follows for order n to order m) as indicated in Section 4.4 (Equation (4.17)).

4.5.2 Code verification

The example case of a few-moded simple waveguide-fed cavity

The behaviour of some simple offset absorbing cavity configurations was examined. The aim is to capture as much incident power as possible in the detector region and thus maximise absorption in the bolometer.

The type of cavity considered is a simple closed cylindrical waveguide fed by a cylindrical waveguide of smaller radius (see Figure 4.21). A bolometric detector (an absorber modelled as a lossy ohmic sheet) was placed inside the cavity and various factors were investigated in order to maximise absorption in the detector region. These factors included: the position of the detector from the back of the cavity, the surface resistance of the absorber and its size. The waveguide feeding the cavity was then offset so that the impact of the offset on the power absorbed could be measured.

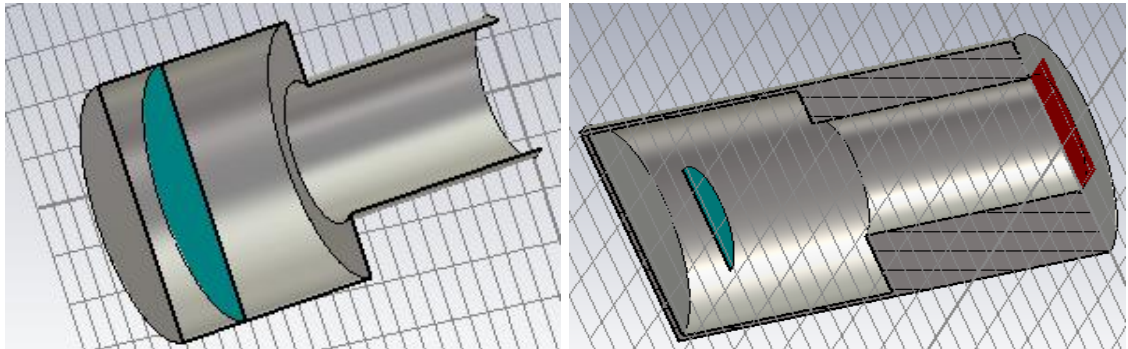


Figure 4.21: Waveguide feeding cavity containing an ohmic sheet

The length and radius of the feeding guide are 4.00 mm and 1.391 mm, respectively. The length and radius of the cavity are 3.895 mm and 2.491 mm respectively. The wavelength λ at the centre of the band (75 GHz) is 4.00 mm and the behaviour of the cavity was examined between 65 GHz and 85 GHz.

The absorber in the cavity was represented by an ohmic sheet with the surface resistance R_S of the ohmic sheet set to $90 \text{ } \Omega/\text{Sq}$ and $300 \text{ } \Omega/\text{Sq}$ and its radius was set either equal to the cavity radius ($R_{abs} = R_{cav}$, so that it filled the waveguide) or alternatively to half the cavity radius ($R_{abs} = 0.5 \times R_{cav}$). The absorber was placed at different distances from the back of the cavity (the effective backshort for the detector).

The initial results used CST (Microwave Studio) as a benchmark software tool to verify the results obtained by GAMMA for a number of simulations for the system described above. Generally, CST can only be used for electrically small configurations, of course, as discussed earlier.

The reflected power (*i.e.* the $[S_{11}]^2$ $TE_{11} \rightarrow TE_{11}$ term at the waveguide entrance port obtained by both CST and GAMMA) were compared with the presence of an offset at the junction between the waveguide and the cavity. For this case the distance from the absorber to the backshort was set to $\lambda_0/4$ at the centre of the band ($\lambda_0 = 4.0 \text{ mm}$, 75 GHz) and the absorber chosen has $R_{abs} = R_{cav}$ and $R_S = 90 \text{ } \Omega/\text{Sq}$. The verification results are illustrated in Figure 4.22 and Figure 4.23. The graph in Figure 4.22 only shows the result obtained by GAMMA only since on-axis examples have been compared in Section 4.3.

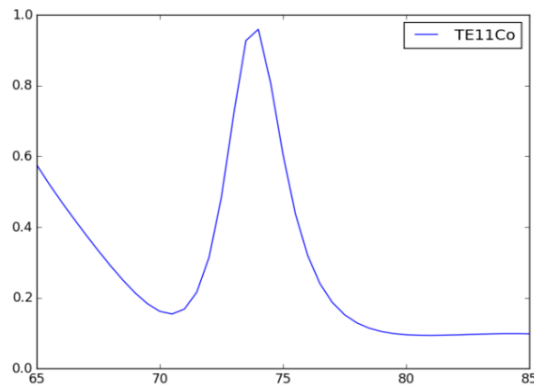


Figure 4.22: Reflected power obtained for the co-polar TE_{11} mode from GAMMA for the case where there is **no offset**. The input fields were the co-polar fields of the TE_{11} mode. Because of the symmetry we get identical results for both the two degenerate TE_{11} mode fields.

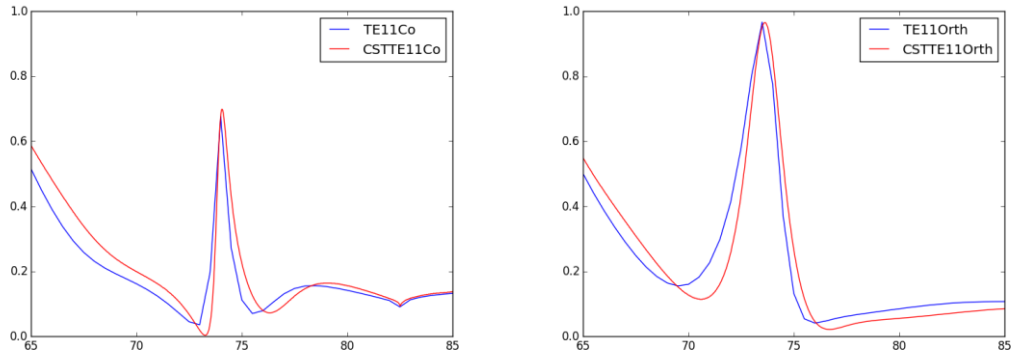


Figure 4.23: Reflected power obtained for the co-polar and orthogonal TE₁₁ mode from GAMMA and CST for the case where there is an **offset of 0.6 mm** in the **x-direction**

Another verification example is shown in Figure 4.24 and Figure 4.25. This time, the absorber diameter is half filling the cavity ($R_{abs} = 0.5 \times R_{cav}$) and the surface resistance was set to 300 Ohm/Sq. For these cases the distance from the absorber to the backshort was also set to $\lambda_0 / 4$ at the centre of the band ($\lambda_0 = 4.0$ mm, 75 GHz). The comparison is again performed by investigating the reflected power (*i.e.* the $[S_{11}]^2$ TE₁₁ \rightarrow TE₁₁ term at the waveguide entrance port) obtained by both CST and GAMMA.

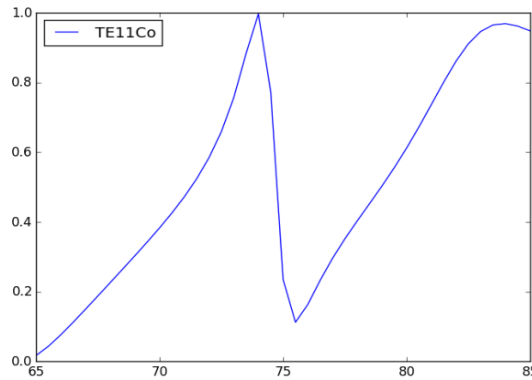


Figure 4.24: Reflected power obtained for the co-polar TE₁₁ mode from GAMMA for the case where there is **no offset** with $R_{abs} = 0.5 \times R_{cav}$ and $R_S = 300$ Ohm/Sq. The input fields were the co-polar fields of the TE₁₁ mode. Because of the symmetry we get identical results for both the two degenerate TE₁₁ mode fields.

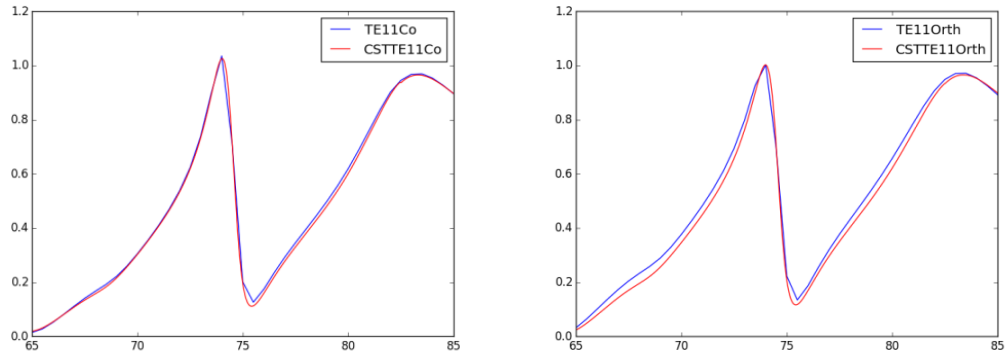


Figure 4.25 : Reflected power obtained for the co-polar and orthogonal TE11 mode from GAMMA and CST for the case where there is an **offset of 0.3 mm** in the **x-direction**

A third verification example is shown in Figure 4.26 and Figure 4.27. This time, the absorber diameter is filling the cavity ($R_{Abs} = R_{cav}$) and the surface resistance was set to 90 Ohm/Sq. For these cases the distance from the absorber to the backshort was set to $\lambda_0 / 3$ at the centre of the band ($\lambda_0 = 4.0$ mm, 75 GHz). The comparison is again performed by investigating the reflected power (*i.e.* the $[S_{11}]^2$ $TE_{11} \rightarrow TE_{11}$ term at the waveguide entrance port) obtained by both CST and GAMMA.

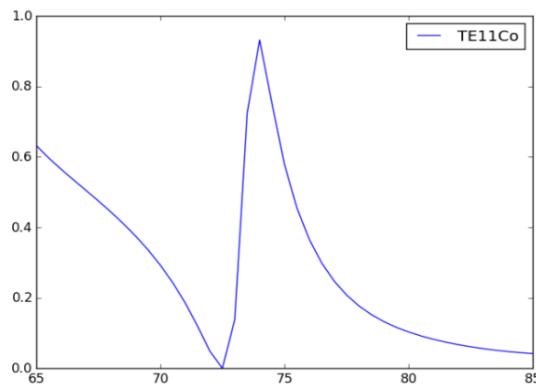


Figure 4.26: Reflected power obtained for the co-polar TE11 mode from GAMMA for the case where there is **no offset** with $R_{Abs} = R_{cav}$ and $R_S = 90$ Ohm/Sq. The input fields were the co-polar fields of the TE_{11} mode. Because of the symmetry we get identical results for both the two degenerate TE_{11} mode fields.

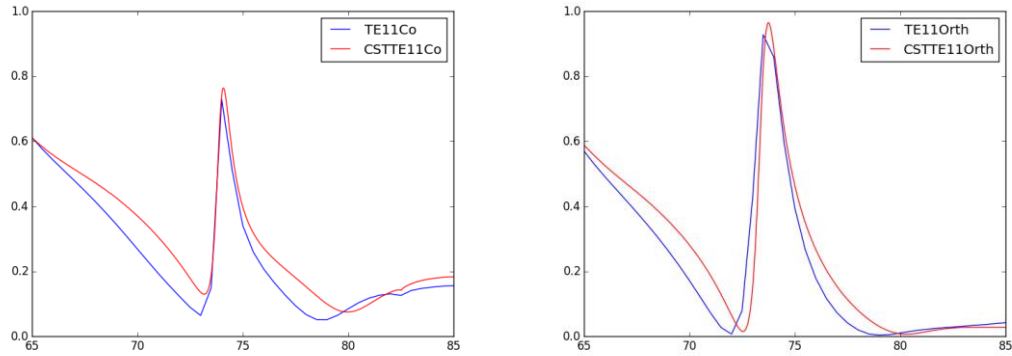


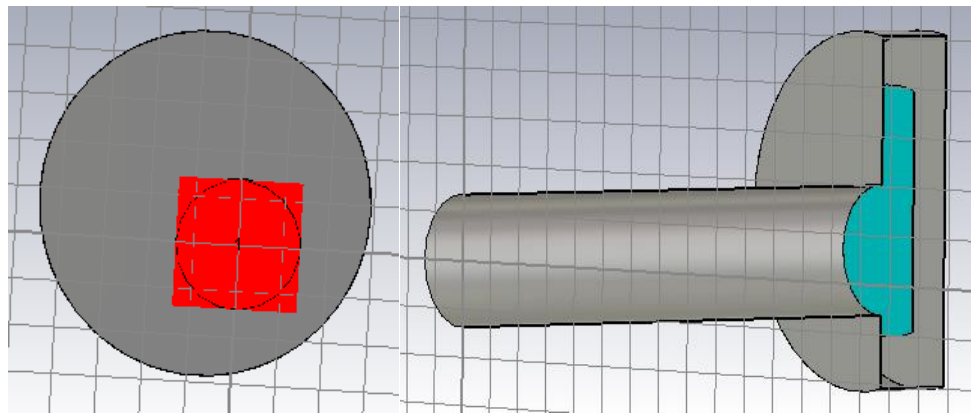
Figure 4.27: Reflected power obtained for the co-polar and orthogonal TE11 mode from GAMMA and CST for the case where there is an **offset of 0.6 mm** in the **x-direction**

The results from both GAMMA and CST display similar trends across the band in all three examples that were investigated. Both CST and GAMMA show a very strong reflection feature around 74 GHz. From comparing the reflected power with an offset present and for the on-axis case, it can be seen that the offset needs to become large in terms of the wavelength of operation in order to see any effect.

Diagonal Offsets

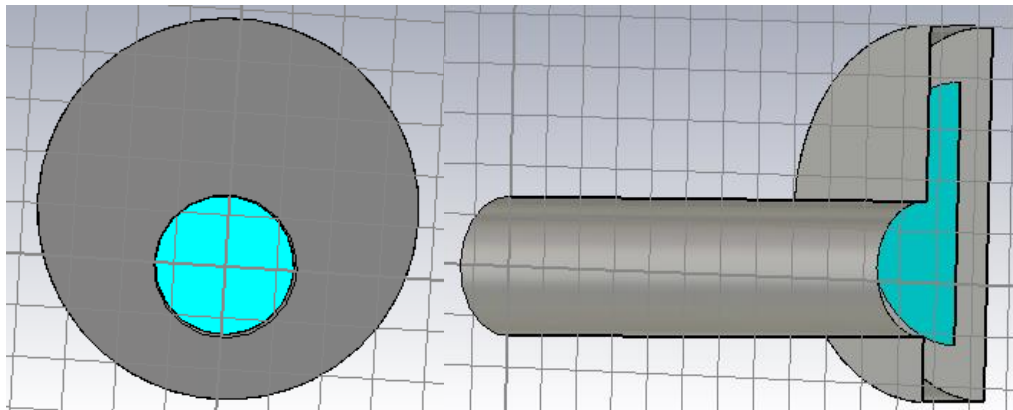
In chapter 2, the modal fields were discussed and it was noted that there exists a $\pi/(2n)$ symmetry between the co-polar field and orthogonal field of a mode, a fact which may also be used to verify the software. Two identical examples were set up, where an offset waveguide was feeding an absorber cavity. In both examples, the feed waveguide length and radius, cavity length and radius, absorber position, size and surface resistance were identical, the only variable was the offset of the waveguide. The investigated frequency range extends from 75 GHz to 110 GHz.

In the first example, the axis of a waveguide feeding an absorber cavity was offset diagonally (0.4 mm in the x-direction and 0.4 mm in the y-direction) an example can be seen in Figure 4.28 (a) and (b). In the second example, the axis of the waveguide feeding the absorber cavity was offset in the y-direction only (by 0.57 mm) (see Figure 4.28 (c) and (d)). The reflected power of the TE_{21} co-polar and TE_{21} orthogonal modes was compared for both examples. The result of this comparison can be seen in Figure 4.28 (e) for the diagonal offset and Figure 4.28 (f) for the offset in y-direction only.



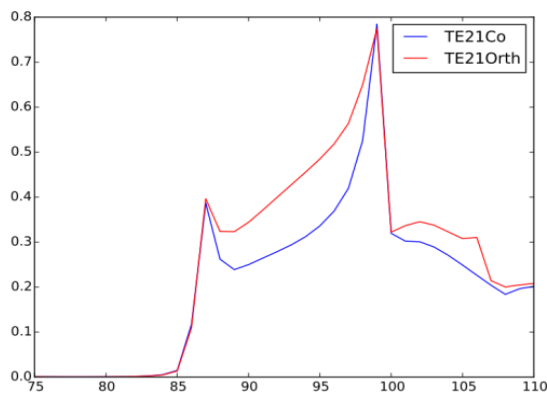
a)

b)

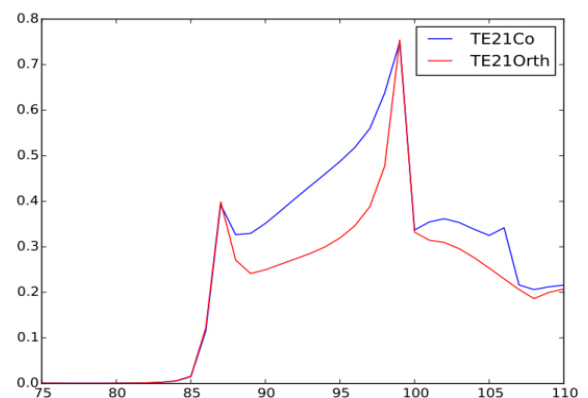


c)

d)



e)



f)

Figure 4.28: Offset comparison of the TE₂₁ orthogonal and co-polar modes showing the top and side-view of the example cases (a) and b) for diagonal offset and c) and d) for offset in y-direction only). The reflected power as a result of the diagonal offset is shown in e) and the reflected power as a result of an offset in the y-direction only is shown in f).

From the example illustrated above in Figure 4.28, it can be seen that the reflection pattern of the TE_{21} co-polar mode across the band with a diagonal offset is identical to the reflection pattern of the TE_{21} orthogonal mode across the band with an offset in the y -direction only (and vice versa).

4.6 Optimization of cavity design

In this section, we investigate methods to increase the absorbed power in the detector region of a cylindrical cavity fed by an offset waveguide. The position of the detector from the back of the cavity and also the size and surface resistance of the detector were varied (note that in all cases the absorber was centered on the cavity axis) over a frequency range from 65 GHz to 85 GHz. The distance of the absorber from the entrance and back of cavity was varied in terms of a fraction of the free space wavelength at the centre of the band, $\lambda = 4.0$ mm, ($\nu = 75$ GHz).

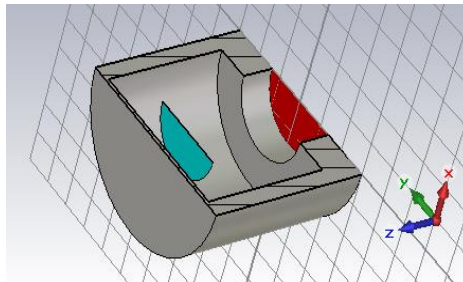


Figure 4.29: Cavity Geometry

Variation of detector position from the back of the cavity

The absorbed power obtained by both CST and GAMMA was compared for a number of different absorber positions from the back of the cavity. The surface resistance of the ohmic sheet was kept constant at $90 \Omega/\text{Sq}$ and the radius was kept constant at R_{cav} . The different absorber positions within the cavity were investigated for absorber - backshort distances of $\lambda_0/2$, $\lambda_0/3$, $\lambda_0/4$ and $\lambda_0/6$ for $\lambda_0 = 4.0$ mm (which corresponds to the free-space frequency at the centre of the band). The waveguide feeding the cavity was offset by 0.3 mm in the x -direction.

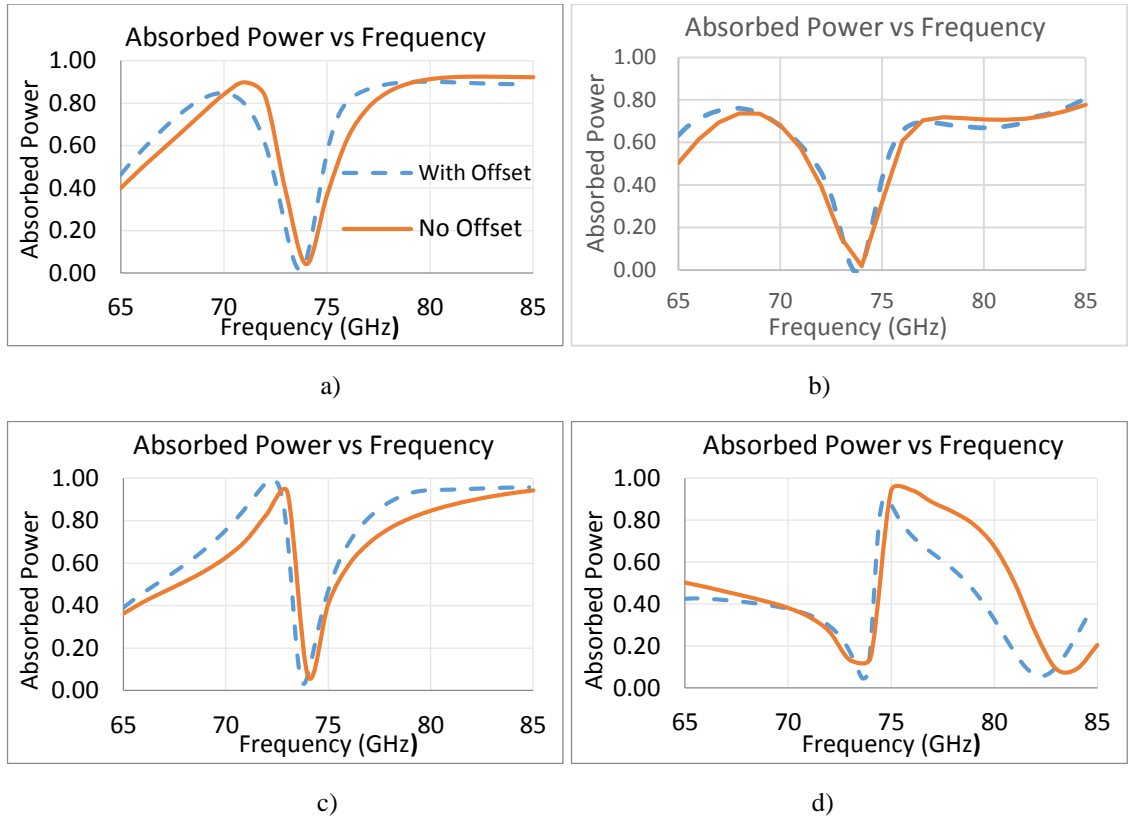


Figure 4.30: Absorbed power using GAMMA and CST for the absorber positioned a) $\lambda/4$ (=1.0 mm) b) $\lambda/6$ (= 0.67 mm) c) $\lambda/3$ (= 1.33 mm) and d) $\lambda/2$ (= 2.0 mm) from the back of the cavity with the absorber filling the cavity diameter with an offset of 0.3 mm in the x-direction

From Figure 4.30 (a) to (d), it is clear that the system is most efficient (most of the power is absorbed) when the absorber is positioned $\lambda_0/4 = 1.0$ mm from the back (at $3\lambda_0/4 = 3.0$ mm from the front) of the cavity and it is least efficient when the absorber is placed midway ($\lambda_0/2 = 2.0$ mm) between the entrance and back of cavity (as expected).

	Fraction of total power absorbed (with offset)	Fraction of total power absorbed (without offset)
$\lambda_0/2$	0.387	0.489
$\lambda/3$	0.739	0.710
$\lambda/4$	0.726	0.750
$\lambda/6$	0.613	0.625

Table 4.3: Absorbed power for the various cases considered in Figure 4.30

Variation of Detector Size and Surface Resistance

Essentially the same example as the previous subsection except here the absorbed power obtained by both CST and GAMMA were compared for a number of different bolometer sizes and surface resistances. The absorber distance from the back of the cavity was kept constant at $\lambda_0/3$ with $\lambda_0 = 4.0$ mm (which corresponds to the free-space frequency at the centre of the band). The waveguide feeding the cavity was offset by 0.30 mm in the y-direction.

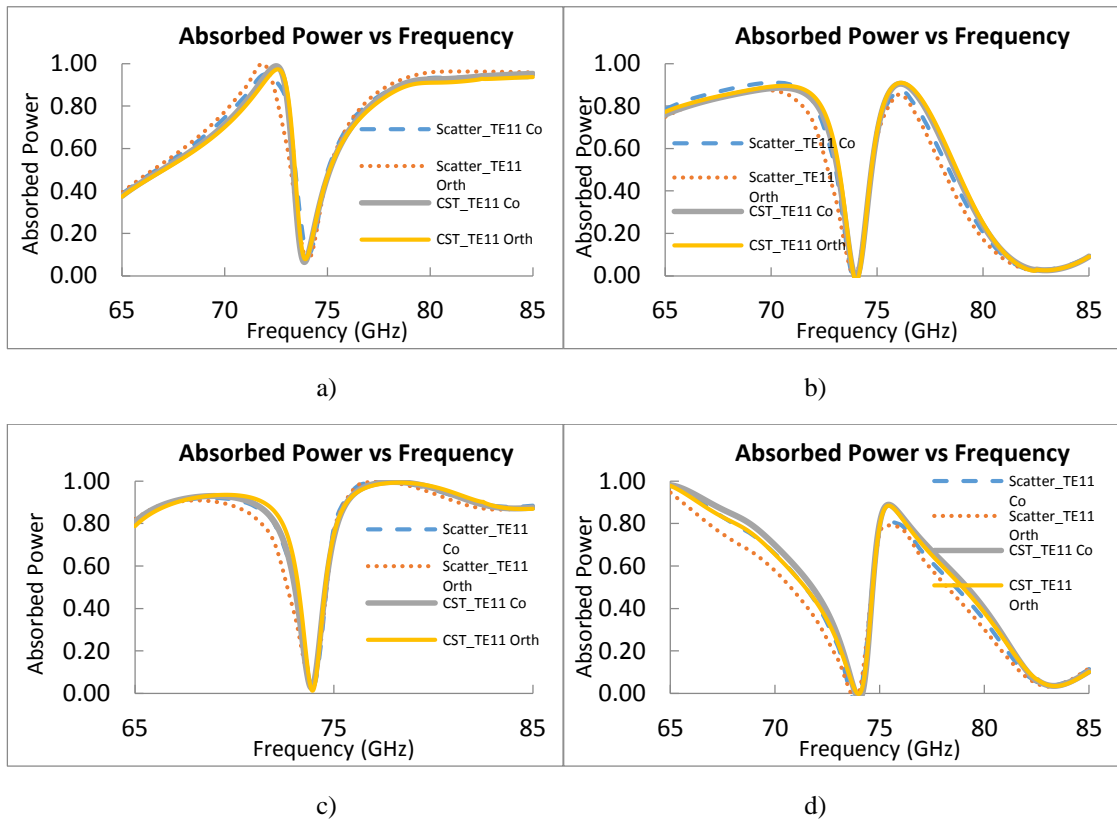


Figure 4.31: Absorbed power predicted by GAMMA and CST for surface resistance and absorber radius of a) $90 \Omega / \text{Sq}$ and $r_{abs} = r_{cav}$ b) $90 \Omega / \text{Sq}$ and $r_{abs} = r_{cav} / 2$ c) $300 \Omega / \text{Sq}$ and $r_{abs} = r_{cav}$ and d) $300 \Omega / \text{Sq}$ and $r_{abs} = r_{cav} / 2$

From Figure 4.31 (a) to (d), it is clear that the system is most efficient when the absorber fills the cavity ($R_{abs} = R_{cav}$) and when it has a surface resistance of $300 \Omega / \text{Sq}$ (as one expects since it is closer to the impedance of free space $377 \Omega / \text{Sq}$).

	90 Ω/Sq	300 Ω/Sq
Half Filling	0.520	0.470
Fully Filling	0.780	0.865

Table 4.4: Absorbed power for the various cases considered in Figure 4.31

Variation in Waveguide Offset

The absorbed power as computed by GAMMA was compared for a number of different offsets in x and y . The surface resistance was kept at $90 \Omega/\text{Sq}$ and the absorber radius was let equal to the cavity radius. The absorber was placed at $\lambda_0 / 4$ ($= 1.0 \text{ mm}$) from the end wall of the cavity. In these examples, only GAMMA was used since the GAMMA software had already been verified in Section 4.5.2.

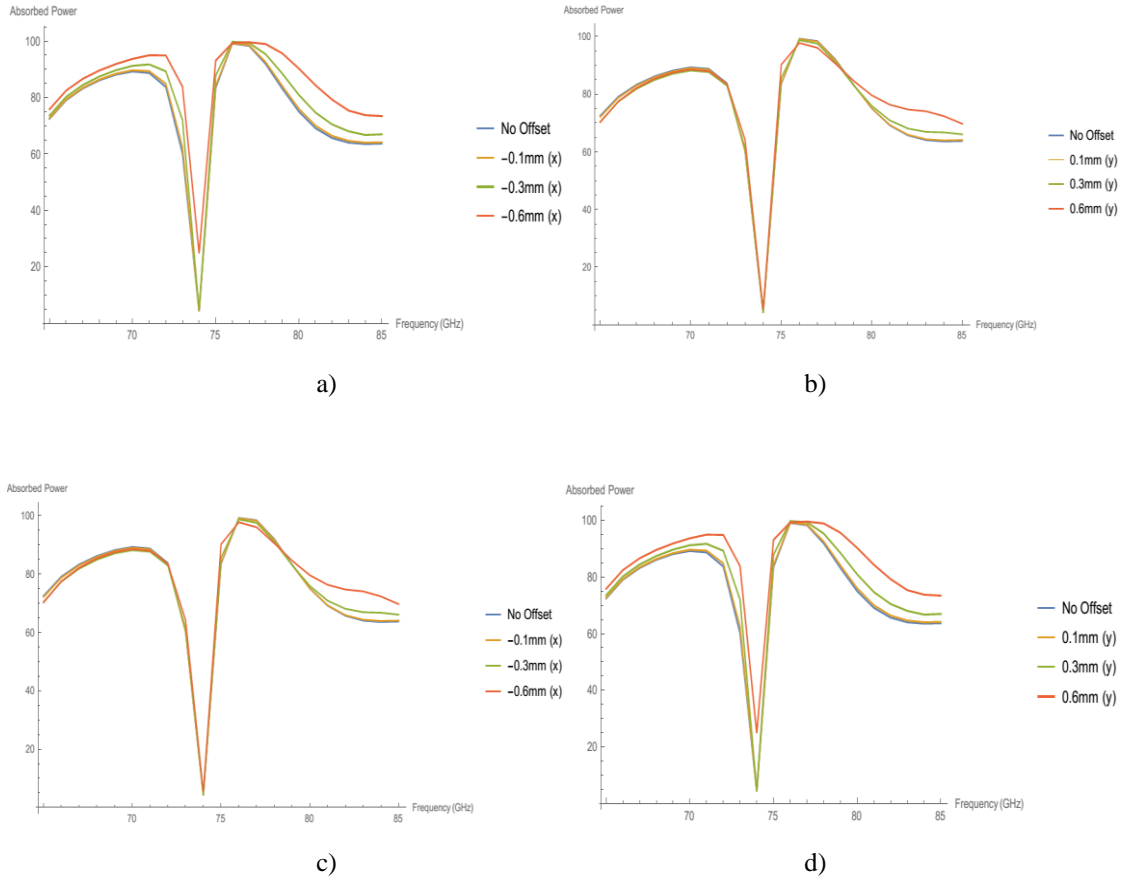


Figure 4.32: Plot of absorbed power versus frequency for various **offsets in the x - and y -direction for the case of the co-polar TE_{11} ((a) and (b)) and orthogonal TE_{11} ((c) and (d)) mode with the absorber placed at $\lambda_0 / 4$ ($= 1.0 \text{ mm}$) from the end wall of the cavity and absorber fills cavity diameter $r_{abs} = r_{cav}$**

From Figure 4.32 (a) to (d) , it can be seen that offsetting the waveguide feeding the cavity improves the performance efficiency of this system. Due to the symmetry of the TE_{11} mode, offsetting the guide in the negative x -direction gives an identical result as offsetting it in the positive x -direction, *etc.* Also, it is worth noting that if the guide were offset in the x -direction, the absorbed power of the co-polar TE_{11} mode was identical to the

absorbed power of the orthogonal TE_{11} mode if it were offset in the y -direction. This is evident in the above curves.

4.7 Conclusion

In this chapter, we have discussed how mode matching may be used to efficiently model cavity coupled bolometers. In-house mode matching software GAMMA, written in Python, was used to model cavity coupled bolometers. The software was verified using CST for electrically small examples (small in terms of wavelength). GAMMA will be much more efficient for electrically large examples compared with CST.

In Section 4.2, an empty cavity was modelled and it was shown that if no absorber is present, all of the power will be reflected back to the entrance waveguide (as expected, showing conservation of power).

In Section 4.3, GAMMA was used to model a few moded waveguide with one end closed, and the results closely agreed with CST when a sufficiently high number of modes was used in GAMMA. The software was then used to model an overmoded waveguide feeding a bolometric cavity over a wide frequency range, excellent agreement was observed between GAMMA and CST for the case when the absorber was partially filling the cavity.

In Section 4.4, the implementation and verification of an absorber of arbitrary shape was discussed. A square absorber within a cylindrical waveguide was investigated, and the results from GAMMA agreed closely with the results from CST for both reflection and transmission. The performance in terms of reflected power of a square absorber in a cylindrical waveguide with one end closed was compared to a circular absorber occupying the same area as the square. The example with the square absorber showed less reflections across the band and therefore more absorption. Again, this is to be expected as breaking the symmetry causes more power scattering within the cavity and therefore results in more power absorption.

In Section 4.5, the theory and some verification examples of an offset cavity being fed by a waveguide were discussed. The results from implementing cavity offsets in GAMMA were compared with CST. Similar trends across the band were observed for the case when an offset is present. It can be seen that including an offset in a fundamentally moded waveguide feeding a detector cavity in the x -direction will have an effect on the absorbed

power of the co-polar TE_{11} mode (due to the symmetry of the mode) and offsetting the waveguide in the y -direction will have an effect on the orthogonal TE_{11} mode. It can also be seen that the effect of small waveguide offsets is negligible when compared to the on-axis case, which is as expected to some extent because of the size of the shift relative to the wavelength. Only when the offset becomes significant (like in the 0.6 mm case for $\lambda_0 = 4.0$ mm) do we begin noticing that more power is absorbed in the cavity.

In Section 4.6, a cavity configuration resulting in most absorbed power was found through simulation. It is clear that there is a strong reflection feature around 73.5 GHz. This would appear to be associated with the cut-on of the TM_{11} mode in the cavity. For a waveguide of radius a the cut-off frequency of a TE_{nl} mode is given by $f_c = (p'_{nl} c) / (2\pi a \sqrt{\epsilon_r})$, where ϵ_r is the relative permittivity of the medium. For a TM_{nl} mode, the cutoff frequency is given by $f_c = (p_{nl} c) / (2\pi a \sqrt{\epsilon_r})$, where p_{nl} and p'_{nl} are the zeros of the Bessel function $J_n(z)$ and its derivative $J'_n(z)$, respectively.

Computing these cut-off frequencies we examined which modes are supported within the cavity across the frequency range (65 GHz to 85 GHz) can be seen in Table 4.5.

	65	67	69	71	73	74	76	78	80	81	83	85
TE₀₁						✓	✓	✓	✓	✓	✓	✓
TE₁₁	✓	✓	✓	✓	✓	✓	✓	✓	✓	✓	✓	✓
TE₂₁	✓	✓	✓	✓	✓	✓	✓	✓	✓	✓	✓	✓
TE₃₁										✓	✓	✓
TM₀₁	✓	✓	✓	✓	✓	✓	✓	✓	✓	✓	✓	✓
TM₁₁						✓	✓	✓	✓	✓	✓	✓

Table 4.5: Table showing which modes are supported within the cavity across the operating band

In Figure 4.22 to Figure 4.27 and Figure 4.30 to Figure 4.32, a peak in the reflection curves (a dip in absorption curves) is evident at ~ 73.5 GHz. This appears to be due to the fact that the TE_{01} and TM_{11} modes begin to propagate in this cavity at this frequency. Another S - parameter peak (dip in absorbed power) can be seen at ~ 81 GHz, which is just above the cutoff frequency of the TE_{31} mode, meaning that mode begins to propagate in the cavity above the cut-off frequency although coupling to this mode may be weak. The reflection at 74 GHz is higher than at 81 GHz (more pronounced peak in the reflection curves) since 2 different modes cut on above this frequency. The TE_{01} and TM_{11} modes have different field distributions, but same cutoff frequency, meaning that they are degenerate modes. However, modes of the same azimuthal order will tend to couple more strongly for small off-sets.

Another issue to be investigated is the effect on the optical efficiency of the detectors when free space gaps are present, through which power can escape. To model these effects requires GAMMA, which calculates the scattering matrices in waveguide structures only, to be further extended to handle free space propagation including free space gaps between waveguides. This work is reported on in Chapter 6.

In the following chapter, we apply the results of the modelling of absorbing cavities for the case of the two multimode channels of the HFI instrument on the ESA Planck satellite.

5 The Planck Multimode Channels

5.1 Introduction

In this chapter we discuss the application of some of the innovations made to the waveguide mode matching approach (discussed in earlier chapters) to the 857 and 545 GHz multimode channels of the Planck HFI instrument. In particular, the goal of this work is to improve on the agreement between previous predictions and both laboratory and in-flight measurements.

The Planck mission concept originally began as two separate missions, COBRA and SAMBA, which were later combined into the COBRA-SAMBA mission and then renamed Planck. The Planck mission (Tauber *et al.*, 2010a) was first proposed in 1992, shortly after the release of the results from the Cosmic Background Explorer (COBE) satellite (Boggess *et al.*, 1992). The main achievements of COBE were the measurement of the shape of the spectrum of the cosmic microwave background (CMB) by the Far-InfraRed Absolute Spectrophotometer (FIRAS) instrument, and the detection of spatial anisotropies of the temperature of the CMB by the Differential Microwave Radiometer (DMR) at the level of several degrees on the sky. The Planck mission was devised to collect and characterise radiation from the CMB in order to produce high precision maps of anisotropies of the CMB. Later it was decided that Planck should also probe its polarization properties following their detection by the DASI instrument (Church *et al.*, 2003).

The primary scientific objectives of Planck (Planck Collaboration, 2014 (I)) can be summarised as follows:

- (i) To complete a full sky measurement of the intensity and polarization anisotropies of the CMB with an improved temperature sensitivity of $\Delta T/T = 10^{-6}$ at all angular resolutions greater than 10 arcminutes
- (ii) To test inflationary models of the early universe
- (iii) To measure the amplitude of structures in the CMB with physical scales between $100 h^{-1}\text{Mpc}$ and $1000 h^{-1}\text{Mpc}$, where h is the Hubble parameter

- (iv) To undertake measurement of frequency dependant Sunyaev-Zeldovich effect in galactic clusters
- (v) Determine a more precise value for the Hubble constant

In May of 1993, the development of Planck began. Two proposals were presented to the European Space Agency (ESA): (i) COsmic Microwave Background Radiation Anisotropy Satellite (COBRAS) (Mandolesi *et al.*, 1993), and (ii) SAteellite for Measurement of Background Anisotropies (SAMBA) (Puget *et al.*, 1993). Both the COBRAS and SAMBA teams proposed an instrument consisting of an offset Gregorian telescope focusing the collected light onto an array of detectors fed by corrugated horns. The two proposals led to the design of a payload where an off-axis tilted Gregorian telescope with a primary mirror measuring $1.9 \text{ m} \times 1.5 \text{ m}$ and a secondary of $1.1 \text{ m} \times 1.0 \text{ m}$ fed two instruments: (i) a COBRAS-like Low Frequency Instrument (LFI) and (ii) a SAMBA-like High Frequency Instrument (HFI).

The LFI (Bersanelli *et al.*, 2010) used microwave radiometers to map the sky in frequency bands from 27 GHz to 77 GHz. The radiometers were based on low noise amplifiers using indium-phosphide high electron mobility transistors (HEMT) and they were operated at 20 K. The LFI detectors were designed to be polarisation sensitive and orthomode transducers were used to separate the two orthogonal linear polarisations. The LFI consisted of 11 corrugated feed horns feeding 22 radiometers.

The HFI (Lamarre *et al.*, 2010) on the other hand, consisted of 52 bolometric detectors designed to map the sky in six frequency bands from 100 GHz to 857 GHz. The bolometers were fed by corrugated feed horns. Twenty spider-web bolometers were sensitive to total power only, while the remaining 32 pixels were arranged in pairs of orthogonal polarisation sensitive bolometers. All of the detectors on the HFI were cooled to 100 mK.

The frequency range of the two instruments (LFI and HFI) was designed to cover the peak of the CMB spectrum as well as to characterize the spectra of the foregrounds (Figure 5.1) (synchrotron and free-free emission at low frequencies, and dust emission at high frequencies). In order to ensure high spatial resolution, the detectors on Planck were single mode, with the exception of the two highest frequency channels (545 GHz and 857 GHz) which were designed to be multimode.

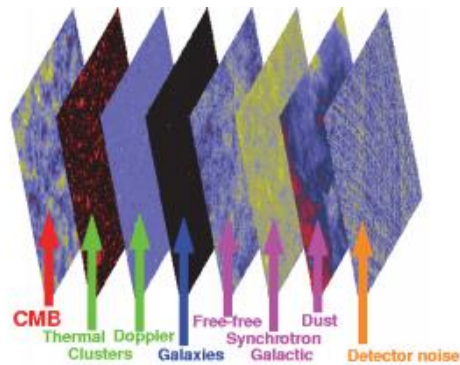


Figure 5.1: In order to map the anisotropies in the CMB, the observations must first be corrected for many layers of intervening foregrounds

This chapter is specifically concerned with the modelling of the performance of the two highest frequency channels of the HFI. These channels used specialized feed horns and were dedicated to the observation foreground sources (referred to above). The two bands were centered on 545 GHz and 857 GHz (with a bandwidth of $\pm 15\%$) and were multimode. In essence this means that the waveguide feeding the horn antenna is oversized, so that potentially higher order waveguide modes as well as the fundamental mode are capable of coupling signal power to the detector (Murphy *et al.*, 2010). The spider-web bolometers are incoherent detectors and thus absorb all of the power in the propagating modes transmitted by the corrugated horns (which couple the detectors to the off-axis Gregorian telescope). Furthermore, all of the waveguide and horn sections are corrugated and effectively only hybrid modes can propagate through the system, rather than pure *TE* or pure *TM* modes (normally associated with smooth walled guides). Such hybrid modes are difficult to model directly because of the waveguide boundaries have to be approximated by equivalent impedance walls, which leads to an awkward mathematical formulation. Instead, using a mode matching technique, the corrugated system is regarded as a large series of very short smooth walled sections representing the corrugation slots and fins with waveguide steps in radius recurring where the fin meets the slot. This produces accurate models of waveguides and horns, but at a computational cost due to the large number of slots and fins and the large amounts of scattering at each step.

The pixel consisted of a spider-web bolometer fed by a detector horn, which was fed by a back-to-back horn and a filter stack. Figure 5.2 shows a schematic of the back-to-back horn arrangement coupled to the detector horn. IR blocking filters were used to thermally

insulate the detector horn and bolometer while band pass filters define the operating frequency band. The filters are assumed to be transparent and have no effect on the beams propagating through them.

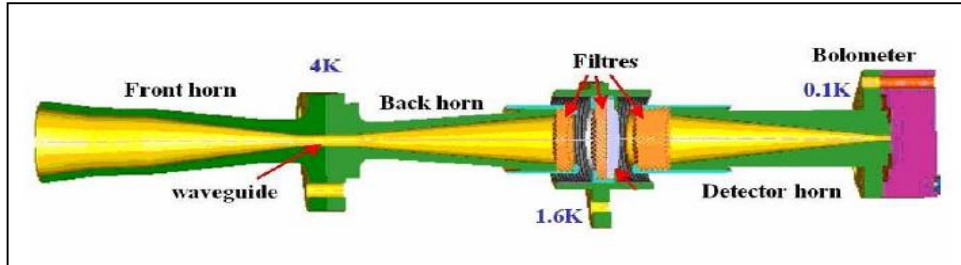


Figure 5.2: Diagram of the 857 GHz pixel consisting of the back-to-back horn and the detector feed horn assembly used on the multimode HFI channels (Lamarre, 2010)

5.2 Hybrid Modes

Hybrid modes form a basis set of modes with which the field of a corrugated horn can be represented. A cylindrical hybrid mode is considered to be made up of a linear combination of TE and TM modes. A horn is said to be single mode if only the fundamental HE_{11} hybrid mode is propagating. When the horn is multimode a number of higher order hybrid modes also propagate.

In multimode horns the generated hybrid mode fields are incoherent with respect to one another. This means that if one is interested in propagating the beam from a multimode horn through a telescope system and onto the sky, each of the hybrid modes needs to be propagated separately and the intensity patterns combined on the sky. If directly propagating waveguide modes were to be used as a basis to obtain the beam on the sky in a multimode horn, this would create a large number of fields that would need to be calculated making the task of obtaining beam patterns on the sky computationally challenging and time consuming. However, with hybrid modes the number of fields that need to be propagated to the sky is noticeably reduced as will now be discussed.

In order to obtain the hybrid modes, Singular Value Decomposition (SVD) can be used. The scattering matrix may be re-written as $[S_{21}] = [U][\Sigma_{21}][V]$ using singular value decomposition, where $[\Sigma_{21}]$ is an $m \times n$ rectangular diagonal matrix containing the singular values. The columns of $[U]$ and $[V]$ are the output and input singular vectors respectively.

For the case of the Planck 857 GHz horn, 5 azimuthal orders were considered with 60 modes per azimuthal order, this results in some 300 waveguide modes needed to accurately describe the scattering matrix. After performing SVD, the number of hybrid modes then needed to propagate to the sky is reduced to 17. These hybrid modes are of course special combinations (linearly independent combinations) of the 300 waveguide modes. This follows the procedure as described in Ian McAuley’s thesis (McAuley, 2015: 100). Also as noted in his thesis, because the modes are normalized in power the singular values for these hybrid modes should be unity (or less if there is some loss due to reflections or absorptions). Figure 5.3 shows the farfield pattern of the full 857 GHz pixel illustrating that the hybrid modes provide a valid approximation to the field as produced by the waveguide modes.

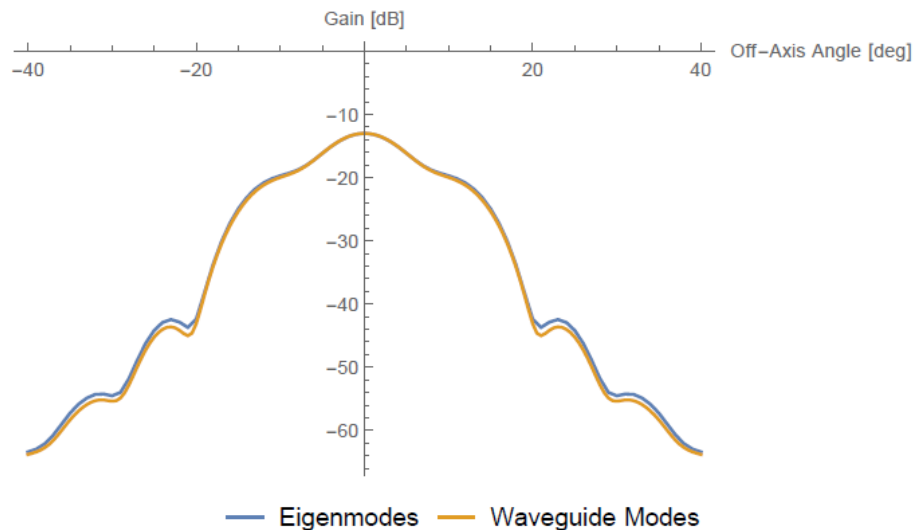


Figure 5.3: Farfield pattern of the full 857 GHz pixel as predicted by GAMMA using waveguide modes and by using hybrid modes

5.3 Beam pattern simulations of the 857 GHz channel

Simulations of the beam patterns of the 857 GHz channel were performed across the operating band to determine the beamwidth, sidelobe levels and gain. A waveguide mode matching technique was used to model the electromagnetic propagation through the structure as described above.

In-house CylindricalSCATTER software written in Mathematica contained the relevant tools needed to perform this analysis. However, due to the large number of modes required to accurately model the system, it is a computationally intense problem, resulting

in lengthy calculation time. Therefore, as part of the work of modelling the 857 GHz Planck channel, generalised absorber mode matching analysis (GAMMA) software, based on the scattering matrix approach, was written in Python to speed up the computations as described in Chapter 2. When compared with the existing mode matching software CylindricalSCATTER, written in Mathematica, GAMMA showed a factor 10 increase in time.

The most straightforward approach to take when modelling the full Planck pixel is to assume it has the form of a continuous waveguide (no free space gaps) and also treat the cavity as a perfect blackbody radiator, so that all of the waveguide modes in the waveguide attached to the cavity are excited equally and with the same power (Murphy *et al.*, 2012). This was the approach taken originally in the definition phase of the horns on the Planck project. In this section, we will begin by assuming the original simplest scenario, where the 857 GHz pixel will be modelled with a perfect blackbody absorber cavity, and with the thermal filter section treated as a continuous waveguide (see Figure 5.4). From a thermodynamic argument, we expect to couple $\frac{1}{2}k_B T$ of power into any degree of freedom (*i.e.* a propagating mode) which we then normalise to unity.

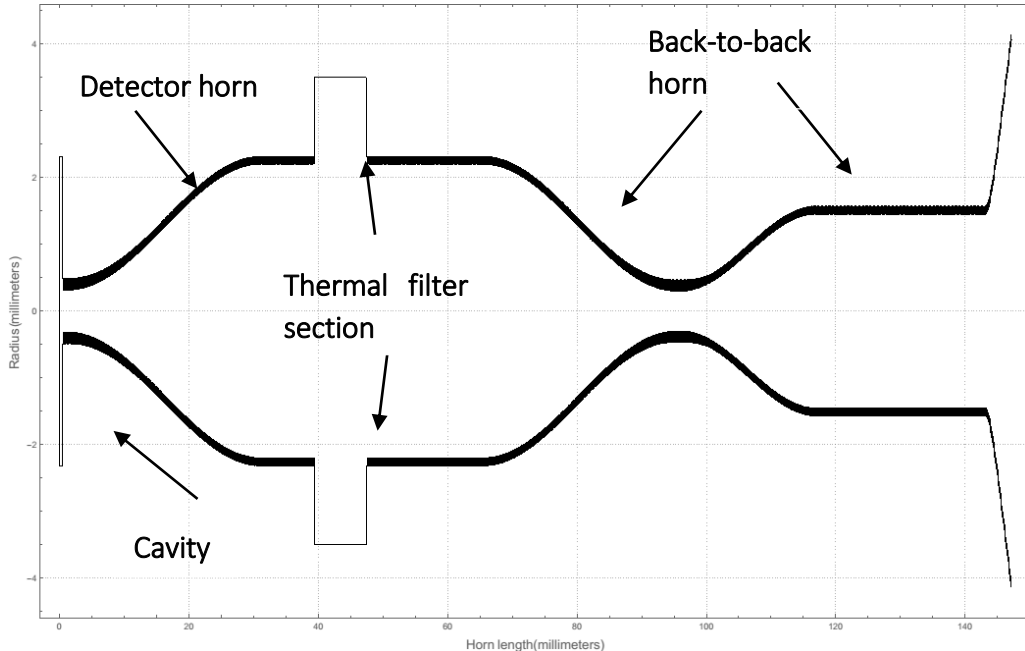


Figure 5.4: Geometry of the 857 GHz horn with the thermal filter gap as a continuous waveguide section and the bolometer as a perfect blackbody absorber

The frequency range of the 857 GHz horns extends from 729 GHz to 986 GHz ($\sim 30\%$ bandwidth). In order to cover this frequency range, farfield beam pattern simulations were

performed at intervals of 1 GHz. This is needed for producing a reliable and accurate simulated broadband farfield beam pattern (discussed in Section 5.7) by appropriate combination of the beam patterns. Figure 5.5 (a) to (d) below shows the resulting beam patterns as predicted by the in-house Python mode matching software, GAMMA, at some spot frequencies across the operating band.

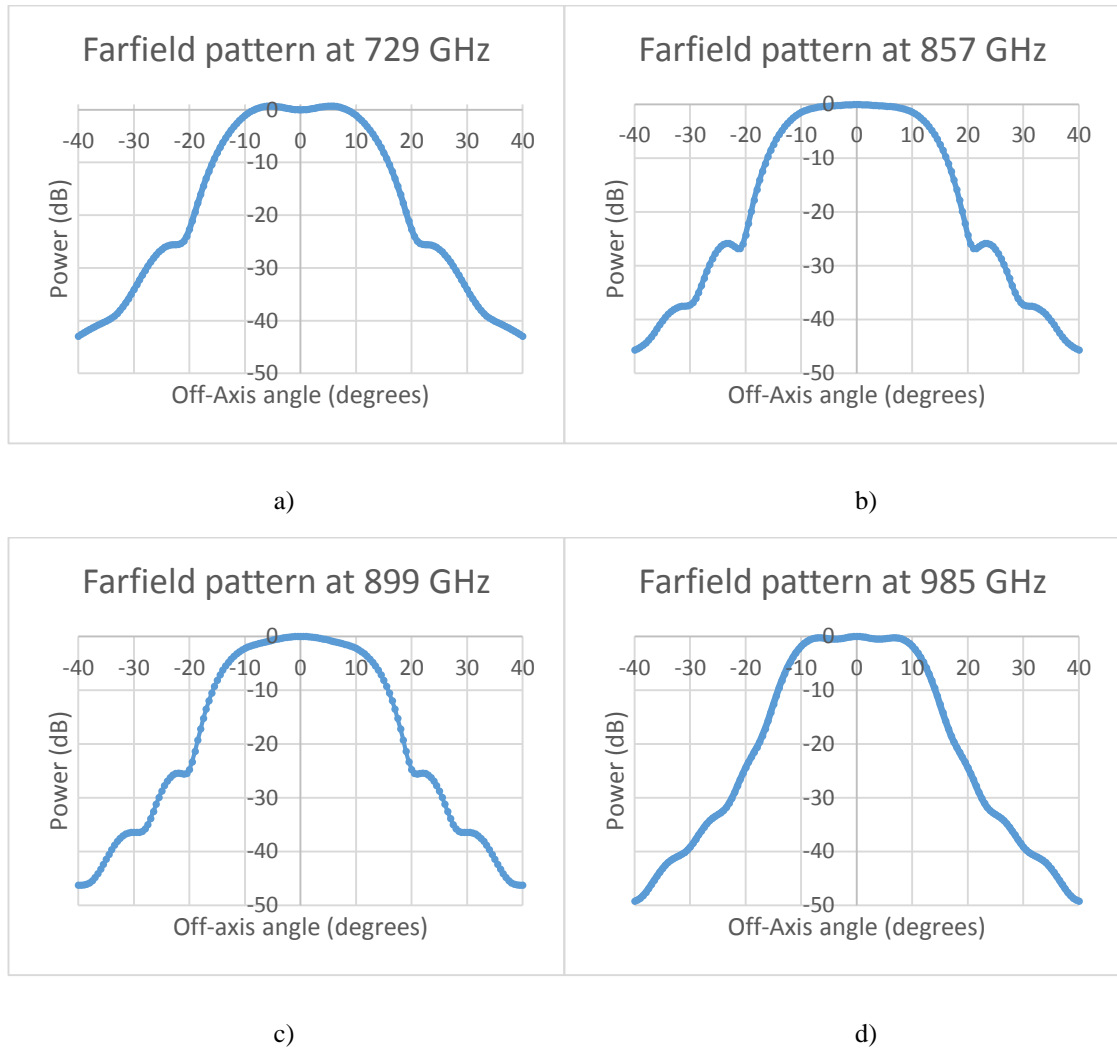


Figure 5.5: Beam pattern simulations produced by Python mode matching software at a number of spot frequencies across the band

This is clearly an approximation, especially for two possible reasons: (i) the assumption that the cavity is a perfect blackbody effectively implies all waveguide modes in the waveguide feeding the cavity are perfectly matched to the cavity, thus, ignoring reflections at the step into the cavity and the fact that the absorber is not perfect; (ii) the filter section could allow power to escape through free space gaps and this should be more accurately included in the modelling. Table 5.1 below summarises the results in terms of

singular values of the $[S_{2l}]$ matrix for the horn as a whole for the case when the thermal filter gap was treated as a continuous waveguide section and the bolometer was approximated as a perfect blackbody source.

Azimuthal order and mode number										
	01	02	03	11	12	13	21	22	31	41
729 GHz	1	1	-	1	0.551	-	1	-	0.954	-
857 GHz	1	1	-	1	0.993	0.95	1	0.955	0.889	0.811
985 GHz	1	0.985	0.837	1	0.972	0.950	1	0.884	1	0.996

Table 5.1: The singular values of the $[S_{2l}]$ matrix for propagating hybrid modes represented from above at some spot frequencies across the band

Clearly, as discussed above, it is an approximation to model the thermal filter gap as a continuous waveguide section (because the filters are in place effectively in a metal cylinder). In fact, it is better modelled as a section of waveguide with the walls missing at the steps into the back-to-back horn and the detector horn. Power carried by the individual modes may be lost through the gap on both sides of the filter section where it meets the detector horn and the back horn. Thus, we need a more thorough approach to model the system as almost inevitably power will be lost from propagating modes there and in an unequal manner which is likely to distort the previously predicted beam patterns.

5.4 Including the filter gap

As an initial analysis of what is happening at the filter section we compute the $[S_{2l}]$ for the system up to that point, still regarding the cavity as a perfect blackbody radiator, which stimulates all modes at the throat of the detector horn equally. We can diagonalise the $[S_{2l}]$ to extract the hybrid modes using the SVD approach outlined in Section 5.2 and Section 5.3 using the $[S_{2l}]$ for the detector horn and filter section (see Figure 5.6). The power carried by each mode can then be calculated from the singular value. We then propagate the modes through the filter section and compute how the singular values of the $[S_{2l}]$ matrix after the filter section are degraded.

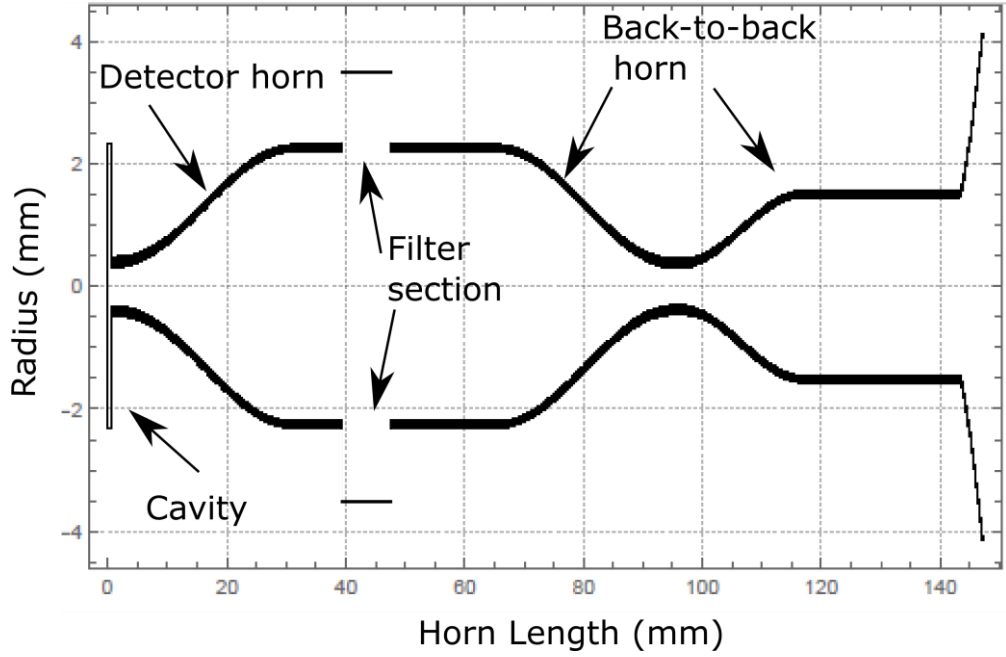


Figure 5.6: Geometry of the 857 GHz horn, including the filter gap

It will now be discussed how this was achieved including the method implemented in the existing smooth walled GAMMA code to take account of this. A metal cylinder effectively encased the filter and this is treated as essentially a waveguide structure for the propagating modes as noted above. However, the conducting walls normally present at a waveguide junction are missing at the ends of the filter section (free space gap). Thus the usual scattering matrix relationships cannot be used and some approximations need to be made. Since the horn apertures (detector and back horn) are large, we can assume no reflections as modes that propagate into the filter section only suffer negligible reflection at the interface to the horn apertures, as there is little conducting material there facing them at the transverse plane of the junction. We therefore assume no reflections at the two interfaces to the filter section from the two horns. In terms of the interface shown in Figure 5.7, this implies $[S_{11}] = [S_{22}] = 0$ for the junction and $[P][A] = [Q][D]$ since $[B]$ and $[C]$ are independent of $[A]$ and $[D]$ (backward and forward propagating waves) or $[S_{21}] = [Q^{-1}][P]$, where $[P]$ is the usual power coupling matrix with elements $P_{m'n'} = \int_{S_L} e_n^L \times h_{n'}^{*R} \cdot dS$ and $[Q]$ is the diagonal self-coupling matrix on the RHS of a junction with $Q_{n'n'} = \int_{S_R} e_{n'}^R \times h_{n'}^{*R} \cdot dS$. But for electrically larger guides we can ignore approximately evanescent modes so that $[Q^{-1}] \approx [I]$ which implies $[S_{21}] \approx [P]$.

A similar argument relating to the backward propagating, [B], and reflection mode amplitudes, [C], gives $[R^*][B] = [Q][P^\dagger][C]$, implying $[S_{12}] \approx [R^*]^{-1}[P^\dagger] \approx [P^\dagger]$ where [R] is the diagonal self-coupling matrix on the LHS of a junction with $R_{nn} = \int_{S_R} e_n^L \times h_n^{*L} \cdot dS$

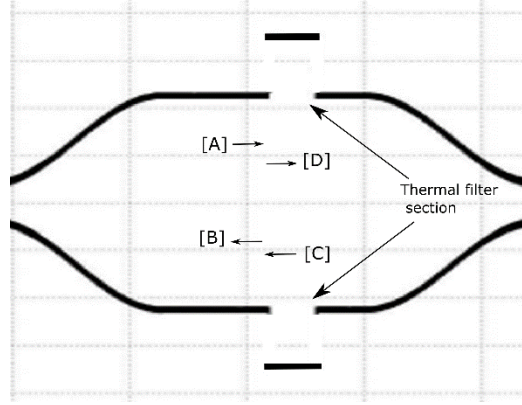


Figure 5.7: The free space gap of the 857 GHz pixel

Thus, the scattering matrices for the waveguide (detector horn aperture) to filter through the free-space section can be approximated as:

$$[S_{11}] = [S_{22}] = [0] \quad (5.1)$$

$$[S_{12}] = [S_{21}]^\dagger = [P] \quad (5.2)$$

where [P] represents the power coupling between the sections of smaller and the larger radius. Similarly, the scattering matrices for a free-space to waveguide section are:

$$[S_{11}] = [S_{22}] = [0] \quad (5.3)$$

$$[S_{21}] = [S_{12}]^\dagger = [P] \quad (5.4)$$

To summarize, this assumes the conducting apertures of rims of the horns at either end of the filter present essentially zero cross section to the modes in the filter section and also that the modes in the back and detector horns do not notice the impedance change into the wider filter section because these horn apertures are already large in terms of the wavelength. Then, effectively because there are essentially no reflections, the power coupled between the modes in the horn and the modes in the filter waveguide is given by the usual power coupling integrals of the [P] matrix in the mode matching scattering theory.

The power losses due to the gap were then investigated again using a perfect blackbody absorber source and extracting the singular values of the $[S_{2l}]$ matrix for the complete waveguide structure immediately before and after the gap. A reduction in singular values (as seen in Table 5.2) points to a loss of power in the resultant hybrid modes propagating into the back horn from the filter section.

Azimuthal order and mode number (at 857 GHz)										
	01	02	03	11	12	13	21	22	31	41
Singular value before filter section	1	1	0.999	1	1	1	1	1	1	1
Singular value after filter section	0.896	0.844	0.620	1	0.730	0.515	0.739	0.970	0.481	0.46

Table 5.2: Singular values of the $[S_{2l}]$ matrix of the propagating modes at the centre of the band (857 GHz) immediately before and after the thermal filter gap

Figure 5.8 (a) to (c) shows the comparison of the resulting farfield beam patterns of the pixel (horn plus filter) as predicted by the in-house GAMMA software at some spot frequencies across the operating band with the gap included. In one case, the losses due to the thermal filter gap were accounted for and the bolometer considered was a perfect blackbody absorber, in the other case the ideal system was considered.

From Figure 5.8 (a) to (c) it can be observed that the beam pattern changes significantly both in terms of shape and gain when the free space gap is being considered. When the gap is accounted for in the GAMMA simulations we observe a decrease in on-axis power, indicating that some power is lost through the gap.

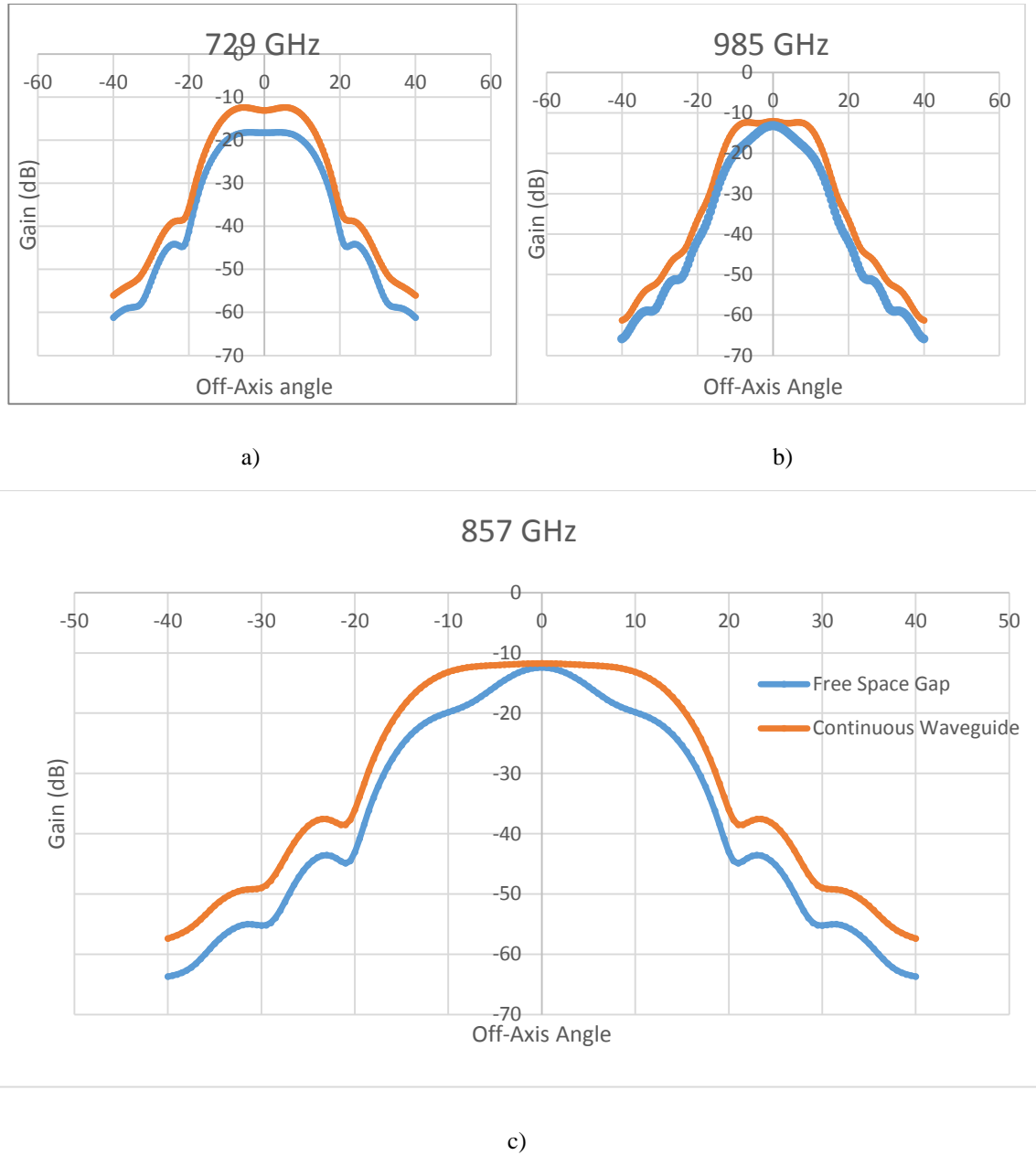


Figure 5.8: Beam pattern simulations of the pixel produced by Python mode matching software at the middle of the operating band, 857 GHz, showing the changes due to the thermal filter gap

Azimuthal order and mode number										
	01	02	03	11	12	13	21	22	31	41
729 GHz	0.662	0.401	-	0.653	0.157	-	0.398	-	0.523	-
857 GHz	0.744	0.292	-	0.92	0.531	0.384	0.516	0.188	0.2	0.25
985 GHz	0.957	0.522	0.322	0.895	0.284	0.103	0.622	0.172	0.275	0.443

Table 5.3: Singular values of the $[S_{2l}]$ matrix for the whole Planck 857 GHz of the propagating modes at the lower edge, middle and upper edge of the operating band

Table 5.3 summarises the singular values at the lower, middle and upper edge of the band for the case when the effects of the filter gap and included and the cavity considered is a blackbody source. These values indicate significant loss of power for several of the modes.

5.5 Modelling the detector in the cavity

This subsection describes the approach taken to improve the model further by including the detector in the cavity in the simulations (rather than a blackbody cavity). If we calculate the reflection scattering matrix, $[S_{II}]$, for the system as a whole, treating the pixel now as a receiver rather than a radiator as in the previous section, and including the horn antenna, waveguide feed and cavity, we can infer that power that is not reflected back into backward propagating modes at the horn aperture must have been absorbed by the cavity or lost through the filter gap.

Firstly, in order to isolate the absorption of the bolometric detector in the cavity, we first assume that the filter section is a continuous waveguide, as in section 5.3, so there is no power lost. This is what we regarded previously as the ideal case. The cavity structure is essentially the last section to be cascaded on to the overall structure and is regarded as a waveguide structure with one end closed, taking into account that power is lost due to absorption by the bolometer detector, which we can approximate as a current sheet. With this approach, it is then possible to recover the absorbed power for each propagating n at the horn aperture (input port) that is coupled to the incident field from the sky (a plane wave at the antenna generated by a point source at infinity in the direction (θ, ϕ)). The relative power absorbed as the source is moved around the farfield gives the power pattern of the horn. This can be calculated from the $[S_{II}]$ matrix at the horn aperture to produce the beam on the sky $P_{sky}(\theta, \phi)$.

Using the relationship given in Equation (5.5) the power pattern may be obtained (see Figure 5.9).

$$\mathbf{e}_{ff}(\theta, \phi) = \sum_n (1 - \sigma_n^2) \mathbf{e}_{n,ff}(\theta, \phi) \quad (5.5)$$

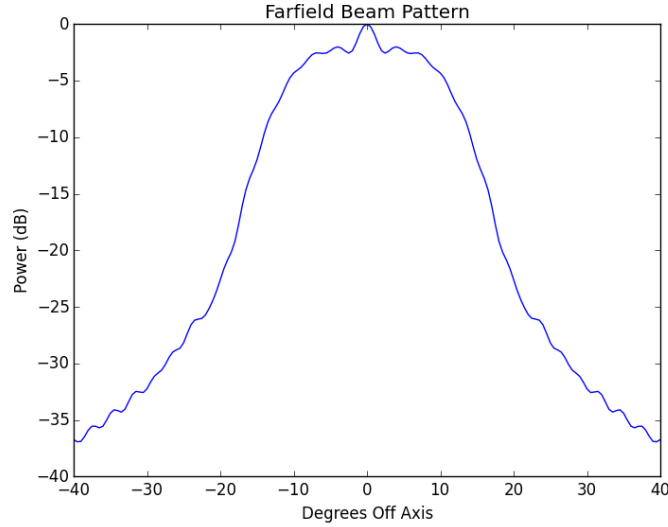


Figure 5.9: Simulated farfield power pattern at 857 GHz

where $\mathbf{e}_{n,ff}$ in Equation (5.5) are the farfields of the output singular vectors of the singular value decomposition of the $[S_{II}]$ matrix and $(1 - \sigma_n^2)$ is the power absorbed by the j^{th} singular vector. Care must be taken with evanescent modes in this approach as such modes do not propagate to the farfield, but are completely attenuated. To remove these, a section of parallel cylindrical waveguide is added to the front of the horn and the propagation constants in the $[V]$ matrix are set equal to $V_{nn} = |e^{i\gamma_{nn}z}|$ thus giving unity for propagating modes and 0 for evanescent modes.

Clearly, this approach cannot be used if there is another source of loss in the system such as a free space gap through which signal power can escape as is the case for the Planck pixels. Using the $[S_{II}]$ matrix directly, in this case it is not possible to distinguish between the power absorbed in the cavity and power lost through any gaps in the system. Thus, in order to model the full bolometer system including the free space gap, we split the system into two different parts: (i) the absorbing cavity plus its feed waveguide and (ii) the rest of the system, including any feed horn and waveguide sections with gaps, and we also apply reciprocity as previously (treating the horn as a radiator) in contrast to the approach above, where the horn aperture is the input port. The overall $[S_{21}]$ matrix of the whole system (required to determine the beam pattern of the horn using reciprocity) is obtained by cascading the resulting scattering matrices for the cavity and the rest of the system:

$$[S_{21}^{full}] = [S_{21}^{horn}] \cdot [I] - [S_{22}^{cav}] \cdot [S_{21}^{horn}]^{-1} \cdot [S_{21}^{cav}] \quad (5.6)$$

where the *cav* clearly refers to cavity and its input waveguide, and *horn* refers to the rest of the system including the back to back and detector horns and the waveguide filter structure with the lossy gap. Again, we assume the pixel is a radiator. Thus, this equation essentially indicates that in order to model the absorbed power and include both the lossy sections in the detector element (free-space gap) and the bolometer in the cavity, the cavity can again be modelled as a radiator with an appropriate $[S_{21}]$ derived.

We can construct an approximation to the $[S_{21}^{cav}]$, again using an SVD approach. We begin with, singular value decomposition (SVD) applied to reflection from the cavity as viewed from the detector horn looking into the cavity (*i.e.* exit port of cavity):

$$[S_{22}] = [U][\Sigma_{22}][V^\dagger] \quad (5.7)$$

where, as before, $[\Sigma_{22}]$ is a diagonal matrix of singular values

$$[\Sigma_{22}] = [\sigma_1, \sigma_2, \sigma_3, \dots] \quad (5.8)$$

and $[U]$ and $[V]$ are the left and right singular vectors of $[S_{22}]$. We can regard the U and V matrices as the natural modes of the cavity as viewed from its exit port. The resulting $[S_{21}]$ matrix is then constructed using these modes and a set of singular values that represent the fraction of the power that is not reflected:

$$[S_{21}] = [U][\Sigma_{21}][V^\dagger] \quad (5.9)$$

where $[\Sigma_{21}]$ is a diagonal matrix of singular values

$$[\Sigma_{21}] = [\sqrt{1-\sigma_1^2}, \sqrt{1-\sigma_2^2}, \sqrt{1-\sigma_3^2}, \dots] \quad (5.10)$$

Table 5.4 shows the singular values of the total $[S_{21}]$ scattering matrix extracted at the aperture of the horn at the central frequency of the band (857 GHz) for the complete pixel, for the various cases considered. The singular values are compared for the case where (i) no losses were modelled in the structure (thermal filter gap treated as a continuous waveguide junction and cavity modelled as a perfect blackbody absorber, original approach taken in the design of the Planck 857 GHz horns), (ii) the losses due to the filter gap were included and the cavity was modelled as a perfect blackbody absorber, and (iii) the losses due to the filter gap were included and the bolometer was modelled within the cavity. It can be seen in Table 5.4 and Figure 5.10 to Figure 5.12 that the free-space gap

at the thermal filter section has a significant effect on the singular values and beam patterns and the effect of a more realistic model of the cavity is only marginal. This, of course, implies the cavity acts as a near perfect absorber for the system.

Azimuthal order and mode number (857 GHz)										
	01	02	11	12	13	21	22	31	41	$\sum_n \sigma_n^2$
Singular Values (Ideal Case)	1	1	1	0.993	0.95	1	0.955	0.889	0.811	14.49
Singular Values (Gap)	0.762	0.301	0.986	0.526	0.411	0.516	0.197	0.201	0.25	4.32
Singular Values (Gap and Bolometer)	0.744	0.292	0.92	0.531	0.384	0.516	0.188	0.2	0.25	4.00

Table 5.4: The singular values of the propagating modes at the centre of the band, comparing the ideal case and the lossy cases

The rightmost column of Table 5.4 above includes the sum of the singular values of the propagating modes at 857 GHz for the three variations of the pixel that were investigated. Note that modes with azimuthal order $n = 0$ are only included once and modes with $n > 0$ need to be included twice to also account for the orthogonal modes. It can be seen that for the ideal pixel, this sum is 14.49. For the case of modelling the losses due to the free space filter section and using a perfect blackbody cavity, the sum of the propagating hybrid modes drops to 4.32, indicating a significant amount of the power was lost through the filter gap. Modelling the losses associated with both the bolometer and the free space filter section, the sum of the propagating singular values sums to 4.00, indicating that the bolometer absorbs most power incident on it. This is clearly illustrated in Figure 5.10 to Figure 5.12.

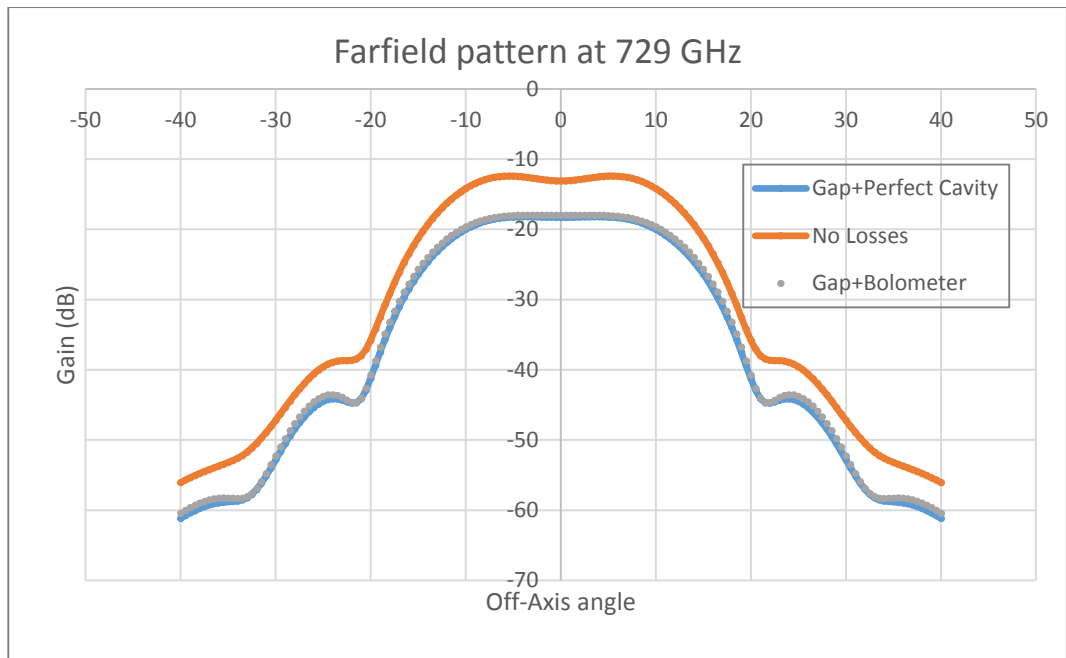


Figure 5.10: Beam patterns comparing the case where no losses are present (orange line) in the structure with the case where the free-space gap was modelled (blue line) and also where both the free-space gap and bolometer inside the cavity were modelled (grey dotted line) at 729 GHz

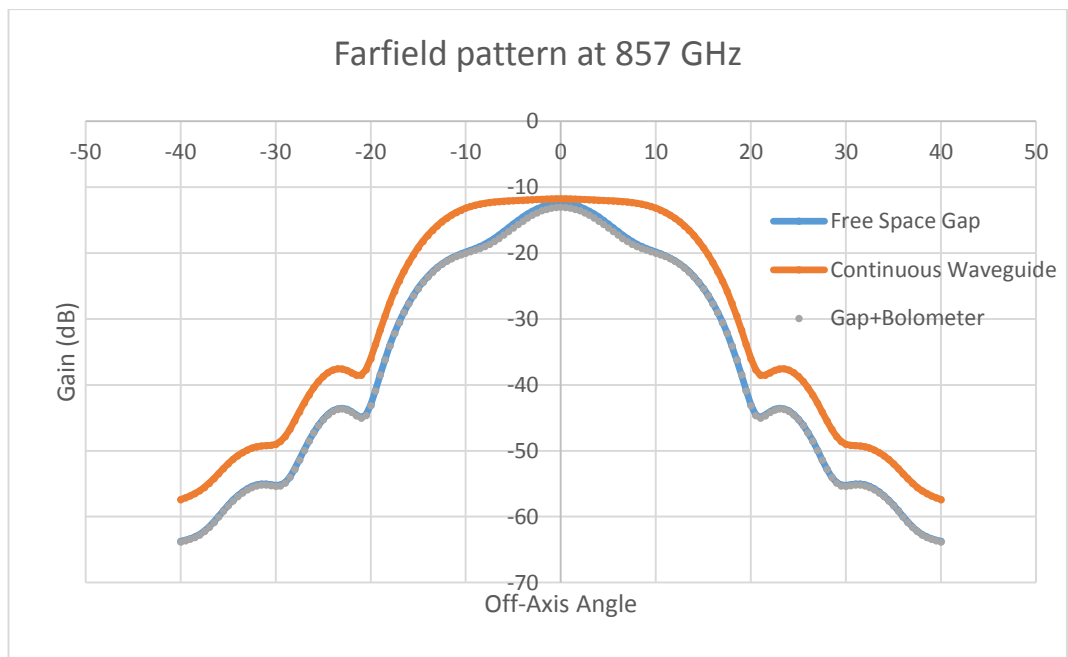


Figure 5.11: Beam patterns comparing the case where no losses are present (orange line) in the structure with the case where the free-space gap was modelled (blue line) and also where both the free-space gap and bolometer inside the cavity were modelled (grey dotted line) at 857 GHz

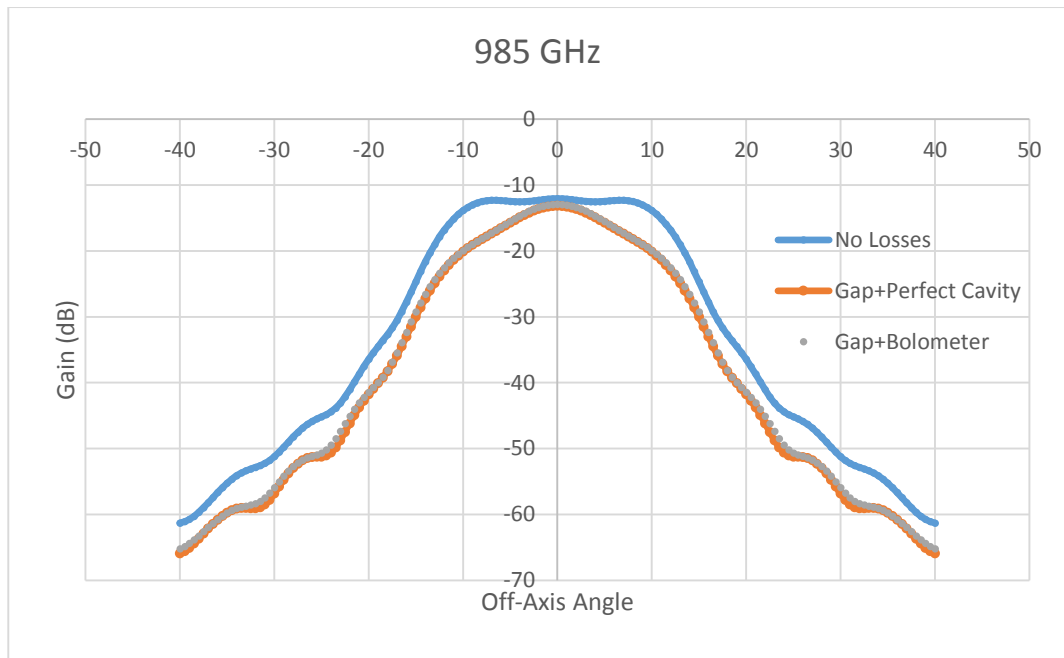


Figure 5.12: Beam patterns comparing the case where no losses are present (blue line) in the structure with the case where the free-space gap was modelled (orange line) and also where both the free-space gap and bolometer inside the cavity were modelled (grey dotted line) at 985 GHz

Figure 5.13 and Figure 5.14 below shows the resulting farfield beam patterns of the full Planck 857 GHz pixels (free space gap was modelled and bolometer effects were included) as simulated by GAMMA in 5 GHz steps across the operating band. The figures illustrate how the beam changes over the operating band, both in terms of on-axis power levels and the beam shape. For clarity only cuts for $\phi = 0^\circ$ (not across the beam at $\phi = 0^\circ$ and $\phi = 180^\circ$) are given.

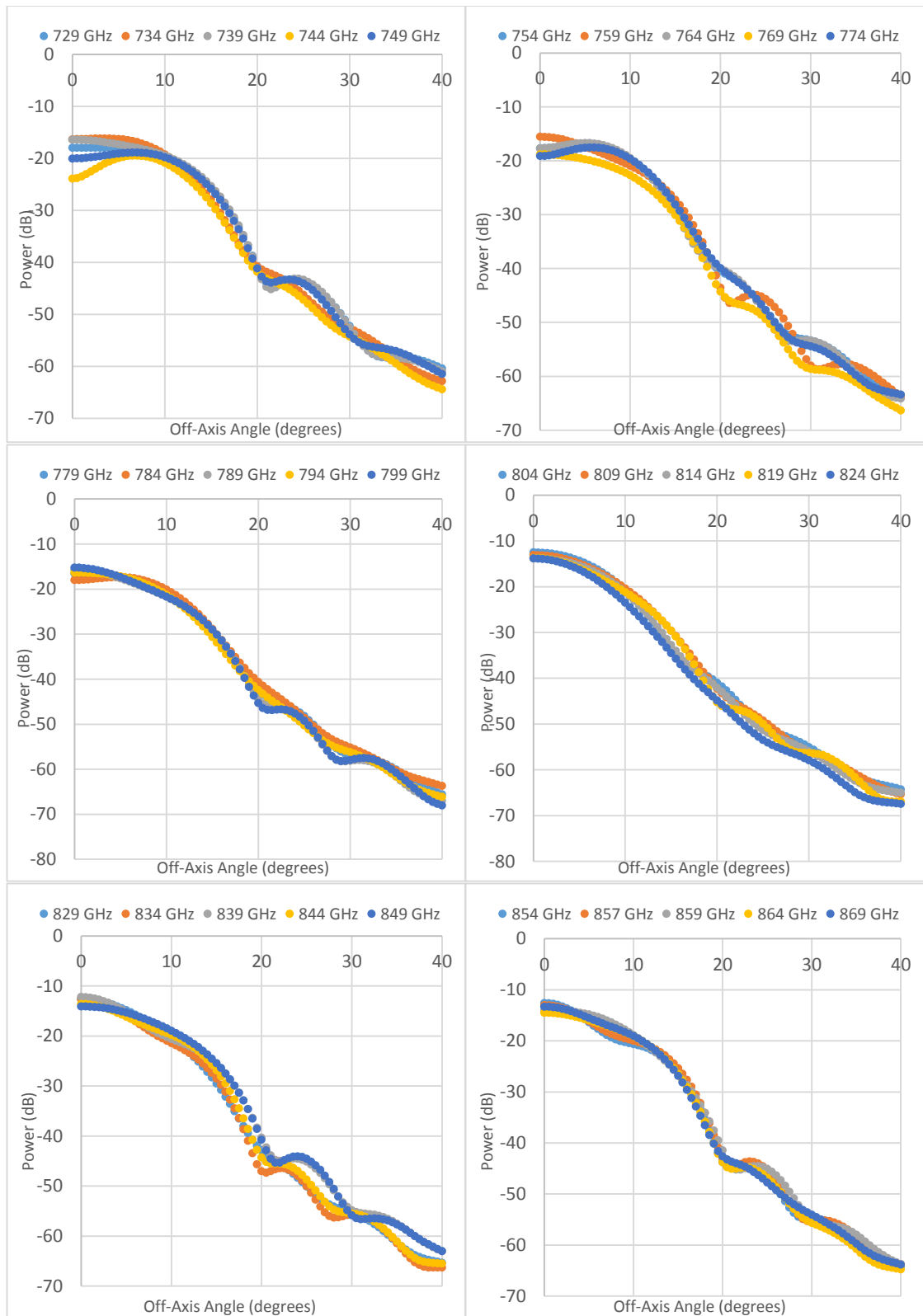


Figure 5.13: Farfield plots of the 857 GHz horn from 729 GHz to 869 GHz in steps of 5 GHz

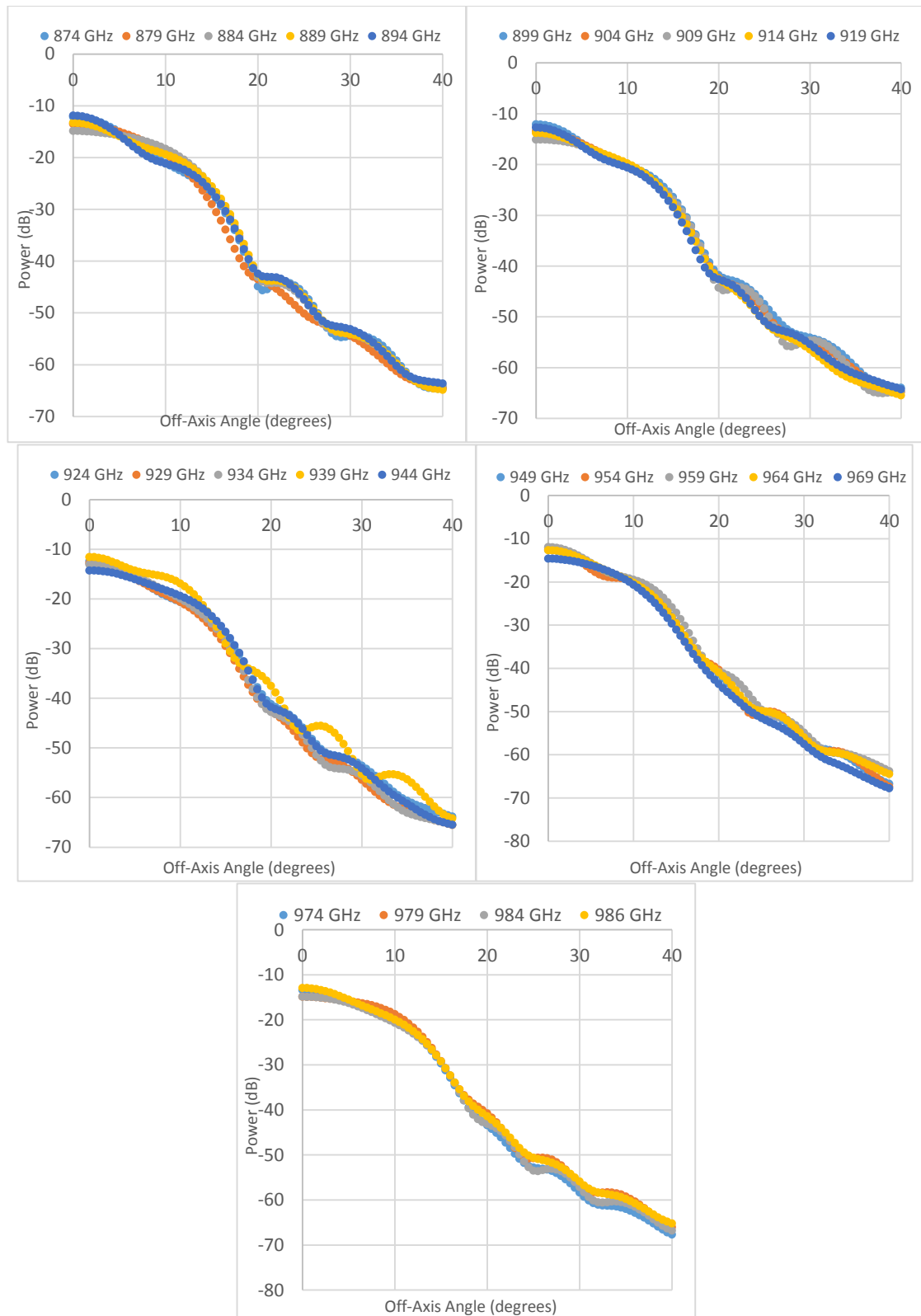


Figure 5.14: Farfield plots of the 857 GHz horn from 874 GHz to 986 GHz in steps of 5 GHz

5.6 Modelling of the Planck telescope in GRASP9

We now consider how the various levels of approximation when modelling the Planck pixel feed into the beam predictions on the sky. In order to calculate the beams, physical optics provides the most accurate results for reasonable computation efficiency. GRASP9 was used to carry out the simulations. A description of the GRASP9 software can be seen in Section 3.3.

The known aperture field from the horn was read in by GRASP9 as a *Tabulated Planar Source*. Since the detector is overmoded, it is important to maintain relative power levels between the modes as they do not contribute equally to the field at the aperture. A grid file to be read in by GRASP9 was created for each propagating hybrid mode. A Mathematica script was written to generate the grid files. The Mathematica script first reads in the scattering matrices ($[S_{21}]$) generated by the GAMMA software for each azimuthal order n . The scattering matrix may be re-written as $[S_{21}] = [U][\Sigma_{21}][V]$ using singular value decomposition, where $[\Sigma_{21}]$ is a rectangular diagonal matrix containing the singular values. The waveguide mode amplitude coefficients for the hybrid modes are given by the columns of the $[U]$ left singular value matrix. Thus, for azimuthal order (n) the j^{th} hybrid mode \mathbf{e}_{nj} is given by:

$$\mathbf{e}_{nj} = \sum_{n=1}^N U_{ij}^{(n)} \mathbf{e}_{ni}^{TE/TM} \quad (5.11)$$

where N represents the total number of modes used, U_{ij} is the ij^{th} element of the $[U]$ left singular value matrix for the n th order and $\mathbf{e}_{ni}^{TE/TM}$ is the appropriate waveguide mode depending on how the modes are ordered. The contribution to the total aperture field due to each orthogonal hybrid mode pair to be read in by GRASP9 is given by

$$\mathbf{e}_{ap} = \sigma_{jj}^{(n)} \mathbf{e}_{nj}, \quad (5.12)$$

where σ_{jj} is a singular value along the diagonal of $[\Sigma_{21}]$ and is less than unity because of the attenuation of the mode in the filter section.

The radius at the aperture of the 857 GHz pixel was 4.231 mm, thus a square grid of data was implemented with a mask to zero pad the region outside the aperture. The resulting patterns were specified in a file containing appropriate GRASP9 header data including the dimensions of the waveguide and the sampling interval of the fields, as well as the

frequency and co-ordinate system being used. The source file had to be referenced to a co-ordinate system within GRASP9, where the source itself was located within the xy -plane and the phase centre was located at the origin of the co-ordinate system. The input generated for every hybrid mode by GAMMA was in the form of the E-field. GRASP9 allows for the possibility of normalising the radiated power to 4π Watts, however, this normalisation was not carried out since the 857 GHz horns are multimode, and it was important to maintain relative power levels between the modes.

The farfield pattern of the 857 GHz horn was obtained by both GAMMA (by summing the far-field patterns of the modes) and GRASP9 and is shown in Figure 5.15, where (a) and (b) show the farfield pattern for both the ideal and lossy case normalized to 0 dB. It can be seen that both GAMMA and GRASP9 predict an identical farfield pattern as expected (verifying GAMMA code for farfield patterns of horns). Figure 5.15, (c) and (d) shows the farfield pattern of the 857 GHz, with the power levels not normalized to 0 dB on-axis so that the power loss due to the filter section on the horn beam patterns could be visualised. In both cases there is an on-axis power difference of 1.3 dB.

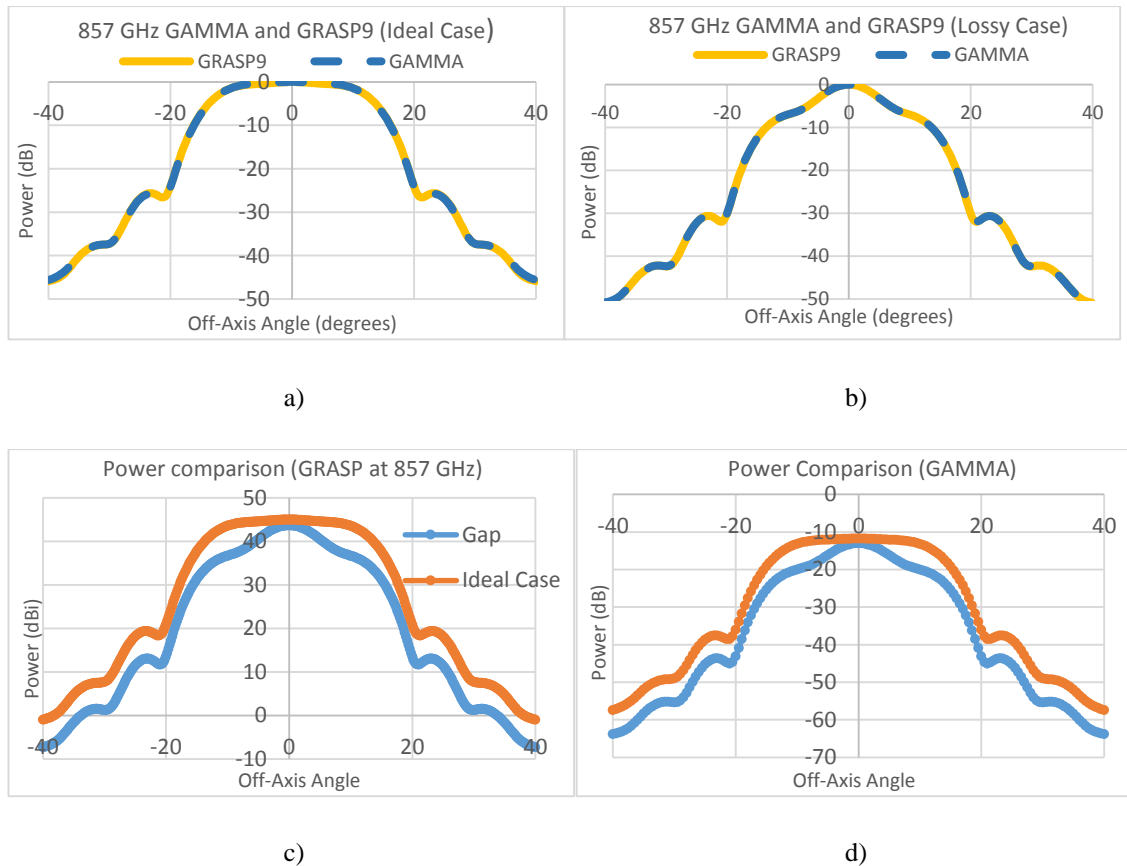


Figure 5.15: Farfield patterns of the ideal and lossy 857 GHz pixel as predicted by GRASP9 (a and c) and GAMMA (b and d) normalized to 0 dB on-axis in a) and b)

The beams on the sky were then obtained by propagating the individual attenuated hybrid mode aperture fields, through the telescope and onto the sky. The accuracy to which the field should be measured on the surface of interest was automatically specified in GRASP9. This was determined by the PO sampling. The beams on the sky were then added in quadrature (*i.e.* the intensities of the hybrid mode power patterns were added). The model (see Figure 5.16) was simplified by excluding all payload blockages, which will have some effect on far-out side lobe structures (Wilson, 2014: 110).

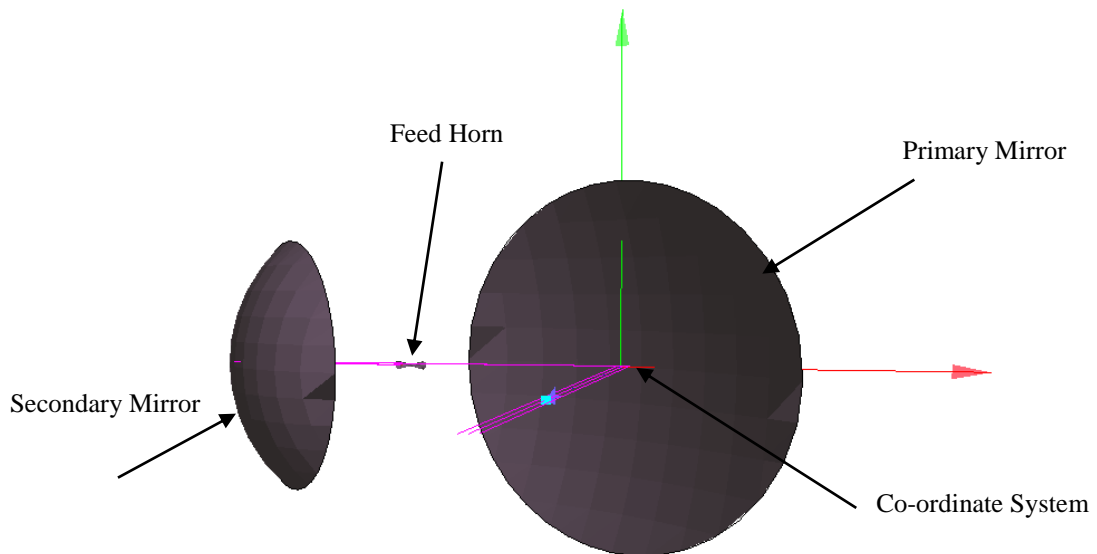


Figure 5.16. GRASP9, Primary, Secondary, Feed, Co-ordinate system and Output Grid

To begin with, the currents on the secondary reflector need to be computed. The secondary mirror was specified as a Physical Optics object. The *Get Currents* command triggered the computation of PO currents on the secondary mirror from the illuminating source. The *Get Field* command was used to compute the fields from the given source at the points specified in the relevant *Field Storage* object. Once the currents on the sub-reflector were calculated, they were then used as the source for calculating the currents on the main reflector. A similar procedure was used for the primary mirror and the beams on the sky.

We now wish to compare these computed fields with published data on the Planck 857 GHz pixels. Figure 5.17 below shows the scanning beams reconstructed from observations of planets plotted in logarithmic contours (Planck Collaboration, 2014(VII)). The layout of the focal plane on Planck can also be seen in Figure 5.17, indicating the positions of the various frequency channels.

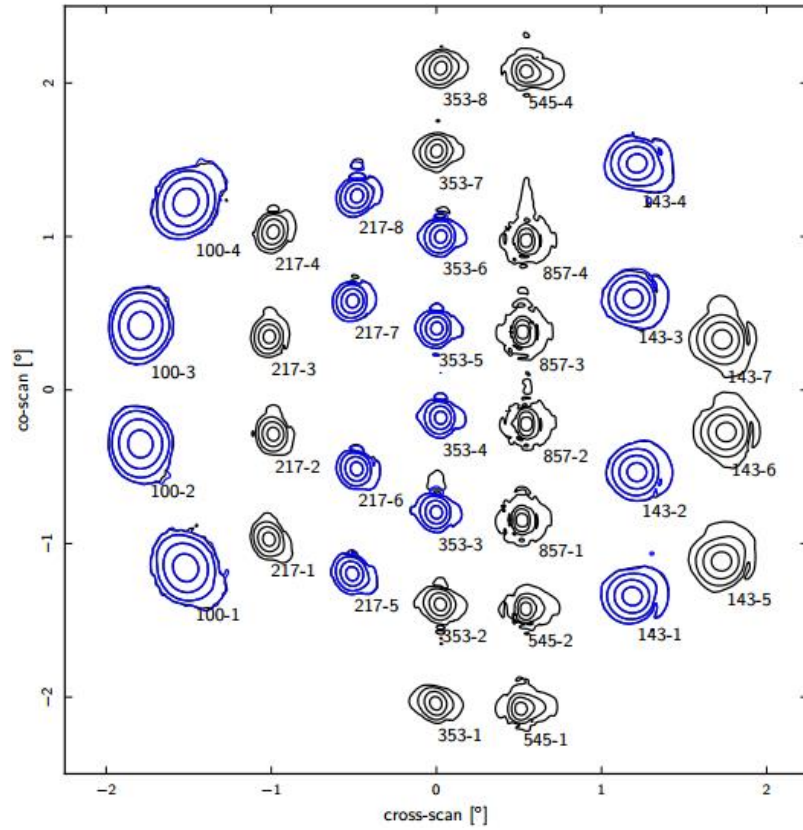


Figure 5.17: Focal Plane Unit of Planck

The beams on the sky were computed and examined for the pixel located at 857-1 on the focal plane unit. Figure 5.18 to Figure 5.23 below show the beams on the sky, with the 857-1 horn used as the source, comparing the ideal case (no losses in pixel) with the lossy case (free-space gap in the filter section of the pixel included and a cavity with the bolometer also included in the model). The beams were examined at three spot frequencies across the band. These frequencies correspond to the lower (729 GHz), middle (857 GHz) and upper (986 GHz) edge of the operating band. At each frequency, two cuts of the contour beam are presented, with one cut taken along the direction of the scan (co-scan) as in Figure 5.18 (a), Figure 5.20 (a) and Figure 5.22 (a), and the other cut taken in the orthogonal direction (cross-scan) as in Figure 5.18 (b), Figure 5.20 (b) and Figure 5.22 (b).

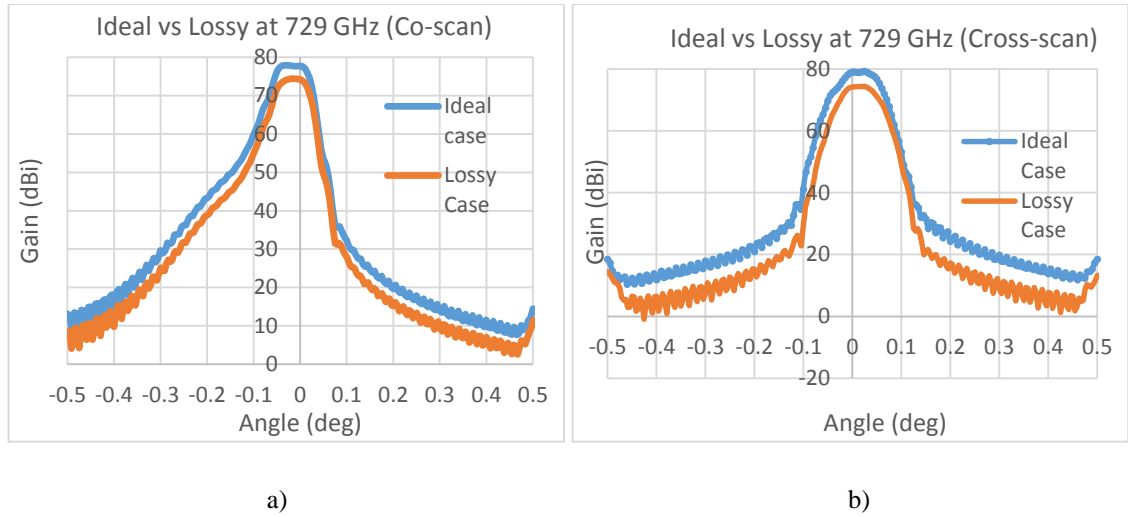


Figure 5.18: Resulting beams on the sky along the co-scan (a) and cross-scan (b) direction modelled at 729 GHz for the case where no losses were considered (blue) and for the case where a bolometric cavity and free-space gap were modelled (orange)

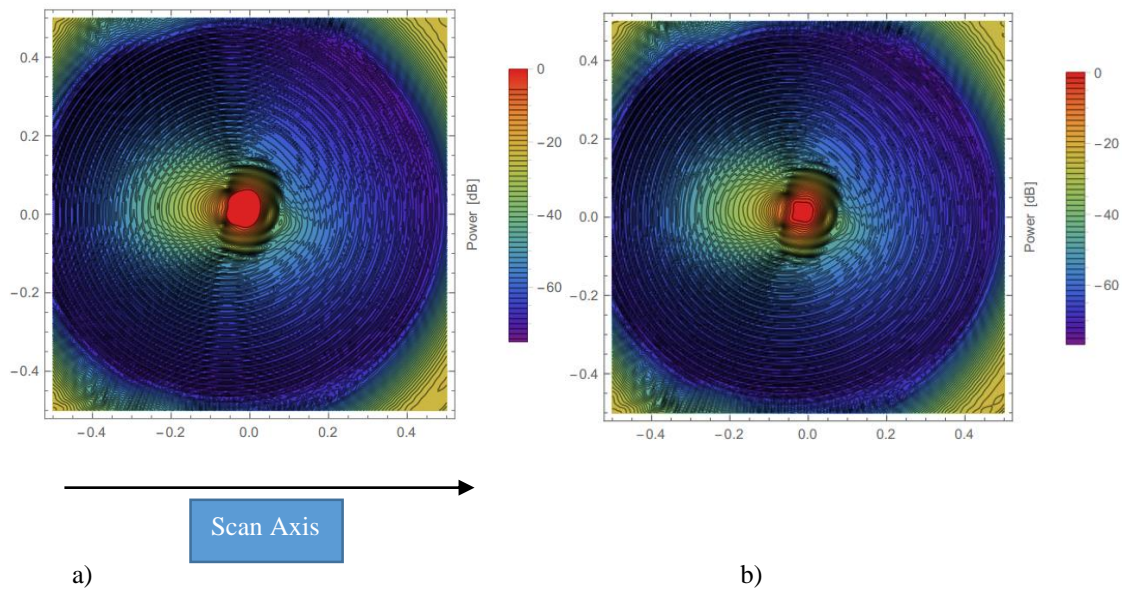
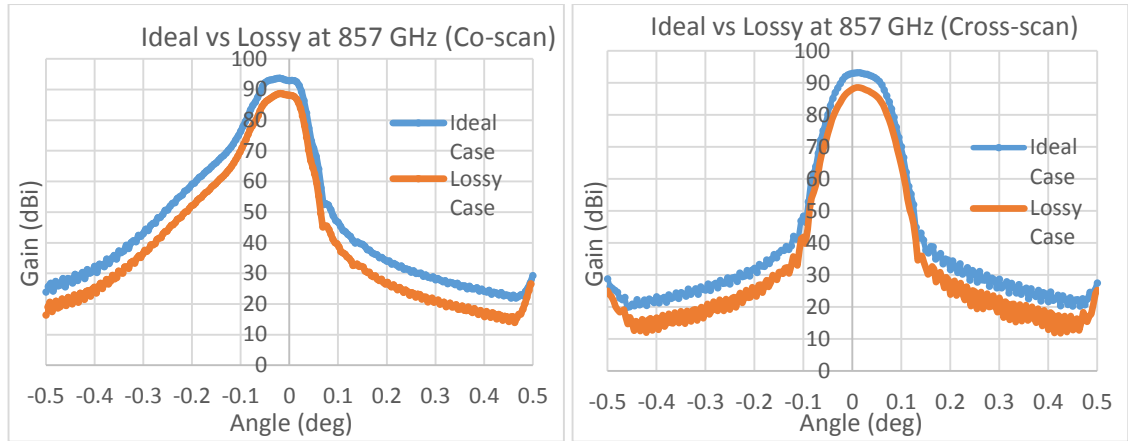


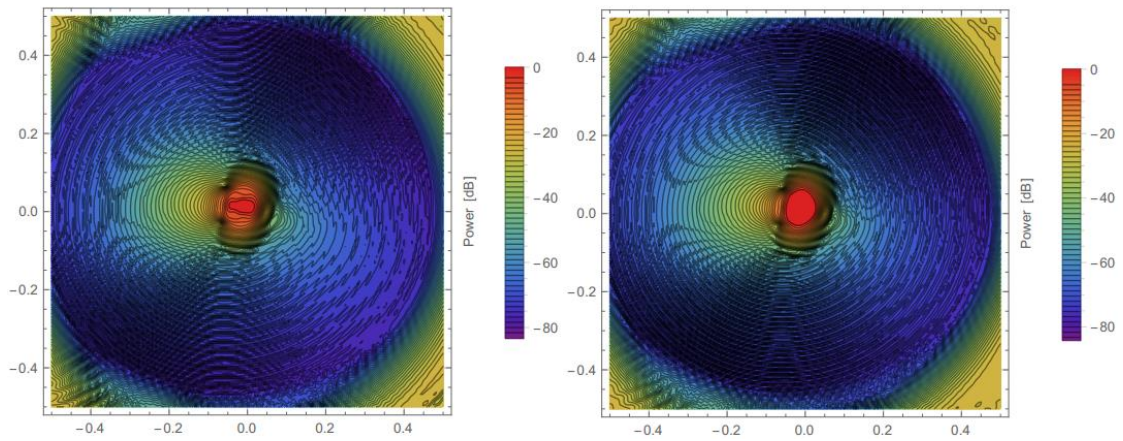
Figure 5.19: Resulting contour beams on the sky modelled at 729 GHz for the case where no losses were considered (a) and for the case where a bolometric cavity and free-space gap were modelled (b)



a)

b)

Figure 5.20: Resulting beams on the sky along the co-scan (a) and cross-scan (b) direction modelled at 857 GHz for the case where no losses were considered (blue) and for the case where a bolometric cavity and free-space gap were modelled (orange)



a)

b)

Figure 5.21: Resulting contour beams on the sky modelled at 857 GHz for the case where no losses were considered (a) and for the case where a bolometric cavity and free-space gap were modelled (b)

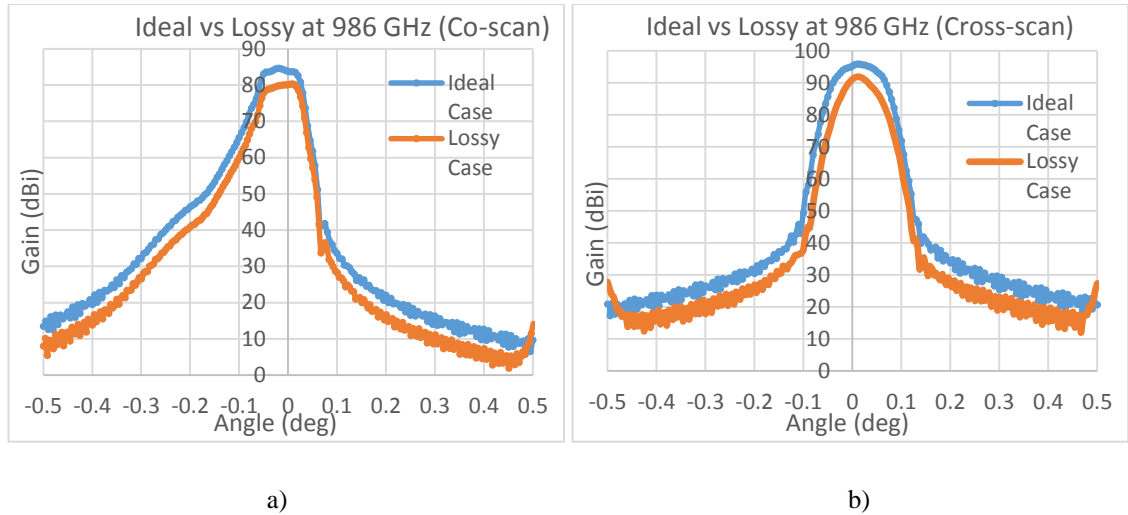


Figure 5.22: Resulting beams on the sky along the co-scan (a) and cross-scan (b) direction modelled at 986 GHz for the case where no losses were considered (blue) and for the case where a bolometric cavity and free-space gap were modelled (orange)

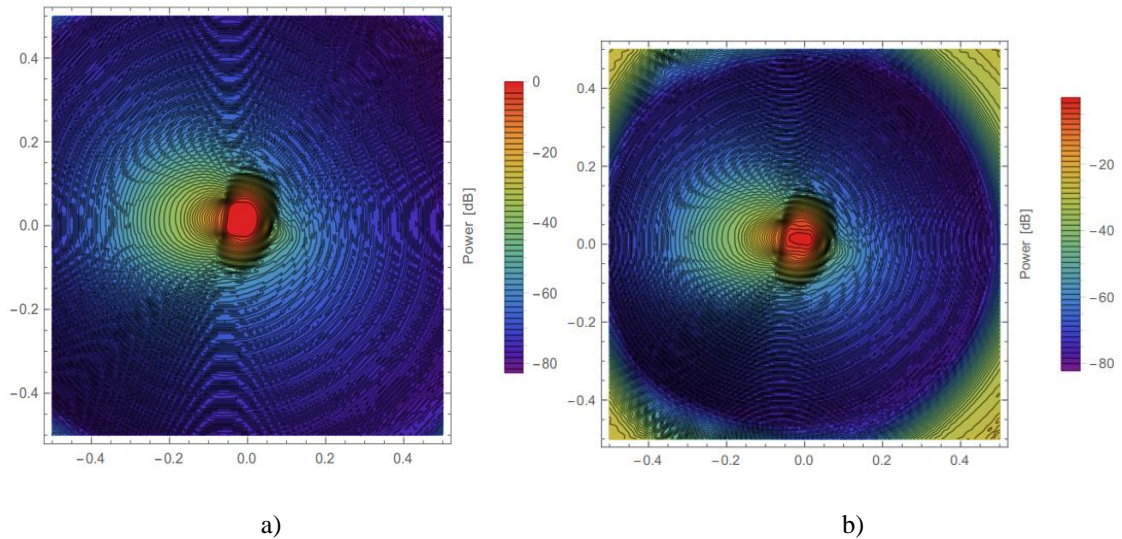


Figure 5.23: Resulting contour beam on the sky modelled at 986 GHz for the case where no losses were considered (a) and for the case where a bolometric cavity and free-space gap were modelled (b)

From Figure 5.18 (a), Figure 5.20 (a) and Figure 5.22 (a) above, a change in the shape of the beam on the sky is observed when the filter section has been accounted for with the beams becoming less top-hat like (indicating power was lost in the higher order modes), a drop in the on-axis gain of ~ 4 dB is also observed. When taking a cut of the beam in the direction that is orthogonal to the scan, the beams are more symmetric as expected, although the on-axis gain and beam width are still reduced, again consistent with power loss through the filter section. Note that the scan direction defined the axis of asymmetry

in the telescope (as is clear from Figure 5.17), and therefore the cross-scan direction defines the axis of symmetry.

Broadband beams

The beam patterns on the sky were computed at 5 GHz steps across the operating band of the 857 GHz horn ($\pm 15\%$). The beam patterns produced were azimuthally and band averaged to simulate the broadband beam pattern. The contour plot in Figure 5.24 is a 241×241 grid of values, which were averaged across the band in 5 GHz steps.

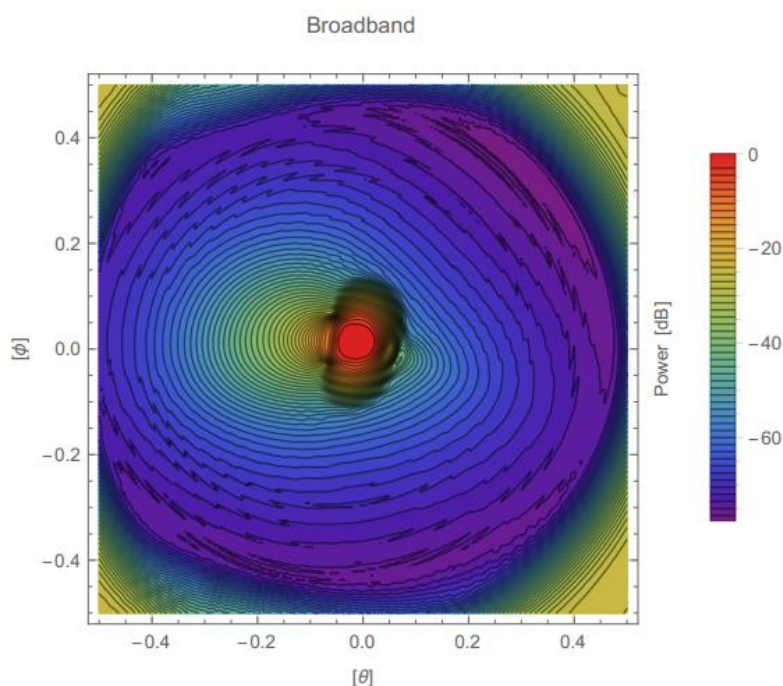


Figure 5.24: Resulting broadband contour beam on the sky for the case where a bolometric cavity and free-space gap were modelled

Taking a cut through along the co-scan and cross scan axis produces the beams shown in Figure 5.25 (a) and (b).

In order to compare with the detailed published beams (Planck Collaboration, 2014 (VII)) on the sky measured using published data on the planets, we need to azimuthally average these beams to include the effect of the convolution of the planet with the telescope beam as presented in the paper (Planck Collaboration, 2014). This can be achieved by dividing the beam into annuli rings (as in Figure 5.26) of radius r and azimuthally averaging the

beam intensity for that value of r , *i.e.* $P_{av}(r) = \frac{\int P(r, \phi) dA_r}{\int dA_r}$, where dA_r is a segment of

the annulus of radius r . The contour beam was divided into annuli rings of varying radius. The area of each annulus (with the exception of the innermost disc) is defined by:

$$A = \pi(r_{outer}^2 - r_{inner}^2) \approx 2\pi r_{av} \Delta r \quad (5.13)$$

where $\Delta r = r_{outer} - r_{inner}$ and $r_{av} = \frac{r_{outer} + r_{inner}}{2}$.

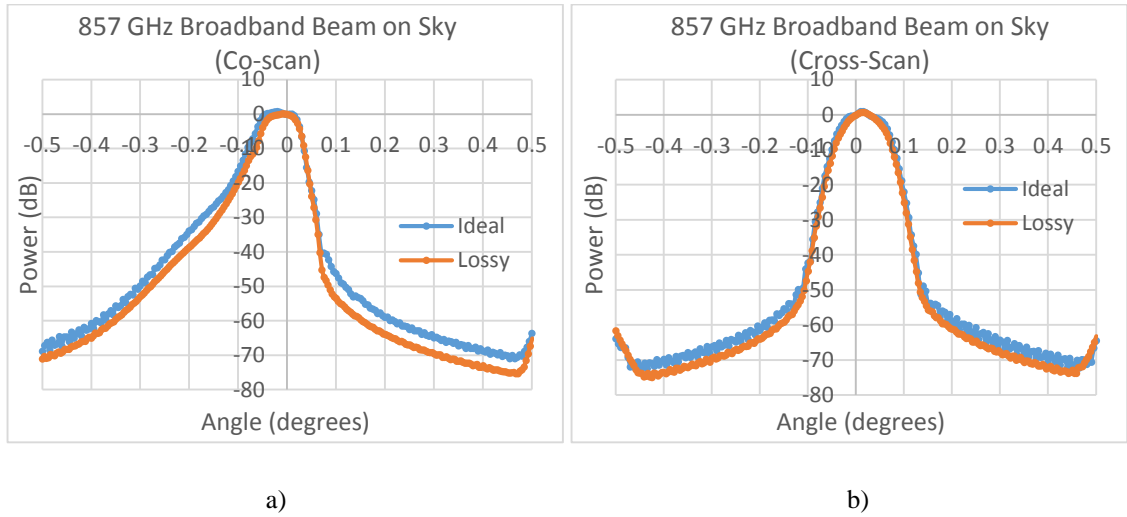


Figure 5.25: Cut along the co-scan (a) and cross-scan (b) direction of the broadband contour beam on the sky both for the ideal case (blue) and for the case where a bolometric cavity and free-space gap were modelled (orange)

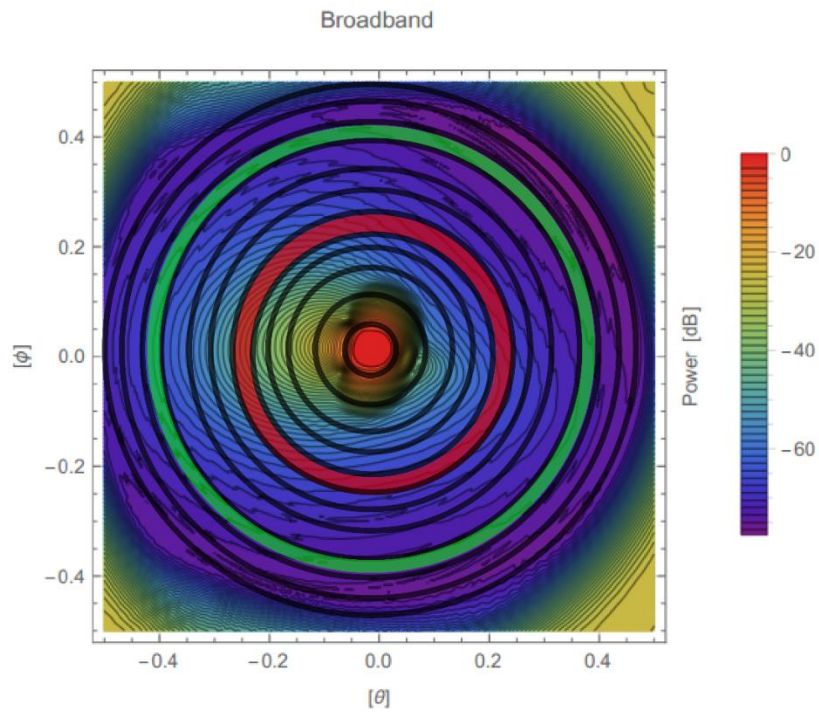


Figure 5.26: Resulting broadband contour beam on the sky for the case where a bolometric cavity and free-space gap were modelled divided into rings of increasing radius (dr)

The annulus was then further sub-divided into a large number of segments, N_i subtended at an angle $\Delta\phi$, where each segment is approximately rectangular of sides $\Delta r \times r_{av}\Delta\phi$ (as indicated in Figure 5.27).

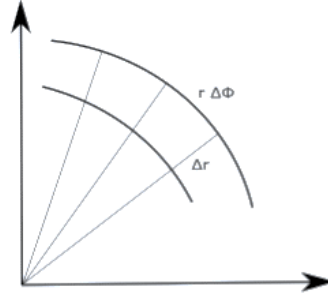


Figure 5.27: A cylindrical co-ordinates grid

Thus the band averaged beam is given by:

$$P_{av}(r_i) = \frac{\sum_i P(r_i, \phi_{ij})}{2\pi r_i \Delta r} = \frac{r_i \Delta r \Delta\phi_i}{2\pi r_i \Delta r} \quad (5.14)$$

In order to avoid over-sampling in the inner region and under-sampling in the outer regions, the number of samples taken at each annulus was set proportional to the radius of that particular annulus, *i.e.* $N_i \propto r_i$.

Figure 5.28 below shows the azimuthally and band averaged simulated beam (both ideal and lossy) compared with the main beam profile derived from observations of planets (Planck Collaboration, 2014 (VII)).

Good agreement between the simulated (lossy) and observations is observed to ~ -15 dB level. The simulated ideal beam is wider as expected because the lossy filter section is not included in the model. Note the fact that the observed beam deviates from the simulated beam beyond 5 arcmin is due to spill over and scattering effects not included in the simulations (see discussion in (Wilson, 2014: 149)).

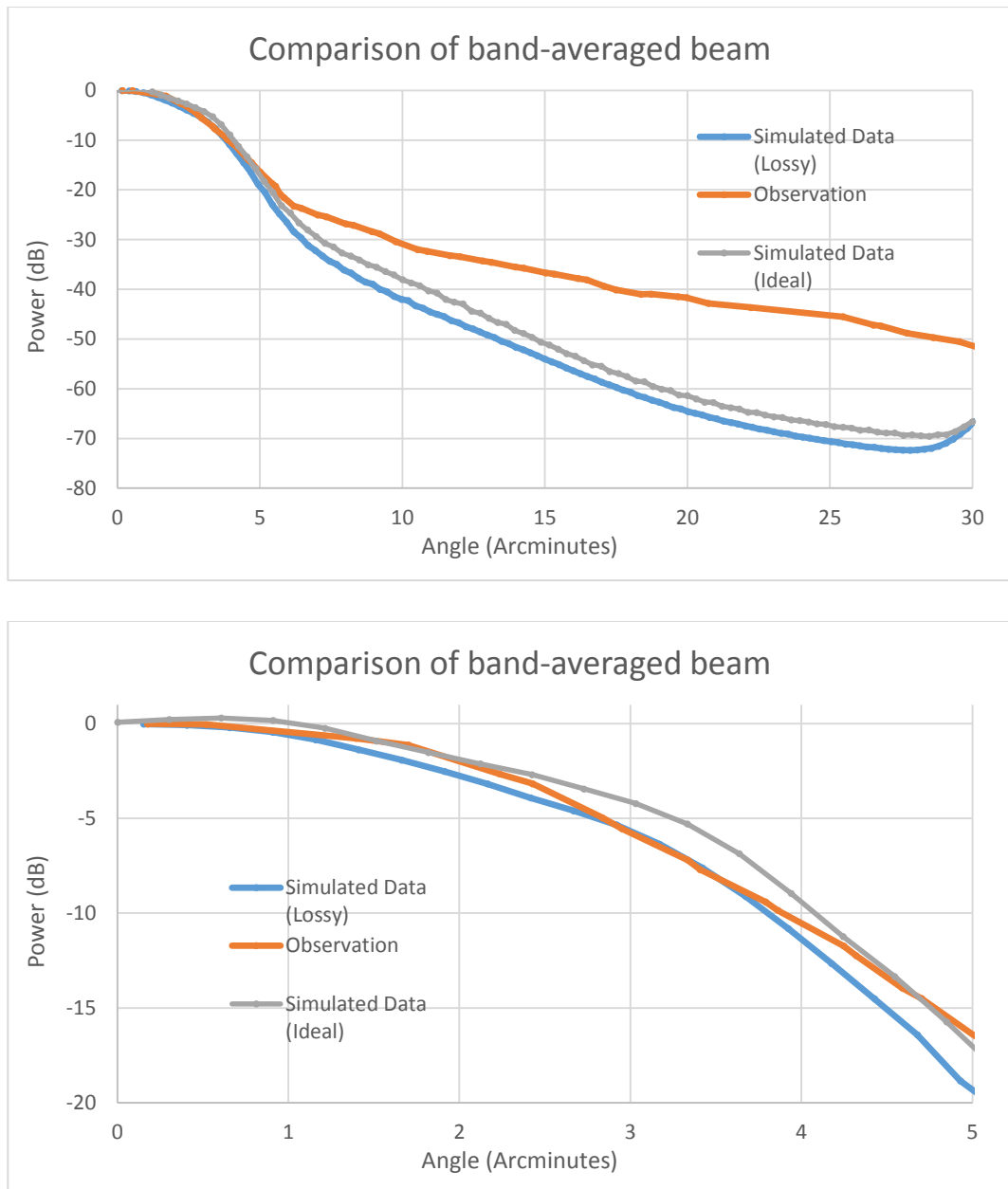


Figure 5.28: (Top) Band averaged main beam profiles comparing the mode matching and PO model (blue line for lossy case, grey line for ideal case) with main beam profile derived from observations of planets (orange line). (Bottom) Same as above, but concentrating on the main beam

5.7 Pre-Launch Laboratory Measurements

A pre-launch laboratory campaign was performed (in 2008) in Cardiff University on the prototype qualification horn to determine how the 857 GHz back-to-back horn section of the pixel itself was operating as a multimode radiator at its operational frequencies.

A He3 cryogenic detector system, was used for an integrated pixel test since the Planck 0.35K detector itself was unavailable initially. Figure 5.29 represents one of the early test set ups, in which just the back-to-back horn section was measured rather than the full pixel. A standard parabolic (Winston cone) triple horn relay was set up within the cryostat with the Planck back-to-back horn located externally (as in Figure 5.29). Thermal filters between the cryostat entrance window and the back-to-back horn pair were used to reflect out near-infrared power. The relay system of three Winston cones then couple power into the detector bolometer cavity. The full Planck pixel was also subsequently measured as precisely as possible with the back-to-back horn inside the dewar.

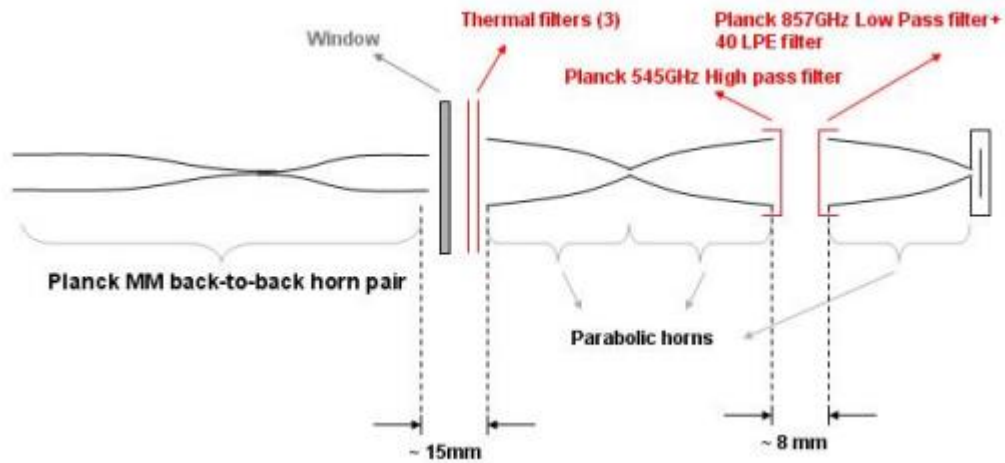


Figure 5.29: Test set up in Cardiff University for the measurement of the beam pattern of the Planck back-to-back horns.

Broad band beam pattern simulations were carried out on the 857 GHz Planck pixel using mode matching software GAMMA. The simulations were then compared to broad band frequency measurements of the horn farfield made at Cardiff University using a mercury arc lamp (MAL) as a blackbody source.

Figure 5.30 below shows the broadband beam pattern resulting from simulations and measurement. The grey line refers to the simulated broadband beam using mode matching for the ideal case (filter gap treated as a continuous waveguide and an ideal blackbody cavity as in Section 5.3). The orange line refers to the simulated broadband beam using mode matching for the lossy case (filter gap accounted for and bolometer modelled inside the cavity). The blue points refer to the results from the measurement campaign in Cardiff.

It can be seen that there is a significant discrepancy in Figure 5.30 between the simulated (ideal case) and measured beam patterns, the simulated beam is broader and more top hat like than the measured beam. It is clear that the losses in the pixel need to be accounted for in order to achieve a reasonable agreement between simulations and measurements, indicating that some power was in fact lost at the filter section.

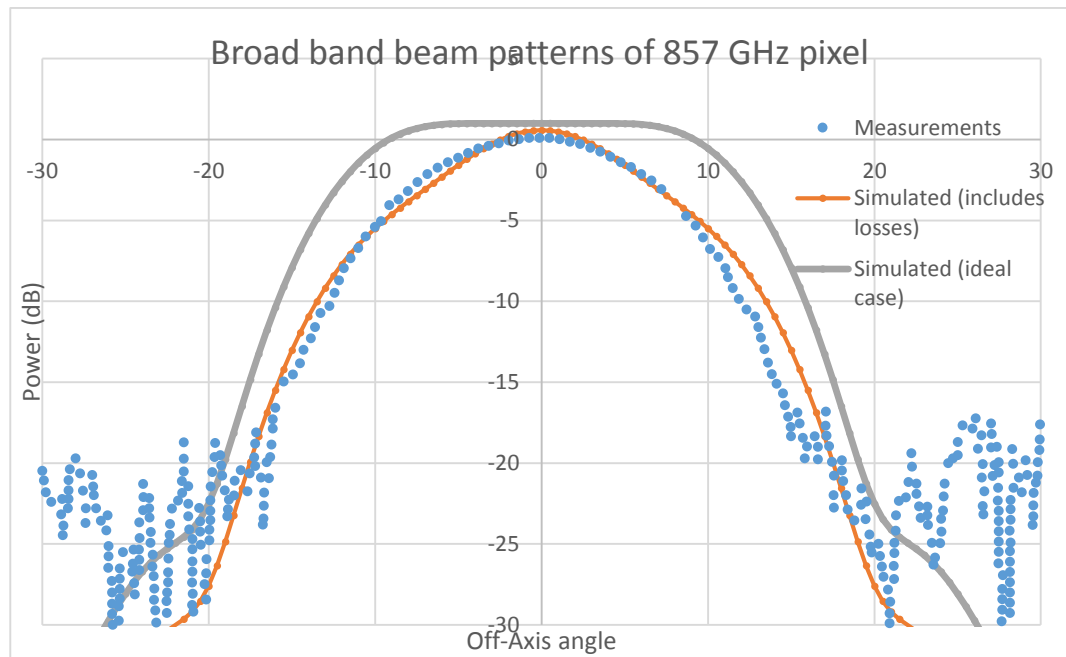


Figure 5.30: Broad band beam pattern comparison of the simulations (both ideal and lossy) and measurements

The measurement data in Figure 5.30 above is asymmetric about the on-axis direction. In Figure 5.31 below, the negative and positive angles have been averaged to reduce the effect of the asymmetry. The averaging was performed for the measured beam and for the simulated beam (lossy).

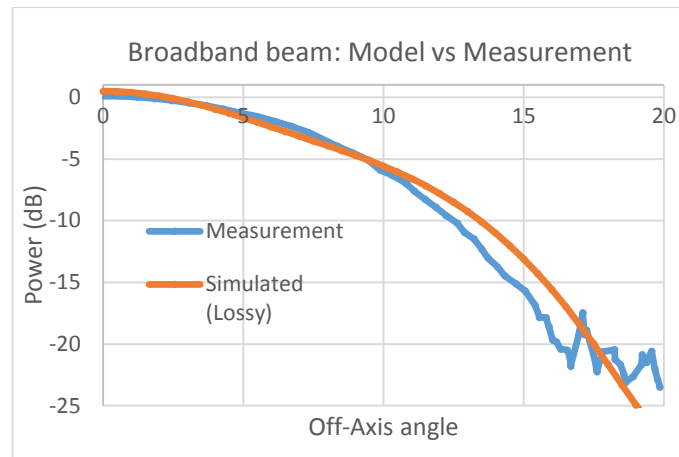


Figure 5.31: Broad band beam pattern comparison of the simulations (lossy) and measurements. Here, the data for the positive and negative angles has been averaged

Test measurements at four spot frequencies (739.5 GHz, 782 GHz, 819.5 GHz and 842 GHz) were also carried out at Cardiff University. Although agreement was not perfect at the test frequencies, the agreement between simulations and model is far better than for the ideal horns, particularly at 782 GHz and 819 GHz. The single frequency measurements generally suffered from significant noise below the -20 dB level possibly due to standing wave effects. A comparison of the measured results and simulated results (lossy case) can be seen in Figure 5.32 (a) to (d) below.

Overall, it can be seen that including loss in the filter filter section using the approximate model in this section gives a much better approximation of the beam patterns. It is clear also from the shape of the beams that the higher order modes suffer more loss than the lower order modes.

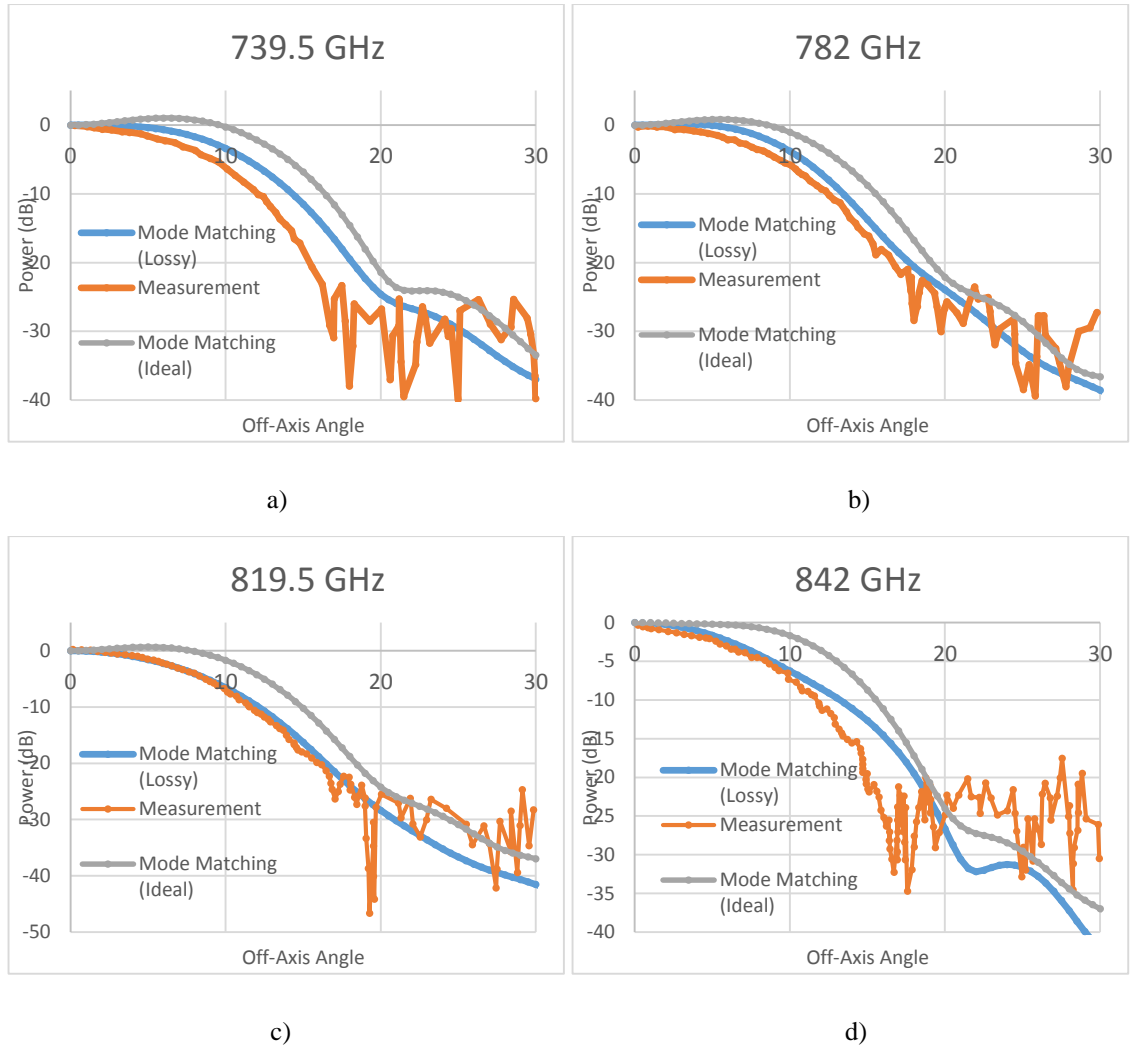


Figure 5.32: Beam pattern comparison of the simulations, both ideal (grey curve) and lossy (blue curve), and measurements (orange curve) at spot frequencies. The data for the positive and negative angles has been averaged

5.8 Planck 545 GHz channel

Up to this point, the main focus of this chapter has been about the higher frequency multimode HFI channel centered on 857 GHz. In this section we discuss the second multimode HFI channel centered on 545 GHz, which was also primarily used for the detection of foreground sources.

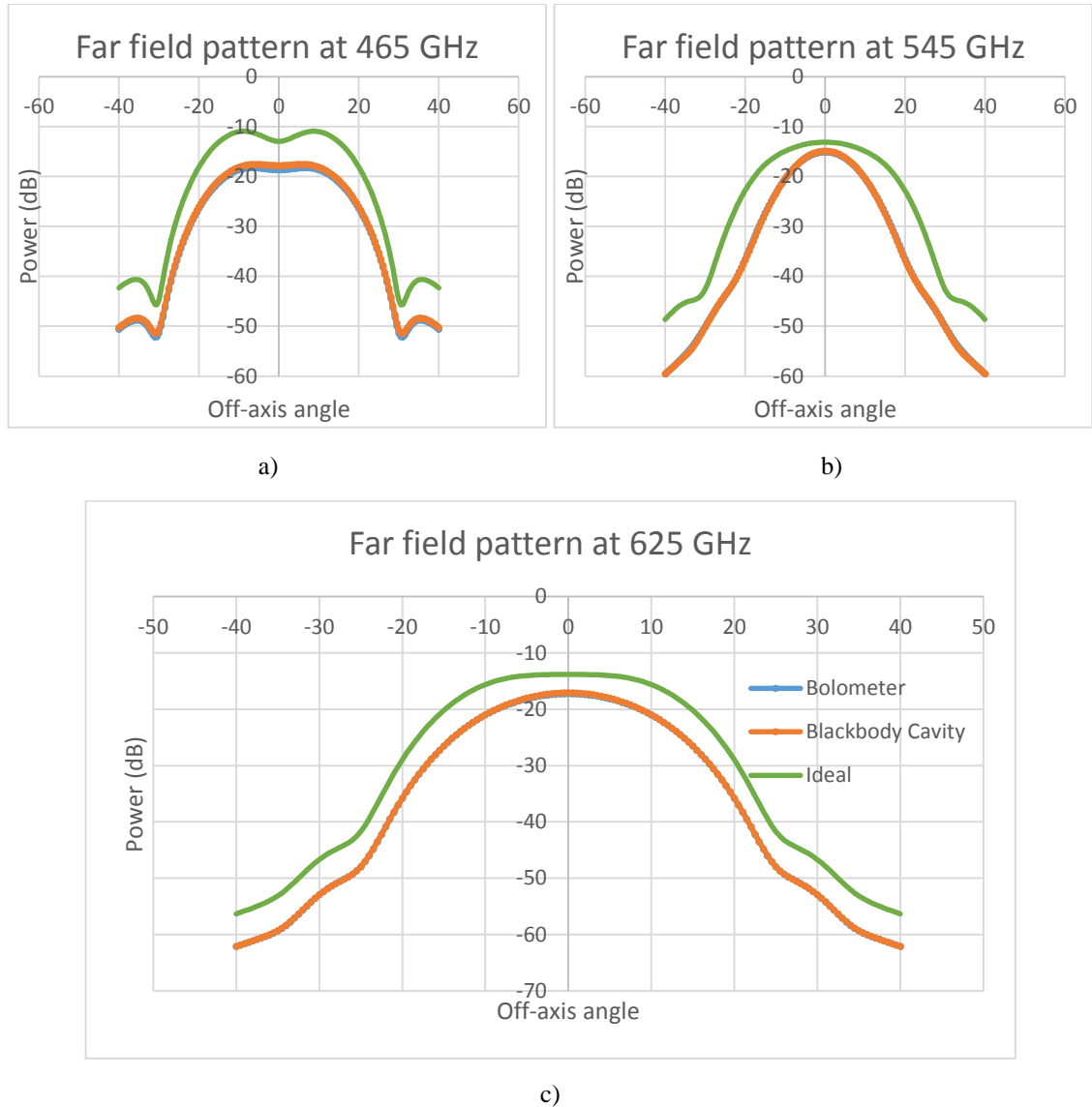


Figure 5.33: Beam patterns comparing the case where the free-space gap was modelled (blue line) and also where both the free-space gap and bolometer inside the cavity were modelled (orange line) at 465 GHz, 545 GHz and 625 GHz

For the case of the 545 GHz channel, two different cavities were considered in Figure 5.33 above, one was an ideal blackbody radiator cavity, the other was the bolometric cavity, with the free-space gap between the back horn and the detector horn was considered in both cases. The ideal scenario (ideal blackbody cavity and no loss in gap) was also considered in Figure 5.33., however, it was not considered in the broadband simulations and also when propagating the beams through the Planck telescope and onto the sky. The frequency range covered by the 545 GHz pixel ranges from 465 GHz to 625 GHz. Figure 5.33 above shows the resulting comparison of the two cases mentioned above at some spot frequencies across the operating band.

Figure 5.34 and Figure 5.35 below shows the simulations of the farfield beam patterns of the full 545 GHz pixel (free space gap and bolometer effects accounted for) carried out in GAMMA in 5 GHz steps across the operating band. The figures illustrate how the beam changes over the operating band, both in terms of on-axis power levels and the beam shape.

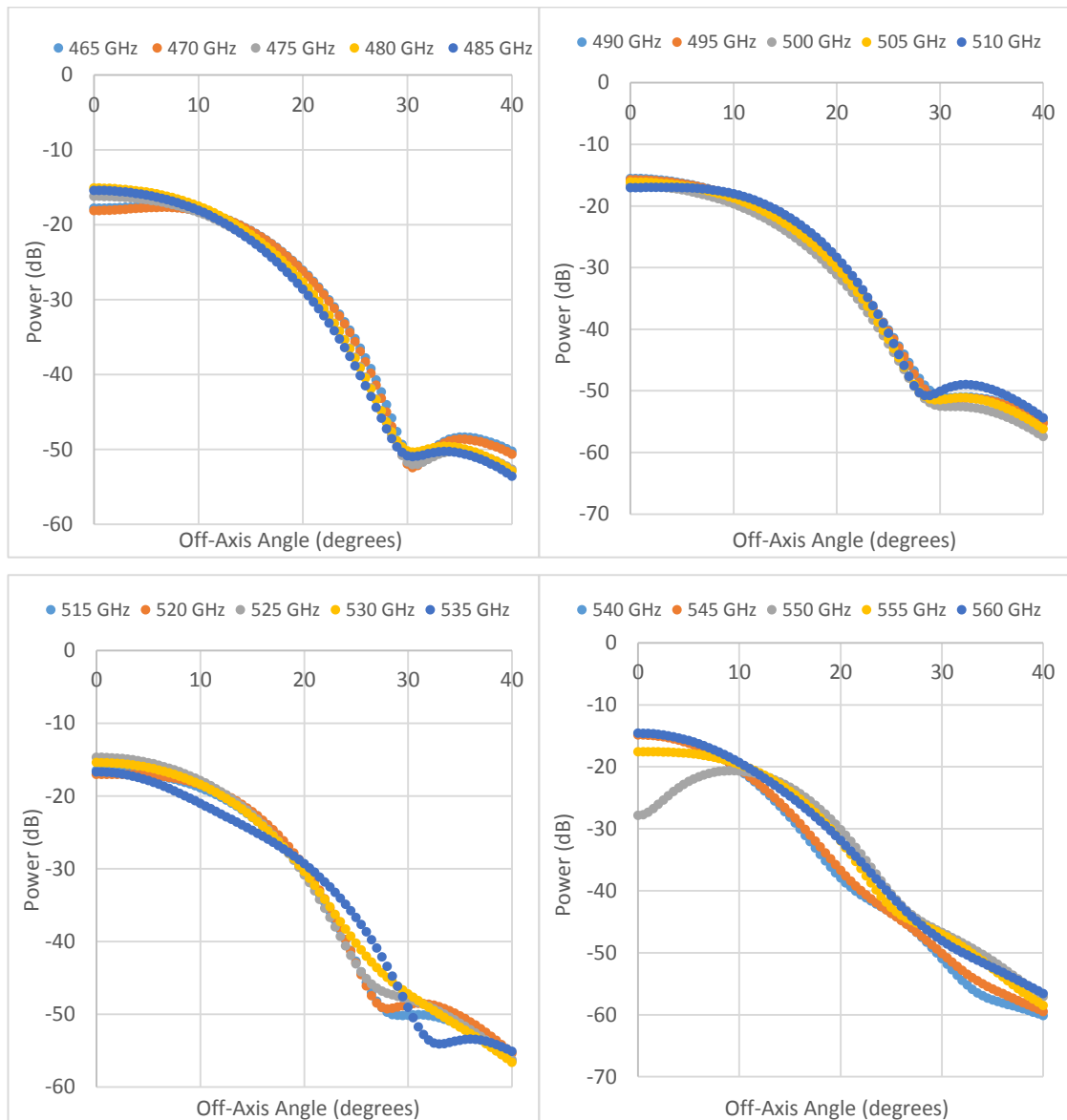


Figure 5.34: Farfield plots of the 545 GHz horn from 465 GHz to 560 GHz in steps of 5 GHz

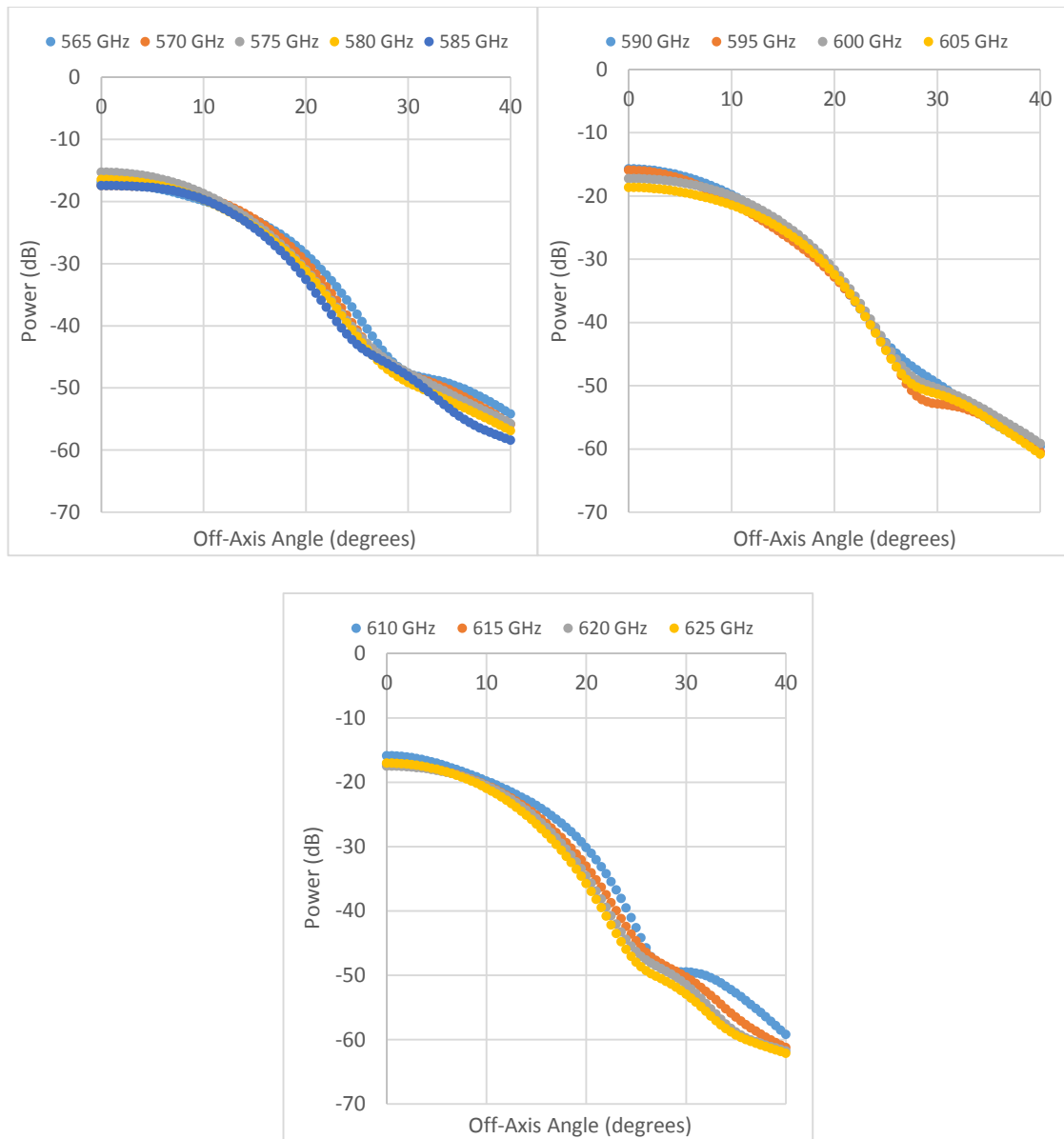


Figure 5.35: Farfield plots of the 545 GHz horn from 565 GHz to 625 GHz in steps of 5 GHz

Figure 5.36 below shows the simulated broadband beam pattern of the 545 GHz pixel assuming a flat spectrum. Frequency samples were taken at 1 GHz steps across the operating band.

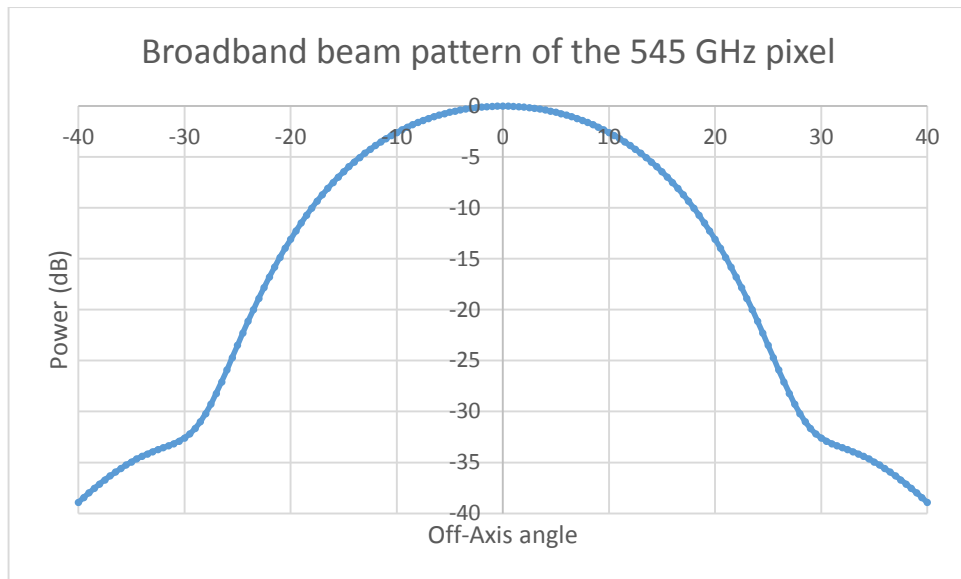


Figure 5.36: Simulated broadband beam pattern for the 545 GHz Planck pixel

We now consider how the various levels of approximation when modelling the Planck 545 GHz pixel feed into the beam predictions on the sky. Just as for the 857 GHz pixel, physical optics provides the most accurate results for reasonable computation efficiency. GRASP9 was used to carry out the simulations.

If the aperture field of the horn is known, it can be read in by GRASP9 as a tabulated planar source. Just as in the case of the 857 GHz pixel, the detector is overmoded, meaning that it is important to maintain relative power levels between the hybrid modes as they do not contribute equally to the field intensity at the aperture. The beams on the sky were computed (assuming uniform spectral response across the band) and examined for the pixel located at 545-2 on the focal plane unit (see Figure 5.17). Figure 5.37 to Figure 5.39 below show the beams on the sky (both contours and cuts), with the 545-2 horn used as the source, with the free-space gap in the filter section between the back horn and the detector horn included, and the cavity used was a bolometric cavity.

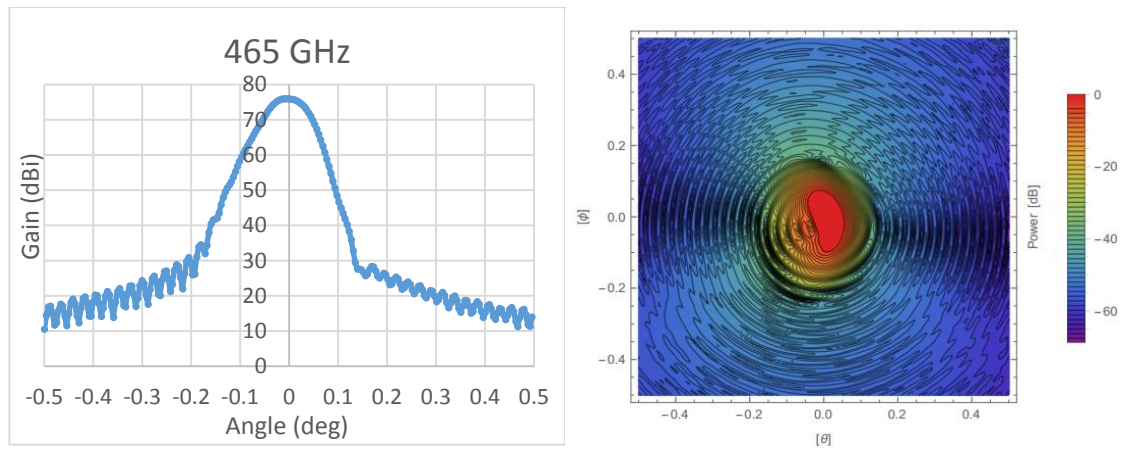


Figure 5.37: Resulting beams on the sky modelled at 465 GHz for the case where a bolometric cavity and free-space gap were modelled

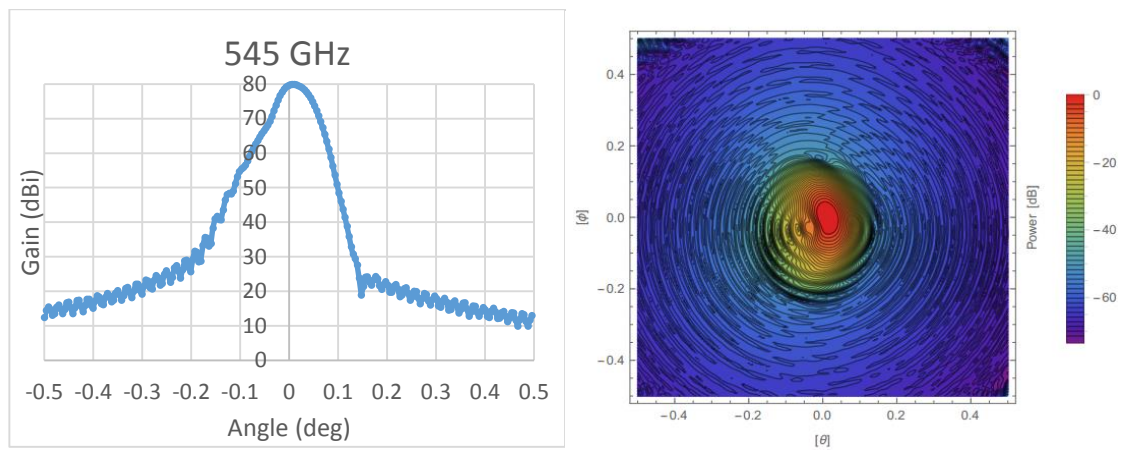


Figure 5.38: Resulting beams on the sky modelled at 545 GHz for the case where a bolometric cavity and free-space gap were modelled

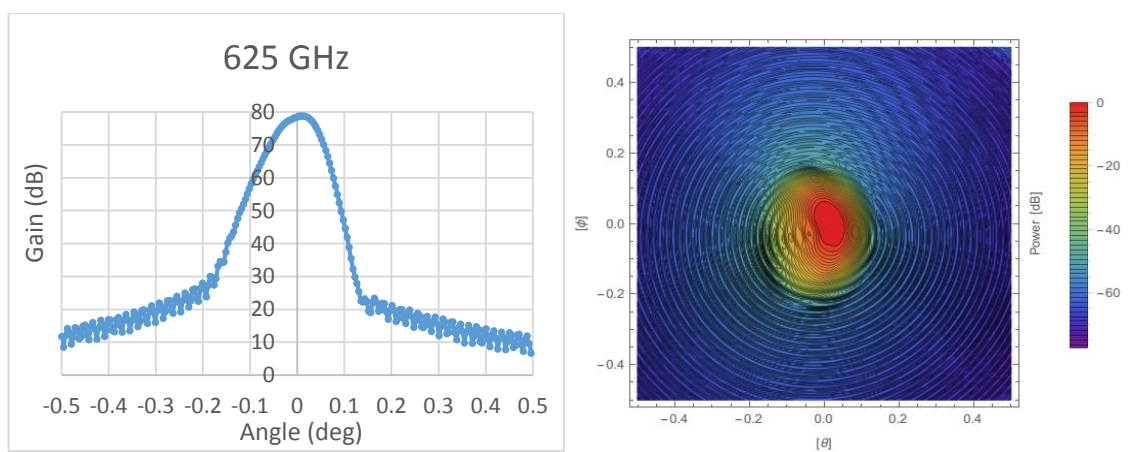


Figure 5.39: Resulting beams on the sky modelled at 625 GHz for the case where a bolometric cavity and free-space gap were modelled

Figure 5.40 below shows the azimuthally and band averaged simulated beam compared with the main beam profile derived from observations of planets (Planck Collaboration, 2014(VII)). The azimuthal averaging was performed by following the same procedure as was used for the 857 GHz channel (outlined in Section 5.6).

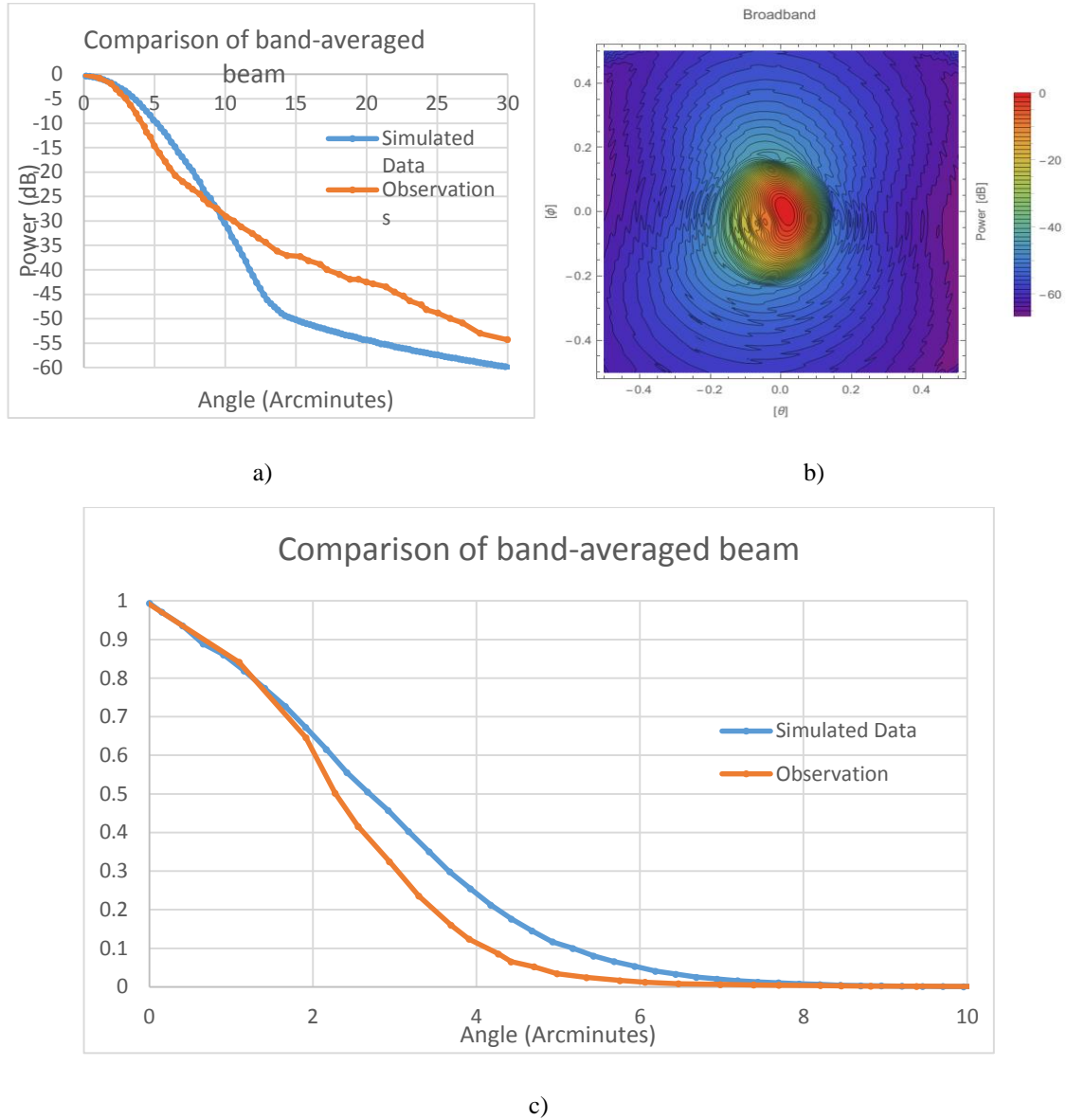


Figure 5.40: Band averaged main beam profiles comparing the mode matching and PO model with main beam profile derived from observations of planets using a dB scale (a) and linear scale (c). The resulting contour beam of the PO model is shown in (b)

The agreement between the measured and simulated beam on the sky (Figure 5.40) is not quite as good as in the 857 GHz case. However, the measured and simulated beams agree until ~ -2.5 dB level and the beamwidth on the sky is essentially very similar.

5.9 Conclusion

In this chapter, it was discussed how mode matching can be used to efficiently model multimode systems. The 857 GHz pixel, the highest frequency channel of the HFI on the ESA Planck satellite, is highly overmoded and the GAMMA software (based on mode matching), written in Python, was used to model the 857 GHz pixel.

In Section 5.3, the thermal filter gap was modelled as a continuous waveguide section, producing top hat beams. The beams measured in the laboratory at Cardiff as discussed in Section 5.7 were narrower than predicted and were not top hat in shape. This indicated power carried by the individual modes may be lost through the gaps at the ends of the filter section, meaning that a more thorough approach was needed to model the system.

Section 5.4 describes the steps taken to include the filter gap. The software was extended to include free-space gaps in the structure. The beam patterns for the two cases (ideal and lossy) were then compared, showing significant changes on the predicted beam patterns of the HFI 857 GHz channel on Planck.

The inclusion of the detector in the cavity was described in Section 5.5. Initially, the power was extracted from the overall $[S_{11}]$ matrix of the horn-waveguide-bolometric cavity system. However, this approach proved to be a poor approximation of the absorbed power, since there was another source of loss in the system (*i.e.* power blockage in the filter section). The 857 GHz pixel was then split into two parts ((i) the absorbing cavity plus its feeding waveguide, and (ii) the rest of the system including any feed horn and waveguide sections with gaps). The beam patterns were compared for all three cases ((i) ideal case, (ii) lossy case (ideal blackbody absorbing cavity), and (iii) lossy case (bolometer in the detector cavity)). The results show: (i) there is a significant change in gain and beam width from the ideal case to the lossy case, and (ii) the bolometer on the Planck 857 GHz system closely approximates an ideal blackbody source. This shows we can approximate the cavity coupled bolometer as an ideal blackbody absorber.

Section 5.6 describes the steps taken toward obtaining beams on the sky both for various spot frequencies across the band and also broadband beams. The beams on the sky were compared for the ideal and lossy (bolometer) cases. The beam on the sky is less top hat like once the losses have been accounted for. The beams were computed at 5 GHz intervals and, assuming a flat spectral source, were added to simulate the broadband beam on the sky. In order to produce an approximation of the band averaged beam, the values

of the contour beam were azimuthally averaged. The PO model was compared with the azimuthally and band averaged beam derived from observations of planets. Agreement between simulations of the lossy case and observations was observed to ~ -15 dB level.

In Section 5.7, the simulations of the beam patterns of the horn across the band were discussed, providing a brief description of the measurement setup. The broadband measurement results were compared with the simulated results (computed at 1 GHz intervals across the band), both ideal and lossy (bolometer).

In Section 5.8, the simulations of the beam patterns of the 545 GHz pixel both across the band and at some spot frequencies were reported on, including the beams on the sky. The beams were computed at 5 GHz intervals and were added to simulate the broadband beam on the sky. In order to produce an approximation of the band averaged beam, the values were azimuthally averaged. The PO model was compared with the azimuthally and band averaged beam derived from observations of planets in the same manner as was done for the 857 GHz pixel. Agreement with both pre-launch laboratory measurements and with the beams on the sky indicated that some power was in fact lost at the filter section. Although agreement was not perfect, very similar beam widths were obtained compared with those reported in the Planck HFI beams paper (Maffei et.al., 2010).

6 Including free space propagation and open cavities in GAMMA

6.1 Introduction

In this section, we describe how the mode matching approach was extended for the case of free space gaps in the waveguide configuration with open cavities in which absorbers (effectively locally in free space) can be placed. The implementation of such a structure in GAMMA will be discussed in this section (see for example Figure 6.1). This will be the case proposed, for example, for SAFARI as the array of detectors lie on a chip with an array of horns feeding them on the frontside and an array of backshort cavities on the backside to optimize the coupling of the incoming signal.

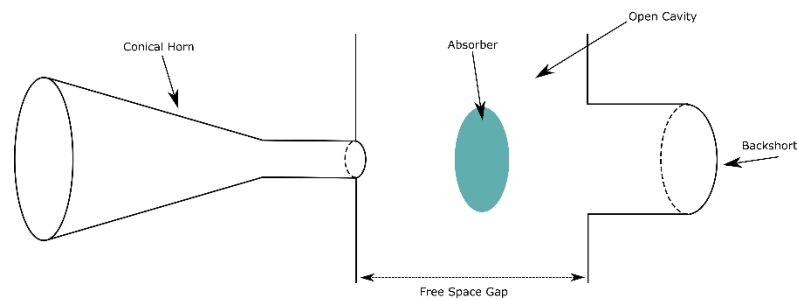


Figure 6.1: Horn feeding an absorber cavity with the absorber in a free space gap

A crucial issue that needs to be investigated therefore is the effect on the optical efficiency of the detectors when a free space gap is present. For the purpose of modelling such a pixel, a method of integrating a free space section of waveguide into GAMMA needs to be developed. It is possible to model such a pixel in electromagnetic solving packages (such as CST microwave studio), however, as the structures tend to be electrically large in terms of wavelength, such problems would prove computationally intensive to solve and would require the use of distributed high power computing. Thus, it is more practical to make use of mode matching and introduce a means of modelling such systems in a mode matching software (such as GAMMA) particularly if there is a lot of symmetry present. Note this is rather different to the free space gap discussed in the case of the Planck pixels in the last chapter, where this gap occurred just at the junction between two structures.

6.2 Waveguide to free space coupling

At the junction to free space, as before (Chapter 2) the transverse electric and magnetic fields on both sides of the junction must be equal over the waveguide cross section. The appropriate modes for free space (open cavity) are Bessel beams (free space modes), which form a continuous basis set with respect to which any field can be decomposed. The usual modal sums for decomposing the fields ($\mathbf{E} = \Sigma A_n \mathbf{e}_n$) are then replaced by integrals of the form $\mathbf{E} = \int_{k_\rho} \alpha_n(k_\rho) \mathbf{e}(k_\rho) 2\pi k_\rho dk_\rho$, where $\mathbf{e}(k_\rho)$ is the modal field (Bessel beam). Some care, however, has to be taken with the normalisation of these modes, as discussed below. For *TM* modes (cylindrical polar coordinates r and ϕ) the axial component of the electric field is

$$E_z = \alpha_n \cdot J_n(k_\rho r) \begin{Bmatrix} \cos n\phi \\ \sin n\phi \end{Bmatrix} \exp(j(\omega t - \beta z)), \quad (6.1)$$

where n is the azimuthal index of the mode and where the $\cos n\phi$ and $\sin n\phi$ terms represent the two possible orthogonal solutions to the wave equation and we sum/integrate over the continuous variable k_ρ . This implies (as in Section 2.3) that for the transverse components for a Bessel beam with transverse wave number k_ρ (where the term $\exp(j(\omega t - \beta z))$ has been suppressed)

$$\mathbf{e}_{n,k_\rho, TM} = \alpha_n(k_\rho) \left[J'_n(k_\rho r) \begin{Bmatrix} \cos n\phi \\ \sin n\phi \end{Bmatrix} \hat{r} + \frac{n J_n(k_\rho r)}{k_\rho r} \begin{Bmatrix} -\sin n\phi \\ \cos n\phi \end{Bmatrix} \hat{\phi} \right], \quad (6.2)$$

$$\mathbf{h}_{n,k_\rho, TM} = \frac{\alpha_n(k_\rho)}{Z_{TM}(k_\rho)} \left[\frac{n J_n(k_\rho r)}{k_\rho r} \begin{Bmatrix} \sin n\phi \\ -\cos n\phi \end{Bmatrix} \hat{r} + J'_n(k_\rho r) \begin{Bmatrix} \cos n\phi \\ \sin n\phi \end{Bmatrix} \hat{\phi} \right]. \quad (6.3)$$

The impedance of a *TM* mode is given by

$$Z_{TM}(k_\rho) = \frac{\beta(k_\rho)}{\omega \epsilon} = \frac{\beta(k_\rho) Z_0}{k_0}. \quad (6.4)$$

The normalisation factor $\alpha_n(k_\rho)$ should be normalised to unity as explained below and the waveguide equation is given by: $k_0^2 = \beta(k_\rho)^2 + k_\rho^2$ which thus relates k_0, k_ρ and β . The general power coupling integral between two *TM* free space modes (orthogonality relationship) is given by:

$$\begin{aligned}
 & \int_0^{2\pi\infty} \int_0^\infty \mathbf{e}_{n1,TM}(k_{\rho 1}) \times \mathbf{h}_{n2,TM}(k_{\rho 2})^* r dr d\phi \\
 &= \frac{\alpha_{n1}(k_{\rho 1}) \cdot \alpha_{n2}(k_{\rho 2})^*}{Z_{TM}(k_{\rho 2})^*} \frac{\pi}{2} \left[\int_0^\infty J_{n1+1}(k_{\rho 1} r) J_{n2+1}(k_{\rho 2} r) + J_{n1-1}(k_{\rho 1} r) J_{n2-1}(k_{\rho 2} r) r dr \right] \\
 &= \frac{\pi \alpha_{n1}(k_{\rho 1}) \cdot \alpha_{n2}(k_{\rho 2})^*}{Z_{TM}(k_{\rho 2})^*} \cdot \frac{[\delta[k_{\rho 1} - k_{\rho 2}]]}{k_{\rho 2}} \delta_{n1,n2}
 \end{aligned} \quad (6.5)$$

which gives the self-coupling integrals when integrated over all k_ρ as:

$$\begin{aligned}
 & \int_0^\infty \left(\int_0^{2\pi\infty} \int_0^\infty \mathbf{e}_n(k_{\rho 1}) \times \mathbf{h}_n(k_{\rho 1})^* r dr d\phi \right) 2 \pi k_\rho dk_\rho \\
 &= \frac{2 \pi^2 |\alpha_n(k_{\rho 1})|^2}{Z_{TM}(k_{\rho 1})^*} \int \delta[k_{\rho 1} - k_\rho] dk_\rho = 2 \pi^2 \cdot \frac{k_0}{Z_0 \beta(k_{\rho 1})^*} |\alpha_n(k_{\rho 1})|^2
 \end{aligned} \quad (6.6)$$

We can therefore normalise the *TM* free space modes for simplicity by setting

$$|\alpha_n(k_\rho)| = \sqrt{\frac{Z_0 |\beta(k_\rho)|}{2 \pi^2 k_0}}, \quad (6.7)$$

and therefore

$$\int_0^\infty \left(\int_0^{2\pi} \int_0^\infty \mathbf{e}_n(k_{\rho 1}) \times \mathbf{h}_n(k_{\rho 1})^* r dr d\phi \right) k_\rho dk_\rho = 1. \quad (6.8)$$

Note that this is different from waveguide modes, in which it is the term in the brackets that is normalized to unity (depending on the units chosen). Similarly for the *TE* free space modes we have for the axial magnetic field (n the azimuthal index of the mode)

$$H_z = \chi' \cdot J_n(k_\rho r) \begin{Bmatrix} \cos n\phi \\ \sin n\phi \end{Bmatrix} \exp(j(\omega t - \beta z)) \quad (6.9)$$

which implies that the corresponding transverse fields are given by:

$$\mathbf{e}_{n,te}(k_\rho) = \chi_n(k_\rho) \left[\frac{n}{k_\rho r} J_n(k_\rho r) \begin{Bmatrix} \sin n\phi \\ -\cos n\phi \end{Bmatrix} \hat{r} + J'_n(k_\rho r) \begin{Bmatrix} \cos n\phi \\ \sin n\phi \end{Bmatrix} \hat{\phi} \right] \quad (6.10)$$

$$\mathbf{h}_{n,te}(k_\rho) = \frac{\chi_n(k_\rho)}{Z_{TE}} \left[J'_n(k_\rho r) \begin{Bmatrix} -\cos n\phi \\ -\sin n\phi \end{Bmatrix} \hat{r} + \frac{n J_n(k_\rho r)}{k_\rho r} \begin{Bmatrix} \sin n\phi \\ -\cos n\phi \end{Bmatrix} \hat{\phi} \right] \quad (6.11)$$

The impedance of a TE mode is given by

$$Z_{TE} = \frac{\omega\mu}{\beta} = \frac{k_0 Z_0}{\beta}, \quad (6.12)$$

where the waveguide equation is given by: $k_0^2 = \beta^2 + k_\rho^2$. Again, the normalisation factor $\chi_n(k_\rho)$ should be appropriately chosen. In a similar way to TM modes for the coupling integrals for TE modes we have:

$$\begin{aligned} & \int_{0,0}^{\infty,2\pi} \mathbf{e}_{n1}(k_{\rho1}) \times \mathbf{h}_{n2}(k_{\rho2})^* r dr d\phi \\ &= \chi_{n1}(k_{\rho1}) \cdot \chi_{n2}(k_{\rho2})^* \cdot \frac{\pi}{2} \cdot \frac{1}{Z_{TE}(k_{\rho2})^*} \cdot \\ & \left[\int_0^\infty J_{n1+1}(k_{\rho1}r) J_{n2+1}(k_{\rho2}r) + J_{n1-1}(k_{\rho1}r) J_{n2-1}(k_{\rho2}r) r dr \right] \delta_{n,nd} \\ &= \chi_{n1}(k_{\rho1}) \cdot \chi_{n2}(k_{\rho2})^* \cdot \frac{\pi}{Z_{TE}(k_{\rho2})^*} \cdot \frac{[\delta[k_{\rho1} - k_{\rho2}]]}{k_{\rho1}} \delta_{n1,n2}. \end{aligned} \quad (6.13)$$

Therefore, for the TE - TE self-coupling type terms for free space (for the Q matrix in deriving the scattering matrices) we get:

$$\begin{aligned} & \int_0^\infty \left(\int_0^{2\pi} \int_0^\infty \mathbf{e}_n(k_{\rho1}) \times \mathbf{h}_n(k_\rho)^* r dr d\phi \right) 2\pi k_\rho dk_\rho = \\ & \frac{2\pi^2 |\chi_n(k_{\rho1})|^2}{Z_{TE}(k_{\rho1})^*} = \frac{2\pi^2 \beta(k_{\rho1})^*}{k_0 Z_0} |\chi_n(k_{\rho1})|^2 \end{aligned} \quad (6.14)$$

We therefore normalise the TE modes for simplicity by setting

$$|\chi_n(k_\rho)| = \sqrt{\frac{k_0 Z_0}{2\pi^2 |\beta(k_\rho)|}}, \quad (6.15)$$

and therefore

$$\int_0^\infty \left(\int_0^{2\pi} \int_0^\infty \mathbf{e}_n(k_{\rho1}) \times \mathbf{h}_n(k_\rho)^* r dr d\phi \right) k_\rho dk_\rho = 1. \quad (6.16)$$

We then proceed to calculate the modal scattering matrices for the step from waveguide to free space in the same way as for a step between two waveguides. For various power coupling integrals $P_{L \rightarrow R}$ going from left (waveguide) to right (free space) we obtain (after some algebraic manipulations) that :

$$P_{n,l,TE \rightarrow n,k\rho,TE} = -(1 + \delta_{n0})\pi \frac{A_L A_R^*}{Z_{ie}(k_\rho)^*} \times \frac{(q_{nl} J_n(q_{nl}) J'_n(k_\rho a))}{[k_\rho^2 - (q_{nl}/a)^2]} 2\pi k_\rho \Delta k_\rho, \quad (6.17)$$

$$P_{n,l,TM \rightarrow n,k\rho,TM} = (1 + \delta_{n0})\pi \frac{A_L A_R^*}{Z_{im}(k_\rho)^*} \times \frac{(k_\rho J'_n(p_{nl}) J_n(k_\rho a))}{[k_\rho^2 - (p_{nl}/a)^2]} 2\pi k_\rho \Delta k_\rho, \quad (6.18)$$

$$P_{n,l,TE \rightarrow n,k\rho,TM} = (1 + \delta_{n0})\pi \frac{A_L A_R^*}{Z_{im}(k_\rho)^*} \times \frac{n a (J_n(q_{nl}) J_n(k_\rho a))}{q_{nl} k_\rho} 2\pi k_\rho \Delta k_\rho, \quad (6.19)$$

where the p_{nl} and q_{nl} are the usual zeros of $J_n(z)$ and $dJ_n(z)/dz$ terms, respectively, and A_L and A_R are the corresponding normalisation factors for the waveguide (left) and free space (right), respectively. Δk_ρ corresponds to the sampling interval used for dk_ρ in numerically calculating the various integrals over k_ρ space. In this case for free space the corresponding (self-coupling integrals) Q_{nm} are given by:

$$Q_{n,TE,k\rho \rightarrow n,TE,k\rho} = \frac{\beta(k_\rho)^*}{|\beta(k_\rho)|} 2\pi k_\rho \Delta k_\rho, \quad (6.20)$$

$$Q_{n,TM,k\rho \rightarrow n,TM,k\rho} = \frac{|\beta(k_\rho)|}{\beta(k_\rho)^*} 2\pi k_\rho \Delta k_\rho \quad (6.21)$$

The scattering matrices can be derived from the usual relationships:

$$[S_{11}] = [[R^*] + [P^+][Q^{-1}][P]]^{-1} \cdot [[R^*] - [P^+][Q^{-1}][P]], \quad (6.22)$$

$$[S_{12}] = [[R^*] + [P^+][Q^{-1}][P]]^{-1} \cdot [2[P^+]], \quad (6.23)$$

$$[S_{21}] = [[Q] + [P][R^*]^{-1}[P^+]]^{-1} \cdot [2[P]], \quad (6.24)$$

$$[S_{22}] = [[Q] + [P][R^*]^{-1}[P^+]]^{-1} \cdot [[Q] - [P][R^*]^{-1}[P^+]]^{-1}. \quad (6.25)$$

Propagation through free space is implemented using the appropriated V matrix with the phase term now expressed as: $V_{mm} = \exp(-j(\beta(k_\rho)z))$ in the same way as for a waveguide mode.

The expressions above (6.17, 6.18 and 6.19) assume an infinite ground plane in the step from the waveguide. There is a problem with the infinite ground plane in that the free space modes are not attenuated at the step. Thus we get perfect power coupling (no loss) as the incident power is shared between the reflected waveguide modes and transmitted free space modes. Thus we need to assume a *finite ground plane* (of radius R) (see for example Figure 6.2) and that there are no reflections in the region beyond radius R (an

approximation). Therefore just beyond the finite ground plane there is an absorbing screen with a large aperture of radius R . Assuming no reflections at the screen (an approximation) we get $[S_{11}] = [S_{22}] = 0$, In that case the power coupled from side (1) to side (2) is given by the usual power coupling integrals

$$\int_0^R \mathbf{e}_n \times \mathbf{h}_m^* d\mathbf{A}, \quad (6.26)$$

but now over the finite aperture, giving

$$[S_{21}] = [S_{12}] = [U] = \int_0^R \mathbf{e}_n \times \mathbf{h}_m^* d\mathbf{A}, \quad (6.27)$$

If we treat the two junctions together (the step into finite ground plane and the absorbing aperture), it is possible to show that:

$$[S_{11}] = [[R^*] + [P^+ [Q^{-1} [P]]]^{-1} \cdot [[R^*] - [P^+ [Q^{-1} [P]]], \quad (6.28)$$

$$[S_{12}] = [[R^*] + [P^+ [Q^{-1} [P]]]^{-1} \cdot [P^+] \cdot [[I] + [Q^{-1} [U]], \quad (6.29)$$

$$[S_{21}] = [[Q] + [P][R^*]^{-1} [P^+]^{-1} \cdot [2 [P]], \quad (6.30)$$

$$[S_{22}] = -[[Q] + [P][R^*]^{-1} [P^+]^{-1} \cdot [[U] - [P][R^*]^{-1} [P^+]^{-1}], \quad (6.31)$$

where for both TE to TE and TM to TM modes the elements of the U matrix are given by

$$U_{TE/TM, n, k_{\rho 1} \rightarrow TE/TM, n, k_{\rho 2}} = A_L A_R \frac{(1 + \delta_{n0}) \pi R^*}{Z_R^*} \times \frac{(k_{\rho 2} J'_n(k_{\rho 1} R) J_n(k_{\rho 2} R) - k_{\rho 1} J'_n(k_{\rho 2} R) J_n(k_{\rho 1} R))}{[k_{\rho 2}^2 - k_{\rho 1}^2]} 4 \pi^2 k_{\rho 1} k_{\rho 2} \Delta k_{\rho 1} \Delta k_{\rho 2} \quad (6.32)$$

while for the TE to TM and TM to TE modes:

$$U_{TE/TM, n, k_{\rho 1} \rightarrow TM/TE, n, k_{\rho 2}} = A_L A_R \frac{(1 + \delta_{n0}) \pi R^*}{Z_R^*} \times \frac{n J_n(k_{\rho 1} R) J_n(k_{\rho 2} R)}{k_{\rho 1} k_{\rho 2}} 4 \pi^2 k_{\rho 1} k_{\rho 2} \Delta k_{\rho 1} \Delta k_{\rho 2} \quad (6.33)$$

where A_L and A_R are the appropriate normalisation factors for the incident and reflected free space modes at the ground plane, respectively.

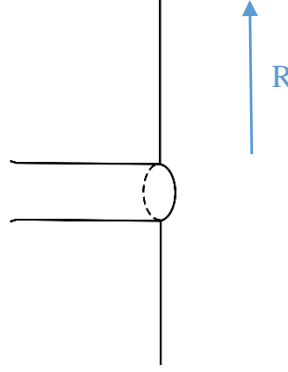


Figure 6.2: Waveguide to free space interface, where the ground plane is finite in size

It is important to note that this is an approximation, as in general there will also be a reflection in the region beyond the finite ground plane of radius R . In order to model this reflection, an extra port would need to be included in the system, requiring a modal description of any field propagating outside the waveguide, which would be difficult to implement. However, for reasonable sized ground planes we would expect this approach to be adequate for analysing such systems.

6.3 Implementing an absorber in free space

For the case of an *absorber in free space* a similar analysis can be undertaken as for an absorber in a waveguide to calculate the scattering matrices except here using free space modes. In this case, as before, the scattering matrices can be derived from Equations (2.74) and (2.75), where in this case the elements of the $[T]$ matrix (for the case of an absorber of radius b) are given by (for TE to TE and TM to TM):

$$T_{TE/TM, k_{\rho 1} \rightarrow TE/TM, k_{\rho 2}} = A_L A_R^* (1 + \delta_{n0}) \pi b \times \frac{(k_{\rho 2} J'_n(k_{\rho 1} b) J_n(k_{\rho 2} b) - k_{\rho 1} J'_n(k_{\rho 2} b) J_n(k_{\rho 1} b))}{[k_{\rho 2}^2 - k_{\rho 1}^2]} 2\pi k_{\rho 2} \Delta k_{\rho}, \quad (6.34)$$

$$T_{TE/TM, k_{\rho 1} \rightarrow TM/TE, k_{\rho 2}} = A_L A_R^* (1 + \delta_{n0}) \pi b \times \frac{n J_n(k_{\rho 1} b) J_n(k_{\rho 2} b)}{k_{\rho 1} k_{\rho 2}} 2\pi k_{\rho 2} \Delta k_{\rho}, \quad (6.35)$$

where again A_L and A_R are the appropriate normalisation factors for the incident and reflected free space modes at the ground plane, respectively.

Next we consider how to directly calculate the power absorbed by such an absorber in a waveguide or a free space gap within a waveguide horn structure. Previously we assumed that we could use the $[S_{11}]$ matrix for a waveguide only system.

As mentioned previously in Section 4.2, when using mode matching the absorbed power can be obtained from the overall $[S_{11}]$ (reflection) matrix for the horn-waveguide-absorbing cavity system by treating the aperture as the input port and using that power (real power) not reflected back at the horn aperture must have been absorbed by the absorber. As was already discussed, this approach cannot be used when there is another source of loss in the system, such as a free space gap through which signal power can escape as in an open cavity, as for example in Chapter 5 on the Planck HFI multimode horns. Clearly, this is also the case for an absorber in a free space gap, such as discussed in the introduction (Section 6.1) and shown in Figure 6.3.

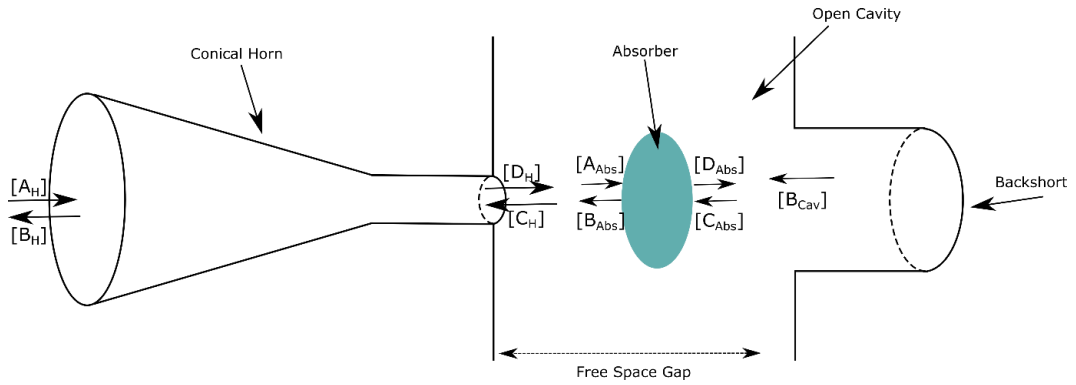


Figure 6.3: Horn feeding an absorber cavity with the absorber in a free space gap

A better alternative approach would be to extract the absorbed power at the absorber directly. Furthermore, knowing the power absorbed at the absorber and the overall S_{11} matrix, it would be possible to also calculate exactly the amount of power lost in the open cavity gap.

In order to extract the power absorbed by the absorber, the system in Figure 6.3 above needs to be split up into three different parts: (i) horn and cavity as far as the absorber, (ii) the absorber, (iii) propagation to the back wall of the backshort.

The power flow into the absorber may be expressed as $P = \int_{Abs} \mathbf{E} \times \mathbf{H}^* \cdot d\mathbf{A}$, where the integral of the Poynting vector is over both surfaces of the absorber.

First consider the case of an absorber in a closed waveguide cavity. The electric and magnetic fields at the absorber are given by

$$\mathbf{E}_L = \sum_{n=1}^N \{A_n + B_n\} \mathbf{e}_{nl}, \quad (6.36)$$

$$\mathbf{H}_L = \sum_{n=1}^N \{A_n - B_n\} \mathbf{h}_{nl} \quad (6.37)$$

$$\mathbf{E}_R = \sum_{n=1}^N \{D_n + C_n\} \mathbf{e}_{nr} \quad (6.38)$$

$$\mathbf{H}_R = \sum_{n=1}^N \{D_n - C_n\} \mathbf{h}_{nr} \quad (6.39)$$

where n denotes the mode number, N denotes the total number of modes, $\mathbf{e}_{nL,nR}$ and $\mathbf{h}_{nL,nR}$ denote the fields to the left or right of the absorber for the n^{th} mode. A_n and B_n are the forward and reflected coefficients of the n^{th} mode on the left side of the absorber and D_n and C_n are the forward and reflected coefficients of the n^{th} mode on the right side of the absorber (subscript ‘L’ denotes left and ‘R’ denotes right).

The power flow on the LHS of the absorber (see Figure 6.3) is given by:

$$P_L = \int_{Abs} \mathbf{E}_L \times \mathbf{H}_L^* \cdot d\mathbf{A} \quad (6.40)$$

Expressing the electric and magnetic field in terms of the forward and reflected coefficients, the expression for power on LHS of the absorber becomes:

$$\int_{Abs} \mathbf{E}_L \times \mathbf{H}_L^* \cdot d\mathbf{A} = \sum_n \left(|A_n|^2 - |B_n|^2 \right) Q_{nn} + \left(B_n A_n^* - A_n B_n^* \right) Q_{nn} \quad (6.41)$$

Q_{nn} in the above equation represents the self-coupling of a free space mode at the absorber (*i.e.* $Q_{nn} = \int \mathbf{e}_n \times \mathbf{h}_n^* \cdot d\mathbf{A}$). Both real and imaginary power are included, and negative power implies power travelling backwards while positive power implies power flowing into the absorber (positive z -direction).

Similarly, the power on the RHS of the absorber is given by:

$$\int_{Abs} \mathbf{E}_R \times \mathbf{H}_R^* \cdot d\mathbf{A} = \sum_n \left(|D_n|^2 - |C_n|^2 \right) Q_{nn} + \left(C_n D_n^* - D_n C_n^* \right) Q_{nn} \quad (6.42)$$

Thus, the total net power flowing into the absorber may be computed from:

$$P_{total} = \sum_n \left(|A_n|^2 - |B_n|^2 - |D_n|^2 + |C_n|^2 \right) Q_{nn} + \left(B_n A_n^* - A_n B_n^* - C_n D_n^* + D_n C_n^* \right) Q_{nn} \quad (6.43)$$

where in this case positive power corresponds to power flowing out of the absorber and negative power flowing into the absorber.

The power has both real and imaginary terms, since Q_{nn} is imaginary for evanescent modes. The real part corresponds to Joule losses, which is what we are interested in in the case of bolometers. Therefore, the propagating modes contribute through the first term and the evanescent modes through the second. The relevant equation in free space is then given by

$$P_{total} = 2\pi \sum_{k\rho} \left(\left(|A(k_\rho)|^2 - |B(k_\rho)|^2 - |D(k_\rho)|^2 + |C(k_\rho)|^2 \right) + \left(B(k_\rho)A(k_\rho)^* - A(k_\rho)B(k_\rho)^* - C(k_\rho)D(k_\rho)^* + D(k_\rho)C(k_\rho)^* \right) \right) Q(k_\rho), \quad (6.44)$$

where $Q(k_\rho)$ is given by Equations (6.20) and (6.21).

The above equation contains the power absorbed in an absorber in terms of the forward and reflected coefficients $A(k_\rho)$ and $B(k_\rho)$ on the LHS of the absorber and the forward and reflected $D(k_\rho)$ and $C(k_\rho)$ on the RHS of the absorber, which now need to be calculated. In order to do so, it is convenient to split up the system above in Figure 6.3 into three different parts as in the previous example, remembering again that we are treating the system as in reception (not radiating).

Thus, three sets of scattering matrices should be computed for the structure in Figure 6.1: (i) S_H , representing the scattering between modes at the input to the horn or waveguide structure with modes at the input port (*i.e.* LHS of the absorber) propagated all the way up to the absorber, including the transition to and propagation in the cavity, (ii) S_{Abs} , representing the scattering between modes at the input and output ports at the absorber (LHS and RHS), and (iii) S_{Cav} , representing the scattering between modes in the cavity, between the output port of the absorber (RHS) and the backshort plane.

As will be shown below, it was also convenient to extract the cascaded scattering matrix of the absorber and the cavity, this scattering matrix will be called $S_{Abs+Cav}$, with the absorber scattering matrix being first in the cascading chain.

We begin with an expression for the transmission coefficient of the horn or waveguide structure where A_H represents the mode coefficients for the input field (for the source being detected), which is known.

$$D_H = S_{21_H} A_H + S_{22_H} C_H \quad (6.45)$$

The backward field incident at the output plane of the horn, C_H , comes from the reflection at the absorber, B_{Abs} . Thus, we have that $C_H = B_{Abs}$. The reflection at the absorber is clearly given by the scattering matrix of the absorber-cavity combination

$$B_{Abs} = S_{11_{Abs+Cav}} A_{Abs} + S_{12_{Abs+Cav}} C_{Abs+Cav} \quad (6.46)$$

However, as discussed previously (in Section 4.2), no modes can propagate from the output port to the input port of the cavity, meaning that $[S_{12}]$, $[S_{22}]$ and $[S_{21}]$ will all be zero matrices for the absorber cavity combination and by conservation of power, all power incident at the input of the cavity, must be reflected back (if there is no absorber within the cavity). The reflection is described by the $[S_{11}]$ matrix for the absorber cavity combination. Thus Equation (6.46) becomes $B_{Abs} = S_{11_{Abs+Cav}} A_{Abs}$.

Similarly, of course, the output of the horn (D_H) is equal to the input to the absorber (A_{Abs}), $D_H = A_{Abs}$. Using this fact and also that $C_H = B_{Abs}$, A_{Abs} may be re-expressed as

$$A_{Abs} = S_{21_H} A_H + S_{22_H} (S_{11_{Abs+Cav}} A_{Abs}), \quad (6.47)$$

which implies

$$A_{Abs} = [I - S_{22_H} S_{11_{Abs+Cav}}]^{-1} S_{21_H} A_H = T_{21_H} A_H. \quad (6.48)$$

We now need to obtain an expression for the forward and reflected coefficients (D_{Abs} and C_{Abs}) at the output plane of the absorber, which are also the forward and reflected coefficients (A_{Cav} and D_{Cav}) and the input to the cavity (*i.e.* $A_{Cav} = D_{Abs}$ and $B_{Cav} = C_{Abs}$). As discussed previously, no modes can propagate from the output port to the input port of the cavity, $C_{Cav} = 0$ and $D_{Cav} = 0$. The reflection at the cavity is given by

$$B_{Cav} = S_{11_{Cav}} A_{Cav} = C_{Abs}. \quad (6.49)$$

We are now able to calculate C_{Abs} and D_{Abs} in terms of A_{Abs} and ultimately A_H . The transmission coefficient of the absorber is given by

$$D_{Abs} = S_{21_{Abs}} A_{Abs} + S_{22_{Abs}} S_{11_{Cav}} D_{Abs}, \quad (6.50)$$

which implies

$$D_{Abs} = \left[I - S_{22_{Abs}} S_{11_{Cav}} \right]^{-1} S_{21_{Abs}} A_{Abs} = T_{21_{Abs}} A_{Abs} = T_{21_H} A_H. \quad (6.51)$$

Similarly, the reflection co-efficient C_{Abs} may be re-expressed as

$$C_{Abs} = S_{21_{Cav}} D_{Abs} = S_{21_{Cav}} T_{21_H} A_H \quad (6.52)$$

In summary, the reflection and transmission coefficients at LHS and RHS of the absorber may all be expressed in terms of scattering matrices that can be computed from the input A_H at the horn, which are known and depend on the source field at the input to the system.

$$A_{Abs} = T_{21_H} A_H, \quad (6.53)$$

$$B_{Abs} = S_{11_{Abs+Cav}} T_{21_H} A_H, \quad (6.54)$$

$$C_{Abs} = S_{21_{Cav}} T_{21_{Abs}} T_{21_H} A_H, \quad (6.55)$$

$$D_{Abs} = T_{21_{Abs}} T_{21_H} A_H, \quad (6.56)$$

where $S_{Abs+Cav}$ is the cascaded scattering matrix of the absorber and the cavity plus backshort, with the absorber scattering matrix being first in the cascading chain, $T_{21_H} = \left[I - S_{22_H} S_{11_{Abs+Cav}} \right]^{-1} S_{21_H}$ and $T_{21_{Abs}} = \left[I - S_{22_{Abs}} S_{11_{Cav}} \right]^{-1} S_{21_{Abs}}$ are the transmission matrices for the horn and the absorber also re-expressed in terms of the scattering matrices. Clearly, the power absorbed by an absorber in an open cavity can be derived in a similar way for an absorber in a waveguide.

6.4 Example case of absorber in an open cavity with infinite walls

In order to verify this method, a system consisting of a waveguide feeding an absorber cavity, with the absorber located in an open cavity with an infinite ground plane was examined. A diagram of the system can be seen in Figure 6.4.

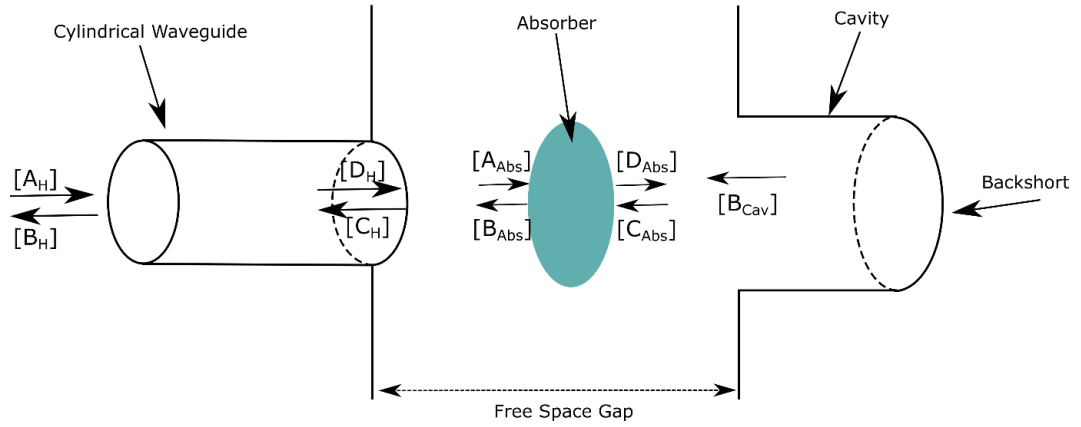


Figure 6.4: Waveguide feeding an absorber cavity with the bolometer in a free space gap

Assuming no power is lost in gap for the case of infinite walls, it is expected that the following equation will be true for the j^{th} mode at the input to the cylindrical waveguide

$$\text{Re} \left[\sum_{i=1}^N |S_{11j}|^2 Q_{ii} \right] + P_{Abs_j} = 1 \quad (6.57)$$

where $[S_{11}]$ refers to reflections at the entrance to the waveguide feeding the cavity and R_{ii} to the power associated with a mode. The first term involves summing the real reflected powers in the waveguide modes at the input port. This implies that any real power returning to the input of the waveguide added to real power absorbed at the absorber should equal to 1.

As an example to test the approach, a waveguide fed open cavity, as in Figure 6.2, was implemented in GAMMA for a millimetre-wave system. The waveguide consisted of a section 6 mm in length which had a radius of 2.5 mm. The cavity used was a cylindrical waveguide with one end closed (backshort), the length of which was 3 mm with a radius of 2.5 mm, connected to an open cavity which had a length of 3 mm. The free space walls (ground planes) were assumed to be infinite in extent at the open cavity, meaning that no power can escape through the free space gap between the perfectly electrically conducting (PEC) walls (this is only true for infinite ground plane walls, of course). An absorber of radius 5 mm and surface resistance of $188.5 \Omega/\text{Sq}$ was placed midway in the free space gap (1.5 mm from the waveguide and 1.5 mm from the cavity entrance). The number of free space modes, used in the analysis was 600, which were sampled over finely spaced radial wavenumbers separated by an amount of $\Delta k_j = 2.0$.

The frequency range investigated was 60 – 600 GHz in 1 GHz steps, where both the power reflected back through the incident waveguide and the power absorbed by the absorber were computed for various different modes at the input to the waveguide in 1 GHz steps. Modes of azimuthal orders, $n = 0, 1, 2$ and 3 were examined in particular for the cases of the TE_{01} , TE_{11} , TE_{31} , TM_{01} , TM_{11} and TM_{21} modes. Figure 6.5 to Figure 6.10 below show both the real power absorbed by the absorber and the real power reflected back to the incident waveguide. The sum of the real power absorbed and real power reflected is also displayed, which as discussed previously should equal to unity, as no power should be lost in the gap in this case, it can be seen that perfect agreement is achieved, thus verifying the GAMMA code.

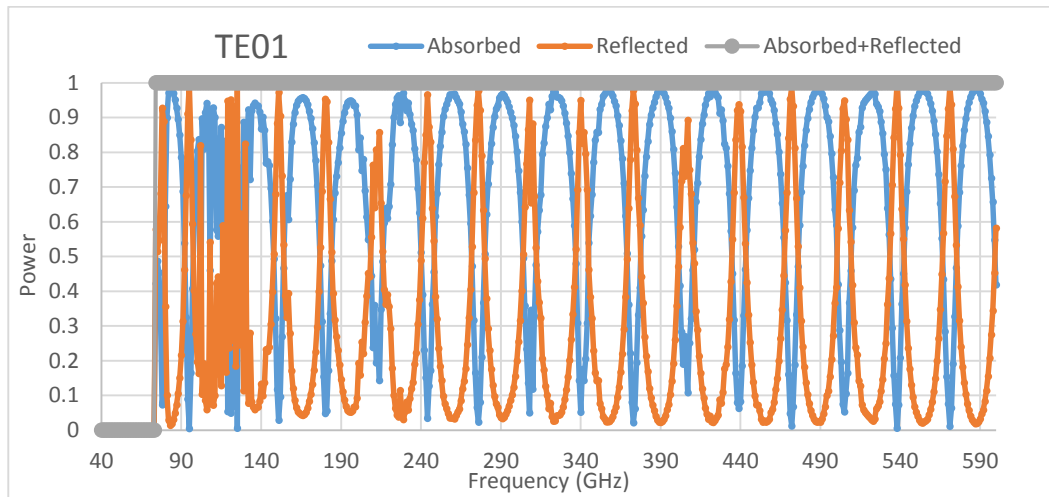


Figure 6.5: Power absorbed at the absorber (blue), power reflected back in the incident waveguide (orange) and the sum of both reflected and absorbed (grey) for a TE_{01} mode at the waveguide input

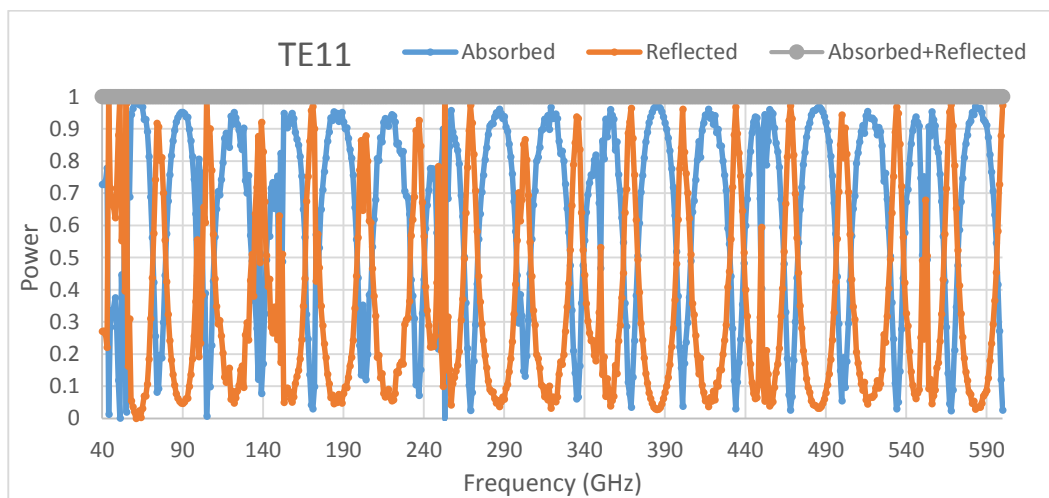


Figure 6.6: Power absorbed at the absorber (blue), power reflected back in the incident waveguide (orange) and the sum of both reflected and absorbed (grey) for a TE_{11} mode at the waveguide input

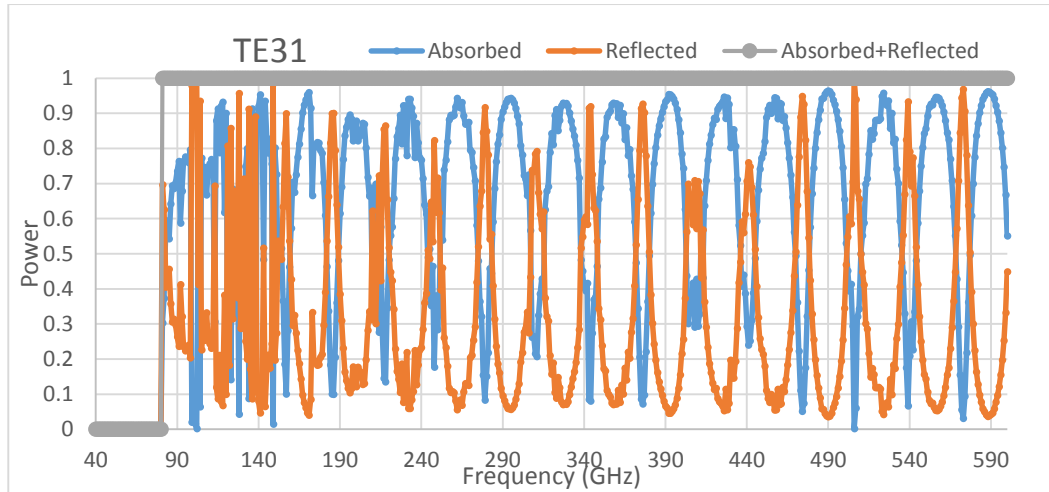


Figure 6.7: Power absorbed at the absorber (blue), power reflected back in the incident waveguide (orange) and the sum of both reflected and absorbed (grey) for a TE_{31} mode at the waveguide input

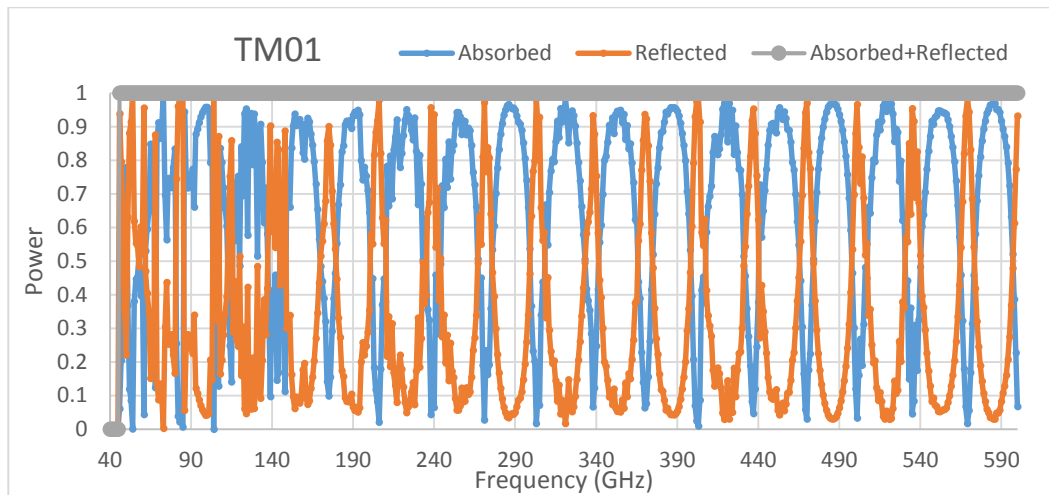


Figure 6.8: Power absorbed at the absorber (blue), power reflected back in the incident waveguide (orange) and the sum of both reflected and absorbed (grey) for a TM_{01} mode at the waveguide input

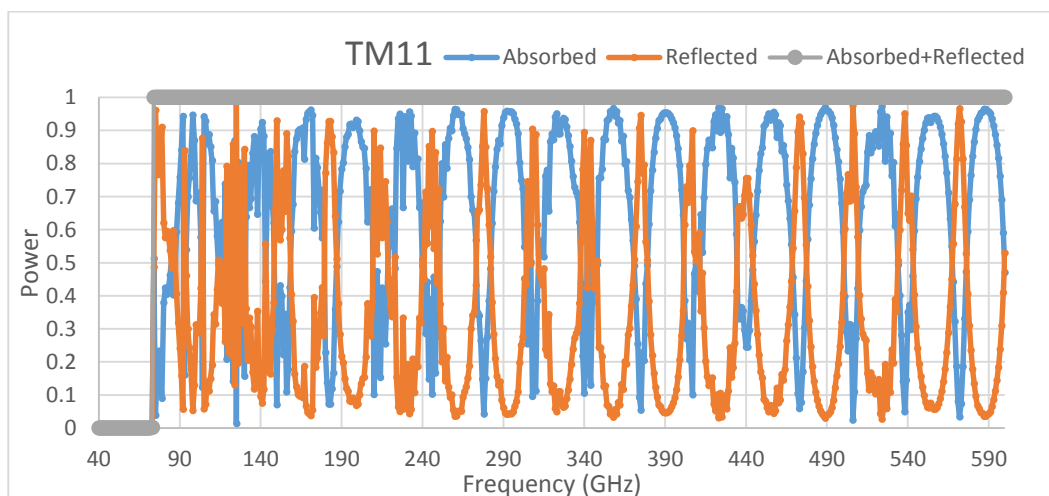


Figure 6.9: Power absorbed at the absorber (blue), power reflected back in the incident waveguide (orange) and the sum of both reflected and absorbed (grey) for a TM_{11} mode at the waveguide input

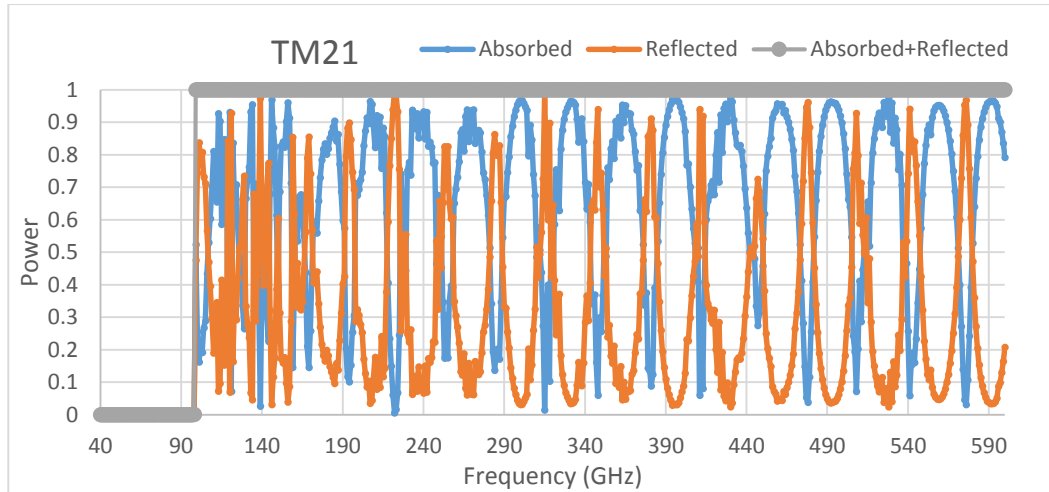


Figure 6.10: Power absorbed at the absorber (blue), power reflected back in the incident waveguide (orange) and the sum of both reflected and absorbed (grey) for a TM_{21} mode at the waveguide input

Figure 6.5 to Figure 6.10 above represent a first direct calculation of the power absorbed at the absorber. As can be seen, a significant amount of ‘ringing’ is seen in both absorbed and reflected patterns across the band for all investigated modes. This may be due to the large number of reflections present within the system since no loss is possible theoretically for the open cavity with infinite ground plane walls. This will be investigated further in the next section.

6.5 Example case of absorber in an open cavity with power loss through the gap

Clearly the case of an open cavity with infinite PEC walls is very idealized. Therefore the previous example, now with finite PEC walls, was next implemented in GAMMA, again for a millimetre wave system. Thus, a better approximation was implemented to model the open cavity by allowing for the possibility of power leaking through the region beyond the finite walls as described on page 210.

The frequency range investigated was again 60 – 600 GHz, where both the reflected power and the power absorbed by the absorber were computed for various different modes at the input to the waveguide, again, in 1 GHz steps. Modes of azimuthal orders $n = 0, 1, 2$ and 3 were examined in particular as before for the cases of the TE_{01} , TE_{11} , TE_{31} , TM_{01} , TM_{11} and TM_{21} modes. Figure 6.11 to Figure 6.16 below show the absorbed power by the absorber (blue curve), where the calculation of the absorbed power was performed

directly at the absorber, the power reflected back in the incident waveguide (orange curve) and also the power lost through the free space gap (green data points). The power lost through the free space gap was calculated by assuming conservation of power and subtracting the power absorbed by the absorber and the power reflected back at the input from 1.

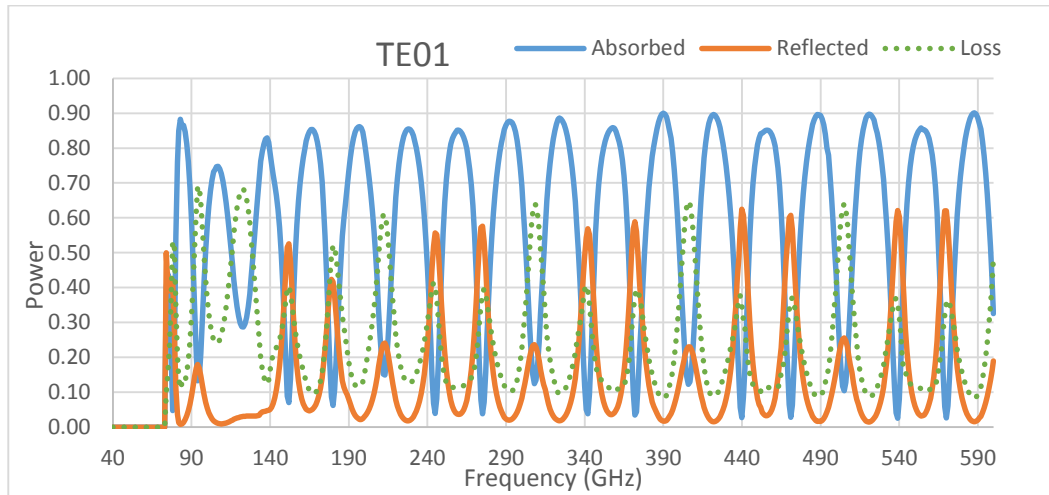


Figure 6.11: Power absorbed at the absorber (blue), power reflected back in the incident waveguide (orange) and power lost through the free space gap (green data points) for a TE_{01} mode at the input

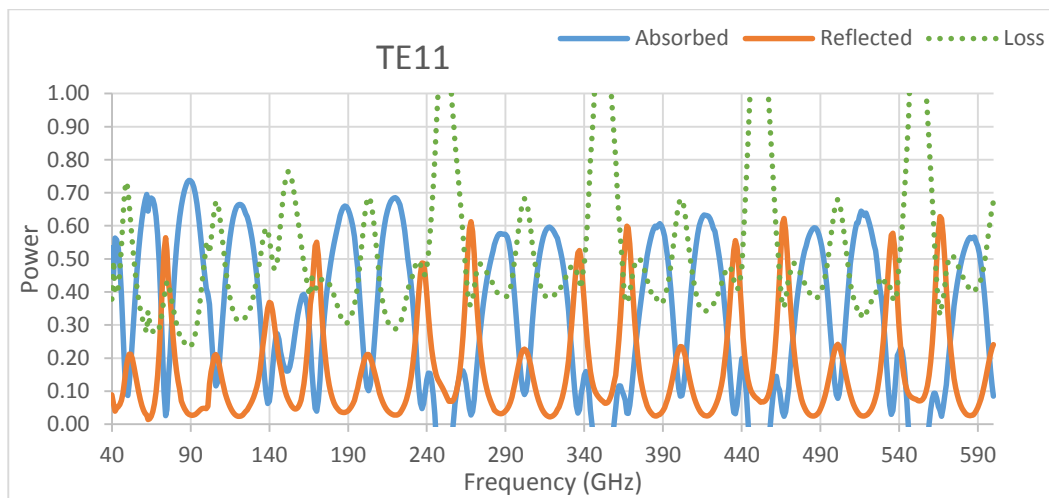


Figure 6.12: Power absorbed at the absorber (blue), power reflected back in the incident waveguide (orange) and power lost through the free space gap (green data points) for a TE_{11} mode at the input

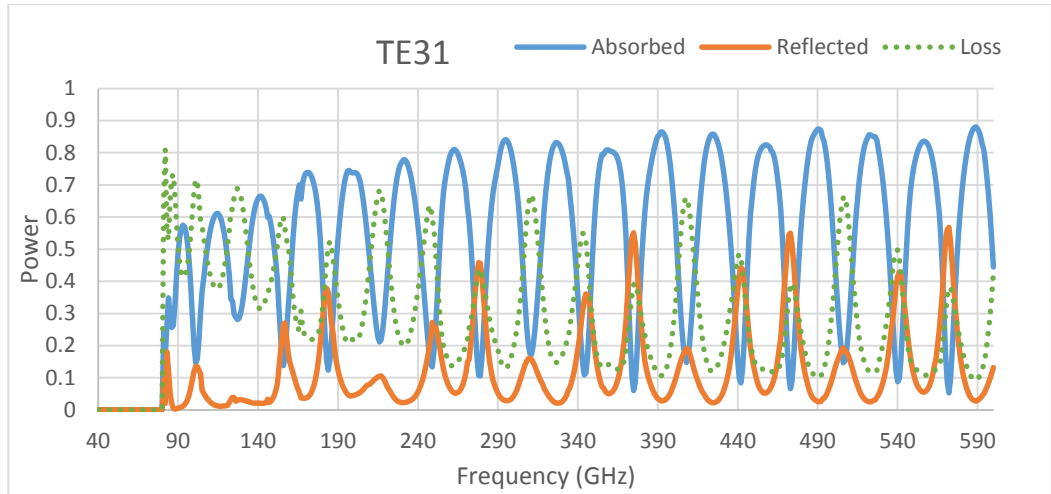


Figure 6.13: Power absorbed at the absorber (blue), power reflected back in the incident waveguide (orange) and power lost through the free space gap (green data points) for a TE_{31} mode at the input

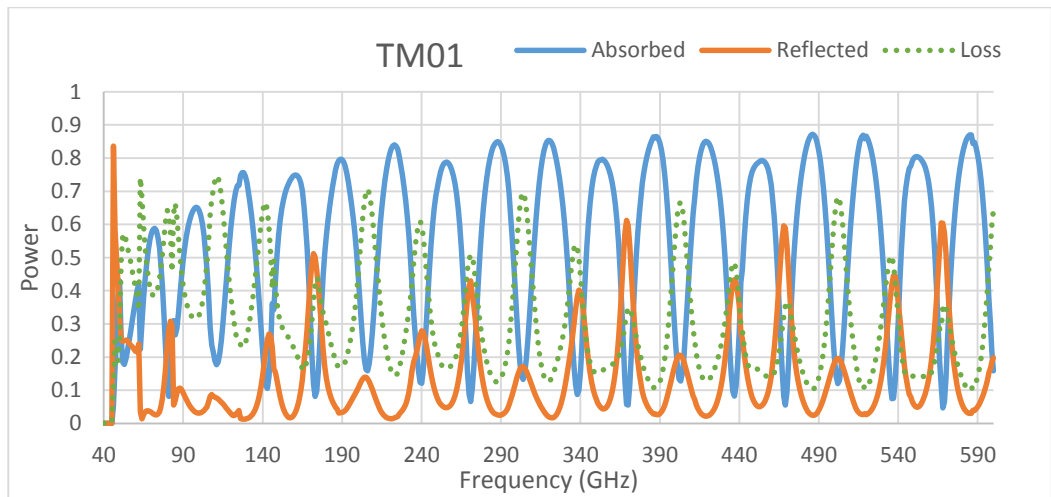


Figure 6.14: Power absorbed at the absorber (blue), power reflected back in the incident waveguide (orange) and power lost through the free space gap (green data points) for a TM_{01} mode at the input

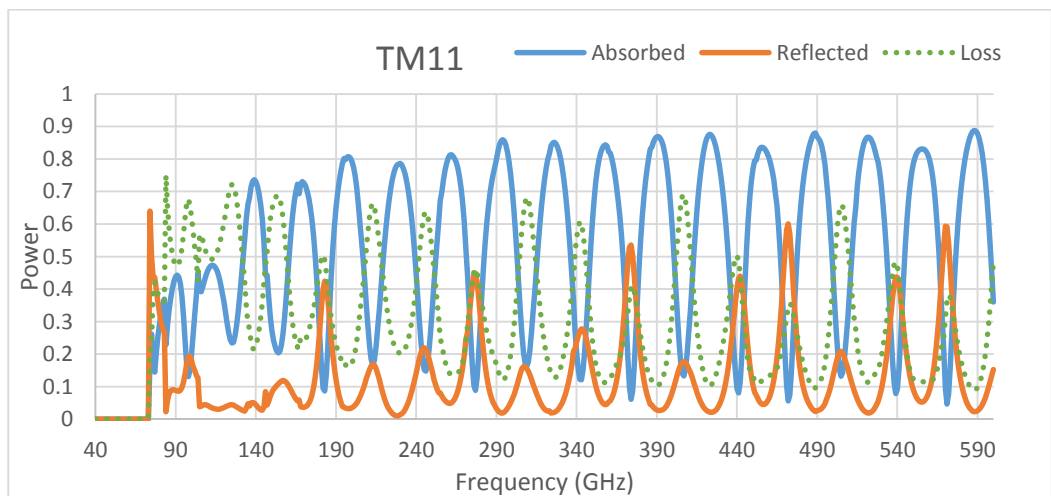


Figure 6.15: Power absorbed at the absorber (blue), power reflected back in the incident waveguide (orange) and power lost through the free space gap (green data points) for a TM_{11} mode at the input

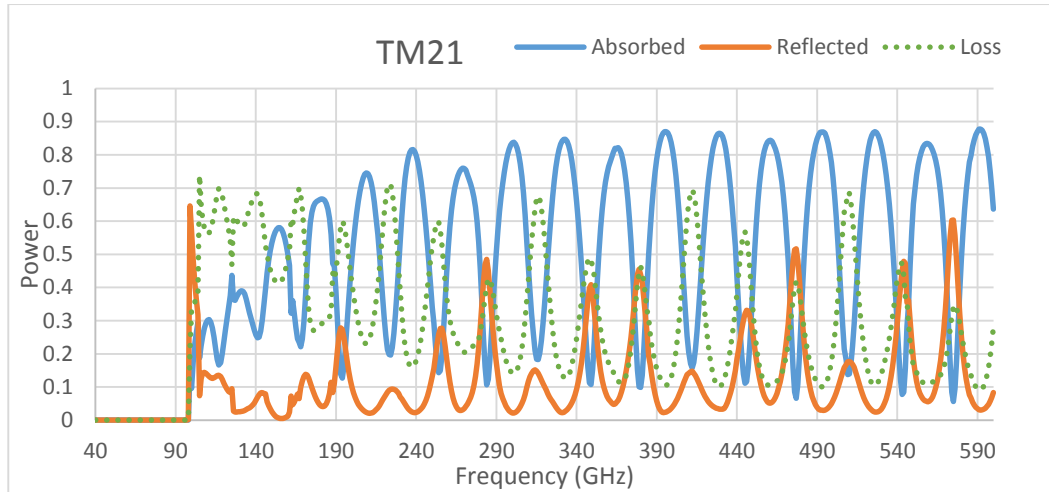


Figure 6.16: Power absorbed at the absorber (blue), power reflected back in the incident waveguide (orange) and power lost through the free space gap (green data points) for a TM_{21} mode at the input

In the finite PEC wall case, the real power reflected in the waveguide was computed from the $[S_{11}]$ matrix for the system and the real power absorbed by the absorber do not add up to unity. We can interpret the missing power as power lost in the gap. Figure 6.11 to Figure 6.16 above show the power absorbed by the absorber and power escaped through the free space gap of the open cavity. The overall reflected power back through the incident waveguide is also presented. The patterns presented in Figure 6.11 to Figure 6.16 above have no sharp ringing or resonant like features compared with those in Section 6.4, suggesting there are less multiple reflections in this system as the free space walls are now finite in length. The method implemented is still in approximation however, as we assume that there are no reflections in the region beyond the finite ground plane of radius R as discussed above. Nevertheless, the assumption of no reflections beyond the finite ground plane is a reasonable approximation.

In Figure 6.12, which displays the absorbed power at the absorber, the reflected power at the input port and power lost through the gap for a TE_{11} mode, it is observed that at some frequencies (250, 350, 450 and 550 GHz) the power absorbed by the absorber is negative, which is an unphysical result. In our model, we assume that there are no reflections at the free space plane interface beyond the region of the finite PEC walls. This interface essentially is assumed a perfect absorber which is non-physical. The feature observed in Figure 6.12 is most likely due to the approximations in the model breaking down. This we might expect if both the reflection in the waveguide and the power absorbed by the absorber are low for some physical reasons and thus there is significant power in the

region of the free space interface (which would not normally be the case). Clearly, this issue did not occur for the infinite ground plane case.

6.6 Modelling a SAFARI-like Pixel

In previous sections a generic millimetre wavelength absorbing cavity was simulated using the GAMMA software. In this section, we discuss how the techniques outlined in Section 6.2 and Section 6.3 may be applied to model a SAFARI-like pixel which operates at much higher terahertz frequencies. The pixel consists of an open hemispherical cavity backed by a multimode waveguide, with the detector placed in the free space gap of the open cavity. Figure 6.17 illustrates the pixel including the dimensions used in the analysis.

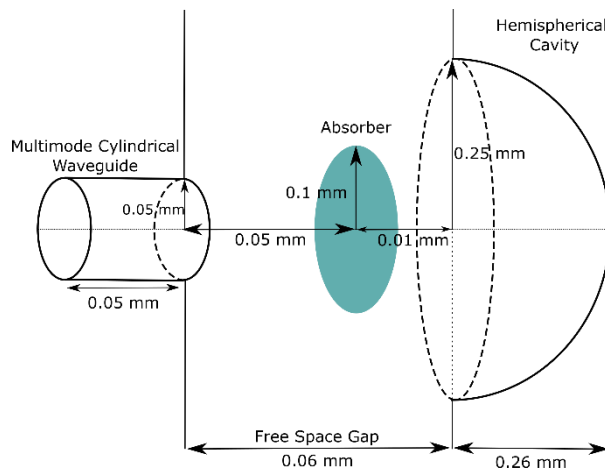


Figure 6.17: Hemispherical cavity backed by a multimode cylindrical waveguide separated by a free space gap containing the detector

The power absorbed by the absorber, the power reflected back through the incident waveguide and the power lost through the gap were obtained for the system as shown in Figure 6.17. The resistance of the absorber was set to $300 \Omega/\text{Sq}$ (assumed well matched to free space) and the investigated frequency range was 5 – 10 THz, the SAFARI S-band.

Modes of azimuthal orders $n = 0, \dots, 7$ were considered in the analysis as modes of azimuthal order $n = 7$ can propagate in the waveguide at 10 THz. Since the system is symmetric, meaning that there will be no scattering between modes of different azimuthal orders, it is the radius of the waveguide that determines how many azimuthal orders need to be considered, although the radius of the hemispherical cavity is much larger than that of the waveguide. If the absorber in Figure 6.17 was square in shape, then scattering

between modes of higher azimuthal orders would be possible and therefore more azimuthal orders would need to be considered in the analysis. Thus, higher orders generated at the absorber could potentially be capable of coupling signal power back to the detector and such modes would be trapped in the cavity (especially if it's closed or has semi-infinite walls).

However, since the example considered in this section is symmetric, the radius of the cavity provides an estimate of the minimum number of waveguide modes to be included for every azimuthal order. In this example, 40 waveguide modes (20 *TE* and 20 *TM*) were considered for every azimuthal order. The number of free space Bessel beams used in the analysis was 600, which were separated by a finite sampling interval of $\Delta k_j = 2.0$.

Figure 6.18 shows the power absorbed directly at the absorber for the *TE*₀₁, *TE*₁₁, *TE*₂₁, *TE*₃₁, *TE*₄₁, *TE*₅₁, *TE*₆₁, *TE*₇₁, *TM*₀₁, *TM*₁₁, *TM*₂₁, *TM*₃₁, *TM*₄₁, *TM*₅₁ and *TM*₆₁ modes excited at the waveguide. The frequency range investigated was 5 to 10 THz, with samples taken every 0.1 THz. It can be seen that the power absorbed by the circular absorber decreases with increasing azimuthal order. Similarly, Figure 6.19 shows the modes which were excited at the feed waveguide reflected back at the input port after propagating through the free space gap. It can be seen that the reflections are low, except for when the modes begin propagating, a maximum in the reflections is seen.

Figure 6.20 then shows the power that was lost when propagating through the free space gap for the modes excited at the input waveguide. The power lost through the free space gap was calculated by assuming conservation of power and subtracting the power absorbed by the absorber and the power reflected back at the input from 1. It can be seen that a significant amount of power escapes through the free space gap of the open cavity, particularly in the higher order modes.

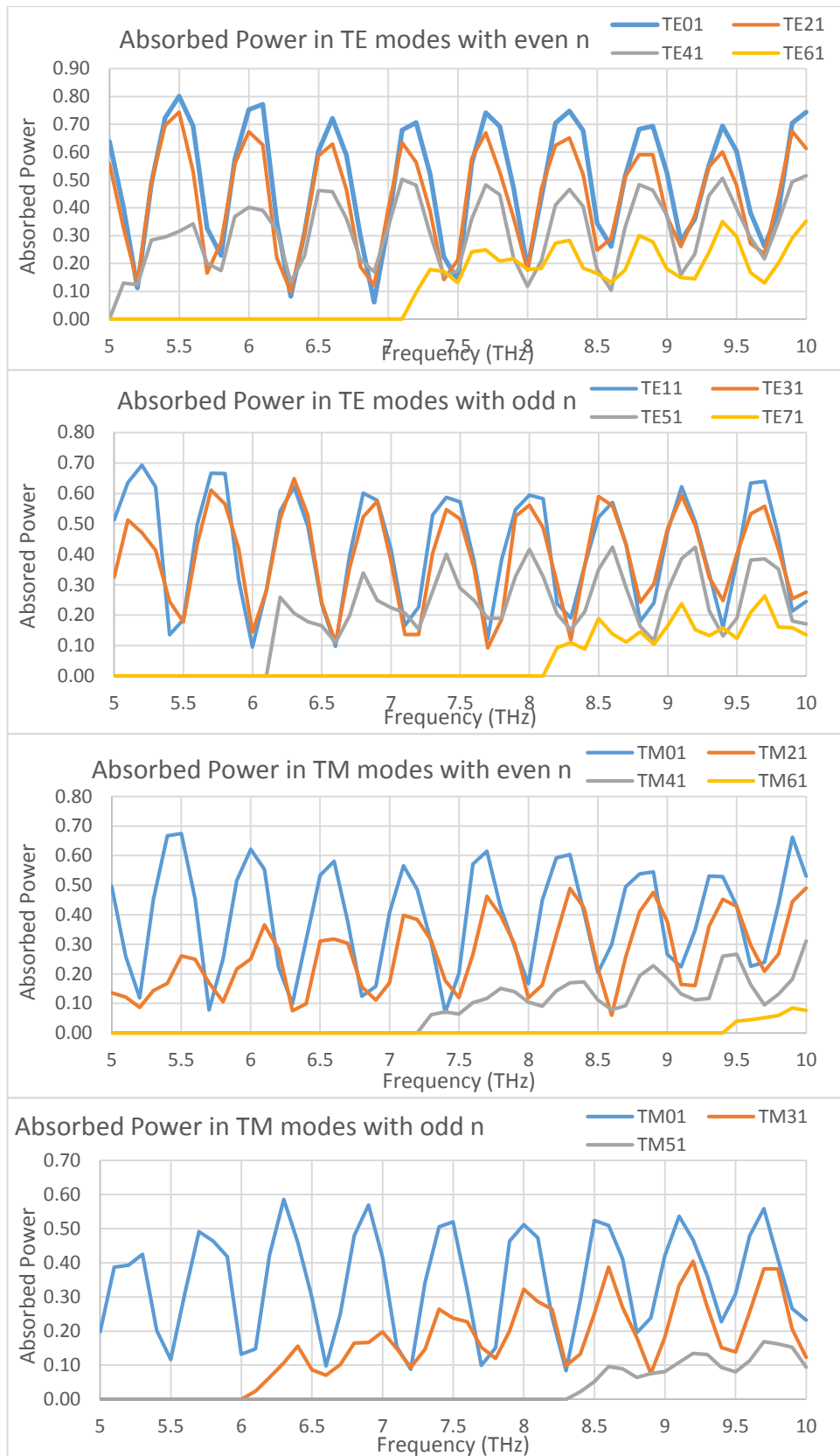


Figure 6.18: Power absorbed by the absorber for the modes excited at the input feed waveguide

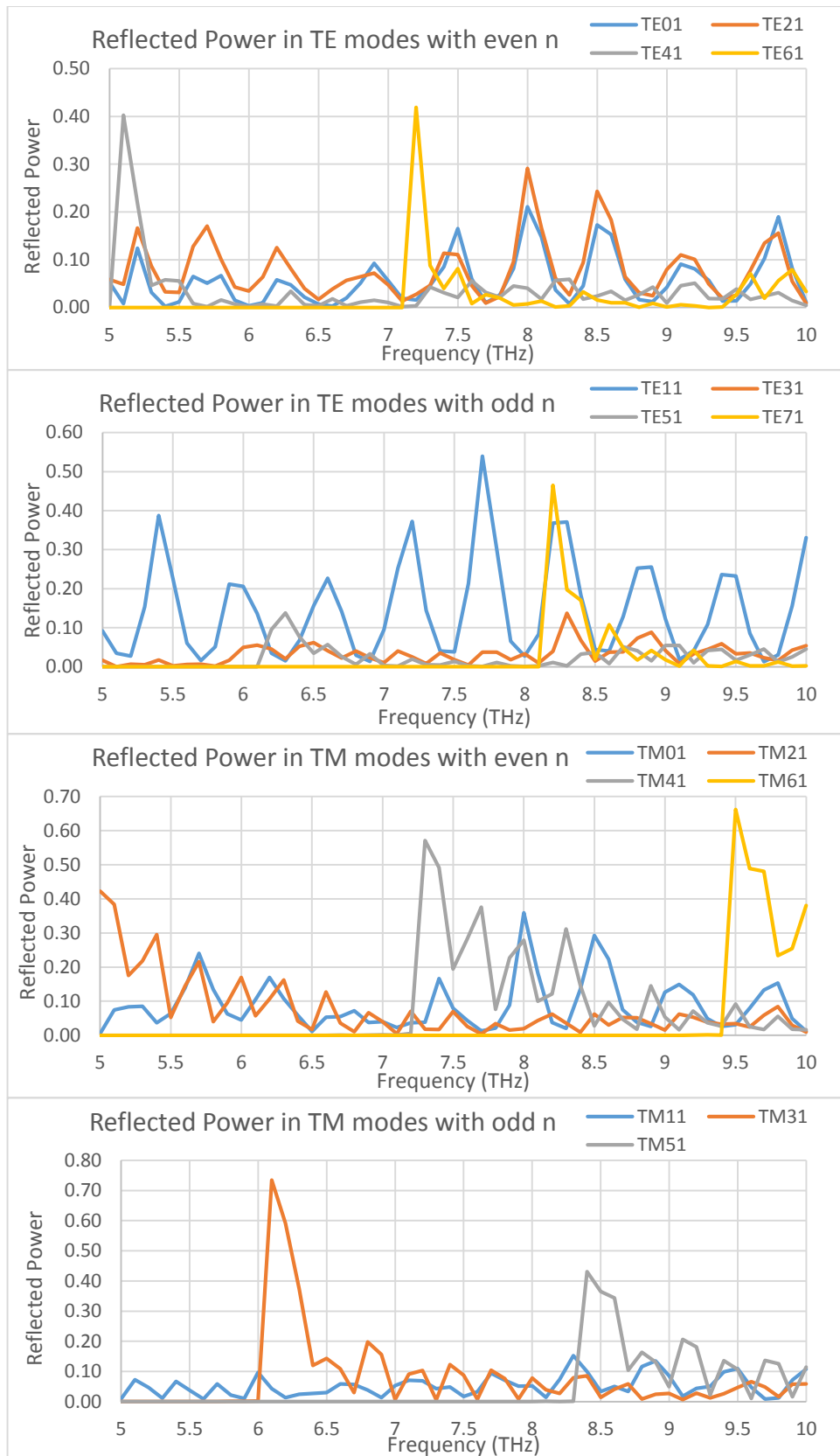


Figure 6.19: Reflected power of the excited modes back through the incident waveguide feed

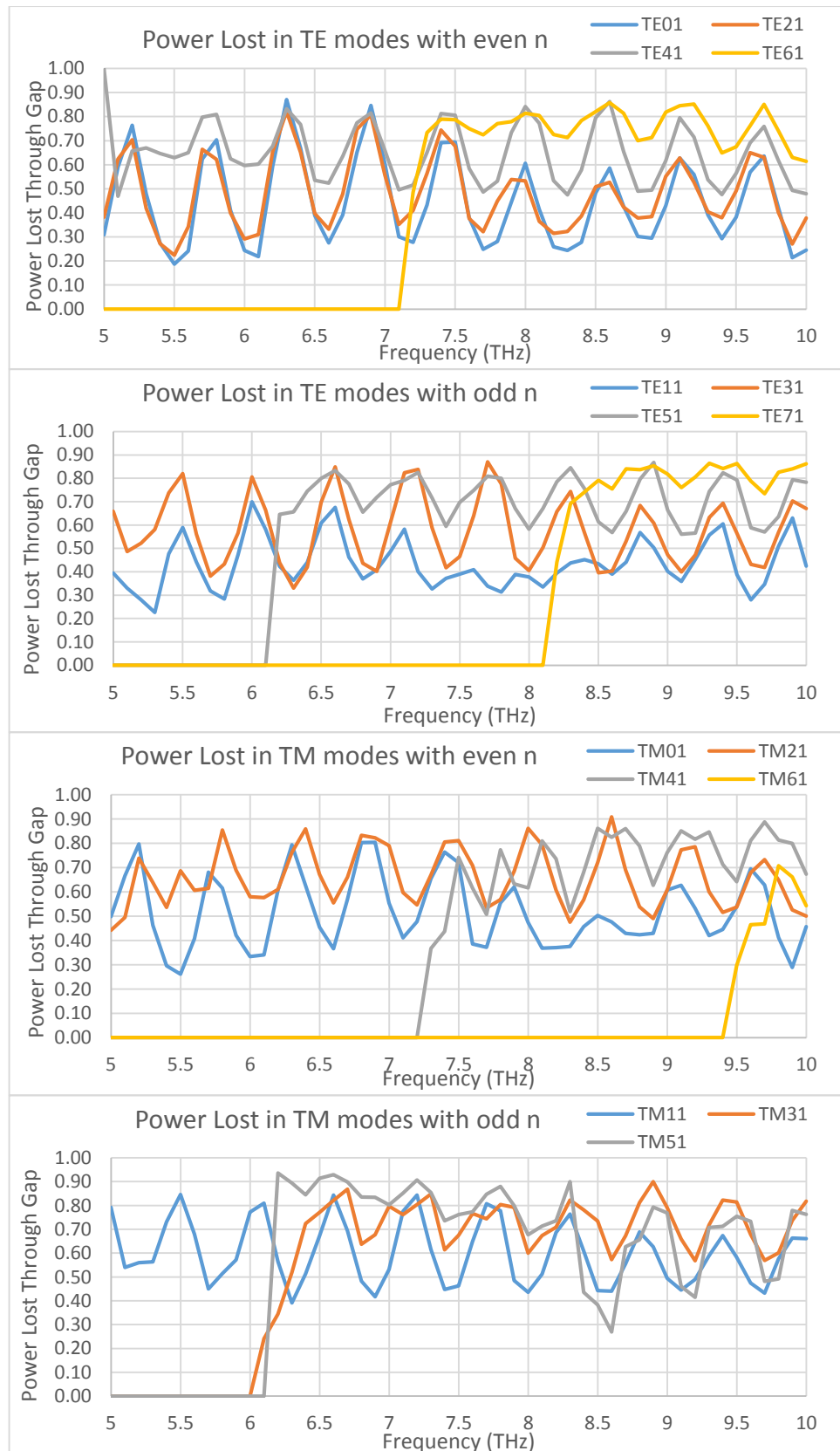


Figure 6.20: Power lost through the free space gap for the modes excited by the input waveguide feed

In this section we have presented how the approach outlined in Sections 6.2 and 6.3 can be applied to model a SAFARI-like pixel. The power absorbed at the absorber, the power

reflected back through the incident waveguide and the power lost through the free space gap of the open cavity was presented in Figure 6.18 to Figure 6.20. It is noted that the free space gap has a more dramatic effect on modes of higher azimuthal order as there seems to be more power lost through the gap. This would perhaps indicate that an absorber, for example, square in shape might perform better in terms of absorbed power. This could be investigated further in future studies for the SAFARI pixel design.

The example in Figure 6.17 was extended to include a smooth-walled conical horn antenna (instead of the waveguide only) feeding the open hemispherical cavity. The horn had a length of 9.26 mm with an aperture of 1.12 mm, a diagram of this horn can be seen in Figure 6.21.

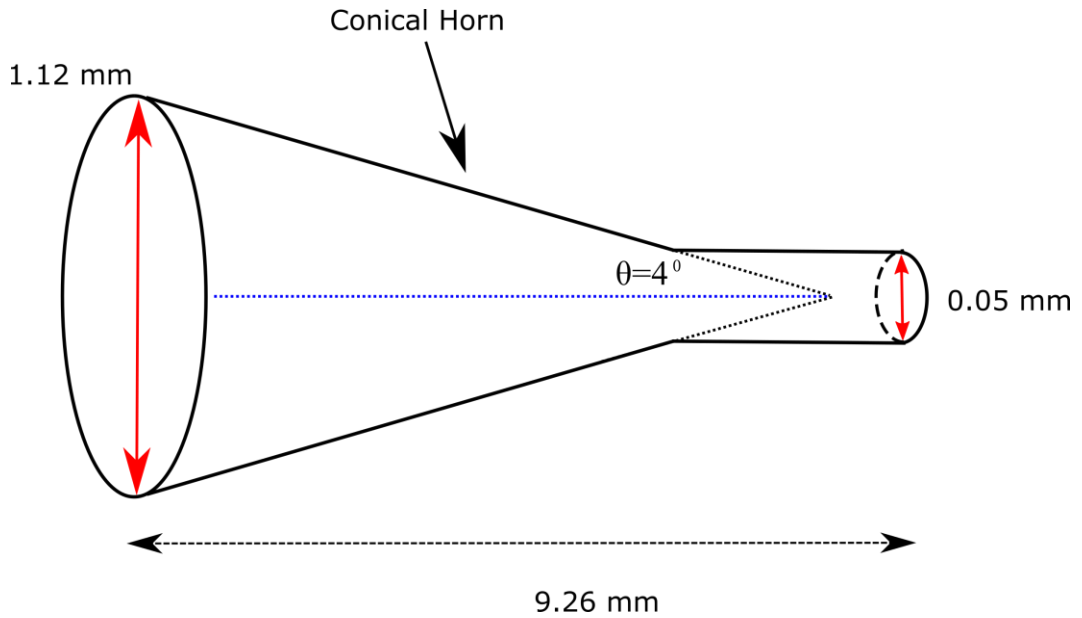


Figure 6.21: Dimensions of the conical horn used in the example in Figure 6.17

Modes of azimuthal orders $n = 0, \dots, 4$ were considered in the analysis with 40 waveguide modes (20 TE and 20 TM) considered for every azimuthal order. The number of free space modes, used in the analysis was 600, which were separated by a finite sampling interval of $\Delta k_j = 2.0$. The beam pattern in Figure 6.22 was calculated using the power absorbed directly by the absorber at 5 THz.

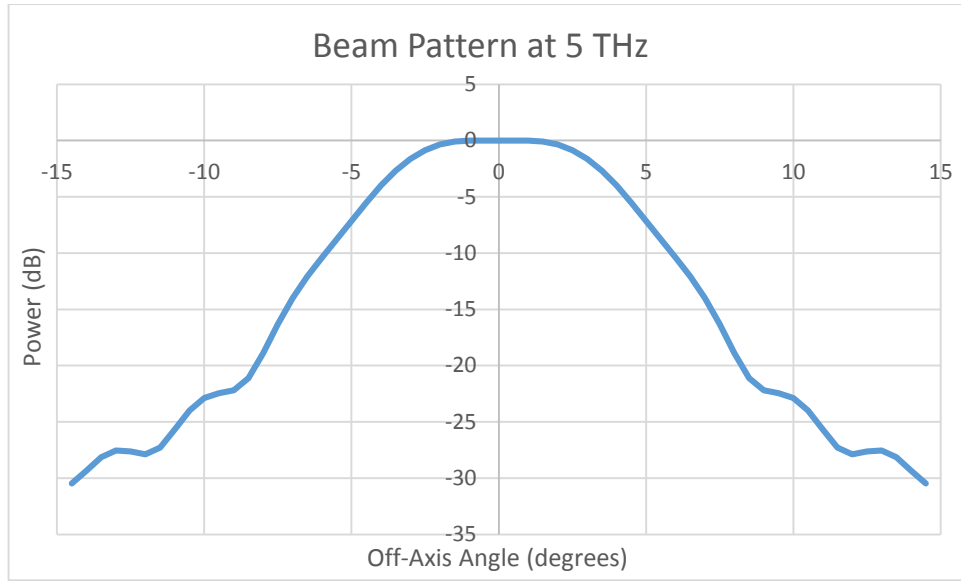


Figure 6.22: The beam pattern of a SAFARI-like pixel at 5 THz normalized to 0 dB on-axis

The above beam pattern was obtained using Equation (6.44), which directly calculates the power absorbed by an absorber in free space. The various coupling coefficients (A_H) were calculated for the various angles of horn illumination (-15 to 15 degrees), which were then used to calculate the $A(k_\rho)$, $B(k_\rho)$, $C(k_\rho)$, and $D(k_\rho)$ at the absorber. These forward and reflected coefficients were then used in the calculation of the absorbed power. The top-hat shape of the beam in Figure 6.22 clearly illustrates the multimode behaviour of this pixel.

6.7 Conclusion

In this section, we have discussed how mode matching may be used to efficiently model waveguide backed open cavities with an absorber effectively in free space. Bessel beams were used to model the modes in the free space gap (open cavity).

Previously, the $[S_{11}]$ matrix was used to model the reflected (and absorbed) power of a closed waveguide system with continuous PEC walls. However, if there was another source of loss in the system (such as a free space gap), it was impossible to distinguish between power absorbed by the absorber and power escaped through the free space gap. Thus, a technique was developed which enabled us to calculate the power absorbed directly at the absorber. This way, knowing the power absorbed by the absorber, and the power reflected back through the incident waveguide, it is possible to compute the power lost in the free space gap in a straightforward manner.

The technique was first tested by considering a waveguide backed open cavity with an absorber in free space with infinite ground plane walls. Figure 6.5 to Figure 6.10 show a significant amount of reflections present within the system (particularly in the gap), nevertheless, the sum of the absorbed and reflected power was equal to unity consistently across the frequency band investigated indicating that the infinite walls prevented any power being lost through the open walls at infinity.

An approximation was then implemented to be able to model any power loss within the gap using finite ground plane walls. Figure 6.11 to Figure 6.16 show much less reflected power into the waveguide within the system, as the power is now allowed to leak through the gap. However, as seen in Figure 6.12, the absorbed power of the TE_{11} mode is negative at certain frequencies. This may be due to the approximations applied to this modelling approach or it could be that some matrices making up the absorbed power calculations (Equations (6.53) to (6.56)) become numerically unstable.

A SAFARI-like pixel was then modelled using the techniques outlined in Sections 6.2 to 6.3. The open cavity backshort is hemispherical in this case, meaning that many waveguide modes had to be included in the analysis due to the scattering that takes place. The system was modelled by considering 8 azimuthal orders in the simulation ($n = 0, \dots, 7$), 40 waveguide modes per azimuthal order, and 600 free space modes separated by a finite sampling interval of $\Delta k_j = 2.0$. The software was able to model this system for a frequency range from 5 to 10 THz in steps of 0.1 THz in a computationally efficient and timely manner. It was also observed that the power absorbed by the absorber decreased as the azimuthal mode index was increasing. This may be due to the fact that this is a symmetric system. Future development of the software could include a study of the effects of the shape of the absorber itself. Breaking the symmetry by using, for example, a square absorber would allow for the possibility of scattering between modes of different azimuthal orders which would result in more power absorbed by the absorber (higher order modes being trapped in the cavity). Finally, the beam pattern for a potential SAFARI-like pixel was computed for an example multimode horn antenna feeding the system at 5 THz using the direct calculation of the power absorbed by an absorber in free space. This example shows how the formalism described in this chapter can be used to directly calculate the power absorbed by the detector in a realistic terahertz receiver system.

7 Conclusions

This thesis was concerned with the electromagnetic and quasi-optical modelling of millimetre wave and far-infrared receiver systems. The main driver for the work reported in this thesis was a successful proposal by Maynooth University under the ESA science programme for the Strategic Initiative for Irish Industry, Academia and Research Institutions. This proposal was concerned with the development of receiver technology for future mm-wave and far-infrared space applications. One of the work packages of the programme of work had as its main objective the development of efficient mode matching software to model electrically large horn antenna structures feeding complex cavity coupled bolometers.

In chapter 1 we provide the arguments for the need to extend the pre-existing in-house mode matching software (SCATTER) the result of which was the GAMMA (Generalised Absorber Mode Matching Analysis) software. GAMMA is structured in a similar way to SCATTER, but it is now written in Python by the author of this thesis. GAMMA is able to model electrically large structures in a more time efficient manner than the SCATTER code which runs on a Mathematica platform. As an example, both GAMMA and SCATTER were used to model the idealised HFI 857 GHz pixel with the same accuracy, with GAMMA showing a factor of 10 decrease in the time needed to do so.

In chapter 2, we present an introduction to the mode matching technique and how it is applied in the GAMMA software, which allows the performance of various horn and waveguide structures to be predicted. An introduction to the background theory of TE and TM mode analysis of waveguide structures of cylindrical and rectangular cross-sections is provided. The scattering matrix method of modelling such systems, which further allows the output field patterns of these structures to be predicted, is also outlined, with the differences in the approach for cylindrical and rectangular structures highlighted. We also outline the implementation of mode matching in cylindrical waveguides when an absorber is included and provide the analytical expressions for mode coupling at a circular absorber in circularly symmetric systems.

Utilizing the millimetre-wave measurement laboratory facility at Maynooth University Experimental Physics Department, a measurement campaign was undertaken to

demonstrate multimode propagation behaviour in a rectangular waveguide-horn antenna structure, which consisted of a back-to-back horn antenna with a waveguide filter. The extension to GAMMA to handle rectangular structures and a modification which allows for back horn illumination with an off-axis beam was also implemented and simulation was compared with the results obtained from the measurements. It was observed that the relative balance with which the modes are excited changes as a function of the illumination angle. For some angles of illumination, a clear off-axis null was observed, indicating that a higher order mode was present in the waveguide filter and interfering with the fundamental mode. The measured and experimental beams were also shown to agree well, providing some verification of the modelling process and the experiments verified the clear overmoded operation of the system.

In Chapter 3, we illustrate the horn design and quasi-optical analysis process for the specific example of the new 4 mm receiver for the Onsala Space Observatory 20 m millimetre-wave telescope, in particular also looking at manufacturing tolerance issues. Gaussian Beam Mode Analysis was used to determine the design of the receiver feed and Physical Optics was used for the analysis of the optical relay system and the telescope to determine the far-field beam on the sky.

A study was undertaken which was focused on tolerancing issues for the case of the feed horn manufacture. It was seen that they have a minimal effect on the co-polar beam patterns for the feed itself and the beams on the sky, confirming the insensitivity of the beam patterns to manufacturing errors at the millimetre wavelengths in question. This is true both for the farfield pattern of the horn and the beams on the sky. A minor effect was noticed in the cross-polar beam pattern from the horn, particularly at the band edges. Examining the cross-polar beam patterns on the sky, an increase in the peak cross-polar levels was also noted. This increase at 86 GHz was ~ 9 dB, however, this is clearly not a major disadvantage, since the peak cross-polar level is still 30 dB below the on-axis co-polar maximum.

In Chapter 4, the modelling of cavity coupled bolometers using GAMMA was discussed and the work undertaken to investigate cavity effects on the signal coupling to the bolometer was reported on, with the bolometer modelled as a thin current sheet of finite surface resistance. The predictions indicated by GAMMA were verified using CST as a benchmark. Examples of multi-moded waveguide-fed cavities were set up in both

GAMMA and CST and the results were compared for test cases where the absorber was partially and fully filling the waveguide-cavity diameter, with the agreement becoming almost perfect when a sufficient number of modes is included in GAMMA. It does, however, need to be noted that it becomes more difficult to model electrically large structures in CST compared with GAMMA, particularly for symmetric structures, and this is reflected in the time taken to run these simulations. GAMMA showed a factor of 10 decrease in the time for electrically large structures compared to CST.

We have also investigated the impact of offsetting the axis of a cylindrically symmetric cavity from that of a circular waveguide feeding it. This involved a number of changes to GAMMA, as the presence of an offset resulted in the possibility of scattering between modes of different azimuthal orders and polarisation orientations. This meant that the power coupling between modes at the junction had to be represented numerically, resulting in a larger power coupling and scattering matrices, which can no longer be split into separate azimuthal orders. The code was verified using CST for electrically compact systems but may also be applied to large multimode systems. It was shown that the offset needs to become quite large in terms of wavelength in order to see any effects on the power absorbed in the cavity.

An attempt to optimize a cavity coupled bolometer system was also carried out by varying the size, surface resistance and positioning of the absorber within the cavity. It was found that a larger absorber which is well matched to free space performs better. In terms of positioning the absorber, it was found that at a particular wavelength an absorber positioned at $\lambda/2$ (where λ is the wavelength in the centre of the band being investigated) results in least absorption and an absorber positioned at $\lambda/4$ from the cavity backshort yields the best performance. Further investigation in this matter may be required for highly overmoded designs in the future.

Another contributing factor for which power absorption was investigated was the shape of the absorber itself and GAMMA was extended to deal with arbitrary shapes, the example given being a square absorber in a cylindrical cavity. This extension to the in-house software was also verified by setting up identical simulations in GAMMA and in CST with good agreement observed between both softwares. Once the numerical approach was verified, a comparison study was carried out in GAMMA to calculate the reflected power from a waveguide housing a circular and then a square absorber, with the

absorbers positioned at the same location in the cavity and occupying the same area. It was seen that the square absorber in a circular waveguide performs generally better than a circular absorber in the same waveguide. This is to be expected of course, since having a square absorber in a circular cavity results in possibilities of power scattering between modes of different azimuthal orders, meaning that the higher order modes are trapped in the cavity and ultimately absorbed.

In Chapter 5, we discuss the application of GAMMA to model the 545 GHz and 857 GHz multimode Planck HFI pixels, with a goal to improve on the agreement between previous predictions (based on previous mode matching code) and both laboratory measurements and in-flight measurements. At first, the analysis of the idealised pixel was carried out, which was the approach taken originally in the definitions phase of the horns on the Planck project. Although the original in-house Mathematica SCATTER contained the relevant tools to perform the analysis, the large number of waveguide modes (300) required for accurate predictions meant that it is a computationally intense problem to model, thus GAMMA was used to speed up the computations. Agreement between previous predictions and the predictions made by GAMMA was observed, and thus GAMMA was used to obtain the beam patterns at a larger number of frequencies than was previously achieved.

The idealised pixel is clearly an approximation, as power carried by the individual modes may be lost through the filter gap. Thus a more rigorous approach was applied to model the gap as a waveguide section with the missing walls at the steps into the back-to-back horn and the detector horn. A change in the shapes of the beam patterns was observed, as well as a decrease in on-axis power, indicating that some power is indeed lost through the gap. The software was then modified to include an absorber in the integrating cavity and an approach based on the natural eigenfields of the absorbing cavity was implemented. The results show that the bolometer on the Planck 857 GHz pixel closely approximated an ideal blackbody source verifying previous assumptions.

We have also considered how the various levels of approximation when modelling the Planck pixel have an impact on the predictions of the beam on the sky. The analysis was initially carried out at the band edges and at the central frequency, and it was noted that the shape of the beam (its effective beam width) and the on-axis gain undergo a change when the losses in the pixel were accounted for. This analysis was extended (both for the

ideal and lossy case) to predict the sky beam patterns at more frequencies and to produce an azimuthally and band averaged beam, which was then compared with the main beam profile derived from observations of planets as indicated in the literature (Planck collaboration, 2014(VII)). Good agreement between simulations and measurements was observed down to a level of -15 dB for the 857 GHz pixel and -3 dB for the 545 GHz pixel.

GAMMA was then used for predictions of the broadband beam from the horn itself for both the 545 GHz and 857 GHz pixel, with the beam from the highest frequency channel (857 GHz) compared with pre-launch laboratory measurements carried out in Cardiff University. The poor original agreement between previous predictions and the measurements was improved with the filter losses implemented. This indicates how necessary the extra modifications introduced into GAMMA for accounting for loss are, and also for modelling the absorber more accurately in a cavity.

With the development of large detector arrays, many real systems now employ a free space gap between the feed horn and the detector cavity, with the absorber placed in the free space gap. In Chapter 6 therefore, we discuss the extension of GAMMA to be able to handle free space propagation also. Even though it is possible to model such structures in CST, the structures are electrically large and would be computationally intense to model, potentially requiring use of distributed high power computing. The modes used to represent free space propagation in GAMMA were Bessel beams. The fact that the absorber was placed in free space meant that it was necessary to calculate the power absorbed by the absorber directly and this also allows for the possibility to distinguish between power absorbed by the absorber and power lost through the free space gap.

In the process of verifying the techniques outlined in chapter 6, we have considered an example of a millimetre-wave system where the free space PEC walls were assumed infinite in extent, meaning that the absorber was the only source of power loss in the system and what was not absorbed was reflected back to the input port. We then modified the technique to be able to approximately model finite length PEC free space walls, thus introducing another loss mechanism in the system. The big achievement is that we are now able to differentiate between the two different means of power loss present in the system. In both examples a large number of free space modes (600) was used and

GAMMA was able to produce results for a large number of frequency samples (540) with reasonable computation times.

We then proceeded to include a model of a terahertz system, a SAFARI-like pixel, which consisted of an overmoded input feed and a hemispherical multimode cavity backshort, separated by a free space gap with the absorber placed midway in the gap. The simulations were carried out using a single computer with moderate processing power. The analysis was performed from 5 THz to 10 THz and the absorber was assumed to be circular. The results show that with increasing azimuthal order the power absorbed by the absorber decreases and more power is lost through the free space gap, rather than reflected back to the input port. This may be due to the fact that the system is symmetric, for example placing a square absorber in the free space gap may result in the possibility of power scattering between modes of different azimuthal orders (for example higher order modes scatter into lower order modes) and yield better performance in terms of absorbed power as was seen in waveguide systems. This is something that will be optimized in any real detector design in the future.

Finally, an example of a multimode horn feeding an open cavity with the absorber placed in a free space gap (essentially a SAFARI-like pixel) was considered. The beam pattern was produced at 5 THz and the forward and reflected coefficients were calculated directly at the absorber and in turn used to produce the beam pattern. The beam exhibits a top-hat shape, clearly indicating the multimode behaviour of the pixel considered. The example illustrates the power of the approach presented in this thesis, for directly predicting the power absorbed by a terahertz detector in a likely configuration in next generation systems.

One possibility of improving on the efficiency of GAMMA in the future is the implementation of dynamic calculation of the number of modes needed to represent each section in a horn antenna. In the current version of GAMMA, the same number of modes are used to represent each side of a junction. Smaller waveguide sections (in terms of wavelength) do not need to be represented with the same number of modes as larger waveguide sections (except if the smaller waveguide section is housing an absorber, particularly if the absorber is partially filling the structure), as stated by (James, 1981) the number of modes needed to accurately model a waveguide section is approximately 10 times the ratio of the waveguide diameter to the wavelength.

Currently GAMMA is capable of coupling cylindrical waveguide modes to free space Bessel beams, thus, another area where the capabilities of the software may be extended is to be able to model rectangular horns feeding open hemispherical (or pyramidal, cylindrical, *etc.*) cavities. This would require analytical expressions to represent the coupling of rectangular modes to free space Bessel beams for speedy computations. Similarly, GAMMA could be extended to be able to model absorbers of arbitrary shape in free space. This would involve extending the code to model absorbers of arbitrary shape in waveguides.

We have discussed the development and extension of the in-house mode matching software GAMMA and applied it to improve on the agreement between simulations and measurements of existing systems and showed how the advancement of previous code capabilities can be used for efficient modelling of future systems. Some suggestions to develop the code in the future and some possible applications were outlined also. For example, since GAMMA can model misalignments between waveguide sections, this feature of the software can potentially be applied to tolerance analysis of section misalignment using the stacked rings approach, such as those designed for the QUBIC (Qubic Collaboration, 2011) project.

In summary, this thesis has essentially been concerned with the development of fast and efficient Python code (GAMMA) for more complete modelling of the kinds of waveguide – horn feed structures with the cavity coupled bolometric detectors that are being suggested for future millimetre-wave and astronomical receivers. Such hypersensitive systems will be required to answer current open questions in astronomy concerning star and planetary formation, solar system physics as well as galaxy evolution and interaction.

8 References

Ade P.A., Wyld R.J., Zhang J., ‘Ultra-Gaussian Horns for Clover – a B-Mode CMB Experiment’. 20th International Symposium on Space Terahertz Technology, 2009.

Audley M.D., de Lange G., Gao, J.-R., Khosropanah P., Mauskopf P.D., Morozov D., Trappe N.A., Doherty S., Withington S., ‘Optical characterization of ultra-sensitive TES bolometers for SAFARI’. Proceedings Volume 9153, Millimeter, Submillimeter, and Far-Infrared Detectors and Instrumentation for Astronomy VII; 91530E (2014). DOI: 10.1117/12.2056037

Audley M.D., de Lange G., Gao J.-R., Khosropanah P., Hijmering R., Ridder M.L., ‘Optical performance of prototype horn-coupled TES bolometer arrays for SAFARI’ Proceedings Volume 9914, Millimeter, Submillimeter, and Far-Infrared Detectors and Instrumentation for Astronomy VIII; 991408 (2016). DOI: 10.1117/12.2231088

Balanis, C.A., ‘Advanced Engineering Electromagnetics’, Wiley, 2012

Bersanelli, M., Mandolesi, N., Butler, R. C., *et al.*, ‘Planck pre-launch status: Design and description of the Low Frequency Instrument’, *Astronomy & Astrophysics*, Volume 520, Article Number: A4, Published: 2010, DOI: 10.1051/0004-6361/200912853

Bogges, N. W., Mather, J. C., Weiss, R., *et al.*, ‘The COBE Mission: Its Design and Performance Two Years After the Launch’, *Astrophysical Journal*, Volume 397(2), Published: 1992, DOI: 10.1086/171797

Bracken, C., ‘Electromagnetic Techniques for Analysis and Design of Ultra Sensitive Receivers for Far-Infrared Astronomy’, Ph.D. Thesis, NUI Maynooth, 2015

Carroll B.W., Ostlie D.A., ‘An Introduction to Modern Astrophysics’ 2nd Edition, Pearson Education, 2007

Church S., *et al.* ‘QUEST and DASI: A South-Pole CMB polarisation experiment.’ *New Astron. Revs*, 47:1083-1089, 2003.

Clarricoats, P.J.B., ‘Corrugated Horns for Microwave Antennas’, Peter Peregrins (for IEE), 1984

Colgan R., 'Electromagnetic and quasi-optical modelling of horn antennas for far-IR space applications'. Ph.D. Thesis, NUI Maynooth, 2001.

CST Website, 'CST – Computer Simulation Technology', <http://cst.com>, 2017

Dexheimer S.L., 'Terahertz Spectroscopy : Principles and Applications'. CRC Press, 2008

Dicke R., Peebles P., Roll P., Wilkinson D., 'Cosmic Black-Body Radiation' The Astrophysical Journal (142), 414-419, 1965.

Doherty, S., 'Optical and Quasi-Optical Design and Analysis of Astronomical Instrumentation including a Prototype SAFARI Pixel', Ph.D. Thesis, NUI Maynooth, 2012

Dole H., Lagache G., *et al.*, 'The Cosmic Infrared Background Resolved by Spitzer. Contributions of Mid-Infrared Galaxies to the Far-Infrared Background', eprint arXiv:astro-ph/0603208

Downey P.M., Jeffries A.D., Meyer S.S., Weiss R., Bachner F.J., Donnelly J.P., Lindley W.T., Mountain R.W., Silversmith D.J., 'Monolithic silicon bolometers', Applied Optics 23, 910-914, 1984

Doyle S., 'Lumped Element Kinetic Inductance Detectors', Ph.D. Thesis, Cardiff University, 2008

ESA Website, 'Herschel Fact Sheet', <http://sci.esa.int/herschel/47356-fact-sheet/>, 2010

ESA Website, 'M51, Comparing Herschel/PACS and Spitzer/MIPS', <http://sci.esa.int/herschel/45073-m51-with-herschel-pacs-and-spitzer-mips/>, 2009

ESA Website, 'Multi Wavelength view of Messier 16', <http://sci.esa.int/herschel/49866-multi-wavelength-view-of-messier-16/>, 2012

Gleeson, E., 'Single and Multi-moded Corrugated horn Design for Cosmic Microwave Background Experiments', Ph.D. Thesis, NUI Maynooth, 2004

Gleeson E. *et al.*, 'Corrugated waveguide band edge filters for CMB experiments in the far infrared', Infrared Phys. Technol. 46, 493, 2005.

Goldsmith, P.F., 'Quasioptical Systems', IEEE Press, 1998

- GRASP9, Reference Manual. TICRA Engineering Consultants, 2010.
- Griffiths D.J., 'Introduction to Electrodynamics', Prentice Hall international editions, 1999
- James G.L., 'Analysis and design of TE_{11} to HE_{11} corrugated cylindrical waveguide mode converters.' IEEE Trans. MTT, 29:1059-1066, 1981.
- Johansen P.M., 'Uniform physical theory of diffraction equivalent edge currents for implementation in general computer codes'. Antennas and Propagation Society International Symposium. Volume 2 (784-787), 1996.
- Lamarre, J.-M., Puget, J.-L., Ade, P. A. R., *et al.*, 'Planck pre-launch status: The HFI instrument, from specification to actual performance', Astronomy & Astrophysics, Volume 520, Article Number: A9, Published: 2010, DOI: 10.1051/0004-6361/200912975
- Lesurf J., 'Millimetre-wave optics, Devices and Systems'. IOP Publishing Ltd., 1990.
- Liddle A., 'An Introduction to Modern Cosmology', Wiley, 2003
- Maffei B., Ade P., Tucker C., Wakui E., Wylde R., Murphy J.A., Colgan R. 'Shaped corrugated horns for cosmic microwave background anisotropy measurements.' International Journal of Infrared and Millimeter Waves, 21(12): 2023-2033, 2000.
- Maffei B. *et al.*, 'Planck-HFI beam expectations from the optical optimisations of the focal plane', Astronomy & Astrophysics, 520, A12 ,2010.
- Maffei B., Gleeson E., Murphy J.A., Pisano G., 'Study of corrugated Winston horns', Proc. SPIE 5498, Millimeter and Submillimeter Detectors for Astronomy II, 8212, 2004.
- Mandolesi, N., & Smoot, G. F. 1993, Proposal for COBRAS – the Cosmic Background Anisotropy Satellite, submitted to ESA in 2003 in answer to the M3 call for mission ideas
- McAuley I., 'Analysis and Measurement of Horn Antennas for CMB Experiments', Ph.D. Thesis, Maynooth University, 2015.
- Murphy, J.A., Egan, A., 'Examples of Fresnel diffraction using Gaussian modes', Eur. J. Phys, 1993
- Murphy, J. A., *et al.*, 'Multi-mode horn design and beam characteristics for the Planck satellite', Journal of Instrumentation, 2010 (5), DOI: 10.1088/1748-0221/5/04/T04001

Murphy, J. A., *et al.*, 'New developments in waveguide mode-matching techniques for far-infrared astronomy', SPIE 8261, Terahertz Technology and Applications V, 82610F (2 March 2012); DOI: 10.1117/12.908068.

Murphy, J.A., *et al.*, 'Radiation patterns of multi-mode corrugated horns for far-IR space applications', *Infrared Phys. Technol.*, 2001 (42), DOI:

NASA Website, 'COBE', <http://science.nasa.gov/missions/cobe>, 2016

NASA Website, 'Wilkinson Microwave Anisotropy Probe', <http://map.gsfs.nasa.gov>, 2017

Neugebauer G., Habing H.J., *et al.* 'The Infrared Astronomical Satellite (IRAS) mission', *Astrophysical Journal* (278), L1-L6, 1984. DOI: 10.1086/184209

Nystrom, O., 'Design, Characterization, and Calibration of Low-Noise Terahertz Receivers', PhD Thesis, Chalmers University of Technology, 2011

Olver A.D., Clarricoats P.J.B., Kishk A.A., Shafai L., 'Microwave Horns and Feeds', IEEE Press, 1994

Onsala Space Observatory, 'Technical description (20 m telescope)'. <https://www.chalmers.se/en/researchinfrastructure/oso/radioastronomy/20m/Pages/Description.aspx> , 2018a

Onsala Space Observatory, '3/4 mm Receiver Onsala 20 m Antenna'. <https://www.chalmers.se/en/projects/Pages/34-mm-Receiver-Onsala-20m-Antenna.aspx>, 2018b

O'Sullivan C., Murphy J.A., 'Field Guide to Terahertz Sources, Detectors, and Optics', SPIE Field Guides, Volume FG28, 2012.

Penzias A., Wilson R., 'Measurement of Excess Antenna Temperature at 4080 Mc/s'. *The Astrophysical Journal* (142), 419-421, 1965.

Pilbratt G., 'Herschel space observatory mission overview', *Astronomical Telescopes and Instrumentation*, pp. 586-597, International Society for Optics and Photonics, 2003.

- Planck Collaboration, 'Planck 2013 results. I. Overview of Products and Scientific Results', *Astronomy and Astrophysics*, Volume 571, Article Number: A1, Published: 2014, DOI: 10.1051/0004-6361/201321529
- Planck Collaboration, 'Planck 2013 results. VII. HFI time response and beams', *Astronomy and Astrophysics*, Volume 571, Article Number: A7, Published: 2014, DOI: 10.1051/0004-6361/201321535
- Planck Collaboration, 'Planck 2013 Results. XI. All-sky model of thermal dust emission', *Astronomy & Astrophysics* (571) A11 (2014(XI))
- Planck Collaboration, 'Planck 2015 Results. XXXVIII. The Planck Catalogue of Galactic Cold Clumps', *Astronomy & Astrophysics* (594) A27 (2016(XXXVIII))
- Pontoppidan K., 'GRASP9: Technical Description', TICRA, 2005
- Pozar D.M., 'Microwave Engineering', Wiley, 2012
- Puget, J. L. 1993, Proposal for SAMBA – the SATellite Measurements of Background Anisotropies, submitted to ESA in 2003 in answer to the M3 call for mission ideas
- Puget J.-L., Abergel A., Bernard J.-P., Boulanger F., Burton W.B., Desert F.-X., Hartmann D., 'Tentative detection of a cosmic far-infrared background with COBE', *Astronomy & Astrophysics* (308), 1996
- Python Software Foundation. Python Language Reference, version 3.1. Available at <http://www.python.org>
- QUBIC collaboration, 'QUBIC: The QU Bolometric Interferometer for Cosmology', *Astroparticle Physics*, Vol 34 (9), 2011
- Ramo S., Whinnery J.R., Van Duzer T., 'Fields and Waves in Communication Electronics', Wiley, 1994
- Smoot G., Bennet C., *et al.*, 'Structure in the COBE Differential Microwave Radiometer First-Year Maps', *The Astrophysical Journal* (396) 1-5, 1992
- SPICA Website, 'A window on the cold Universe: the SPICA mission', <http://www.spica-mission.org/>, 2017

Tauber, J. A., Norgaard-Nielsen, H. U., Ade, P. A. R., *et al.*, ‘Planck pre-launch status: The Planck mission’, *Astronomy & Astrophysics*, Volume 520, Article Number: A1, Published: 2010, DOI: 10.1051/0004-6361/200912983

TICRA. GRASP9. Available at <http://www.ticra.com>

Trappe, N., Murphy, J. A., Withington, S., *et al.*, ‘Gaussian beam mode analysis of standing waves between two coupled corrugated horns’, *IEEE Transactions on Antennas and Propagation*, Volume 53, Published: 2005, DOI: 10.1109/TAP.2005.846453

Walker, G., ‘Design and Analysis of the Onsala 4 mm Receiver and other Antenna Configurations for Millimetre Wave Astronomy’, MSc Thesis, Maynooth University, 2016

Wexler A., ‘Solutions of waveguide discontinuities by modal analysis’, *IEEE Transactions on Microwave Theory and Techniques*, MTT-15 (9),508-517, 1967.

Wilson D., ‘Quasi-Optical Modelling of Telescope Systems for Planck and STEAMR’, Ph. D. Thesis, NUI Maynooth, 2014.

Wolfram Research, Inc., *Mathematica*, Version 10.1

Wylde R.J., Martin D.H., ‘Gaussian Beam-Mode Analysis and Phase-Centers of Corrugated Feed Horns’. *IEEE Transactions on Microwave Theory and Techniques*. Volume 41 (A10), 1993.

Publications

Kalinauskaitė, E., Murphy, J.A., *et al*, ‘Radiation patterns of multimode feed-horn-coupled bolometers for FAR-IR space applications’, *Terahertz, RF, Millimeter and Submillimeter-Wave Technology and Applications X*, Proceedings of SPIE Vol. 10103, 101030N (2017), DOI: 10.1117/12.2249869

Kalinauskaitė, E., Murphy, J.A., *et al*, ‘Modelling multimode feed-horn coupled bolometers for millimetre-wave and terahertz astronomical instrumentation’, *Millimeter, Submillimeter and Far-Infrared Detectors and Instrumentation for Astronomy VIII*, Proceedings of SPIE Vol. 9914 (2016), DOI: 10.1117/12.2231444

Walker, G.W., Kalinauskaitė, E., *et al*, ‘Optical design and verification of a 4mm receiver for the 20m telescope at Onsala Space Observatory’, *Millimeter, Submillimeter and Far-Infrared Detectors and Instrumentation for Astronomy VIII*, Proceedings of SPIE Vol. 9914 (2016), DOI: 10.1117/12.2232576

Burke, D., Gayer, D., *et al*, ‘Optical modelling and analysis of the Q and U bolometric interferometer for cosmology’, *Terahertz, RF, Millimeter and Submillimeter-Wave Technology and Applications XI*, Proceedings of SPIE Vol. 10531 (2018), DOI: 10.1117/12.22871

